Multiscale Modeling and Optimization of Flow Batteries: From Electrode Microstructure to Cell-Scale Design

Zur Erlangung des akademischen Grades eines

DOKTORS DER INGENIEURWISSENSCHAFTEN (DR.-ING.)

von der KIT-Fakultät für Chemieingenieurwesen und Verfahrenstechnik des
Karlsruher Instituts für Technologie (KIT)

genehmigte

DISSERTATION

von

Amadeus Wolf, M. Sc.
aus Pforzheim

Tag der mündlichen Prüfung:	15.05.2025
Erstgutachter:	Prof. Dr.-Ing. habil. Hermann Nirschl
Zweitgutachter:	Prof. Dr. rer. nat. habil. Wolfgang Bessler

Acknowledgement

This thesis was created during my time as a research associate at the Institute of Mechanical Process Engineering and Mechanics (MVM) at the Karlsruhe Institute of Technology. In the following, I would like to thank those people who have made a significant contribution to its success.

I would like to express my deep gratitude to Prof. Dr.-Ing. habil. Hermann Nirschl for the trust placed in me over the years. I particularly appreciate the freedoms granted in combination with a consistently open ear for problems and discussions. Thank you for giving me the opportunity to do my PhD. I also would like to sincerely thank Prof. Dr. rer. nat. habil Wolfgang Bessler for taking over the co-lecture of the dissertation.

Sincere appreciation is extended to Assoc. Prof. Em. William C. Rose for the fruitful discussion on data fitting. The collaboration with Dr. M. J. Krause has been an enriching experience, and his expertise on mathematical optimization has significantly shaped the outcome of our publication. Special thanks go to Adj. Assoc. Prof. Dr.-Ing. Jens Noack for his expertise in flow batteries, which greatly improved the quality of our research. I also want to thank Prof. Dr. Emmanuel Baudrin for providing experimental data and fruitful discussions on organic flow battery systems.

Warmest thanks go to all employees of the MVM for creating a supportive and inspiring work environment, with special appreciation to the administration department, Ms. Schnepf, Ms. Schwab, and Ms. Samur for their invaluable assistance and dedication behind the scenes. The professional and personal exchange with doctoral colleagues during seminars, conferences, coffee breaks and leisure activities was not only important for the progress of this work, but also made the time at MVM unforgettable. The many friendships that have developed and continue to exist during my time at the institute are the most valuable achievements of my doctoral studies. Special thanks go to my office colleagues Felix Gerbig, Susanne Kespe and Kirsten Ullmann for the time spent together. A huge thanks to Anshuman Chauhan, Timo Dobler, Lucas Jakob, Benjamin Radel, Felix Reinke and Tolga Yildiz for the countless lunch breaks that were always the highlights of my day, filled with great discussions, laughter, and much-needed distractions from work. My thanks go to the CoT.

On top of this, heartfelt appreciation goes to my friends and family for their unwavering support, patience, and encouragement throughout this journey.

I gratefully appreciate the financial support for this work by the European Union's Horizon 2020 Research and Innovation Programme under Grant Agreement no. 875489. Special thanks goes to the whole SONAR project consortium.

The author acknowledge support by the state of Baden-Württemberg through bwHPC.

The author acknowledges that this work has utilized generative AI technology, specifically ChatGPT and DeepL, to improve the spelling and general readability. The AI support was supervised by the author, who ensured the accuracy and integrity of the final content.

Abstract

This dissertation focuses on the multiscale modeling and optimization of flow batteries. Specifically, it includes the development of a three-dimensionally resolved microstructural model of the flow battery electrode and the creation of a framework for topology and shape optimization at the two-dimensional cell level. In addition, a multiscale modeling approach was developed to couple the models at different scales using the mass transfer coefficient.

The microstructural model was developed to improve the understanding of the complex interactions between electrode structure, electrolyte flow, and electrochemical reactions. The computational domain represents an excerpt of the flow battery half-cell at the micrometer scale. The model resolves the real microstructure of the graphite felt electrode and the electrolyte region separately, solving the physical and electrochemical processes in these regions using distinct equations. Additionally, the current collector is explicitly modeled, while the membrane is incorporated as a boundary condition. Electrolyte flow is described using the Navier-Stokes equations, and the mass transport equation accounts for the convection, diffusion, and migration of chemical species. Charge conservation and transport are computed in both the solid and liquid regions of the model. At the interface, the electrochemical reaction is described using the Butler-Volmer equation, which also serves to couple the regions. The numerical solution of the model equations is based on the finite-volume method. The model can be adapted to various material systems. In this study, the focus is on the vanadium system and the novel organic MV/TEMPOL system. It provides detailed distributions of current density, voltage, electrolyte velocity, and species concentration within both regions and their interface, as well as the overall half-cell potential at the current collector.

A reconstruction process was developed to accurately represent the real microstructure of the graphite felt electrode in a digital twin. Micro-computed tomography images of the felt were captured and subsequently converted into a computational grid suitable for simulations. The model was successfully validated using polarization curves, employing various flow battery models and experimental data from the MV/TEMPOL system.

The developed computational model was initially tested with simplified cylindrical electrode designs and the TEMPOL system to investigate the effects of varying active electrode surface areas and concentrations on the half-cell potential. Designs with larger active surface areas exhibited higher half-cell potentials at the same current density because of reduced overpotentials. However, the increased surface area also resulted in higher pressure losses due to increased flow resistance. Furthermore, higher concentrations of active material in the electrolyte led to lower overpotentials, as improved conductivity facilitated electrochemical processes.

Investigations using the digital twin of the microstructure were focused on the TEMPOL system, analyzing the distribution of active material, current density, and potentials as a function of different flow rates. An optimal Reynolds number of approximately 10^{-2} was identified, ensuring the minimum flow rate necessary to maintain a sufficient half-cell potential, regardless of the state of charge. At low electrolyte concentrations (0.1 M TEMPOL in 1 M NaCl) and high current densities ($80\,\mathrm{mA\,cm^{-2}}$), mass transport limitations were observed, leading to a decline in performance. In contrast, at low current densities ($20\,\mathrm{mA\,cm^{-2}}$), the initial concentration and flow rate did not have a significant impact on the power density. A structured cylindrical fiber electrode design of the same size and active surface area as the digital twin exhibited slight differences in velocity and concentration profiles. However, because of its regular structure, this domain demonstrated superior mass transport properties and higher performance under identical operating conditions.

To bridge the gap between microscale and homogenized cell-scale modeling, an innovative multiscale modeling approach was developed, utilizing mass transfer coefficients. A 2D half-cell model with homogenized properties was created, incorporating Brinkman-type Navier-Stokes equations and a transport equation for a single species in porous media. The reaction term is based on a simplified approach that employs mass transfer coefficients extracted from the microscale model. Parameterization was carried out under operating conditions of 0.1 M TEMPOL in 1 M NaCl and a discharge current density of $80\,\mathrm{mA\,cm^{-2}}$ at various velocities. This approach enables a more accurate prediction of species conversion and reveals significantly faster conversion rates compared to empirical correlations from the literature. The results suggest reducing cell height and using additional information from the microscale model to further optimize cell performance.

In addition, an optimization framework for topology and shape optimization at the cell-scale was developed and successfully integrated with the described 2D cell-scale model. The underlying optimization problem is based on a multi-objective functional aimed at minimizing the pressure drop within the cell while maximizing the reaction rate in the electrode.

Topology optimization was employed to determine an optimal porosity distribution within the electrode. Various porosity intervals were investigated, with a linear inverse relationship defined between porosity and active surface area. The results demonstrated that, under certain operating parameters, a distinct porosity distribution is more effective than a homogeneous porosity. The optimization favored a structure with low porosity values and increased surface area immediately behind the inlet regions of the electrode, while the transition to higher porosity values occurred abruptly in the lower third of the electrode. The resulting design with a two-part porosity distribution was compared to electrodes with homogeneous porosity and showed superior performance under specific operating conditions. Furthermore, topology optimization was applied to novel cell designs from the literature. These studies confirmed a tendency towards a porosity distribution similar to that of the standard design.

Shape optimization focused on investigating the optimal geometric parameters of the cell design in line with the objective function, while maintaining uniform electrode porosity. For rectangular and trapezoidal cell designs with porosities below 0.9, the optimization showed a preference for a horizontal orientation due to the lower pressure drop. For radial cell designs, optimization consistently identified the maximum possible angle as optimal, as it most effectively reduced the pressure drop by expanding the flow cross section.

Zusammenfassung

Die vorliegende Arbeit befasst sich mit der multiskaligen Modellierung und Optimierung von Flow-Batterien. Konkret umfasst dies die Entwicklung eines dreidimensional aufgelösten Mikrostrukturmodells der Flow-Batterie-Elektrode sowie die Entwicklung eines Frameworks zur Topologie- und Formoptimierung auf der zweidimensionalen Zellebene. Zusätzlich wurde ein Multiskalenansatz erarbeitet, der die verschiedenskaligen Modelle mithilfe des Massentransferkoeffizienten miteinander koppelt.

Das Mikrostrukturmodell wurde entwickelt, um die komplexen Wechselwirkungen zwischen der Elektrodenstruktur, der Elektrolytströmung und der elektrochemischen Reaktion besser zu verstehen. Die Berechnungsdomäne bildet einen Ausschnitt der Flow-Batterie-Halbzelle im Mikrometermaßstab nach. Dort werden die reale Mikrostruktur der Graphitfilzelektrode und der Elektrolytbereich separat aufgelöst und die dort stattfindenden physikalischen und elektrochemischen Prozesse mit unterschiedlichen Gleichungen gelöst. Zusätzlich wird der Stromabnehmer mit aufgelöst, wohingegen die Membran als Randbedingung berücksichtigt wird. Zur Beschreibung der Elektrolytströmung werden die Navier-Stokes-Gleichungen genutzt und die Gleichung für den Massentransport berücksichtigt Konvektion, Diffusion und Migration der chemischen Spezies. Der Erhalt und Transport von Ladung wird in den festen und flüssigen Regionen des Modells gleichermaßen berechnet. An der Grenzfläche wird die elektrochemische Reaktion mittels der Butler-Volmer-Gleichung beschrieben, die außerdem zur Kopplung der Regionen dient. Die numerische Lösung der Modellgleichungen basiert auf der Finite-Volumen-Methode. Das Modell kann auf verschiedene Stoffsysteme angepasst werden. In dieser Arbeit liegt der Fokus auf dem Vanadium- und dem neuartigen, organischen MV/TEMPOL-System. Es liefert eine detaillierte Verteilung von Stromdichte, Spannung, Elektrolytgeschwindigkeit und Spezieskonzentration in beiden Regionen und deren Übergangsfläche, sowie ein generelles Halbzellenpotenzial am Stromabnehmer.

Ein Rekonstruktionsprozess wurde entwickelt, um die reale Mikrostruktur der Graphitfilzelektrode in einem digitalen Zwilling präzise abzubilden. In diesem wurden Aufnahmen des Filzes mit Mikro-Computertomographie getätigt und diese in ein für die Simulation geeignetes Rechengitter transferiert. Das Modell wurde zudem erfolgreich mit Polarisationskurven validiert, wobei sowohl verschiedene Flow-Batterie-Modelle als auch experimentelle Daten des organischen MV/TEMPOL-Systems herangezogen wurden.

Das entwickelte Rechenmodell wurde zunächst mit vereinfachten, zylinderförmigen Elektrodendesigns und dem TEMPOL-System getestet, um die Auswirkungen verschiedener aktiver Elektrodenoberflächen und Konzentrationen auf das Halbzellenpotenzial zu untersuchen. Designs mit größerer aktiver Oberfläche zeigten bei gleicher Stromdichte ein höheres Halbzellenpotenzial aufgrund geringerer Überpotenziale. Gleichzeitig führte die größere Oberfläche jedoch zu einem erhöhten Druckverlust infolge des höheren Strömungswiderstands. Zudem führten höhere Konzentrationen von Aktivmaterial im Elektrolyten zu geringeren Überpotenzialen, da die verbesserte Leitfähigkeit die elektrochemischen Prozesse begünstigte.

Untersuchungen mit dem digitalen Zwilling der Mikrostruktur fokussierten sich auf das TEMPOL-System und analysierten die Verteilung von Aktivmaterial, Stromdichte und Potentialen in Abhängigkeit von unterschiedlichen Volumenströmen. Eine optimale Reynolds-Zahl von etwa 10^{-2} wurde identifiziert, die unabhängig vom Ladungszustand den geringstmöglichen Volumenstrom für eine ausreichende Halbzellenspannung gewährleistet. Bei niedrigen Elektrolytkonzentrationen ($0.1\,\mathrm{M}$ TEMPOL in $1\,\mathrm{M}$ NaCl) und hohen Stromdichten ($80\,\mathrm{mA\,cm^{-2}}$) wurden Massentransportlimitierungen beobachtet, die zu einer Leistungsabnahme führten. Im Gegensatz dazu zeigte sich bei niedrigen Stromdichten ($20\,\mathrm{mA\,cm^{-2}}$) kein signifikanter Einfluss von Anfangskonzentration und Volumenstrom auf die Leistungsdichte. Ein strukturiertes, zylinderförmiges Elektrodendesign mit gleicher Größe und aktiver Oberfläche wie der digitale Zwilling wies leichte Unterschiede in den Geschwindigkeits- und Konzentrationsprofilen auf. Dank der regelmäßigen Struktur zeigte diese Domäne jedoch bessere Massentransporteigenschaften und eine höhere Performance unter gleichen Betriebsbedingungen.

Um die Lücke zwischen der Mikroskala- und der homogenisierten Zellskala-Modellierung zu schließen, wurde ein innovativer Multiskalenmodellierungsansatz entwickelt, der auf der Verwendung von Massentransferkoeffizienten basiert. Hierzu wurde ein 2D-Halbzellmodell mit homogenisierten Eigenschaften entwickelt, das die Brinkmann-Typ Navier-Stokes Gleichungen sowie eine Transportgleichung für eine einzelne Spezies in porösen Medien integriert. Der Reaktionsterm basiert auf einem vereinfachten Ansatz, der den aus dem Mikroskalenmodell extrahierten Massentransferkoeffizienten verwendet.

Die Parametrisierung erfolgte unter Betriebsbedingungen mit $0.1\,\mathrm{M}$ TEMPOL in $1\,\mathrm{M}$ NaCl und einer Entladestromdichte von $80\,\mathrm{mA\,cm^{-2}}$ bei verschiedenen Geschwindigkeiten. Der Ansatz ermöglicht eine genauere Vorhersage der Speziesumwandlung und zeigt im Vergleich zu empirischen Korrelationen aus der Literatur eine deutlich schnellere Umwandlung. Basierend auf den Ergebnissen empfiehlt sich eine Reduzierung der Zellhöhe sowie eine intensivere Nutzung zusätzlicher Informationen aus dem Mikroskalenmodell, um die Zellleistung weiter zu optimieren.

Zusätzlich wurde ein Optimierungsframework für die Topologie- und Formoptimierung auf der Zellskala entwickelt und erfolgreich mit dem beschriebenen 2D Zellskala-Modell kombiniert. Das zugrunde liegende Optimierungsproblem basiert auf einer zweiteiligen Zielfunktion, die darauf abzielt, den Druckabfall innerhalb der Zelle zu minimieren und gleichzeitig die Reaktionsrate in der Elektrode zu maximieren.

Die Topologieoptimierung wurde eingesetzt, um eine optimale Porositätsverteilung innerhalb der Elektrode zu ermitteln. Dabei wurden verschiedene Porositätsintervalle untersucht, wobei eine linear inverse Beziehung zwischen Porosität und aktiver Oberfläche definiert wurde. Die Ergebnisse zeigten, dass unter bestimmten Betriebsparametern eine gezielte Porositätsverteilung effektiver ist als eine homogene Porosität. Die Optimierung bevorzugte eine Struktur mit niedrigen Porositätswerten und erhöhten Oberflächenbereichen unmittelbar hinter den Einlassbereichen der Elektrode, während der Übergang zu höheren Werten abrupt im unteren Drittel der Elektrode erfolgte. Das resultierende Design mit einer zweiteiligen Porositätsverteilung wurde mit Elektroden mit homogener Porosität verglichen und zeigte unter bestimmten Betriebsbedingungen eine überlegene Performance. Darüber hinaus wurde die Topologieoptimierung auf neuartige Zelldesigns aus der Literatur angewendet. Dabei bestätigte sich die Tendenz zu einer ähnlichen Porositätsverteilung wie bei dem Standarddesign, was die Robustheit und Übertragbarkeit des Ansatzes unterstreicht.

Die Formoptimierung untersuchte die geometrischen Parameter des Zelldesigns unter Berücksichtigung der Zielfunktion, wobei die Porosität der Elektrode einheitlich blieb. Bei rechteckigen und trapezförmigen Zelldesigns mit einer Porosität von unter 0.9 zeigte die Optimierung eine Präferenz für ein Design im Querformat aufgrund des geringeren Druckverlusts. Für das radiale Zelldesign identifizierte die Optimierung stets den maximal möglichen Winkel als Optimum, da dies den Druckverlust durch die Erweiterung des Strömungsquerschnitts am effektivsten reduzierte.

Contents

Abbreviations and Symbols

Abbreviations

0D	zero-dimensional
1D	one-dimensional
2D	two-dimensional
3D	three-dimensional
CNRS	French National Centre for Scientific Research
CoV	coefficient of variation
EU	European Union
FB	flow battery
FEM	finite element method
FVM	finite volume method
HCSM	homogenized cell-scale model
ICT	Fraunhofer Institute for Chemical Technology
LBM	lattice Boltzmann method
MSM	microscale model
MV	methyl viologen
OAT	one at a time
OCV	open circuit voltage
OFB	organic flow battery
RoC	rate of conversion
SFD	structured fiber domain
SHE	standard hydrogen electrode
SNOPT	sparse nonlinear optimizer
SOC	state of charge
SONAR	Modeling for the search for new active materials for redox flow batteries
TEMPOL	4-hydroxy-2,2,6,6-tetramethylpiperidinyloxyl
VFB	vanadium flow battery
µCT	micro-computed tomography

Symbols

Latin Symbols and Variables

A	Area	$(\mathrm{mm^2})$
A_V	Specific surface area	$(\mathrm{m^{-1}})$
C, c	Concentration	$(\mathrm{M}, \mathrm{mol\,m^{-3}})$
d_f	Fiber diameter	(m)
$d_i^{(j)}$	Elementary effect	(–)
D	Reference domain	(–)
D_e	Effective diffusivity	$(\mathrm{m^2\,s^{-1}})$
D_i	Diffusivity	$(\mathrm{m^2\,s^{-1}})$
F	Faraday constant $\approx 96\,485$	$(\mathrm{C\,mol^{-1}})$
f	State	(–)
h	Height	(mm)
i, i^+	Active species	(–)
$\mathbf{J}$	Current density	$(\mathrm{mA\,cm^{-2}})$
j	Generic species	(–)
K	Permeability	$(\mathrm{m^2})$
k_m	Mass transfer coefficient	$(\mathrm{m\,s^{-1}})$
k	Reaction rate constant	$(\mathrm{m\,s^{-1}})$
P	Power dissipation	(W)
p	Pressure	(Pa)
p_c	Contraction point	(–)
p_e	Expansion point	(–)
p_r	Reflection point	(–)
Q	Flow rate	$(\mathrm{mL\,min^{-1}})$
q	Darcy penalization factor	(–)
R_{min}	Filter radius	(–)
R	Universal gas constant ≈ 8.314	$(\mathrm{J\,mol^{-1}\,K^{-1}})$
Re	Reynolds number	(–)
E^0	Standard redox potential	(V)
$\mathbf{S}$	Strain rate tensor	$(\mathrm{s^{-1}})$
s_1	Scaling factor = 1	$(\mathrm{m^3\,s\,mol^{-1}})$
s_2	Scaling factor = 1	$(\mathrm{W^{-1}})$
T	Temperature	(K)
t	Time	(s)

T_ψ	Deformation function	(–)
U	Velocity magnitude	($\mathrm{m\,s^{-1}}$)
$\mathbf{u}$	Velocity vector	($\mathrm{m\,s^{-1}}$)
V	Volume	($\mathrm{m^3}$)
$\mathbf{x}$	Position in reference domain	(–)
$\mathbf{X}$	Input parameters	(–)
$\mathbf{Y}$	Output parameters	(–)

Greek Symbols and Variables

α	Reaction rate parameter	(–)
α_a	Anodic transfer coefficient	(–)
α_c	Cathodic transfer coefficient	(–)
β	Reaction rate parameter	(–)
β_o	Projection slope	(–)
$\chi(x)$	Characteristic function	(–)
τ	Viscous stress	($\mathrm{N\,m^{-2}}$)
Δ	Step in OAT	(–)
ϵ	Porosity	(–)
η	Overpotential	(V)
γ	Control	(–)
κ_e	Electrolyte conductivity	($\mathrm{S\,m^{-1}}$)
κ_s	Electrode (solid) conductivity	($\mathrm{S\,m^{-1}}$)
ν	Kinematic viscosity	($\mathrm{m^2\,s^{-1}}$)
λ	Control variable	(–)
μ	Mean value	(–)
Ω_i	Structured electrode domains $i = 1,2,3$	(–)
Ω	Subset of material points	(–)
ϕ_e	Electrolyte potential	(V)
ϕ_s	Electrode potential	(V)
ϕ	Potential	(V)
ψ	Control variable	(–)
ρ	Density	($\mathrm{kg\,m^{-3}}$)
σ	Standard deviation	(–)
θ_β	Projection point	(–)
θ_c	Raw control variable	(–)
θ_f	Filtered material volume factor	(–)
θ_P	Penalized material volume factor	(–)

Subscripts

a	Anodic	(–)
act	Activation	(–)
BV	Butler-Volmer	(–)
c	Raw control, cathodic or concentration	(–)
cc	Current collector	(–)
conc	Concentration	(–)
d	Dissipation	(–)
e	Electrolyte	(–)
ext	External	(–)
f	Filtered or fiber	(–)
h	Horizontal	(–)
i	Number of inputs and outputs	(–)
j	Amount of steps in OAT measurement	(–)
m	Mass transfer	(–)
max	Maximum	(–)
mem	Membrane	(–)
min	Minimum	(–)
ohm	Ohmic	(–)
opt	Optimized quantity	(–)
ox	Oxidation	(–)
P	Penalized	(–)
red	Reduction	(–)
s	Solid	(–)
T	TEMPOL	(–)

Superscripts

b	Bulk	(–)
s	Surface	(–)

Other

$\mathcal{G}$	Constraint or side condition	(–)
$\mathcal{J}$	Multi-objective functional	(–)
$\langle\ \rangle$	Volume average	(–)
$\overline{}$	Dimensionless	(–)

1 Introduction and Motivation

1.1 Motivation

The electrical grid is the foundation of the modern industrial world, providing the infrastructure necessary for the distribution of electricity that powers industries, homes, and technological advancements. As the global community faces the pressing challenge of the climate crisis, there is a significant push to transform the grid from the reliance on fossil fuels to renewable energy sources [1]. This transition is essential to reduce greenhouse gas emissions and promote sustainable energy practices. However, the inherent intermittency and variability of renewable energy sources, such as solar and wind, create a critical need for high-performance and cost-effective energy storage technologies to store fluctuating energy and stabilize the grid [2].

Among various energy storage options, batteries have gained increasing popularity due to their flexibility, mobility, and cost-effectiveness. Unlike pumped hydro storage, which requires specific geographical conditions and substantial infrastructure, batteries can be deployed in a wide range of locations and scales [3].

Flow batteries, in particular, are becoming prominent due to their applicability across a wide energy range of the grid infrastructure. The unique concept of the flow battery (FB) is based on the spatial separation of the electrolyte and the electrode, which allows for the independent scalability of power and capacity [4, 5]. This design offers greater flexibility in meeting local grid requirements and is strongly in contrast to other energy storage technologies. The battery works according to the basic principle of the galvanic cell, but stores energy in liquid, water-based electrolytes with dissolved redox-active species that are pumped through an electrochemical cell. In addition, flow batteries boast long operating life cycles, environmental friendliness, and non-flammability, making them a safer and more sustainable choice compared to other predominant storage systems [6, 7]. These advantages position flow batteries as a key technology in supporting the transition to a renewable energy-based electrical grid.

Despite their potential, flow batteries face several general challenges. Most materials used in flow batteries have been limited to transition metal redox couples, such as the most common vanadium flow battery (VFB) [5, 8, 9]. Although these systems have shown promise by the absence of material degradation and capacity fade [10, 11], they still struggle with comparatively high prices and enormous price fluctuations in terms of the electrolyte [12]. Generally, the comparatively low energy density of flow batteries limits their application scenarios. The large-scale implementation of flow batteries for grid applications is still in its early stages and requires significant advances in both technology and infrastructure [13].

Moreover, most types of batteries face concerns about their environmental impact and social aspects. The extraction of critical resources, such as cobalt in lithium-ion technology or vanadium in the context of FB [14], raises significant environmental and ethical issues, including the impact of mining and the geopolitical implications of resource dependency. These factors have spurred a growing interest in transitioning FBs from metal-based systems to those that utilize organic molecules.

The organic flow battery (OFB) presents a promising alternative due to the potential for lower costs, reduced environmental impact, and reduced dependence on the supply chain [15, 16]. Unlike metal-based systems, organic materials are not geographically limited, which can alleviate many of the supply constraints associated with traditional battery technologies. Using widely available and low-cost organic compounds, these batteries can offer sustainable and scalable energy storage solutions, contributing to the advancement of renewable energy integration and grid stability [12].

The improvement of organic redox flow batteries (OFBs) was also behind the initiation of the European Union (EU) SONAR research project ("Modeling for the search for new active materials for redox flow batteries", Grant Agreement ID: 875489). This project focuses on modeling different aspects of flow batteries at every scale: from molecular dynamics and microscale continuum simulation to whole system simulation. The emphasis is on discovering new molecules and providing a high-throughput screening to investigate promising candidates across all model scales. The underlying work was also created as part of the SONAR project, highlighting FB model development and validation on the micro and homogenized scale, multiscale modeling and FB optimization. The structure of the work is as follows.

Chapter 1 provides the motivation of the work and FB fundamental to get an insight into the topic. After a short historical overview, the FB systems and the working principle are presented. The chapter closes with an introduction into FB modeling and optimization, followed by the objectives of this work.

In Chapter 2, the modeling and optimization methodologies are presented. Both the microscale model and the homogenized cell-scale model are introduced with modeling assumptions, computational domain, governing equations, boundary conditions, simulations parameters, and limitations. At the same time, reference is also made to the fundamentals of electrochemistry. The optimization part starts with introducing the actual optimization problem and the cost functional, followed by the methodology of topology and shape optimization.

Chapter 3 characterizes the electrode material that serves as the simulation domain and gives an overview of the reconstruction process from micro-computed tomography images to a simulation mesh.

In Chapter 4 both the microscale model and homogenized cell-scale model undergo rigorous validation with different modeling approaches and experimental data. Therefor, the all-vanadium system and the organic MV/ TEMPOL system are used.

Chapter 5 starts with a review of the literature on microscale modeling and presents hereafter the results, starting with numerical investigations on structured electrodes, followed by detailed investigations of the reconstructed electrode. In the last section, the statistical resilience of the reconstructed microstructure is investigated and compared to an artificially generated domain in terms of battery performance.

In Chapter 6, the multiscale modeling approach using mass transfer coefficients is introduced. In the beginning, a review on homogenized scale models and generic multiscale approaches is given. This is followed by detailed explanations on how the mass transfer is extracted from the microscale, transferred to the homogenized cell-scale, and compared to other empirical formulations.

Chapter7 introduces FB optimization, starting with an extensive review of topology and shape optimization and their application to flow batteries. The chapter continues with investigations on the optimal porosity distribution within the electrode and concludes with the result of shape optimization of different novel cell designs.

Chapter 8 summarizes all relevant findings and provides an overview of possible further research topics.

1.2 Historical Perspective on Flow Batteries

In the 1780s, Luigi Galvani discovered muscle contraction through his famous frog leg experiments. The muscles had to be in contact with both copper and iron and the two metals also had to be connected. Unknowingly, he created an electrical circuit consisting of two metals, an electrolyte (the frog leg), and muscle as an indicator of the current [17]. This work laid the foundation for the development of the galvanic cell by Alessandro Volta. In 1790, Volta demonstrated that electricity could be generated from paper soaked in saline solution, stacked between plates of copper and zinc [18]. In 1836, John Frederic Daniell developed the so-called Daniell cell, consisting of a zinc and a copper half-cell [19]. This development laid the groundwork for all subsequent electrochemical cells we know today, such as lithium-ion batteries, fuel cells, and flow batteries.

The development of flow batteries can be traced back to a patent by Walther Kangro in 1949. In this patent, Kangro described the possibility of storing electrical energy in liquids through redox reactions of dissolved redox pairs at electrodes. He also referred to the use of substances that exhibit three or more valence states [20]. Due to the first oil crisis in the 1970s, NASA began developing novel electrochemical energy storage systems to store renewable energy. This led to the development of the cost-effective iron-chromium system [21].

In the mid-1980s, Skyllas-Kazacos et al. [22] introduced the VFB, which remains the most researched and widely commercialized FB to date. It is characterized by low self-discharge and virtually no aging effects. The main focus of research is on its low energy density, as the active species that store energy constitute only a small fraction of the electrolyte, which is primarily composed of water and sulfuric acid. Detailed reviews on commercial, technical, and chemical aspects can be found in [7, 23–26].

In the 1990s, research on the iron-chromium system was a major focus in Japan, Europe, and the United States [27, 28]. Meanwhile, research on vanadium flow batteries continued to advance in Australia, led by Skyllas et al. [29]. Since the early 2000s, China has also been researching various types of energy storage systems, including flow batteries. Table 1.1 shows a selection of the largest FB installations around the world.

Table 1.1: Selection of FB installations around the world.

Country / Year	Power / Capacity	Application
USA / 2007	250 kW / 2 MWh	Voltage support and rural feeder augmentation [30]
South Africa / 2022	1 MW / 4 MWh	ESS in hybrid mini grid [31]
England / 2022	2 MW / 5 MWh	Hybrid battery for public EV charging hub [32]
Germany / 2019	2 MW / 20 MWh	Wind and Solar output fluctuation stabilization [33]
Japan / 2022	17 MW / 51 MWh	Dispatch Power Source [34]
China / 2022	100 MW / 400 MWh	Peak shaving and ESS for wind and solar [35]

As mentioned above, the reliance on critical raw materials and uncertainties in the supply chain of metals require the exploration of alternatives. Organic molecules have emerged as a promising alternative as a result of their structural diversity and tunable properties.

This allows for a wider design space through molecular engineering, such as modifying the molecular structure or adding functional groups. Moreover, there is the possibility of obtaining active material from sustainable organic sources such as the paper industry [16].

The research focus on organic molecules began in 2007 with the use of tiron (4,5-dihydroxy-1,3-benzenedisulfonic acid) [36]. In 2014, flow batteries using 9,10-anthraquinone-2,7-disulphonic acid (AQDS) were developed [37], followed by the introduction of the popular methyl viologen (MV)/4-hydroxy-2,2,6,6-tetramethylpiperidinyloxyl (TEMPOL) system in 2016 [38]. The latter system is the basis for the microscale modeling investigations in this work and is later described in more detail.

1.3 Flow Battery Systems

Flow batteries represent a versatile and promising class of energy storage systems, with various chemistries offering distinct advantages and challenges. The classification of flow batteries into aqueous and non-aqueous types is common in the literature, primarily on the basis of the composition of the electrolyte. Aqueous FB systems use water-based electrolytes, typically containing dissolved salts and redox-active species. In contrast, non-aqueous FB systems use organic solvents instead of water to dissolve the redox-active species. Due to the electrochemical stability window of water, which is limited by the decomposition of water into hydrogen and oxygen, aqueous flow batteries typically have relatively low cell voltages, usually below 2 V. Aqueous systems are more mature and commercially developed and are the focus of investigation in this work.

The main distinguishing characteristic of different FB systems is the type of active material, in which a distinction is made between metal-based and organic active material. Metal-based FB systems utilize metal ions dissolved in the electrolyte by means of strong acids. Common examples include the vanadium system, the zinc-bromine system [39], or the iron-chromium system [40], where the active material is dissolved in sulfuric or hydrochloric acid. These systems have well-established chemistries but can be limited in energy density because of the intrinsic properties of the metal ions used. Generally, they have well-understood performance characteristics and exhibit long-term stability [41]. However, metal-based systems pose environmental concerns related to the mining, extraction, and disposal of metals. Their costs are often influenced by the price and availability of the metal ions used. Vanadium, for example, can be expensive and subject to significant price volatility [12]. However, metal-based systems, especially vanadium, are already in commercial use and have proven scalability, particularly in large-scale grid applications, as shown in Table 1.1.

Organic FB systems use organic molecules as the redox-active species. These molecules are typically based on carbon compounds and can be synthetically tailored to specific needs using earth-abundant elements only. Most reported organic electrolyte materials are based on a limited number of redox structural units such as quinone, viologen, TEMPOL-like nitroxyl radicals, and ferrocene [42]. These materials offer the potential for higher energy densities because of their tunable redox potential and physicochemical properties. They open up new possibilities for the development of multi-electron-transfer-type molecules, that can significantly enhance energy storage capabilities. Furthermore, organic FB systems generally have a lower environmental impact because they can be synthesized from more abundant and less toxic materials, thus reducing dependence on mining activities. This also has the potential to reduce costs by using inexpensive and widely available organic materials. Despite these promising performance characteristics, challenges remain in ensuring long-term stability and minimizing degradation, as these systems are sensitive to pH conditions [16]. Although research is still in its infancy, ongoing efforts are focused on improving the durability and efficiency of organic flow batteries, making them a promising alternative to traditional metal-based systems.

The systems investigated in this work are the all-vanadium system and the MV/TEMPOL organic system. The former is used for model validation and in the optimization calculation in Chapter 7, while the latter is the focus of investigation in both microscale and multiscale modeling. Detailed explanations of these systems are provided in the following sections to support their respective analyses.

The All-Vanadium System

The all-vanadium FB system stands out as the most developed and commercially implemented FB technology [5]. It utilizes vanadium ions in four different oxidation states in both half-cells, which is why it is referred to as an all-vanadium system [8, 9]. The supporting material in the electrolyte is sulfuric acid, and hydrogen protons act as charge carriers between the two half-cells. One of the main advantages of the VFB systems is the minimal cross-contamination by ion diffusion across the membrane, as only vanadium ions are involved. This unique feature allows the electrolyte to be re-mixed after the end of the operation to bring the battery back to its original state. VFB systems are known for their long cycle life, capable of achieving up to 20,000 cycles and operating efficiently for up to 20 years, making them a reliable and durable energy storage solution [43].

The basic reaction of all batteries is the reduction-oxidation (redox) reaction, in which electrons are transferred between two species. The species is said to be reduced when it gains electrons and oxidized when it loses electrons. Throughout the charging and discharging processes, the reactions occurring within the two FB half-cells can be succinctly represented by the following equations:

$$\text{Positive electrode:} \qquad VO^{2+} + H_2O - e^- \xrightleftharpoons[\text{discharge}]{\text{charge}} {VO_2}^+ + 2\,H^+ \tag{1.1}$$

$$\text{Negative electrode:} \qquad V^{3+} + e^- \xrightleftharpoons[\text{discharge}]{\text{charge}} V^{2+}. \tag{1.2}$$

The standard redox potential of Equation 1.1 is $E^0 = 1.004\,\mathrm{V}$ vs. standard hydrogen electrode (SHE) and $E^0 = -0.255\,\mathrm{V}$ vs. SHE for Equation 1.2. This leads to a general standard redox potential of $E^0 = 1.259\,\mathrm{V}$ vs. SHE for the VFB. The SHE is the standard reference electrode for measuring and comparing the electrochemical potentials of different electrodes. It has a defined potential of 0 V under standard conditions.

The MV/TEMPOL System

The MV/TEMPOL system represents a promising candidate for organic aqueous flow batteries, offering several advantages that make it a compelling alternative for flow batteries [38]. This system demonstrates good electrochemical performance, operating under neutral pH conditions with sodium chloride as the supporting electrolyte and Cl^- as the charge carrier. This setup ensures a stable environment for the electroactive materials, promoting efficient energy conversion processes. One of the key benefits of the MV/TEMPOL system is the comparatively high solubility of organic active materials, which allows higher energy densities to be achieved. In addition, the system can operate at comparatively high current densities, which enhances its overall performance and suitability for large-scale applications.

In this system, methyl viologen ($C_{12}H_{14}Cl_2N_2$) serves as an anolyte. It is well-known for its development and widespread use as a herbicide. However, it is important to note that despite its electrochemical advantages, MV is toxic to humans, necessitating careful handling and safety considerations in its application. TEMPOL or 4-Hydroxy-TEMPO ($C_9H_{18}NO_2$), used as the catholyte, is a stabilized radical that provides robust performance within the battery. It is economically viable on an industrial scale, making it a cost-effective choice for commercial deployment [44].

The general cell reaction is illustrated in Figure 1.1 and can accordingly be stated by the following equations:

$$\text{Positive electrode:} \qquad \text{TEMPOL} \xrightleftharpoons[\text{discharge}]{\text{charge}} \text{TEMPOL}^+ + e^- \tag{1.3}$$

$$\text{Negative electrode:} \qquad MV^{2+} + e^- \xrightleftharpoons[\text{discharge}]{\text{charge}} MV^+. \tag{1.4}$$

The standard redox potential of Equation 1.3 is $E^0 = 0.8\,\mathrm{V}$ vs. SHE and $E^0 = -0.45\,\mathrm{V}$ vs. SHE for Equation 1.4. This leads to a general standard redox potential of $E^0 = 1.25\,\mathrm{V}$ vs. SHE for the OFB.

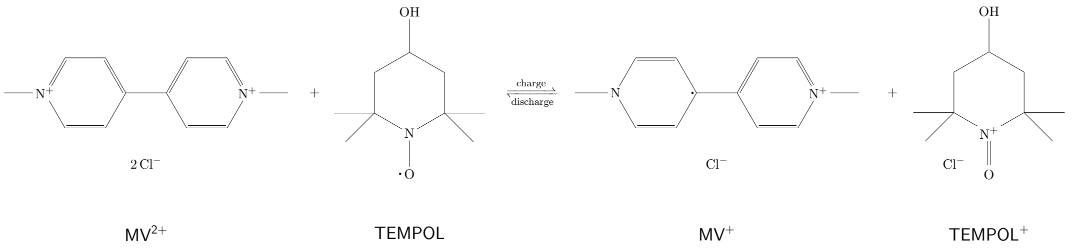

Figure 1.1: Illustration of discharged and charged states of the MV/TEMPOL system and the cell reaction.

1.4 Working Principle

The working principle of a FB is shown in Figure 1.2. The scheme exemplarily features the organic MV/TEMPOL system, but the basic principle applies to all flow batteries. As mentioned above, a FB is a type of galvanic cell comprising two electrodes separated by a membrane (separator) in the middle. This configuration is referred to as a cell. When connected to a power load or source, the electrical circuit is complete. In practical applications, multiple cells are combined in series or in parallel to form a cell stack and achieve the desired voltage and power output.

The primary distinction between flow batteries and other types of batteries is the presence of tanks that store electrolyte solutions containing water-soluble redox-active species. Pumps circulate the electrolyte constantly through the cell, enabling the electrochemical reactions necessary for energy storage and release. The two different electrolytes are also denoted as anolyte and catholyte.

The redox reaction occurs at the solid-electrolyte interface within the electrode. To maximize the use of the respective half-cell volumes, porous materials are employed to enhance the active surface area for the reaction. These are mainly woven and carbonized felts made of polymers. The current collectors are directly connected to the porous material, ensuring electrical connectivity to the external circuit. These are typically made from highly conductive metals such as copper or aluminum.

The membrane separator prevents self-discharge of the anolyte and catholyte by preventing cross-contamination (mixing) and facilitates ion transmission on both sides to balance the redox reactions. They are typically made of ion-selective polymers.

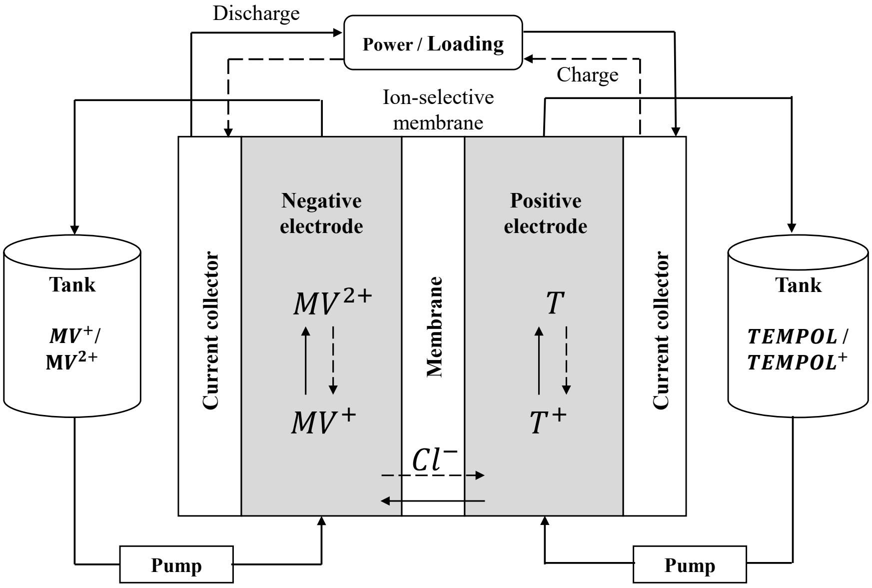

Figure 1.2: Scheme of the organic MV/ TEMPOL FB.

During discharge of the organic system, an electron travels from the load to the current collector of the positive electrode. Then, it is transported to the solid-electrolyte interface of the porous electrode, where the reduction reaction occurs. Here, $TEMPOL^+$ accepts the electron and is reduced to TEMPOL. To maintain charge balance, Cl^- ion migrates through the membrane from the positive electrode to the negative electrode. In the negative electrode, the oxidation reaction takes place, where MV^+ is oxidized to MV^{2+} by donating an electron, which is then returned to the load via the current collector. The charging process operates in the reverse manner. In the accompanying scheme, the discharge process is indicated by solid lines, while the charging process is represented by dashed lines.

1.5 Flow Battery Modeling

FB modeling is crucial for advancing the technology in general, optimize performance, and ensure its economic viability [45]. By enabling virtual investigations, modeling significantly reduces the costs associated with prototyping and experimentation. It provides a deep understanding of the physical and electrochemical mechanisms within the battery, allowing researchers to draw conclusions about the optimal design and operating conditions before physical prototypes are built. In addition, modeling aids in material selection and predicts behavior during scale-up processes, further contributing to cost reduction. Multiscale modeling is particularly important because it allows the examination of battery behavior at different levels, from the degradation behavior of novel active materials to the performance of the entire system when connected to the power grid.

FB modeling spans different dimensions, each offering unique insights and applications. Zero-dimensional (0D) models are the simplest form, focusing primarily on lumped parameters without spatial resolution. They are typically applied for system-level analysis or for the development of control strategies [46]. One-dimensional (1D) models incorporate spatial resolution along a single dimension, making them suitable for studying flow characteristics along a flow channel, charge transport in the through-plane direction, or stack operation [47]. Two-dimensional (2D) models provide more detailed information, allowing analysis of flow distribution or reaction distribution at the cell level, and are often used for investigations on geometry [48]. Three-dimensional (3D) models solve complex partial differential equations for comprehensive analysis. These models can be resolved on the microscale to investigate detailed transport phenomena and reaction processes or used for cell or stack simulations for prototyping, employing homogenized properties [49].

The first FB model was presented by Fetkiv and Watts in 1984 to describe the isothermal operation of a single unit cell in an iron / chromium system [50]. Homma et al. introduced the first VFB model that incorporates the electrode kinetics of steady-state charge and discharge operations [51]. These models proposed the usage of equivalent electric circuits for the different electric and ionic relations within the cell.

However, FB modeling involves multiple interconnected physical and electrochemical phenomena that occur during operation. Developing models that accurately and simultaneously incorporate all these phenomena can be very demanding for numerical solvers and computational resources. In the initial stage, models often employ a reduced number of phenomena, dimensions, or simplifying assumptions to make the problem more tractable. For example, all models typically neglect storage tanks and connecting pipes, instead focusing on the core components of the battery. Modeling efforts are concentrated on volume-averaged, homogenized, or macroscopic calculations of transport processes within the porous electrodes. These processes are often captured using empirical relations, such as Darcy's law for fluid flow and the Bruggeman correction for effective transport properties. Such simplifications help to manage complexity while still providing valuable insights into the performance and optimization of flow batteries.

Since the late 2000s, microscale resolved 3D models have been gaining ground in the modeling of flow batteries. Unlike homogenized 2D models, which rely on averaged quantities, these advanced models overcome the inherent limitations by resolving the spatial geometry at the microscale. Although only excerpts of the electrode can be modeled due to computational constraints, these 3D models provide detailed spatial characteristics of velocity, concentration, voltage, and current density, reflecting the complex structures of the electrode. This enhanced resolution enables a more accurate representation of the electrochemical processes within the electrode, offering insights that homogenized models cannot achieve.

In this work, both a 3D resolved microscale model and a homogenized 2D cell-scale model are developed to enhance understanding of flow batteries. The 3D model provides detailed insights into the microstructural processes, using a reconstructed digital twin of the electrode material to capture the intricate transport phenomena and reaction dynamics within the electrode. In contrast, the 2D model is designed to be relatively simple, facilitating its integration with mathematical optimization calculations and enabling the replication of a real experimental cell. Both models are connected using a novel multiscale modeling approach based on mass transfer coefficients, allowing for a comprehensive analysis that bridges the gap between microscale phenomena and cell-scale performance.

1.6 Flow Battery Optimization

Optimizing flow batteries is crucial as there is always the potential to enhance their performance. Optimization helps improve operating efficiency, which positively affects cycle life, material costs, and overall operational costs, thus making the technology better and more viable for widespread adoption.

Digital optimization is particularly advantageous for FBs due to their complexity. These batteries are intricate systems that involve numerous variables, constraints, and interconnected parameters. Virtual prototyping and optimization can handle this complexity, reducing the need for physical prototypes. By adapting various mathematical optimization techniques, it is possible to find optimal solutions efficiently, which, in turn, reduces development costs and accelerates the pace of design improvement and innovation.

From a mathematical perspective, optimization involves finding the best solution from a set of possible solutions for a given analytical goal, considering side conditions and constraints. The function to be minimized is called the objective function, which measures performance. The decision variables affecting the objective function represent the available choices. In this work, these variables come from the computational FB model. Constraints in optimization problems are equations or inequalities that define the feasible region of possible solutions, ensuring that the optimized solutions are practical and achievable within the given limits.

In this work, topology optimization [52, 53] is used to find the optimal porosity distribution within the electrode, and shape optimization [54] is used to determine the optimal geometric dimensions of novel cell designs. The objective in both cases is to minimize the pressure drop while maximizing the reaction rate within the cell.

Topology optimization, a specific method that originates in structural mechanics, is used to find the optimal layout of materials within a given design space. Fundamentally, it changes the distribution of the material, creating new design structures. For example, in the case of a cantilever beam, where a beam extends horizontally, supported at one end, and applied with a load at the unsupported end, topology optimization is used to minimize the mass of the beam while ensuring it can tolerate the load without breaking [55]. The solutions often result in framework structures similar to those seen in construction cranes. Recently, this method has been applied to optimize flow channels in flow batteries. In this work, it is used to redistribute the electrode porosity effectively.

Shape optimization, a subset of structural optimization, focuses on refining the contour of a given structure to fulfill the optimization task. Unlike topology optimization, which alters the material distribution, shape optimization modifies the external shape of the design while keeping the overall topology fixed. A popular example is the shape optimization of an aircraft foil, where adjustments to the angle of incidence or the curvature of the foil can optimize lift [56]. In the context of flow batteries, shape optimization is used to enhance the cell design, ensuring that the geometric dimensions contribute to improved performance.

Both topology and shape optimization play crucial roles in improving the efficiency and functionality of flow batteries, addressing specific design challenges, and pushing the boundaries of current technology.

1.7 Objectives of the Work

The primary investigations in this work focus on four main topics: micro- and multiscale modeling, FB optimization, and detailed model validation. The objectives of the topics are as follows.

Microscale Modeling The main objective is the development of a detailed microscale model of a FB half-cell, capturing the intricate physical and electrochemical phenomena occurring within the system, namely the flow of electrolytes, the redox reaction, and charge transport. In addition, a reconstruction process is developed to create a digital twin of real electrode material suitable for microscale simulation. In the process, micro-computed tomography (µCT) images are converted into a simulation mesh using image processing techniques.

Once the model is established, a comprehensive parameter study is conducted to investigate the typical characteristics of flow batteries. The presented study addresses the examination of the effects of different active surface areas and concentrations on the half-cell potential. Further, the concentration, potential, and current distribution within the microstructure are characterized for different flow rates. An optimal Reynolds number that results in the lowest possible pressure drop while maintaining the highest potential is identified, ultimately leading to the highest round-trip battery efficiency. Furthermore, the performance and efficiency of the reconstructed electrode material is compared with those of a structured fiber domain (SFD) to evaluate their relative merits and determine whether a detailed reconstruction process is necessary for microscale investigations.

Multiscale Modeling In the second topic of the work, the focus is on multiscale modeling, combining microscale and cell-scale. For this purpose, a 2D homogenized cell-scale model capturing the electrode and manifolds of a half-cell is set up and connected with microscale simulation results to conduct broader investigations.

The key task in this area is to find an efficient method for transferring information from the detailed microscale model to the homogenized cell-scale model, improving the accuracy of cell-scale calculations. This involves developing a robust modeling framework that connects microscale simulations with homogenized cell-scale models using mass transfer coefficients. This approach involves extracting the coefficients from microscale simulations, transferring them to the higher scale, and comparing the results with empirical formulations from the literature.

Optimization The third objective focuses on optimizing the FB on the cell-scale. The centerpiece here is developing a framework for both topology and shape optimization techniques. A multiobjective functional is implemented to optimize opposing quantities simultaneously, specifically targeting the maximization of reaction rate and the minimization of pressure drop.

In the context of topology optimization, the work investigates the optimal porosity distribution within the electrode, challenging the conventional assumption that a homogeneous porosity distribution is ideal. The goal is to minimize the multiobjective functional by redistributing porosity values in different ranges and various operating conditions. For shape optimization, the work explores and identifies optimal dimensions for various novel cell designs such as horizontal formatted, trapezoidal, or radial cells. The eligibility of the established vertical formatted cell design is questioned, and investigations are conducted to determine whether an optimal design exists under specific operating conditions.

Model Validation The final objective is to ensure that both the microscale and homogenized cell-scale models are rigorously validated. This involves comparing the models against other established scale models and experimental data. The validation process includes data from both the all-vanadium system and the organic MV/ TEMPOL system, with experimental data generated within the SONAR research project. Ensuring the robustness and accuracy of the models through validation is essential to the success and reliability of the work.

2 Modeling and Optimization Methodology

In this chapter, the modeling approaches for the 3D resolved microscale model and the homogenized 2D cell-scale model are thoroughly explained. The modeling assumptions and computational domains for each model are presented, followed by a detailed discussion of the governing equations, which offers insights into fluid dynamics and electrochemistry theory. In addition, the boundary conditions, simulation parameters, and limitations of the model are outlined. Moreover, the optimization methodology is explained starting with the introduction of the multi-objective cost functional. Detailed insights on topology and shape optimization are presented, providing a comprehensive overview of the optimization techniques used in this work.

2.1 Microscale Model

The porous electrode is one of the key components in a FB, and its microstructure significantly influences the flow of the electrolyte, the distribution of the reactant and, consequently, the electrochemical reaction, and the overall performance of the battery. Understanding these microstructural effects is crucial for optimizing flow battery designs, but experimental investigations on the micrometer scale pose significant challenges. These experiments are not only time-consuming, but also costly in terms of raw materials and physical resources.

To address these challenges, a 3D resolved microscale model is developed that captures the real geometry of the electrode to provide detailed insight into the microstructural processes occurring within the battery. By directly linking the governing equations of the physical and electrochemical processes to a microstructural representation of the electrode and the surrounding electrolyte, the model offers a powerful tool for understanding how microstructural features affect transport processes and overall cell performance. The developed model will be referred to as microscale model (MSM) in the further course of the work.

The MSM is a self-developed multiregion modeling framework designed to simulate electrolyte flow, species transport, and charge transport within the spatially resolved microstructure. In this model, two nonoverlapping subareas for the electrolyte and electrode coexist, ensuring that the distinct physical properties of each region are accurately represented.

The framework directly solves the governing equations for both the solid (electrode) and fluid (electrolyte) regions. These equations are coupled with a Butler-Volmer-type kinetic boundary condition, which accurately describes the electrochemical reactions at the electrode-electrolyte interface. A schematic representation of the model is given in Figure 2.1. It is based on the 3D flow battery model established by Qiu et al. [57, 58] and is based on the numerical modeling approach for lithium ion batteries by Kespe et al. [59, 60]. Detailed explanation of this numerical implementation can be found in [61].

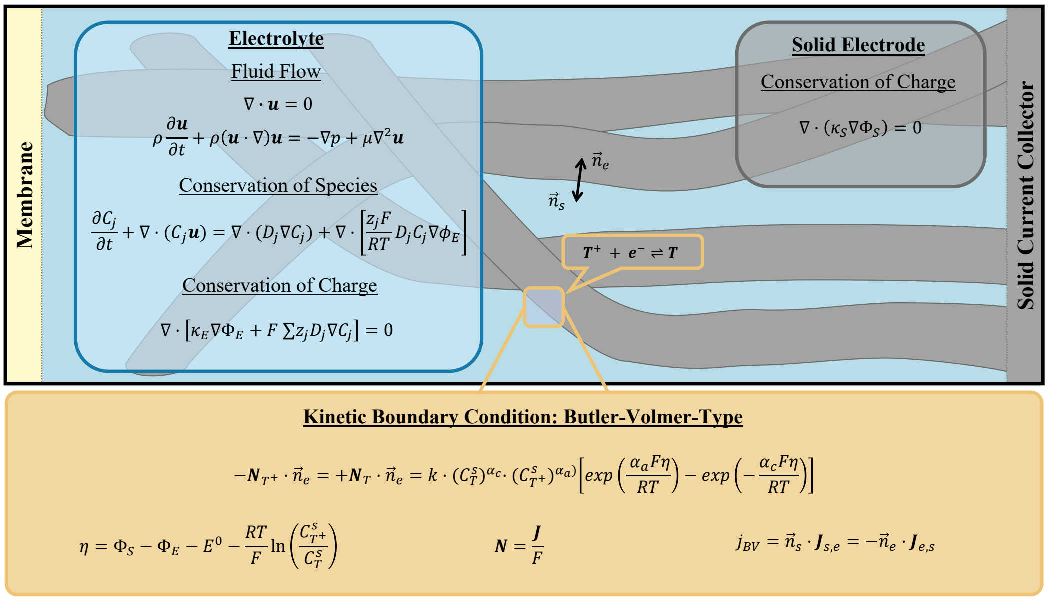

Figure 2.1: Schematic representation of the spatially resolved MSM showing the positive half-cell parameterized with the TEMPOL (denoted as T and T^+) system and the corresponding governing equations.

The focus of the model lies on an excerpt from a half-cell flow battery, where the electrolyte, electrode, and current collector are spatially resolved, while the membrane is considered a boundary condition (cf. Figure 2.1). The approach ensures the conservation of charges and species in all parts of the computational domain, providing a comprehensive understanding of the internal processes of the flow battery.

The model differentiates itself from previously developed microscale models by employing a finite volume method (FVM) approach for both fluid and species transport. In particular, it is one of the first models to be parameterized specifically for the organic TEMPOL system.

Additionally, this model stands out by including detailed validation with all-vanadium models and experimental MV/TEMPOL data , ensuring its flexibility, reliability and relevance for both traditional and cutting-edge flow battery chemistries.

The modeling approach is explained in detail using generic expressions for the respective active species materials, denoted as i and i^+. Specific examples are given for the TEMPOL half-cell as shown in Figure 2.1, but these principles are applicable to all single-electron redox reactions, as outlined in Equations 1.1, 1.2, 1.3, and 1.4.

2.1.1 Modeling Assumptions

All models make assumptions to reduce complexity and focus on the most important and influential properties to allow efficient problem solving while capturing the essential behavior of the system. Consequently, these assumptions strike a balance between model accuracy and computational feasibility, ensuring that key insights are still obtained. The assumptions made in the MSM are as follows:

- Single phase within the respective model regions is assumed.
- Isothermal operation conditions are assumed in both regions.
- The electrolyte flow is assumed to be laminar and steady-state.
- Constant electrolyte density and viscosity are assumed.
- Within the electrolyte, bulk interactions of the species are not considered. No side reactions or degradation occur.
- Nanoscale processes such as double layer formation at the interface are not resolved, and charge neutrality is presumed in the model.

2.1.2 Computational Domain

Microscale modeling aims to investigate physicochemical phenomena and transport mechanisms in the porous microstructure. Hence, the pore and fiber space must be resolved as a result of the equations that are directly linked to the computational grid. Precise information on the fiber geometry is necessary as an input for the simulation. In this work, the microstructure of the electrode is obtained by experimental image reconstruction of a real graphite felt sample (SIGRACELL GFD46, SGL Carbon [62]) explained in detail in Chapter 3. In addition, a structured fiber domain (SFD) made of straight cylinders is generated for comparison. Figure 2.2 shows the reconstructed microstructure (left) and the structured domain (right), which are referred to as GFD46 and SFD respectively in the following course of the work. The electrolyte region is not shown in this view, but it completely surrounds the fibers and exhibits a cubic shape.

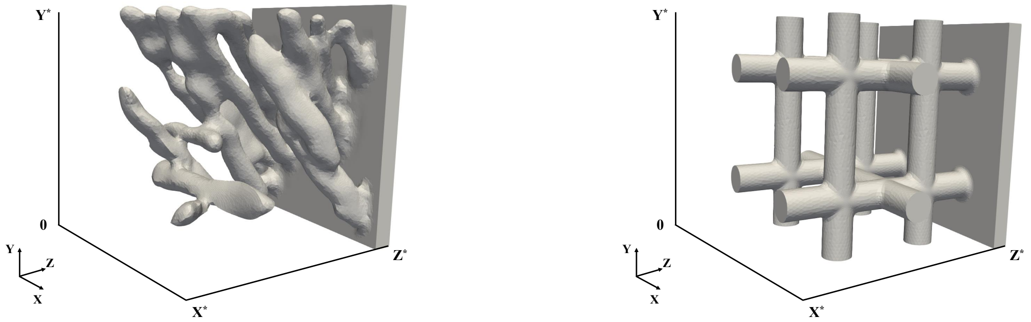

Figure 2.2: Computational domains of the microscale model. Reconstructed graphite felt (left) and structured fiber domain (right). Both domains include a current collector plate.

The line segments of the domains are normalized by their respective lengths to establish unit lengths X^*, Y^* and Z^*. In this context, the X^* direction denotes the spatial distance from the averted ($X^* = 0$) to the facing ($X^* = 1$) surface. Similarly, the Y^* direction signifies the distance from the inlet ($Y^* = 0$) along the flow direction to the outlet ($Y^* = 1$). Furthermore, the Z^* direction captures the distance from the membrane boundary ($Z^* = 0$) to the current collector ($Z^* = 1$). Throughout the study, modifications are made to the flow directions. However, unless otherwise stated, the aforementioned spatial configuration is assumed where the flow is in the positive Y^* direction.

The SFD is constructed from straight and equally sized fibers and provides a contrast to the more randomly arranged fibers of the reconstructed microstructure. It is built to match the geometrical properties of the reconstructed domain to ensure a reliable comparison. In addition, SFD is faster to generate, has fewer computational cells and can therefore be simulated faster. In fact, its main advantage is the implementation of solid periodic boundary conditions in the X^* and Y^* directions. To this end, the same solid-fluid segmentation at opposing boundaries is inescapable and can be easily achieved. Using an excerpt of the real heterogeneous electrode microstructure, we can assure that this is as a result of the natural inhomogeneity of the fiber structure.

The geometric information of the reconstructed microstructure (GFD46) and the structured fiber domain is tabulated in Table 2.1. It becomes apparent that 100% agreement cannot be achieved. The mean fiber size and pore size of the reconstructed domain are calculated on the basis of the entire sampled data.

Table 2.1: Geometrical properties of the reconstructed (GFD46) and structured (SFD) simulation geometry.

Description	GFD46	SFD
Half-cell dimensions	78 µm × 78 µm × 78 µm	
Porosity ϵ	0.914	0.88
Specific surface area	58 471 $m^2\,m^{-3}$	55 604 $m^2\,m^{-3}$
Mean fiber size	14 ± 1 µm [a]	10 µm
Mean pore size	123 ± 31 µm [a]	30 µm
Number of computational cells	2.8×10^6	1.01×10^6
Size of computational cells	0.1 - 2 µm	0.3 - 2.5 µm

[a] Obtained from image processing

It should be mentioned that, in the early stage of the model development, other simulation geometries containing simplified fiber structures are used. They are built to investigate different active surfaces and porosities as presented in Chapter 5.2.

2.1.3 Governing Equations

Fluid Transport The liquid electrolyte flowing through the porous electrode is assumed as an incompressible Newtonian fluid described by the continuity equation and the Navier-Stokes equation given by [57]

$$\nabla \cdot \mathbf{u} = 0 \tag{2.1}$$

$$\rho \frac{\partial \mathbf{u}}{\partial t} + \rho \left(\mathbf{u} \cdot \nabla \right) \mathbf{u} = -\nabla p + \mu \nabla^2 \mathbf{u} \tag{2.2}$$

where $\mathbf{u}$ is the velocity vector, t is the time, ρ is the density, p is the pressure, and μ is the dynamic viscosity of the electrolyte. Viscosity and density are constant over time and uniform throughout the electrolyte. Moreover, the flow is assumed to be laminar and steady-state. In the further course of the contribution, the fluid flow is characterized by means of the Reynolds number (Re number)

$$Re = \frac{U\,d_f}{\nu} \tag{2.3}$$

where U is the magnitude of the velocity and d_f is the fiber diameter. Although the fiber diameter slightly varies in the reconstructed electrode material, it is set to 10 µm within the MSM simulations to define the Re number.

Species Transport The species within the electrolyte are treated based on the theory of dilute solution [63]. This means that the dilute species in the solution behave independently and do not interact with each other. Moreover, it is assumed that the activity of ions is equal to their actual concentration, which facilitates their calculation. The concentration of species can change through the following mechanisms: Convection as a result of the velocity field of the electrolyte, diffusion as a result of a concentration gradient, migration as a result of a potential gradient, or chemical reaction. The MSM considers the transport of a generic species j using the convection-diffusion equation [48]

$$\frac{\partial C_j}{\partial t} + \nabla \cdot \left(C_j \mathbf{u}\right) = \nabla \cdot \left(D_j \nabla C_j\right) + \nabla \cdot \left[\frac{z_j F C_j D_j}{RT} \nabla \phi_e\right] + S_j \tag{2.4}$$

where C_j is the concentration of species j, D_j is the diffusion coefficient of species j, z_j is the charge of species j, F is the Faraday's constant, R is the universal gas constant, T is the absolute temperature, ϕ_e is the electrical potential in the electrolyte, and S_j is the source term of species j. Constant diffusivity and no bulk interaction of the species are assumed throughout the electrolyte. Consequently, the source term is neglected ($S_j = 0$) and the redox reaction takes place only at the electrode-electrolyte interface.

In several microscale simulation approaches in the literature [57, 58, 64], the concentration of a charged species (mainly the supporting electrolyte) is obtained via the electroneutrality condition $\sum z_j C_j = 0$, to ensure the electroneutrality of the system. However, this model solves Equation 2.4 for all species and enforces electroneutrality.

Electrochemical Reaction The kinetics of the electrochemical reaction at the electrode surface is governed by the fundamental Butler-Volmer equation [63, 65]. This equation delineates the relationship between the electrical current and the potential difference between the electrode and the electrolyte. By incorporating both anodic and cathodic reaction rates occurring at the same electrode, the Butler-Volmer equation is essential for understanding how reaction rates depend on applied potential, temperature, and concentration. The equation is expressed as:

$$j = j_0 \left[exp\left(\frac{\alpha_a z_j F \eta}{RT}\right) - exp\left(-\frac{\alpha_c z_j F \eta}{RT}\right)\right] \tag{2.5}$$

where j is the net current density, j_0 is the exchange current density, α_c and α_a are the cathodic and anodic transfer coefficients respectively and η is the overpotential. The exchange current density represents the intrinsic rate of the electrochemical reaction at equilibrium when no net current flows and is defined as

$$j_0 = Fk\left(C^s_{red}\right)^{\alpha_c}\left(C^s_{ox}\right)^{\alpha_a} \tag{2.6}$$

where k is the reaction rate constant, C^s_{red} and C^s_{ox} denote the concentration of reduced and oxidized active species respectively. The cathodic and anodic transfer coefficients represent the symmetry of the activation energy barrier for the electron transfer affected by the overpotential. In the context of this work, the both coefficients are equals 0.5, indicating symmetry of the forward and backward reaction and the same activation energy. The overpotential η is the driving gradient of the reaction, meaning the difference between the applied potential and the standard redox potential. It can be subdivided into the activation, ohmic, and concentration overpotential

$$\eta = \eta_{act} + \eta_{ohm} + \eta_{conc}. \tag{2.7}$$

The activation overpotential is caused by the energy barrier for the electrochemical reaction at the electrode surface. The ohmic overpotential results from the resistance to the flow of ions through the electrolyte and electrons through the electrode (and other components). The concentration overpotential is due mass transport limitations resulting from the concentration gradient of active material near the electrode surface [66]. Within the model the overpotential is denoted as

$$\eta = \phi_s - \phi_e - E \tag{2.8}$$

where $\phi_s - \phi_e$ represents the local potential difference of electrode and electrolyte and E is the effective voltage according to the Nernst equation [63]:

$$E = E^0 - \frac{RT}{F} \ln\left(\frac{C^s_{red}}{C^s_{ox}}\right). \tag{2.9}$$

It states the effect of reactant and product surface concentration on the electrode potential. The standard redox potential is E^0. In addition, the relation between current produced by the reaction and the species flux $\mathbf{N}$ is described by Faraday's laws of electrolysis

$$\mathbf{N} = \frac{\mathbf{J}}{F} \tag{2.10}$$

where $\mathbf{J}$ is the current density vector. Combining Equations 2.5 and 2.10, the molar fluxes $\mathbf{N}_i$ and $\mathbf{N}_{i^+}$ of the single-electron redox reaction of arbitrary active species i and i^+ at the interface between electrode and electrolyte can be expressed as

$$-\mathbf{N}_{i^+} \cdot \mathbf{n}_e = +\mathbf{N}_i \cdot \mathbf{n}_e = k\left(C^s_i\right)^{\alpha_c}\left(C^s_{i^+}\right)^{\alpha_a}\left[exp\left(\frac{\alpha_a z_j F\eta}{RT}\right) - exp\left(-\frac{\alpha_c z_j F\eta}{RT}\right)\right] \tag{2.11}$$

where $\mathbf{n}_e$ is surface unit normal vector pointing outwards the electrolyte domain (cf. Figure 2.1. Applying this equation, the production and depletion of the above mentioned active species is calculated within the MSM.

Charge Transport The conservation of charge is true within the electrode and the electrolyte. Thus, a divergence-free current density field ensues in both domains:

$$\nabla \cdot \mathbf{J} = 0. \tag{2.12}$$

The governing equation for the potential field ϕ_s (solid) in the electrode fibers is represented by Ohm's law

$$\nabla \cdot (\kappa_s \nabla \phi_s) = 0 \tag{2.13}$$

where κ_s is the electrical conductivity of the electrode. The electric current density $\mathbf{J}_s$ within the solid electrode is hence obtained with

$$\mathbf{J}_s = -\kappa_s \nabla \phi_s. \tag{2.14}$$

The potential field in the electrolyte is obtained via

$$\nabla \cdot \left[\kappa_e \nabla \phi_e + F \sum z_j D_j \nabla C_j \right] = 0 \tag{2.15}$$

where κ_e is the ionic conductivity and is defined as

$$\kappa_e = \frac{F^2}{RT} \sum z_j^2 D_j C_j. \tag{2.16}$$

With this, the electrolyte current density J_e is expressed as

$$\mathbf{J}_e = -\kappa_e \nabla \phi_e - F \sum z_j D_j \nabla C_j. \tag{2.17}$$

2.1.4 Boundary Conditions

Fluid Transport For the fluid flow of the electrolyte, the no-slip boundary conditions are indicated at the fluid-solid interface of the electrode, the current collector and the membrane. These conditions enforce zero velocity on the solid boundary. The characteristic average flow velocity is applied at the inlet, whereas a zero-gradient (Neumann) boundary condition [67, 68] is established at the outlet. Furthermore, the velocity profile at the outlet is mapped to the inlet to avoid inflow effects. Regarding the remaining electrolyte boundaries ($X = 0$ and $X = X^*$, compare Figure 2.2), periodic boundary conditions are imposed. This means that the opposing sides are connected and fluid that exit at one boundary, re-enters at the opposing side. To ensure a pressure gradient that drives the electrolyte flow, the pressure is set to zero at the outlet and a zero-gradient boundary condition is set at the inlet. The pressure boundary condition on the electrolyte-solid interface and membrane is zero-gradient. In the

X^* direction also periodic boundary conditions are applied leading to same pressure levels at opposing boundaries.

Species Transport As mentioned before, the MSM allows for two operation modes with different boundary conditions for the concentration of species. To model quasi-steady-state behavior of the cell, a fixed value boundary condition (Dirichlet) [67, 68] is set at the inlet, which guarantees infinite and constant supply of electrolyte. When modeling a complete charge or discharge cycle, the mapped boundary condition is used, where the concentration profiles of all species are mapped from the outlet to the inlet within each time step. Zero-gradient boundary conditions are applied at the outlet in every case. For the remaining electrolyte boundaries ($X = 0$ and $X = X^*$), periodic conditions are imposed.

The initial concentrations of the species are derived from the electrolyte mixture considered and the state of charge (SOC). The SOC quantifies the level of charge of the battery relative to its full capacity. It ranges from zero to one, whereas zero indicates completely discharged and one indicates completely charged. It is defined as

$$SOC = \frac{\frac{1}{V_e} \int C_i\,(x,t)\,dV_e}{C_{i,max}} \tag{2.18}$$

where V_e is the electrolyte volume and $C_{i,max}$ is the maximum active material concentration. In other words, it quantifies the ratio of charged active material to the full amount of active material.

The concentration gradient of chemically active species at the electrolyte-electrode interface is calculated using Equation 2.15, where the inside of the square brackets is equated with the Butler-Volmer current density. This can be determined with Equations 2.11 and 2.10. For numerical reasons, the gradient for one redox partner is calculated, whereas the gradient of the other is set to the reverse. With respect to the organic system, the flux of Na^+ is set to zero at the interface. At the electrolyte-membrane interface, zero-gradient boundary conditions are set for all species. The transport of Cl^- through the membrane in order to account for charge balancing is treated in simplified terms according to Qiu et al. [57]. Hence, the depletion and generation of Cl^- on the active surface are considered to ensure electroneutrality in the bulk. Regarding the boundary conditions in the all-vanadium system, H^+ is treated the same as Na^+, and ${SO_2}^{4-}$ the same as Cl^-.

Charge Transport To ensure current continuity in the solid electrode domain, it is assumed that the potential at the current collector boundary (cc) ($Z = Z^*$) is uniform and for each iteration fixed at a specific value (ϕ_{cc}). Further, the integral electronic current density at the current collector and the ionic current density at the solid-electrolyte interface (s,e) must be identical:

$$\int \mathbf{n}_{cc} \cdot \mathbf{J}_{cc}\, dA_{cc} = -\int \mathbf{n}_s \cdot \mathbf{J}_{s,e}\, dA_{s,e}. \tag{2.19}$$

The surface normal unit vectors pointing outwards the relevant domains are $\mathbf{n}_{cc}$ and $\mathbf{n}_s$, and A is the area. To achieve a certain external charge or discharge current density j_{ext}, the potential at the current collector is iteratively adjusted each time step such that [59, 60]

$$\int \mathbf{n}_e \cdot \mathbf{J}_{s,e}\, dA_{s,e} = j_{ext} \cdot A_{mem}. \tag{2.20}$$

The external current density j_{ext} is a scalar quantity and is related to the membrane area A_{mem} [12]. To fulfill charge conservation between the electrode and the electrolyte, the potential at the electrolyte-solid interface (e,s) is chosen so that

$$j_{BV} = \mathbf{n}_s \cdot \mathbf{J}_{s,e} = -\mathbf{n}_e \cdot \mathbf{J}_{e,s} \tag{2.21}$$

whereas j_{BV} is the Butler-Volmer current density pursuant Equation 2.5. Hence, the electric current density $\mathbf{J}_{s,e}$ at the electrode side interface is equal to the ionic current density $\mathbf{J}_{e,s}$ on the electrolyte side of the interface. On the remaining boundaries of the electrolyte and solid domain, periodic conditions are applied to the potential. As we consider only a half-cell, the membrane potential is set to 0V.

2.1.5 Simulation Parameters

Organic System Regarding the organic system, it is assumed that sodium chloride is completely dissociated into Na^+ and Cl^-. The species considered in the MSM are, therefore, $j \in$ TEMPOL, $TEMPOL^+$, MV^+, MV^{2+}, $Na^+$and Cl^-. Table 2.2 shows the species-related charge and diffusivity.

Table 2.2: Species transport parameters of the MV/TEMPOL system.

Species	Charge (z_j)	Diffusivity (D_j)	Reference
TEMPOL	0	$2.95 \times 10^{-9}\,\mathrm{m^2\,s^{-1}}$	[38]
$TEMPOL^+$	1	$2.95 \times 10^{-9}\,\mathrm{m^2\,s^{-1}}$	[38]
MV^+	1	$2.57 \times 10^{-9}\,\mathrm{m^2\,s^{-1}}$	[38]
MV^{2+}	2	$2.75 \times 10^{-9}\,\mathrm{m^2\,s^{-1}}$	[38]
Na^+	1	$1.33 \times 10^{-9}\,\mathrm{m^2\,s^{-1}}$	[69]
Cl^-	-1	$2.03 \times 10^{-9}\,\mathrm{m^2\,s^{-1}}$	[69]

The values of the physical properties are summarized in Table 2.3. The viscosity and density of the electrolyte are assumed to be the same as for the NaCl solution due to the low solubility of TEMPOL [38]. In the further course of this contribution, mainly two different initial concentration levels are investigated, namely 0.1 M MV/TEMPOL in 1 M NaCl and 0.5 M MV/TEMPOL in 1.5 M NaCl. The latter is the limit of the solubility of TEMPOL.

Table 2.3: Physical properties of the MV/TEMPOL system.

Description	Symbol	Value	Reference
Electrolyte viscosity (1 M)	ν	$0.9380 \times 10^{-6}\,\mathrm{m^2\,s^{-1}}$	[70]
Electrolyte density (1 M)	ρ	$1036\,\mathrm{kg\,m^{-3}}$	[71]
Electrolyte viscosity (1.5 M)	ν	$0.9675 \times 10^{-6}\,\mathrm{m^2\,s^{-1}}$	[70]
Electrolyte density (1.5 M)	ρ	$1055\,\mathrm{kg\,m^{-3}}$	[71]
Reaction rate constant TEMPOL	k	$2.6 \times 10^{-6}\,\mathrm{m\,s^{-1}}$	[38]
Reaction rate constant MV	k	$2.8 \times 10^{-6}\,\mathrm{m\,s^{-1}}$	[38]
Standard redox potential TEMPOL	E^0	$0.8\,\mathrm{V}$	[38]
Standard redox potential MV	E^0	$-0.45\,\mathrm{V}$	[38]

All-Vanadium System Regarding the all-vanadium system, the supporting electrolyte sulfuric acid is assumed to be completely dissolved in H^+ and ${SO_4}^{2-}$. The species considered in the MSM are $j \in V^{2+}, V^{3+}, {VO_2}^+, VO^{2+}, H_2O, H^+$, and ${SO_4}^{2-}$. The transport parameter of the species and the physical properties are listed in Tables 2.4 and 2.5, respectively.

Table 2.4: Species transport parameters of the all-vanadium system.

Species	Charge (z_j)	Diffusivity (D_j)	Reference
V^{2+}	2	$2.4 \times 10^{-10}\,\mathrm{m^2\,s^{-1}}$	[58]
V^{3+}	3	$2.4 \times 10^{-10}\,\mathrm{m^2\,s^{-1}}$	[58]
${VO_2}^+$	1	$3.9 \times 10^{-10}\,\mathrm{m^2\,s^{-1}}$	[58]
VO^{2+}	2	$3.9 \times 10^{-10}\,\mathrm{m^2\,s^{-1}}$	[58]
H_2O	0	$2.3 \times 10^{-9}\,\mathrm{m^2\,s^{-1}}$	[58]
H^+	1	$9.312 \times 10^{-9}\,\mathrm{m^2\,s^{-1}}$	[58]
${SO_4}^{2-}$	-2	$2.2 \times 10^{-10}\,\mathrm{m^2\,s^{-1}}$	[58]

Operating Conditions In the course of this work, two different modes of operation are investigated within the MSM. First, quasi-steady-state simulations are performed assuming

Table 2.5: Physical properties of the all-vanadium system.

Description	Symbol	Value	Reference
Electrolyte viscosity	ν	$4.928 \times 10^{-3}\,\mathrm{m^2\,s^{-1}}$	[72]
Electrolyte density	ρ	$1000\,\mathrm{kg\,m^{-3}}$	^{a}
Reaction rate constant V^{2+}/V^{3+}	k	$1.7 \times 10^{-7}\,\mathrm{m\,s^{-1}}$	[73]
Reaction rate constant ${VO_2}^{+}/VO^{2+}$	k	$6.8 \times 10^{-7}\,\mathrm{m\,s^{-1}}$	[74]
Standard redox potential V^{2+}/V^{3+}	E^0	$-0.255\,\mathrm{V}$	[72]
Standard redox potential ${VO_2}^{+}/VO^{2+}$	E^0	$1.004\,\mathrm{V}$	[72]

^{a} Approximation

an infinite and constant supply of electrolyte at the inlet, allowing for the detailed examination of e.g. concentration or potential profiles. Here, the concentration is homogeneously distributed over the inlet boundary. Second, to model a complete charge or discharge cycle, the mapped mode is applied, in which the outlet concentration profile is mapped at the inlet over time.

The operating conditions, which are independent of the system used, are listed in Table 2.6.

Table 2.6: Operating parameters for both systems.

Description	Symbol	Value	Reference
Solid electrode conductivity	κ_s	$200\,\mathrm{S\,m^{-1}}$	[62]
Temperature	T	$298\,\mathrm{K}$	
Transfer coefficients	α_a, α_c	0.5	^{a}

^{a} Approximation

2.1.6 Limitations

All models are simplifications of reality, designed to capture the essential aspects of complex systems while reducing computational complexity. Therefore, it is inevitable to acknowledge their inherent limitations. The discussion of these limitations provides transparency and credibility to the research, providing a clearer understanding of the applicability and accuracy of the model. In addition, identifying and naming the weak spots of a model offers a solid foundation for further development and refinement. The limitations of the MSM are as follows.

The assumption of negligible bulk interactions between species within the electrolyte holds for the vanadium system, where primarily small monatomic ions are present. However, in organic flow battery systems, the presence of large macromolecules makes this assumption questionable (cf. Section 4.2.2).

Changes in density and viscosity as a result of concentration variations can influence the velocity field, especially with respect to organic systems. The transfer of this information during the simulation runtime, known as back coupling, is not achieved in the underlying model.

To obtain the electrode microstructure, a random section of the sample material is used. For a more accurate representation, a comprehensive statistical analysis of the entire material is necessary. The model assumes a shorter distance between the membrane and the current collector. In reality, this distance is approximately fifty times larger, requiring significantly more computational resources to simulate accurately.

In the reconstructed domain, the solid fibers do not touch the electrolyte boundaries. This setup inaccurately represents the fibers as being exposed to an infinite volume of electrolyte, which is not a realistic depiction of the actual electrode configuration. To address this issue, the SFD is created where the fibers do touch the boundaries, providing a more accurate representation. This domain is used to compare with the reconstructed material to assess the impact of this discrepancy and determine the significance of the differences in the model's predictions.

2.1.7 Computational Details

On the final note, the reader should take into account that the characteristic feature of this model is the independent calculation of fluid flow and scalar transport coupled with electrochemical reaction. In the first part, Equations 2.1 and 2.2 are linked only to the electrolyte domain and solved to obtain a steady-state velocity field of the electrolyte, which depends on the electrode fiber geometry, the fluid properties and the prescribed average velocity. In the second part, the solution algorithm separately solves the equations for the solid and electrolyte domains, which are coupled via boundary conditions. All model equations were implemented in the open-source software OpenFOAM version 7, which is based on the Finite-Volume Method [75, 76]. The simulations were conducted on a high performance computing system using up to 128 cores with an average simulation time of 24 to 48 hours.

2.2 Homogenized Cell-Scale Model

The 2D homogenized cell-scale model (HCSM) considers the in-plane direction of a flow battery half-cell. An essential feature of this modeling approach is the incorporation of fluid dynamics and the transport of a single diluted species that encompasses a homogenized porous medium. The model accommodates the conversion of species through the integration of a fundamental reaction term. Consequently, it is versatile and can be effectively applied to both the cathode and anode half-cells alike. Given its straightforward structure, the model exhibits high flexibility, making it applicable to various systems. Unless otherwise specified, the results in this work always refer to the positive half-cell.

In Chapter 6, the model is used to investigate the mass transfer coefficient extracted from the MSM simulations. Here, it is parameterized with the physical properties of the aqueous TEMPOL system, and the electrode properties are identical to those obtained for the reconstructed microstructure. Regarding the optimization calculations in Chapter 7, the HCSM is parameterized with the all-vanadium system, as this allows for a one-by-one experimental validation. The model is chosen to be as simple as possible, to ensure usability in both cases.

The following section outlines the fundamental physical phenomena underpinning the model, the underlying assumptions, governing equations, and boundary conditions that guide the approach, and the definition of the computational domain. In addition, limitations of the model are discussed as well.

2.2.1 Model Assumptions

The model assumptions made for the HCSM are as follows:

- The electrolyte is modeled as a Newtonian incompressible fluid with constant density and viscosity. The flow regime is assumed to be laminar and steady state.
- Constant temperature is assumed, and thermal effects are neglected.
- Transport and conversion of a single diluted species c are considered, while migration is neglected.
- The presence of other electrolyte compounds, e.g. water, hydrogen, sodium chloride, and sulfuric acid, is not taken into account.
- Membrane transport and side reactions are excluded from consideration.

2.2.2 Computational Domain

The computational domain represents a typical, experimental flow-through lab-scale cell, as illustrated in Figure 2.3. This design is chosen because it allows for accurate experimental validation with the cell introduced by Fraunhofer Institute for Chemical Technology (ICT) [73, 77]. It incorporates a primary manifold at both the inlet and outlet of the electrode to ensure the uniform distribution of the electrolyte. Detailed geometric data are summarized in Table 2.7. The electrolyte flows through the cell from the bottom right (inlet) to the top left (outlet).

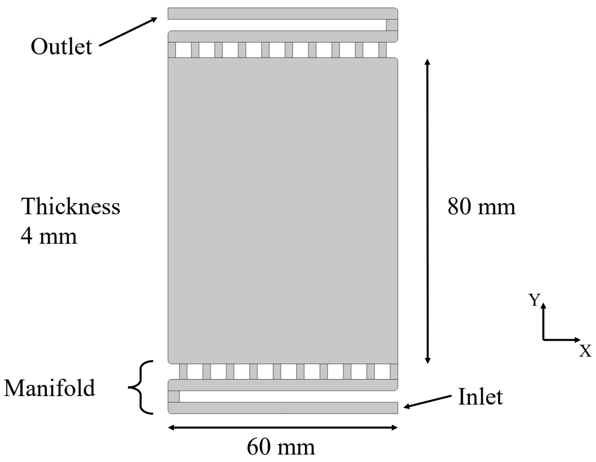

Figure 2.3: Computational domain of the 2D homogenized cell-scale model (HCSM) including inlet and outlet manifold.

Table 2.7: Geometrical properties of the computational domain.

Description	Symbol	Value
Electrode height within the cell	h_c	80 mm
Electrode width within the cell	w_c	60 mm
Manifold channel width	w_m	3 mm
Thickness of distributor inlets	t_i	2 mm
Height of distributor inlets	h_i	4 mm
Number of distributor inlets	n_i	10
Height of vertical channel section	h_{vc}	3 mm
Gap between the respective inflow channels	$(w_c - w_m - n_i \cdot t_i)/(n_i - 1)$	mm
Radius of fillet	r_f	1 mm
Domain thickness	d_d	4 mm

2.2.3 Governing Equations

The flow of electrolyte through the manifold and the porous electrode is described by the Brinkmann-type Navier-Stokes equations given by

$$\nabla \cdot \mathbf{u} = 0 \tag{2.22}$$

$$\rho(\mathbf{u} \cdot \nabla)\mathbf{u} = -\nabla p + \mu \nabla^2 \mathbf{u} - \frac{\mu}{K}\mathbf{u} \tag{2.23}$$

where $\mathbf{u}$ is the velocity, ρ is the density, p is the pressure, μ is the dynamic viscosity of the electrolyte, and K is the permeability of the porous electrode. Using the Carman-Kozeny equation, the permeability is expressed as [78]

$$K = \frac{d_f^2 \epsilon^3}{180\,(1-\epsilon)^2} \tag{2.24}$$

where d_f is the fiber diameter and ϵ is the porosity. Although this relation actually describes flow through packed beds of spherical particles, it can be used for fibrous porous media in flow battery application due to the low Reynolds number and comparatively high porosities [79]. The scalar transport of the active species is described using the following steady state mass balance equation:

$$\mathbf{u} \cdot \nabla c = D_e \nabla^2 c + R_c \tag{2.25}$$

where c is the concentration of the active species, D_e is the effective diffusion coefficient, and R_c is the volumetric reaction rate. In fact, the migration term is neglected in Equation 2.25 due to its minor transport effect in the in-plane direction [72, 80]. To account for the diffusivity in the porous electrode, the diffusion coefficient is calculated according to the Bruggemann correlation [81]

$$D_e = \epsilon^{1.5} D_c \tag{2.26}$$

where D_c is the diffusivity. Throughout this study, a fundamental reaction term R_c is used instead of the nonlinear Butler-Volmer equation, to describe the transformation of active species [82, 83]. The active species is transported by fluid flow and is continuously generated until it reaches its maximum concentration, labeled c_{max}. The reaction rate is given by

$$R_c = k_m A_V (c_{max} - c) \tag{2.27}$$

where k_m is the mass transfer coefficient and A_V is the specific active surface area of the porous electrode. The mass transfer coefficient can be written as [84]

$$k_m = \beta |\mathbf{u}|^{\alpha} \tag{2.28}$$

where β and α are empirical parameters depending on the electrochemical system and electrode.

2.2.4 Boundary Conditions

Fluid Transport At the inlet of the manifold, a Dirichlet boundary condition [67, 68] is set for velocity. The inlet velocity is calculated using a prescribed flow rate and the cross-sectional area of the inlet channel. At the outlet of the manifold, a Neumann boundary condition [67, 68] is applied for the velocity. The pressure is fixed at zero at the outlet and a Neumann condition is set at the inlet.

Species Transport The concentration c is representative of any active material, e.g. TEMPOL, VO^{2+} or VO_2^+ during the charge or discharge operation. The concentration field is initialized with $0\,\mathrm{mol\,m^{-3}}$ as well as the concentration at the inlet. At the outlet, a Neumann boundary condition is applied for the concentration. The maximum concentration is chosen to be $100\,\mathrm{mol\,m^{-3}}$ for a straightforward analysis of the conversion for both the TEMPOL and the all-vanadium system.

2.2.5 Simulation Parameters

When using the HCSM for the multiscale modeling approach in Chapter 6, the same physical and kinetic parameters are used as in the microscale investigations presented in Section 2.1.5. Regarding the optimization calculations in Chapter 7, the default set of all-vanadium parameters used is summarized in Table 2.8.

Table 2.8: Physical and kinetic parameters of the electrolyte and electrode regarding the all-vanadium system.

Description	Symbol	Value	Ref.
Electrolyte viscosity	μ	$4.928 \times 10^{-3}\,\mathrm{Pa\,s}$	[72]
Electrolyte density	ρ	$1354\,\mathrm{kg\,m^{-3}}$	[85]
Diffusivity VO^{2+} and VO_2^+	D_c	$3.9 \times 10^{-10}\,\mathrm{m^2\,s^{-1}}$	[72]
Fiber diameter	d_f	$14 \times 10^{-6}\,\mathrm{m}$	[86]
Active surface	A_V	$58\,471\,\mathrm{m^{-1}}$	[86]
Mass transfer parameter	α	0.4	[84]
Mass transfer parameter	β	1.6×10^{-4}	[84]
Operating temperature	T	$298\,\mathrm{K}$	-

2.2.6 Limitations

The HCSM serves the purpose of facilitating quick and straightforward reaction modeling while being conducive to topology and shape optimization. Although adoption of the Butler-Volmer equation for species is feasible, it entails higher computational costs, particularly when optimization processes are executed concurrently. Consequently, the model does not incorporate current or voltage considerations. Moreover, the omission of migration makes the expansion into three dimensions unnecessary. By prioritizing the exclusion of less utilized parameters, the model retains a high degree of flexibility. In essence, the model stands as a viable initial framework for multiscale modeling or optimization endeavors. However, future research requires inevitable improvements to the modeling approach.

2.2.7 Computational Details

The HCSM is implemented in COMSOL Multiphysics version 6. The software is based on finite element method and handles various physics and engineering applications described by coupled systems of partial differential equations. In this work, the software is chosen because of its ease of use and the pre-implemented optimization framework. In this work the laminar flow, transport of diluted species, topology optimization, and optimization interfaces are used. Regarding the multiscale modeling approach introduced in Chapter 6, the simulation time of an average computation is on the order of a few minutes on a simulation computer using an AMD Ryzen 9 3900X 12-core processor with 3.79 GHz and 64 GB RAM. The optimization calculations last between five to 20 minutes.

2.3 Optimization Methodology

In Chapter 7, topology optimization is adapted to redistribute porosity within the flow battery electrode and shape optimization to find optimized geometric parameters of novel cell designs. In both scenarios, the goal is to minimize the pressure drop while simultaneously maximizing the reaction rate to identify a favorable compromise between these contrasting factors. In porous media, an increase in porosity generally leads to a reduction in pressure drop due to lower flow resistance and improved permeability. Conversely, the reaction rate tends to increase with decreasing porosity, assuming that the available active surface area rises accordingly. However, this relationship is only valid under specific conditions: the structural properties of the porous medium, such as fiber diameter, must remain constant, and a strictly inverse proportionality between active surface area and porosity must be assumed. In more complex porous structures, additional factors - such as increased tortuosity, diffusion limitations, and variations in pore connectivity - can significantly influence both transport and reaction kinetics, potentially deviating from this idealized trend. In the following section, the cost functional of the minimization problem and the optimization methodologies are explained.

2.3.1 Optimization Problem and Cost Functional

A generic formulation of the flow optimization problem is given according to

$$\begin{gathered}\text{find control } \gamma \text{ and state } f \text{ which} \\ \text{minimize } \mathscr{J}\left(f,\gamma\right) \text{ and fulfill } \mathscr{G}\left(f,\gamma\right)=0.\end{gathered} \tag{2.29}$$

Here, the function γ is referred to as the control of the optimization, the function f as the state of the model, the functional $\mathscr{J}$ as the objective or cost functional, and $\mathscr{G}\left(f,\gamma\right)=0$ as the constraint or side condition. The side condition is presented by the governing equations in Section 2.2.3. The objective is formulated as a multiobjective cost functional to simultaneously minimize the inverse reaction rate of concentration and the pressure loss within the cell. According to Oleson et al. [87], the relation between the inlet and the outlet pressure is not a well-posed optimization function. Instead, the total viscous power dissipation P_d is used and defined as

$$P_d = \int_D \tau : \mathbf{S}\, dV \tag{2.30}$$

where τ is the viscous stress and $\mathbf{S}$ is the strain rate tensor. The multiobjective functional $\mathscr{J}$ is

$$\mathscr{J} = \int_D \left(s_1 \frac{1}{R_c} + s_2 P_d \right) dV \tag{2.31}$$

where s_1 and s_2 are scaling factors for each part of the cost functional. Flow batteries face two primary challenges: Power loss resulting from electrolyte pumping and incomplete conversion of active materials during operation. To address these problems, the flow resistance must be reduced by using highly porous electrodes. In contrast, a large active surface area is necessary at the same time to achieve complete conversion. Within this model, the inversely proportional relationship between porosity and active surface area underscores the trade-off inherent in flow batteries, delineating two conflicting optimization objectives. To pinpoint an optimal solution, these quantities are integrated into a single multiobjective cost functional. Each quantity is accompanied by a scaling factor, possessing inverse units of the reaction rate and power dissipation, respectively, to ensure compatibility. The scaling factors not only facilitate the combination of disparate metrics, but also offer the flexibility to weight each quantity as needed within the optimization process. In this stage of research, the scaling factors are initially set to unity as a starting point. The functional $\mathscr{J}$ is used both in topology and shape optimization.

2.3.2 Topology Optimization

The use of topology optimization in this work is inspired by the studies by Yaji et al. [82, 88], where it is used to identify optimized flow field designs in order to maximize the rate of species generation. As previously highlighted, the primary objective of this study is to determine the optimal porosity distribution within the electrode. The method aims at finding the optimal placement of material and void points within a specified domain, relying on finite-element discretization. The characteristic function $\chi(\mathbf{x})$ is

$$\chi(\mathbf{x}) = \begin{cases} 1 & \text{if } \mathbf{x} \in \Omega \\ 0 & \text{if } \mathbf{x} \in D \backslash \Omega \end{cases} \tag{2.32}$$

where $\mathbf{x}$ is the position in the reference domain D and Ω is the subset of material points as shown in Figure 2.4. The discontinuous function $\chi(\mathbf{x})$ of the density topology optimization

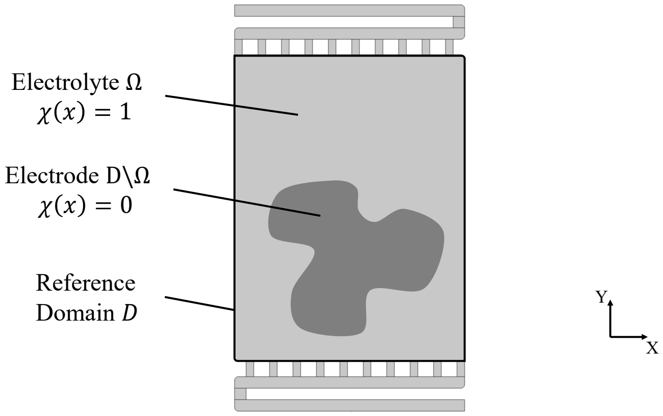

Figure 2.4: Computational domain of theHCSM including the reference domain D and its subset domains Ω and $D \setminus \Omega$ used in topology optimization.

approach [89] is replaced by a continuous function $0 \leq \theta(\mathbf{x}) \leq 1$ to allow differentiation. The optimization process is mesh-dependent because of the allocation of values within the finite element domain. To address this issue and to ensure the smoothness of $\theta(\mathbf{x})$, filtering techniques like the Helmholtz filter, which relies on partial differential equations, are employed [90]:

$$\theta_f = \theta_c + R_{min}^2 \nabla^2 \theta_f \tag{2.33}$$

θ_f is the filtered material volume factor, θ_c is the raw control variable modified by the optimizer, and R_{min} is the filter radius to control the degree of regularization. The use of Helmholtz filtering can lead to a gray scale with no distinct physical meaning. To prevent the emergence of gray scale within the design domain, a smooth step function, known as projection, is formulated:

$$\theta = \frac{tanh\left(\beta_o\left(\theta_f - \theta_\beta\right)\right) + tanh\left(\beta_o\theta_\beta\right)}{tanh\left(\beta_o\left(1-\theta_\beta\right)\right) + tanh\left(\beta_o\theta_\beta\right)} \tag{2.34}$$

where β_o is the projection slope and θ_β is the projection point. In the density approach, interpolation functions are used to penalize intermediate values of the material volume factor. Furthermore, Darcy's interpolation for fluid problems [91] is used in this work

$$\theta_P = q\frac{1-\theta}{q+\theta} \tag{2.35}$$

where θ_P is the penalized material volume factor and q is a parameter for controlling the damping of intermediate design variables. Unless otherwise stated, the parameters in Table 2.9 are used to perform the topology optimization calculations in this work.

Table 2.9: Topology optimization parameters.

Description	Symbol	Value
Filter radius	R_{min}	0.001
Projection slope	β_o	8
Projection point	θ_β	0.5
Initial material volume factor	θ_0	0.5
Darcy penalization factor	q	1

Consequently, the optimization problem is formulated as

$$\underset{\theta}{\text{minimize}}\,\mathscr{J} \quad \text{subject to} \quad 0 \leq \theta(\mathbf{x}) \leq 1\ \forall \mathbf{x} \in D. \tag{2.36}$$

To connect mathematical optimization with the physics of the underlying model, the penalized material volume factor is used to parameterize the porosity and active surface. In this work, we adapt the ansatz of Roy et al. [92] and Olesen et al. [87] and write the porosity and active surface as

$$\epsilon_{opt} = \theta_P(\epsilon_{max} - \epsilon_{min}) + \epsilon_{min} \tag{2.37}$$

$$A_{V,opt} = A_V\left(1-\epsilon_{opt}\right) \tag{2.38}$$

where ϵ_{opt} is the optimized porosity, ϵ_{max} and ϵ_{min} are the porosity limits, and $A_{V,opt}$ is the optimized active surface. The choice of appropriate porosity limits is an important decision in terms of optimization, which is explained in detail in Section 7.2.1. The optimized quantities are used within the physical model. In the context of topology optimization, the porosity term in Equation 2.24 is hence replaced with an optimized porosity ϵ_{opt}:

$$\text{Topology optimization:} \quad \epsilon = \epsilon_{opt} \tag{2.39}$$

By way of example, Figure 2.5 shows the topology optimization history with the cost functional value and the average porosity over the iteration number. In this case, the average porosity of the whole electrode domain is depicted. Selected topology designs are shown for the iteration numbers 5, 10, 20, and 30.

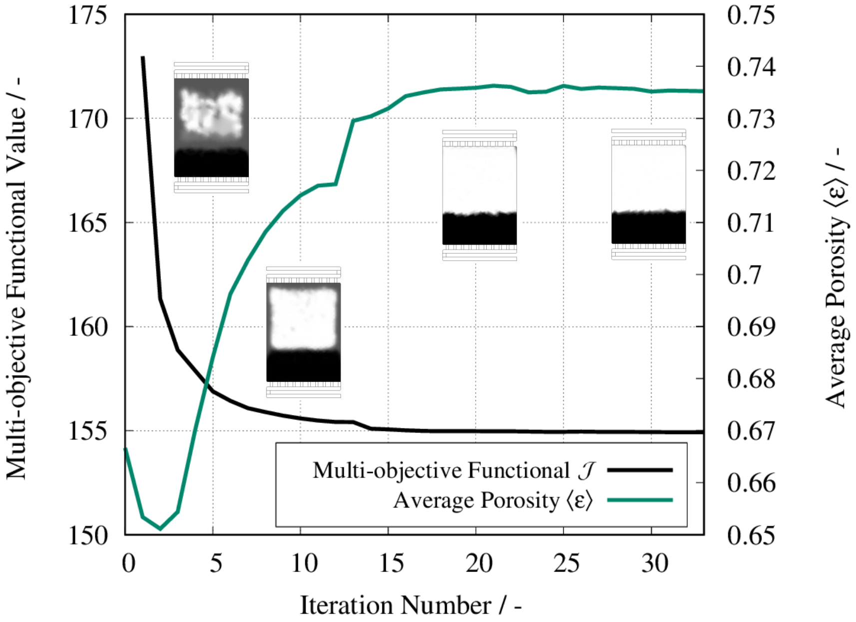

Figure 2.5: Multiobjective functional and averaged porosity versus the iteration numbers of the topology optimization process. Topology designs of the porosity distribution for iteration numbers 5, 10, 20, and 30.

Gradient-based Optimization Gradient-based optimization is one of several mathematical optimization methods, particularly effective when the objective functional can be differentiated [93]. Starting from an initial set of variables, the gradient of the objective functional is calculated. In the context of topology optimization, the decision variables, such as porosity, are iteratively adjusted in the direction of the highest gradient to minimize the value of the objective function. The step size, which determines the extent of adjustment in each iteration, is carefully managed to balance the speed of convergence and accuracy. This iterative process continues until the changes in the objective functional are sufficiently small, indicating that an optimal solution has been found [94].

Gradient-based optimization is well-suited for topology optimization because of its ability to handle a large number of variables, making it scalable in high-dimensional design spaces. It offers comparatively fast convergence compared to non-gradient methods, which is crucial in topology optimization where computational resources are significant considerations. In addition, gradient-based methods are robust and supported by well-established algorithms. In this work, the sparse nonlinear optimizer (SNOPT) algorithm [95], based on sequential quadratic programming, is used for topology optimization.

However, gradient-based methods have disadvantages, such as the potential to get stuck in local minima, failing to find the global minimum. They are also sensitive to initial conditions, and the starting point has a high influence on the outcome. These points are investigated in detail in subsequent chapters (cf. Chapters 7.2.4 and 7.2.8) to ensure the robustness and reliability of the optimization process.

2.3.3 Shape Optimization

As mentioned above, the shape optimization aims to determine the best possible geometric shape of the cell to achieve the minimization of the objective functional. In shape optimization, the targeted quantity is scaled by the control variable. In this context, the novel cell designs introduced by Gurieff et al. [96] are subject to optimization. More precisely, these include the height or both height and width of the rectangular cell, the upper width of the trapezoidal cell, and the angle of the radial cell. The control variable undergoes variations within a constrained parameter space using the Nelder-Mead method until an optimal value is achieved minimizing the cost functional. For a specific control variable, denoted as ψ, the optimization problem is formulated as follows:

$$\underset{\psi}{\text{minimize}}\ \mathscr{J}(D_{opt}) \quad \text{subject to} \quad \psi_{min} \leq \psi \leq \psi_{max} \tag{2.40}$$

where ψ_{min} and ψ_{max} are restrictions of the control variable, e.g. the minimum and maximum height of the cell. The actual bounds and initial values of the respective control variables are presented in Section 7.3. It should also be mentioned that in this investigation the porosity of the electrode is kept uniform and constant within one optimization calculation.

For shape optimization, the electrode reference domain D, as illustrated in Figure 2.4, undergoes a transformation parameterized by the optimization control variable ψ using a deformation function T_ψ.

$$\text{Shape optimization:} \quad D_{opt} = T_\psi(D). \tag{2.41}$$

In the case of optimizing the height of the cell, the deformation function can exemplarily be written as

$$T_\psi(x, y) = (x, \psi \cdot y) \tag{2.42}$$

The Nelder-Mead Method The Nelder-Mead method [97], also known as the simplex method, is a gradient-free optimization technique widely used in shape optimization due to its simplicity and effectiveness. Instead of relying on gradient information, which can be challenging to compute for complex geometries, the method operates by evaluating the objective function at vertices of a simplex, a polytope with $n+1$ vertices in n dimensional space (e.g. a triangle in 2D). Initially, the simplex is defined by these vertices, and in each iteration, the vertex with the worst objective function value is replaced through a series of geometric operations: reflection, expansion, contraction, and shrinkage. Figure 2.6 shows the operations for visualization.

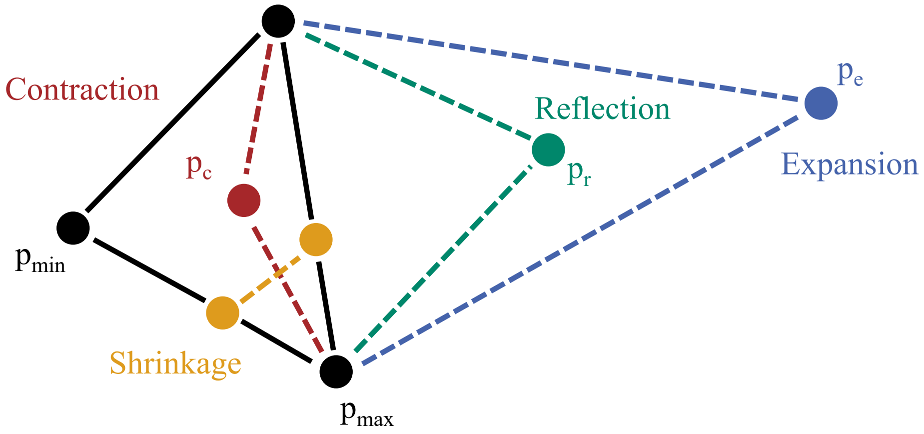

Figure 2.6: Visualization of the Nelder-Mead method in the two dimensional space according to Chen et al. [98]. The basic operations reflection, expansion, contraction, and shrinkage are shown.

These operations adaptively explore the search space until a minimum of the objective function is approximated [98–100]:

1. **Reflection**: The algorithm reflects the worst-performing point p_{min} along the centroid of the remaining n points to the point p_r. In this way, the simplex is stretched away from the worst region. If the function value of p_r is neither the lowest nor the highest, it is used instead of p_{min} to form the simplex for the next iteration.
2. **Expansion**: If the reflected point p_r has the highest function value of the vertices, it is expanded further away from the centroid to point p_e and used to form the simplex of the next iteration.
3. **Contraction**: If the reflected point p_r has the lowest function value of the vertices, it is contracted toward the centroid to point p_c. This point is then used instead of p_{min} to form the new simplex of the next iteration if it has a higher function value than p_{min}.
4. **Shrinkage**: If the contraction point p_c has a lower function value than p_{min}, no improvement of the initial simplex is found. Therefore, all vertices shrink toward the best-performing point p_{max} to form a new simplex.

This procedure repeats until a stop criterion is reached. This can be, for example, a minimal simplex size, an elapsed time period, or a maximum number of iterations.

In shape optimization, the geometric parameters are modified, which makes gradient calculation difficult. The Nelder-Mead method circumvents this challenge by focusing on function evaluations alone, making it suitable for optimizing shapes characterized by discrete or irregular geometries. Its simplicity and computational efficiency allow it to effectively explore design spaces with low dimensions, where each design parameter variation impacts specific geometric features, e.g. adjusting cell height or width.

3 Characterization of Electrode Material

Microscale modeling aims to investigate the physicochemical phenomena and transport mechanisms within the porous microstructure and at the interface of the flow battery electrode. Therefore, it is essential to resolve the pore and fiber spaces, as the equations are directly linked to the computational grid, as shown in Figure 2.1. Consequently, precise information on the fiber geometry is required as input for the simulation. In this work, the information is obtained by imaging a commercial graphite felt electrode material using µCT. The resulting tomogram is processed to reduce imaging errors and then digitally reconstructed into a virtual volume serving as a computational domain.

In general, the electrode microstructure for the computational domain can be obtained either by experimental image reconstruction or by replicating it using computer-aided design software. In the case of image reconstruction, µCT or focused ion beam / scanning electron microscopy (FIB-SEM) images) are widely used. Qui et al. [57, 58] were one of the first to use FIB-SEM and µCT-reconstructed carbon felt electrodes in a FB microscale model. Kok et al. [101] also adapted µCT techniques to obtain the microstructure of electrospun and carbon felt electrode materials for their direct numerical simulation of the mass transfer coefficient. Zhang et al. [64] continued using µCT to obtain the microstructure of carbon paper, graphite felt and carbon cloth electrodes for FB simulation.

Furthermore, electrode microstructures with different shape, size, or orientation can be constructed based on experimentally obtained data. Both Sadeghi et al. [102] and Banerjee et al. [103] used data obtained from µCT to build a representative pore network as an alternative microscale simulation domain. Based on statistical information from FIB-SEM images, Chen et al. [104] created a variety of different electrode microstructures by arranging cylinders with a random number generator. Recently, Hereijgers et al. [105] presented the generation of structured 3D electrode designs derived from static mixers with improved mass transfer properties. The regularly shaped electrodes showed a reduction in pressure drop compared to the commercial felt electrodes.

Considering the latest manufacturing processes such as micromachining or 3D printing, the fabrication of structured electrodes is a promising technique for further improvement of battery and flow battery performance [106, 107]. In general, stochastic generation of electrode simulation geometries is an efficient way to study the microstructure properties. Moreover, numerically beneficial grids of the complex microstructure can be obtained which lead to less error-prone computation.

3.1 Porous Electrode Material

Research has consistently demonstrated the significant impact of electrode structure and material on the performance and efficiency of FBs, highlighting the electrode as a crucial component [108]. The porous electrode provides the necessary surface area for redox reactions, making high specific surface area and electrical conductivity essential properties of the electrode material. In addition, a high degree of wetting by the electrolyte is critical for efficient operation. In this work, the flow-through electrode configuration is adapted, which involves a porous matrix of electronically active solid material through which the liquid electrolyte flows.

Carbon-based materials are used predominantly as FB electrode materials due to their low cost, high electrical conductivity, and electrochemical stability in the acidic environment of the electrolyte. These materials can achieve high porosity levels, up to 95%, which is beneficial in facilitating electrolyte flow and increasing reaction sites. Carbon offers versatility across different FB systems. The manufacturing process for graphite felt electrodes typically involves weaving polymer precursors, such as polyacrylonitrile (PAN) or rayon, into a textile structure with aligned or non-ordered fibers. These woven materials are then carbonized by thermal treatment, such as pyrolysis, conducted at high temperatures in the absence of oxygen. This process yields a carbon-based porous electrode with the desired structural and conductive properties for efficient FB operation [109].

To improve the electrochemical activity and hydrophilic properties of the graphite material, it was further modified. The latest research introduced carbon-based catalysts such as fullerenes, carbon nanotubes, carbon-carbon composites, or biomass carbon as an excellent way to improve electrode performance [110, 111]. Furthermore, alternative electrode materials such as graphene or reticulated vitreous carbon are the subject of current research [24, 26].

However, in this work, a sample of commercial SIGRACELL® GFD 4.6 graphite felt (SGL Carbon SE, Wiesbaden, Germany) [62] is reconstructed via μCT techniques. To account for the compression of the felt during assembly into a cell, the sample is also examined in a compressed state. Several studies have revealed that felt compression reduces ohmic and contact resistances, resulting in enhanced performance [112–114]. The optimal compression depends on various factors, such as the precursor or thermal treatment of the felt. The viscosity of the electrolyte also plays a significant role. Generally, a compression reference of approximately 30% is considered optimal [115], where compression represents the percentage of thickness reduction. To achieve compression within the µCT unit, the sample is clamped between two thin plates. The compression is adjusted using two screws in the plates, which are secured with locknuts. The compression value of 30% is set by using a caliper. The entire compression device is made of polyvinyl chloride to avoid distorting the imaging process.

3.2 Micro-Computed Tomography

Micro-computed tomography is a nondestructive imaging technique that provides high-resolution 3D representations of the internal structure of a sample. The quantity measured is the transmission of X-ray radiation through the sample material. The working principle of the imaging technique is shown in Figure 3.1.

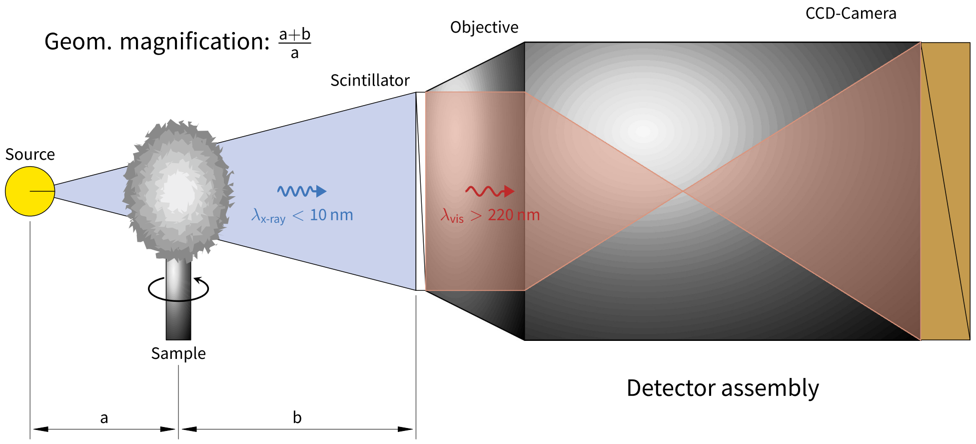

Figure 3.1: Schematic depiction of the working principle of X-ray computed micro-tomography by Dobler and Radel [116]. Reproduced under the terms of the Creative Commons Attribution 4.0 License (CC BY 4.0). No changes have been made.

The radiation spectrum emitted by the X-ray source is scattered and attenuated by the sample. The 2D transmission images, the so-called projections, are recorded by the detector assembly. For three-dimensional alignment, the sample rotates 360 °during the scan, and multiple transmission images are taken from different angles [116].

The scintillator membrane is an additional tool that converts the X-ray spectrum into visible light, which is then captured by a charge-coupled device (CCD) camera coupled with an objective lens. This makes further optical magnification possible. By varying the distances between the source, sample, and detector unit, the geometric magnification of the image can also be adjusted. At the end of the measurement, 16-bit grayscale cross-sectional images of the sample stacked over the height are available.

In this study, the XRadia 520 Versa (Carl Zeiss Microscopy GmbH, Oberkochen, Germany) is used, which achieves a theoretical maximum resolution of 700 nm and a minimum voxel size of 70 nm. The X-ray source uses a tungsten target. The power of the source is adjustable in the range of 2-10 W with associated tube voltages of 30-160 kV.

3.3 Reconstruction of Experimentally Gained Images

The typical workflow for image processing is shown in Figure 3.2 and illustrates the process of transforming raw µCT image data into a virtual volume of the graphite felt electrode as carried out in the course of this study. First, the 16-bit grayscale raw images from the µCT scan are aligned so that the pixels of consecutive images correspond to the same in-plane location (a). Then a representative subset of the scan is cropped from the raw data (b). Filtering techniques such as median filtering [117] or non-local means filtering [118] are applied to reduce image noise and facilitate further segmentation (c). The fiber space is separated on the basis of a pixel intensity threshold, resulting in a segmented binary image stack where pixels belong to the fiber or the pore space (d). The extracted regions of interest are subsequently refined by closing holes in the fiber space and removing islands in the pore space or at the image border (e). Phase connectivity is a crucial parameter in microscale modeling. Electrolyte flow and species transport occur only through the connected pore regions, while electron transport is

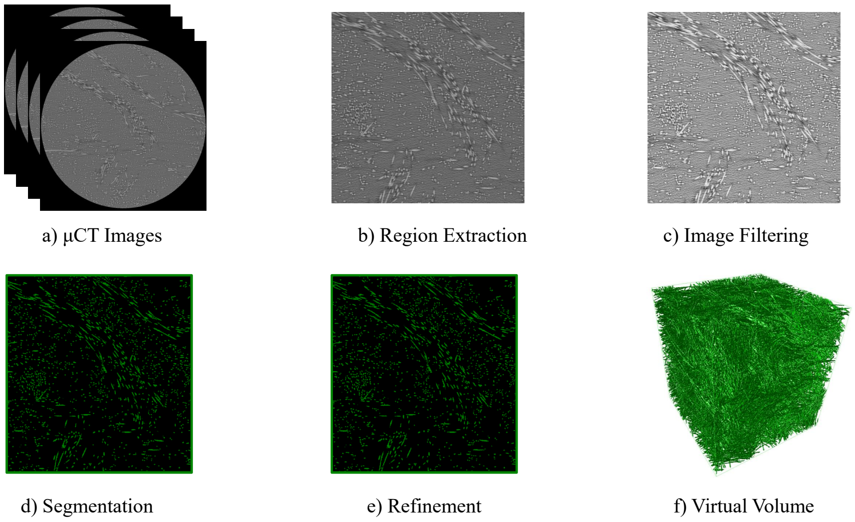
a) µCT Images

b) Region Extraction

c) Image Filtering

d) Segmentation

e) Refinement

f) Virtual Volume

Figure 3.2: Schematic depiction of the reconstruction process steps from µCT images towards a virtual volume.

restricted to the connected fiber regions. Disconnected islands of material do not contribute to the electrochemical simulation. Finally, a virtual volume reconstruction of the scanned graphite felt is performed (f).

To obtain a high-quality mesh for simulation, geometry adjustment algorithms such as smoothing or surface wrapping are adapted. These adjustments are performed on another specific subset of the sample corresponding to the dimensions of the final computational domain. In this step, it is also ensured that all solid fibers are connected to each other and to the current collector plate. On a final note, the reconstructed domain is achieved as shown in Figure 2.2. In order to make the domain compatible with the MSM, a separation is performed between the electrode region and the surrounding electrolyte region. Furthermore, the boundaries and corresponding boundary conditions are stated.

Image processing is performed using the software Dragonfly® (Object Research Systems, Montreal, QC, Canada). The mesh generation is performed with SpaceClaim (Ansys Corporation, Canonsburg, PA, USA) and OpenFOAM®, v1906 (ESI Group Corporation, Rungis, France).

In addition to the creation of the volume mesh, image processing of the microstructure offers the opportunity to digitally examine the electrode structure and determine parameters such as porosity, specific surface area, and fiber or pore size. Figure 3.3 shows the fiber and pore size distribution and Table 3.1 other parameter of the graphite felt obtained by image processing.

Table 3.1: Microscale parameter obtained from image processing of the SIGRACELL® GFD 4.6 graphite felt under 30% compression.

Description	Value
Mean fiber thickness	14 ± 1 µm
Minimum fiber thickness	9.5 µm
Maximum fiber thickness	27.4 µm
Mean pore thickness	123 ± 31 µm
Minimum pore thickness	0 µm
Maximum pore thickness	218 µm
Porosity	92.6

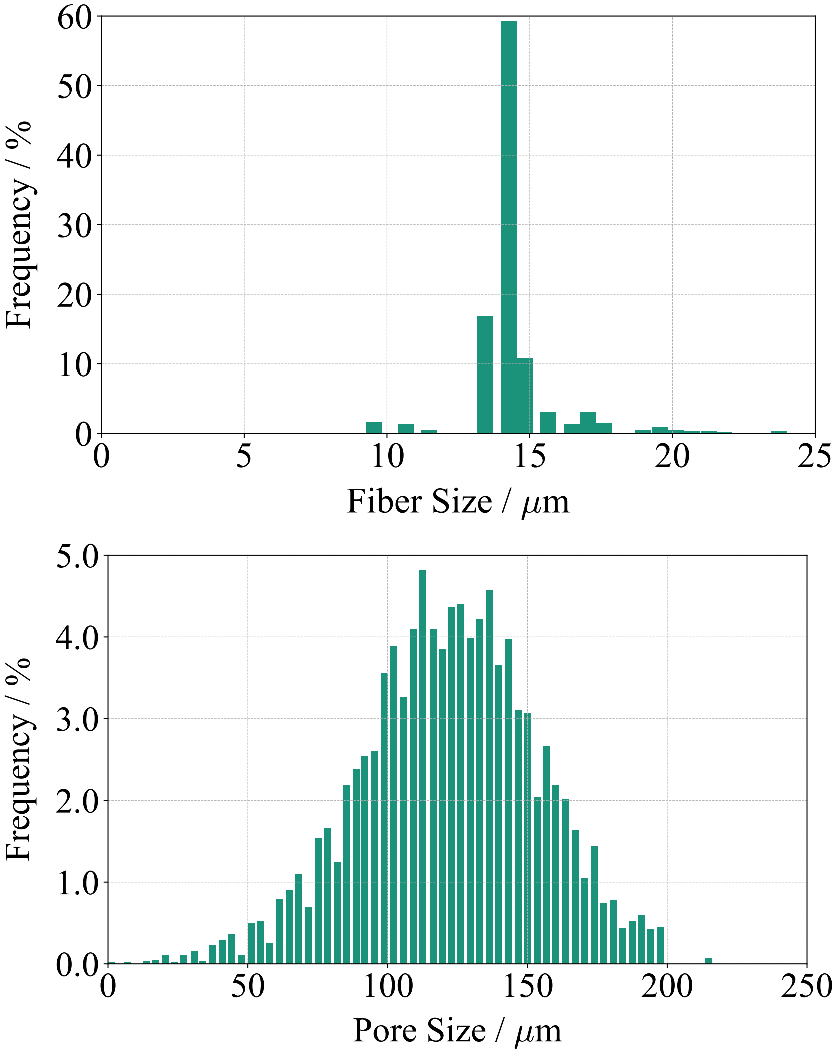

Figure 3.3: Histograms of fiber (top) and pore (bottom) size distribution of the SIGRACELL® GFD46 graphite felt, obtained by image processing of μCT image data.

4 Experimental Validation

To fully understand and optimize flow batteries, it is important to develop accurate models that can reliably predict their behavior under various operating conditions. Therefore, experimental validation is crucial for verifying that the models accurately replicate these phenomena and behavior. The validation process is essential to build confidence in the precision and reliability of models and their application in performance prediction and optimization. The following chapter presents the validation of the MSM and HCSM using literature data and experimental data obtained by ICT and French National Centre for Scientific Research (CNRS) as part of the SONAR project. Brief descriptions of the respective experimental setups are provided, followed by in-depth discussions on various facets of model validation. The MSM is validated against the VFB models from the literature, the TEMPOL half-cell potential obtained from the redoxme flow electrochemical half-cell [119] and MV/TEMPOL power density of the ICT cell. The HCSM is validated against the open circuit voltage (OCV) and cell potential during charge of the ICT cell using the all-vanadium system.

4.1 Experimental Setup

The experimental cell utilized by ICT is a standardized and self-developed laboratory cell featuring a geometric electrode area of 40 cm^2, facilitating comparisons in a variety of materials [4, 120]. In the scope of this validation, measurements conducted with the all-vanadium and MV/TEMPOL system are used. The ICT setup comprises a cell, electrolyte tanks, and a membrane pump, depicted in Figure 4.1 (left), capable of evaluating OCV, cell potential, and individual half-cell potentials at various flow rates. Cell configuration includes an anion exchange membrane (Fumasep FAP-450, FUMATECH BWT GmbH, Bietigheim-Bissingen, Germany) and GFD46/GFA6 graphite felt electrodes (SGL Carbon GmbH, Meitingen, Germany [62]). More information on the experimental setup can be found in [73, 77]. The geometric measures are the same as those presented in Table 2.7.

The galvanostatic experiments conducted by CNRS utilize the redoxme flow electrochemical half-cell depicted in Figure 4.1 (right), employing the TEMPOL and MV system. This setup comprises two chambers separated by an Nafion™, ion-exchange membrane that features a three-electrode configuration with electrolyte circulation mode. The reference electrode is positioned in the same chamber as the working electrode, enabling the measurement of individual half-cell potentials. Within the cell compartment, a glassy carbon electrode interfaces with graphite felt to obtain the potential. In this validation, the half-cell potential of TEMPOL is tracked while MV is used in the other half-cell compartment.

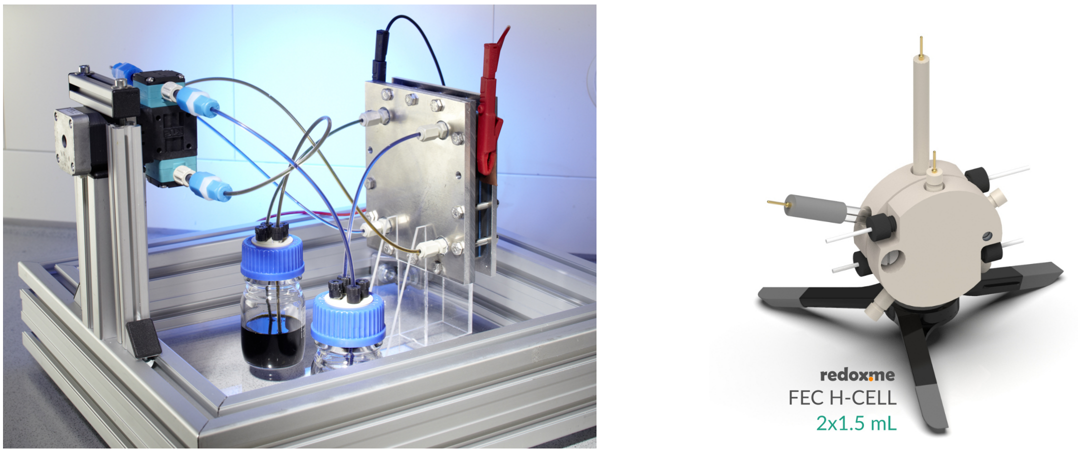

Figure 4.1: Experimental setup of the Fraunhofer ICT 40 cm^2 laboratory cell (left) and the redoxme flow electrochemical half-cell [119] (right). Reproduced with permission and copyright by © Fraunhofer ICT and © redoxme AB.

4.2 Microscale Model

Validating the MSM includes significant challenges due to the complexity and complexity of microscale phenomena. Experimental operations on this scale are difficult and require precise control and measurement. The validation process aims to approximate the experimental results as closely as possible, despite these challenges. To achieve this, three distinct approaches are employed to validate the MSM: comparison with established all-vanadium models from the literature, validation against experimental data obtained with the redoxme half-cell, and assessment against the power density measurements of the ICT cell. Each of these approaches provides a critical perspective in assessing the model's accuracy and reliability.

4.2.1 Validation against Vanadium Models

After the development of the MSM, validation is performed using two distinct all-vanadium models for orientation in the early development stage. The selected models, proposed by You et al. [72] and Qiu et al. [57], respectively, mark significant advances in the field of FB development. You et al. introduced one of the first homogenized models, validated through experiments, which facilitated performance analysis under varying conditions of current density or porosity. Qiu et al. developed the first model capable of resolving the intricate interplay of species transport, fluid dynamics, and charge distribution at the microscale. Both models investigate the all-vanadium system, using the same system parameters. The computational domain used in the MSM is based on the simplified electrode geometry with idealized fibers of Qiu et al.

In this validation study, separate half-cell simulations of the anode and cathode are conducted for specific SOC. To determine the cell potential, the individual half-cell potentials are combined with an assumed membrane potential of 131 mV [121]. The reaction rate constants for the all-vanadium system exhibit significant variability with respect to the concentration and electrode material [122]. In the present calculations, the reaction rate constants are set to $6.8 \times 10^{-6}\,\mathrm{m\,s^{-1}}$ for the positive half-cell and to $1.7 \times 10^{-6}\,\mathrm{m\,s^{-1}}$ for the negative half-cell, respectively. The inlet concentration remains constant for the charge and discharge operation, while the initial vanadium concentration is $1500\,\mathrm{mol\,m^{-3}}$ for both the anolyte and the catholyte. The applied galvanostatic current density is $40\,\mathrm{mA\,cm^{-2}}$.

Figure 4.2 presents the cell voltage as a function of SOC for both charge and discharge operation. The two established reference models are illustrated alongside the outcomes derived from the current modeling approach. The OCV is additionally included for reference.

In general, the results obtained from the MSM demonstrate good agreement with the reference models, exhibiting the characteristic shape derived from the Nernst equation. In particular, the charging process shows closer alignment with the reference models compared to the discharge process. This discrepancy may be due to factors such as the selection of reaction rate constants and the incorporation of the membrane potential. In terms of quantitative comparison, the maximum deviation of the simulated SOC states from the experimentally validated study by You et al. is approximately 3.6 % for the charging process and 6.9 % for the discharge process.

4.2.2 Validation using TEMPOL Half-Cell Potential

Concerning the measurements of CNRS using the redoxme flow electrochemical half-cell, the current density is $2.83\,\mathrm{mA\,cm^{-2}}$ and the initial concentration is 0.011 M TEMPOL in 1 M NaCl. The velocity is estimated to be $0.0177\,\mathrm{m\,s^{-1}}$ corresponding to a flow rate of $30\,\mathrm{mL\,min^{-1}}$ used in the experimental setup. To reproduce the experimental data, the reconstructed microstructure depicted in Figure 2.2 is used.

Figure 4.3 illustrates the half-cell potential plotted against SOC for both charge and discharge operations. The experimentally derived half-cell potential versus SHE is represented by a

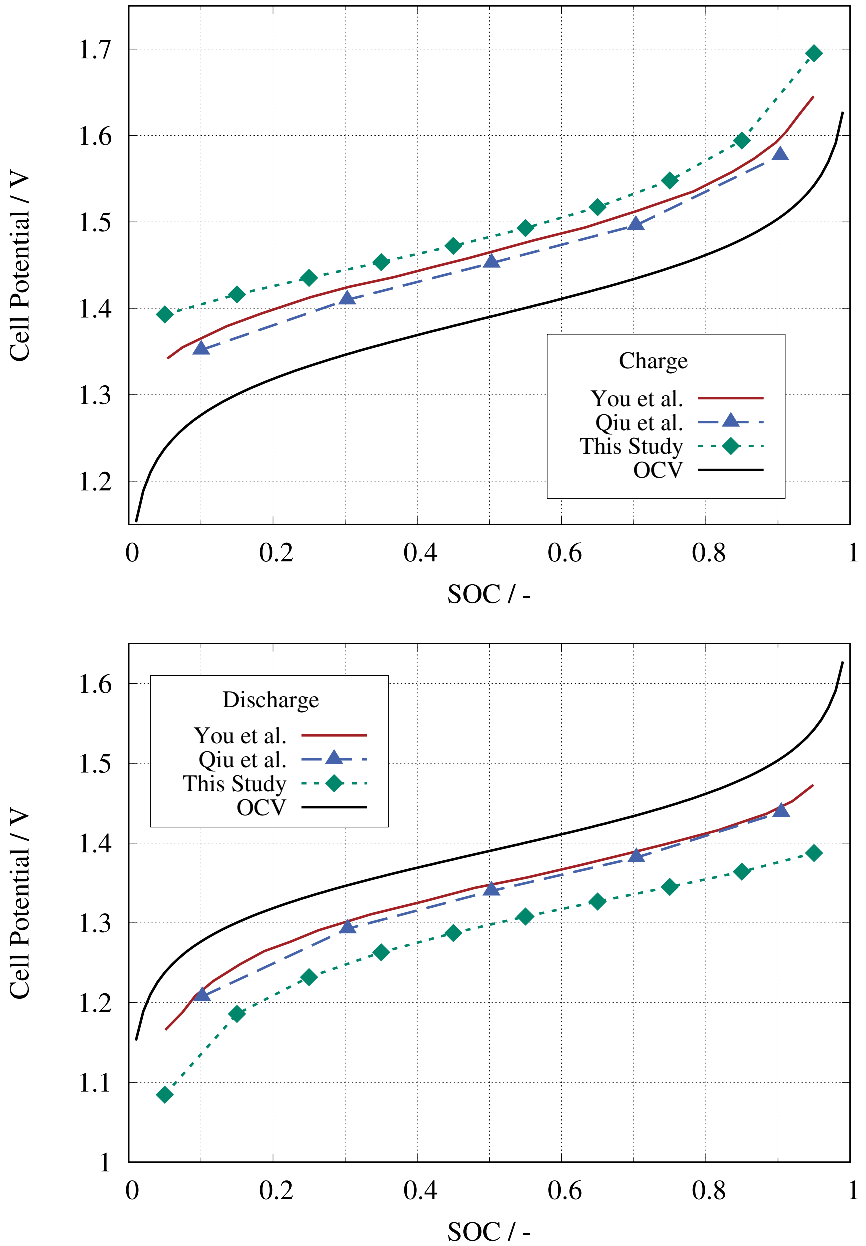

Figure 4.2: Cell potential of the all-vanadium system as a function of SOC for both charge (top) and discharge (bottom) operations. The graphs show the reference models by You et al. [72] (red) and Qiu et al. [57] (blue), alongside the results obtained from the current modeling approach (green). Additionally, the OCV (black) is included for reference. The applied current density is 40 mA cm^{-2} and the initial concentration is 1.5 M vanadium.

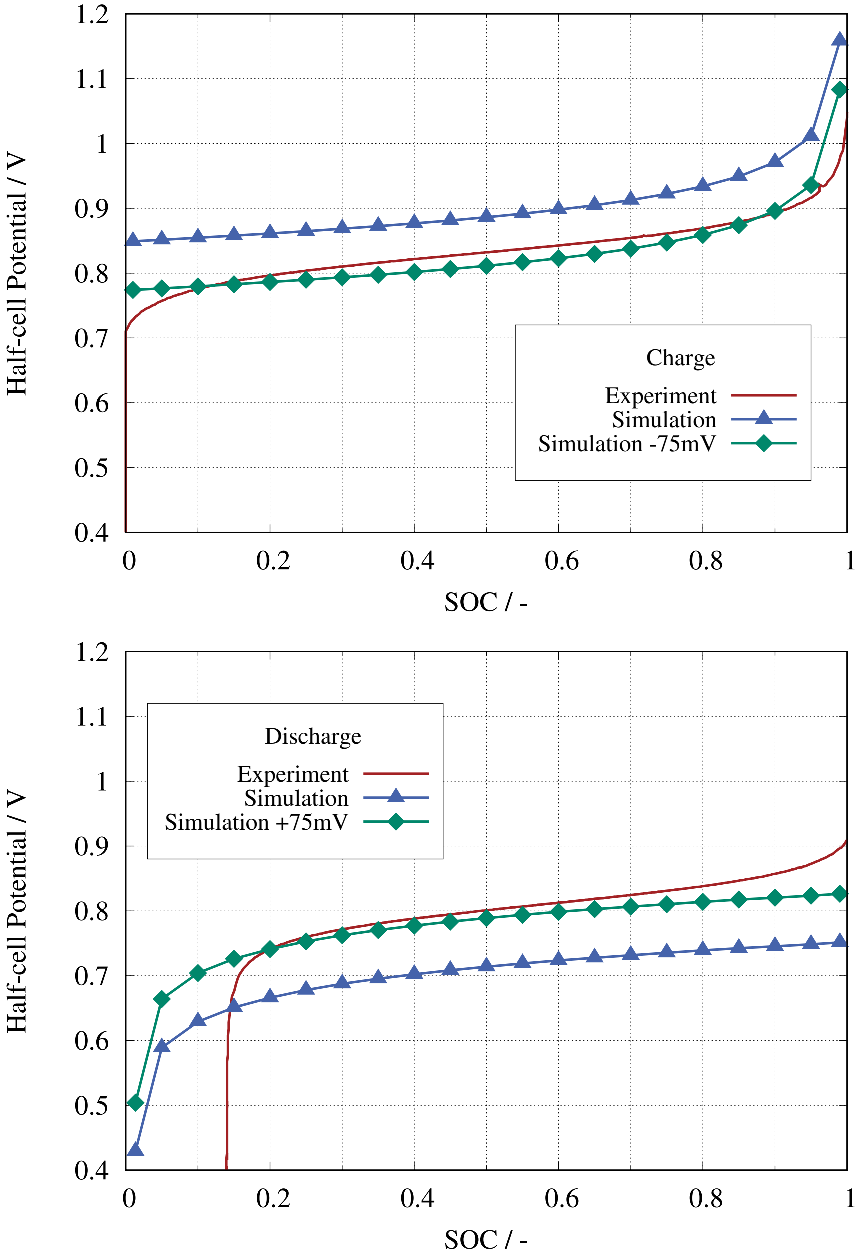

Figure 4.3: Half-cell potential of the TEMPOL system versus SOC. The experimental curve showing the the first charge (top) and discharge (bottom) cycle of the redoxme cell is marked in red. The simulation results are colored in blue and green respectively. To fit the experimental results the actual simulated half-cell potentials are modified with 75 mV. The current density is 2.83 mA cm^{-2} and the concentration is 0.011 M TEMPOL in 1 M NaCl.

solid red line, corresponding to the first charge and discharge cycle of the cell. The initial simulation results are represented in blue. To align with the experimental curve, additional 75 mV are subtracted for the charge and added for the discharge case, as indicated in green. Note that in the simulations certain SOCs are simulated using a quasi-steady-state approach with constant inlet concentration.

The experimental curve exhibits the characteristic trend that stems from the Nernst equation. In the case of discharge, it is observed that the initial SOC cannot be fully attained. This occurrence is attributed to self-discharge due to the crossover and electrochemical instability of the TEMPOL radicals, as discussed by Zhou et al. [123]. The simulation outcomes closely align with the experimentally observed for both charge and discharge. Particularly noteworthy is the accurate reproduction of the curve's shape within the limiting SOC ranges by the model. These limiting ranges are related to high SOC in charge and low SOC in discharge, respectively. In contrast, there is a lack of complete congruence in the opposite regions. The asymmetry in the curve arises from the use of the concentration of $TEMPOL^+$ concentration as the limiting factor, as described in Subsection 2.1.4. To align the potential level of the experimental curve, a voltage adjustment of 75 mV is applied [72, 80, 124]. The mismatch in potential arises from the utilization of dilute solution theory, which assumes the ideal behavior of ions without interaction in the bulk. However, the validity of this theory for aqueous organic electrolytes is questionable as discussed by Mourouga et al. [125]. To address the non-ideal mixing effects, activity coefficients should be incorporated in the Nernst equation instead of concentrations. However, these activities are unknown for the TEMPOL system. Unless otherwise stated, the voltage correction of 75 mV is considered in all MSM simulations using the reconstructed microstructure domain. In summary, the maximum deviation between the experiment and the fitted simulation is 6% for low SOC during charge and 7% for high SOC during discharge.

4.2.3 Validation using the MV/TEMPOL Cell

In a further investigation, the MSM is validated against the full cell assembly of the ICT experimental MV/TEMPOL test cell. To achieve this, the model is additionally parameterized with the MV system. The reference experimental data are sourced from Gerlach et al. [126]. Regarding the validation process, the galvanostatic discharge processes are examined at three different current densities: 12.5, 25.0 and 37.5 $\mathrm{mA\,cm^{-2}}$. In each scenario, the concentration is 0.1 M MV/TEMPOL in 1 M NaCl. The flow velocity of 0.004 $\mathrm{m\,s^{-1}}$ within the electrode corresponds to a flow rate of 40 $\mathrm{mL\,min^{-1}}$ and is determined using the HCSM. The reconstructed microstructure is used in the underlying simulations because the same electrode material is used in the experiment. For each of the specified operating current densities, separate half-cell simulations are conducted for the MV and TEMPOL sides. A comprehensive discharge process is modeled by implementing mapped boundary conditions between the inlet and outlet.

Figure 4.4 shows the discharge behavior of the MV and TEMPOL half-cell potential for the three current densities. With respect to the same amount of active material at the beginning, a higher current density leads to a faster discharge of the cell. All simulations were performed without the restriction of a cut-off voltage that led the simulation to stop automatically. The simulations stop automatically when the concentration of the species to be consumed (MV^+ and $TEMPOL^+$) reaches zero in a certain computational cell in the domain. Therefore, the state of complete discharge for $37.5\,\mathrm{mA\,cm^{-2}}$ cannot be achieved. The simulations end with an SOC of 0.05 for MV and an SOC of 0.08 for TEMPOL.

To compare the simulation with the experiment, we draw and add the averages of the respective half-cell potentials. By multiplying the potential by the appropriate current density, the power density is obtained and serves as a benchmark for validation. Figure 4.5 shows the respective power densities of the experiment and the simulations. With respect to $12.5\,\mathrm{mA\,cm^{-2}}$ and $25.0\,\mathrm{mA\,cm^{-2}}$, the simulation and experiment are in very good agreement. At $37.5\,\mathrm{mA\,cm^{-2}}$, the simulation overpredicts the experiment with a deviation of 8%. This discrepancy probably results from the exclusion of potential values below the SOC limits described above at a high current density.

In general, it is remarkable how well simulation and experiment match up. In the simulations, no membrane potential and no contact resistances between the membrane and electrode are considered. These would actually lead to a reduction in potential and thus power density. Indeed, when polarization curves are looked at, a potential shift is often applied to account for the membrane potential, as was done before. Whether the membrane voltage drop is simply extremely small or whether information is lost during potential averaging cannot be determined exactly. Furthermore, the electrolyte was cycled up to five times for experimental determination of potentials. The associated degradation is also not considered in the simulations.

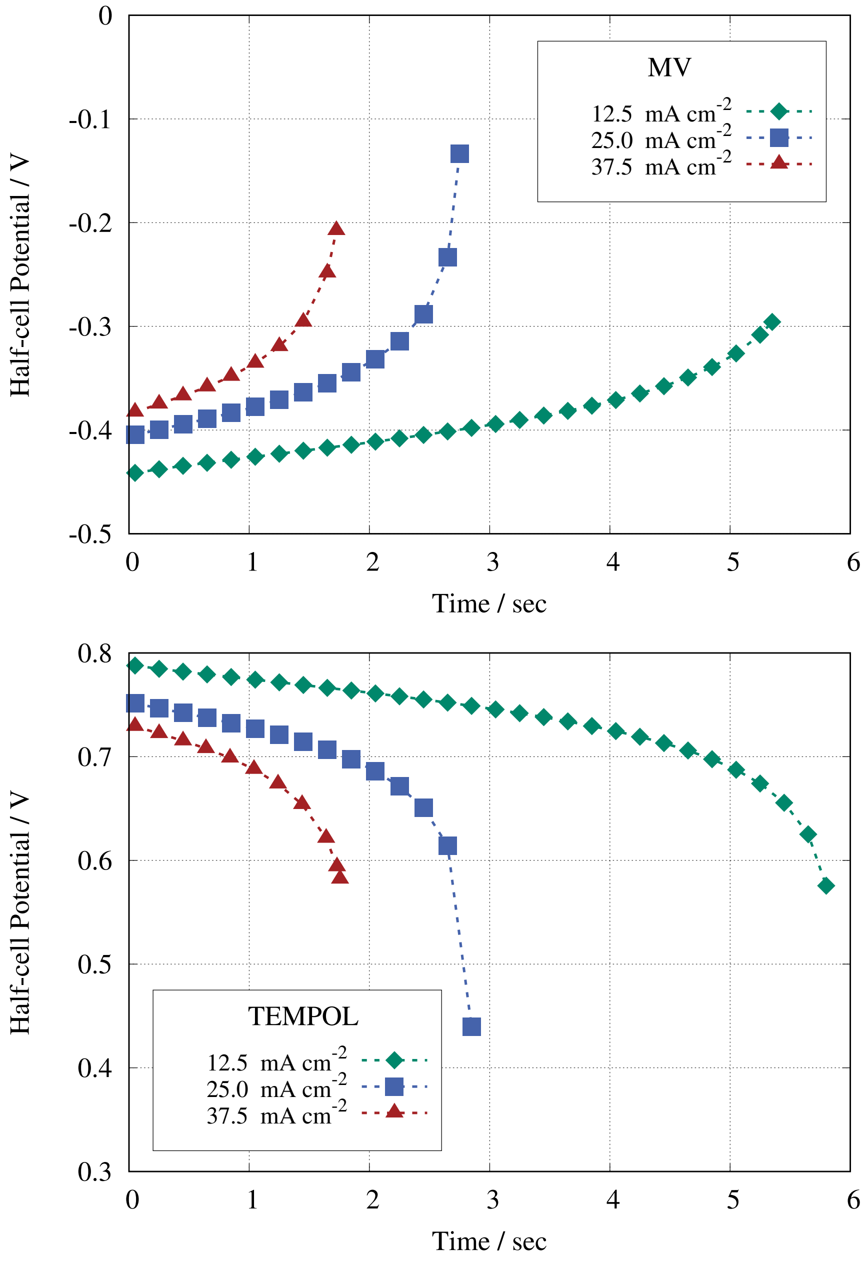

Figure 4.4: Half-cell potential of the MV (top) and TEMPOL (bottom) system over time during discharge operation for three different current densities 12.5, 25.0 and 37.5 mA cm^{-2}. The concentration is 0.1 M MV/TEMPOL in 1 M NaCl.

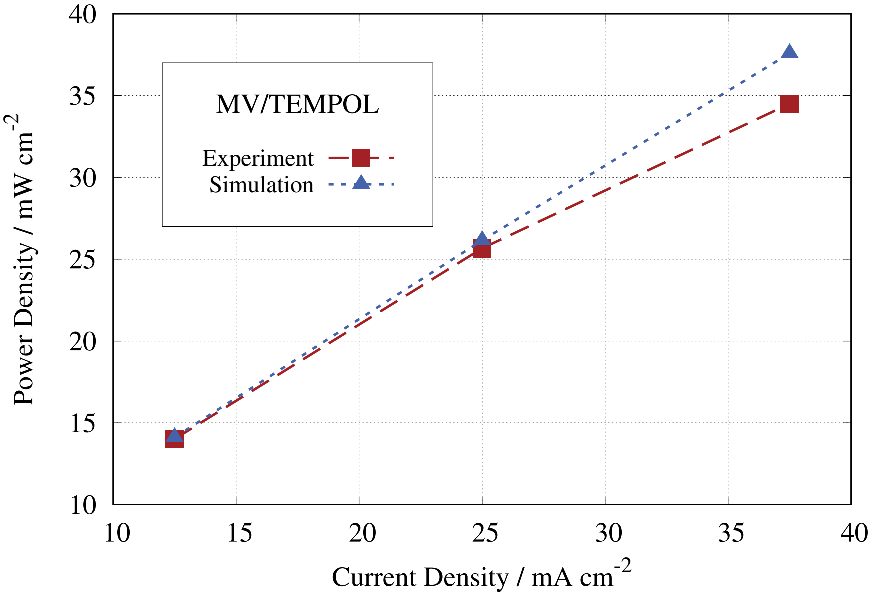

Figure 4.5: Power density versus current density of the experimental cell and the MSM simulations for the MV/TEMPOL system. The concentration is 0.1 M MV/TEMPOL in 1 M NaCl.

4.3 Homogenized Cell-Scale Model

The HCSM is validated against experimentally determined OCV and combined half-cell potentials during charge for the all-vanadium system. It is imperative to note that the model is anchored in the framework of an experimental cell, providing a robust foundation for its applicability and relevance. In the experimental setup, individual half-cell potentials are measured using reference electrodes. The VFB consists of a 40 cm^2 cell with an anion exchange membrane (Fumasep FAP-450, FUMATECH BWT GmbH, Bietigheim-Bissingen, Germany) and GFA6 graphite felt (SGL Carbon GmbH, Meitingen, Germany) as electrodes. As mentioned above, the model is built to replicate the experimental test cell of ICT [73, 77]. The total vanadium concentration is 1.6 M and the tank volume is 60 mL each. The flow rate is 80 mL min^{-1} and the current density is 25 mA cm^{-2}.

To compare the conversion of active species within the model and the measured voltages in the experiment, a modified Nernst equation is used [127]

$$E_N = E^0 + \frac{RT}{zF} \cdot \ln \frac{1 - SOC}{SOC} \tag{4.1}$$

The standard redox potentials E^0 for positive and negative half-cells are 1.004 V and −0.255 V, respectively. Unlike previously described, a transient simulation approach is adapted to cover the charging process.

Figure 4.6 (top) shows the OCV plotted against SOC for both experimental and simulated data. The experimental curve represents the OCV of the entire cell. In contrast, the simulation curve is derived by combining the respective half-cell potentials. In addition, additional 150 mV are incorporated to fit the experimental curve. According to Knehr et al. [121], a discrepancy of around 130 mV to 140 mV between experiments and VRFB models arises because of the incomplete description of the electrochemical double layer using the Nernst equation. Further differences arise from the usage of SOC instead of activities and the neglection of junction potentials. In general, there is a notable alignment between the curves, displaying a minor deviation of approximately 2.6% at the highest SOC.

In Figure 4.6 (bottom), the VRFB charging process is presented over time. The experimental curve represents the sum of individual half-cell potentials without considering the membrane potential. The simulated curve is depicted in green. Here, the previously mentioned 150 mV are incorporated as well. To replicate the charging behavior observed in the experiment, the reaction parameters α and β (as seen in Equation 2.28) are adjusted to 1.37 and 8×10^{-6}, respectively. In addition, the outlet concentration is aligned with the inlet concentration to reflect the circulation of the electrolyte. Notably, the modified Nernst equation shown does not encompass any overpotentials inherent in the charging process. The reasons for these overpotentials include, among others, activation and contact resistance or the conductivity of the electrolyte. To compensate for these overpotentials, an increment of 75 mV is additionally introduced to the simulation curve (orange), resulting in good conformity to the experimental data. The overall voltage correction is therefore 225 mV. The root mean square error between the experiment and the simulation is 0.03, with a maximum deviation of about 10% observed during the initial stages.

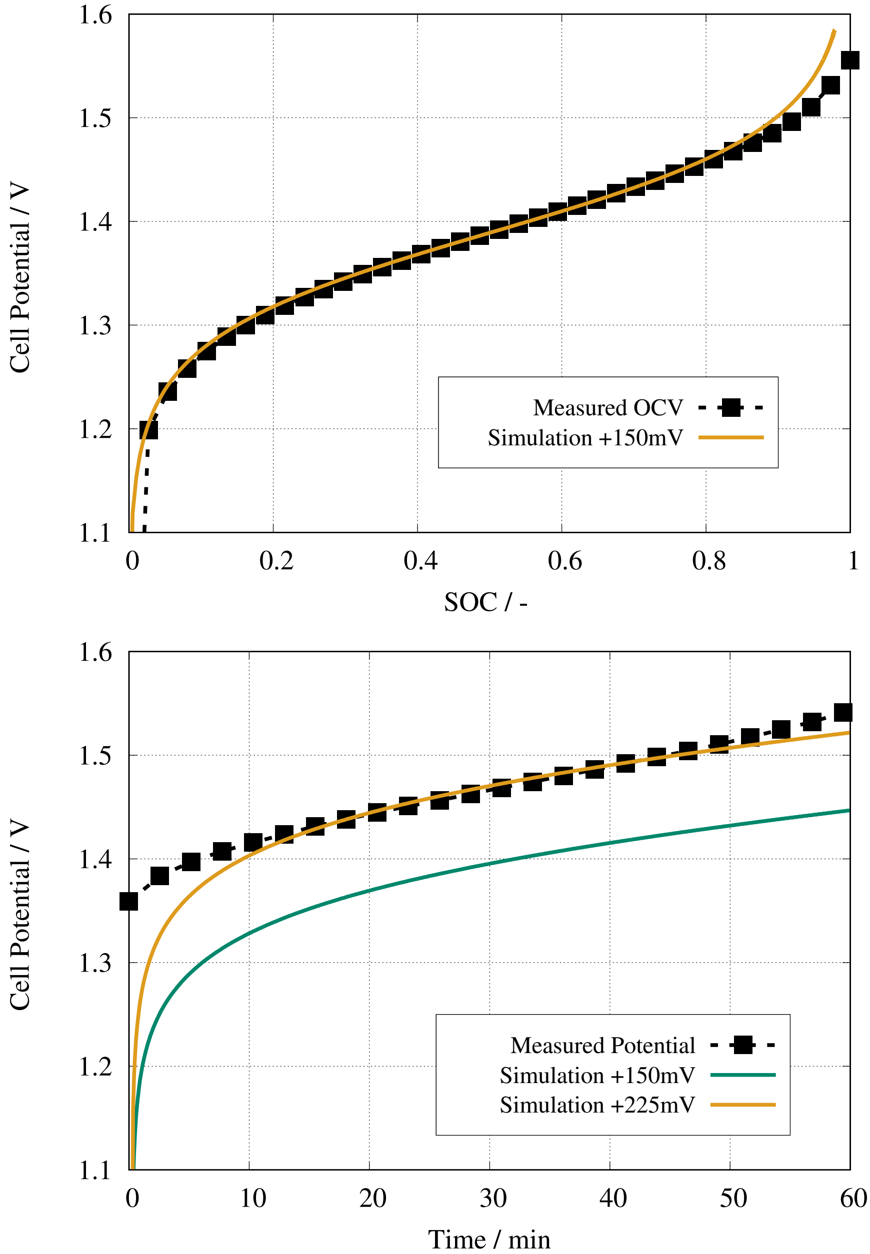

Figure 4.6: Experimental validation of the HCSM. Open circuit cell potential as a function of the SOC (top). Additional 150 mV are included in the simulation to fit the experimental data. Combined half-cell potentials over time during charge operation (bottom). No membrane potential considered. Additional 75 mV are included in the simulation result to address overpotentials that the model does not inherently capture.

4.4 Conclusion

This chapter presented the validation process for both the microscale model (MSM) and the homogenized cell-scale model (HCSM). The MSM validation employed three distinct methods, all of which exhibit satisfactory agreement between simulations and experiment. Initially, the MSM was parameterized using the all-vanadium system and compared against cell potentials derived from two models from the literature. By combining separate half-cell simulations, we effectively represent the entire cell, with additional potential incorporated to address membrane losses in the resulting polarization curves. The influence of the reaction rate constant on the polarization curve is significant. Subsequently, the MSM was compared to the experimentally obtained half-cell potentials of the TEMPOL system, demonstrating good agreement with the experimental polarization curve, although with some discrepancies in shape and necessitating potential corrections. Finally, experimentally determined power densities of the MV/TEMPOL system were utilized for validation, revealing excellent agreement upon the combination of averaged half-cell potentials. However, questions persist about unaccounted for factors such as membrane potential, degradation, or contact resistances. In parallel, the HCSM was validated using separate half-cell potentials derived from an experimental setup. Through the adoption of a modified Nernst equation and mass transfer correlation parameters, the model effectively predicted OCV measurements and charging behavior.

Model validation is an important measure to ensure the reliability of theoretical predictions, help identify limitations, and improve accuracy. However, no model can perfectly capture the full complexity of physical systems, as all models rely on assumptions and simplifications. This is particularly true for the MSM, where intricate details of electrochemical processes are difficult to capture and validate experimentally. Similarly, the HCSM, while more computationally efficient, makes broader assumptions that can overlook finer details. Both types of models provide valuable information, but their limitations must be considered when interpreting the results. In summary, model validation is not about achieving perfection, but about ensuring that models are as accurate and reliable as possible for their intended applications.

5 Microscale Numerical Investigations

Capturing the exact morphology of the electrode microstructure, the MSM is capable of providing precise information of the spatial distribution of key parameters such as velocity or concentration of active materials and their influence on cell performance.

This chapter delves into microscale numerical investigations focused on structured electrodes and the reconstructed graphite felt domain. At first, scientific advancement in this field is presented. The actual investigations begin with simulations conducted on simplified domains to accelerate the model development phase and attain prompt results with fewer computational costs. This approach facilitates the exploration of various parameters such as different initial active material concentrations, different active surface areas, and different flow resistance.

The subsequent section presents the reconstructed electrode for detailed microstructure investigations. Here, the focus extends to the analysis of velocity distributions, concentration profiles, electrical conductivity, current density distributions, and potential profiles within the electrode domain. Furthermore, these investigations aim to elucidate the overall performance characteristics and determine whether there is an optimal Re number to enhance the flow battery efficiency.

The final section of this chapter assesses the statistical robustness of the reconstructed microstructural configuration. Comparative analyzes are conducted between the digitally reconstructed microstructure and the structured fiber domain to assess resilience under varying operational conditions. This comparative approach provides valuable insights on the cases in which reconstruction of the electrode microstructure is necessary and when replication using CAD software is sufficient.

Parts of the results presented in the following correspond to the work entitled *Pore-scale Modeling of Flow Batteries* published in the book *Flow Batteries - From Fundamentals to Applications* [86] and to the work entitled *A Multiscale Flow Battery Modeling Approach Using Mass Transfer Coefficients* published in the journal *Energy Technology* [128].

5.1 State of the Art

The field of microscale modeling of flow batteries has garnered significant attention in recent years, driven by the need for enhanced understanding of complex electrochemical phenomena on this scale and by the increase in computational power necessary for those demanding computations. In the following, a comprehensive overview of the current state of research in flow battery microscale modeling is provided, highlighting key advances, methodologies, and applications.

The first FB microscale model was introduced by Qiu et al. [57, 58] for the vanadium system to be able to make statements about the effect of current and concentration distribution on the cell potential. Fluid flow was simulated using the lattice Boltzmann method (LBM), while coupled species and charge transport were described using the FVM. Battery performance and reactant distribution under different operating conditions were investigated along with the varying morphology of the reconstructed electrode. Chen et al. [104] developed a multiphase and reactive transport model for VFB considering a constant overpotential using LBM. The study highlighted the investigation of the evolution of oxygen bubbles under different electrode properties, gas saturation, and surface characteristics. The fibrous electrode structure was generated on the basis of statistical imaging information. Kok et al. [101] presented a direct numerical simulation method to determine the effect of microstructural anisotropy on the mass transfer coefficient. The LBM was applied on µCT computed digital twins on three different fibrous electrode materials. Dimensionless mass transfer correlations with respect to the permeability of the materials were determined. Zhang et al. developed a 3D model based on LBM to simulate coupled multiphase flow, mass, and species transport, including electrochemical reaction of the VFB system [129]. The focus was on investigating the saturation and surface wetting characteristics during the electrolyte penetration process on the µCT reconstructed microstructure. The same model was later parameterized with a TEMPOL-based redox system and used to investigate the performance of different electrode microstructures [64]. Recently, Fu et al. developed an FB model for multiscale electrode design analysis and investigated the differences in hydrodynamics of laser-perforated electrodes and pristine electrodes [130]. They showed that biporous electrodes should be operated away from the limiting current density conditions. The underlying microscale model is intended to close the research gap by focusing on a fully FVM-based approach with detailed Butler-Volmer-type kinetics applied to the promising organic MV/TEMPOL system.

Pore network modeling (PNM) presents an intriguing alternative for simulating microstructures. This approach overcomes the high computational costs associated with detailed grid-based microstructural modeling by simplifying the complex microstructure into a network of interconnected pores and throats, which are represented by spheres and cylinders, respectively [131]. In the context of FB modeling, different electrodes have been investigated with PNM for their single-phase transport properties and imbibition characteristics by Banerjee et al. [103]. In addition, Sadeghi et al. modeled the multiphysic transport in hydrogen-bromine FB throughout the electrode thickness, focusing on the impact of different electrode porosity and different fiber alignments on electrode performance [102]. Most recently, Lombardo et al. have investigated the concentration distribution of active species in carbon paper using PNM to highlight the difference of pure convection, diffusive transport and migration [132].

For a more detailed roundup of flow battery modeling approaches on different scales, the reader is referred to recent extensive reviews on these fields [45, 48, 49, 133, 134].

5.2 Numerical Investigations on Simplified Electrodes

In the first instance, numerical investigations are conducted on simplified structured electrodes to assess the capability of the MSM in replicating the physical and chemical attributes of the flow battery. The utilization of simplified structures is motivated by their reduced creation complexity and lower computational costs. For this purpose, three domain variants denoted as Ω_1, Ω_2, and Ω_3 are devised, drawing inspiration from the works of Qiu et al. [57] and Zhang et al. [129]. Figure 5.1 illustrates the three different electrode geometries featuring randomly arranged cylindrical fibers and a current collector plate. The surrounding electrolyte region is not shown. The domain size, fiber length, and fiber diameter remain consistent across all cases, differing primarily in their active surface area and porosity.

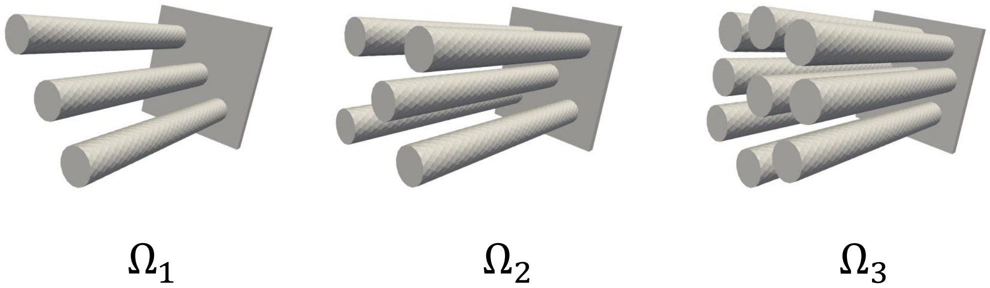

Figure 5.1: Different structured electrodes domains Ω_1, Ω_2, and Ω_3.

Table 5.1 provides details on the geometric and mesh-related parameters of the domains. Subsequently, the influence of the initial concentration of active material and the current density on the half-cell potential is explored for the domain Ω_1. Furthermore, a comparative analysis of the different domains is conducted with regard to half-cell potential and the pressure drop. Throughout the investigations, the quasi-steady-state simulation approach is employed assuming constant input concentrations. The average electrolyte velocity corresponds to a flow with a Re number of 0.5, so mass transfer limitations are not likely to occur. The simulations are carried out on a tetrahedral mesh, with a cell size of approximately 3 µm within the bulk electrolyte and about 0.8 µm at the interface between the electrolyte and the solid electrode, due to local grid refinement.

Table 5.1: Geometry and mesh parameters of the simplified electrodes.

	Ω_1	Ω_2	Ω_3
Domain size	100 µm × 50 µm × 50 µm		
Fiber diameter	10 µm		
Porosity	0.92	0.86	0.75
Specific surface area	43 761 m^{-1}	66 269 m^{-1}	111 283 m^{-1}
Computational cells	114077	138898	168889

5.2.1 Effect of Initial Concentration

The half-cell potential exhibits a strong dependence on both the applied current density and the concentration of active material at the electrode surface. Figure 5.2a depicts the half-cell potential as a function of SOC for a solution containing 0.1 M TEMPOL in 1 M NaCl, while Figure 5.2b depicts the same for a solution containing 0.5 M TEMPOL in 1.5 M NaCl, which represents the solubility limit of TEMPOL in NaCl solution as reported by Liu et al. [38].

The simulations are conducted at specified SOC values, assuming a constant supply of electrolyte at the inlet. Different colors are used to denote various galvanostatic current densities, with dashed lines indicating the charging process and dotted lines representing the discharging process. The range of galvanostatic current densities examined stretches from 20 mA cm^{-2} to 100 mA cm^{-2}, with increments of 20 mA cm^{-2}. To provide context, the OCV is depicted as a solid line in both cases. All simulations are conducted using domain Ω_1.

Increasing the current density results in larger potential differences to the OCV observed during both charging and discharging, regardless of the initial concentration level. This phenomenon arises from heightened overpotentials associated with higher current densities.

Accelerated electrochemical reactions at higher currents contribute to increased accumulation of species at the electrode surface, subsequently elevating activation barriers and leading to increased overpotentials. Furthermore, the ohmic overpotentials in the electrode and electrolyte region increase with rising current densities.

When the different initial concentration levels are compared, it is observed that the curves are closer to the OCV in the case of the more concentrated electrolyte solution. In this scenario, the overpotentials are smaller. This can be attributed to the greater number of ions and the consequent increase in electrolyte conductivity associated with the higher concentration. In this case, the ohmic resistance of the electrolyte decreases.

As previously stated, the overpotential represents the disparity between the thermodynamic redox potential and the potential at which the actual reaction takes place. It exhibits a strong dependency on both the SOC and the current density. Figure 5.3 illustrates the typical behavior of the overpotential with respect to SOC and current density. Sub-plots *a* and *b* depict its dependency for two different current densities and SOC with respect to both charge and discharge operation. Sub-plots *c* and *d* demonstrate the effect of electrolyte solutions with varying concentrations.

The overpotential curve plotted against SOC exhibits a non-linear trend, where its magnitude increases at both high and low SOC, reaching its minimum at medium SOC. At the maximum and minimum SOC limits, the concentration of one redox reactant decreases, which results in a higher energy demand to promote the reaction. The overpotential curve plotted against the current density exhibits a logarithmic course, as described by the Tafel equation [63]. With increasing current density, its magnitude increases. This escalation is attributed to the enhanced reaction speed and the resulting inefficiency of the mass transport of ions toward the electrode surface at higher currents. Consequently, local concentration gradients emerge, contributing to an increased overpotential. Concerning electrolytes with varying concentrations, it has been observed that the overpotential tends to decrease with higher concentration, as mentioned previously. The elevated presence of active species enhances the probability of surface reactions, thereby reducing the energy required to surpass the activation barrier. The sign of charge and discharge operation in this case occurs from the mathematical implementation of the equations and the geometric orientation of the computational domain. In general, the system is supplied with energy during charge. This leads to a positive overpotential because the applied voltage needs to be higher to drive the reaction. During discharge, the process is vice versa.

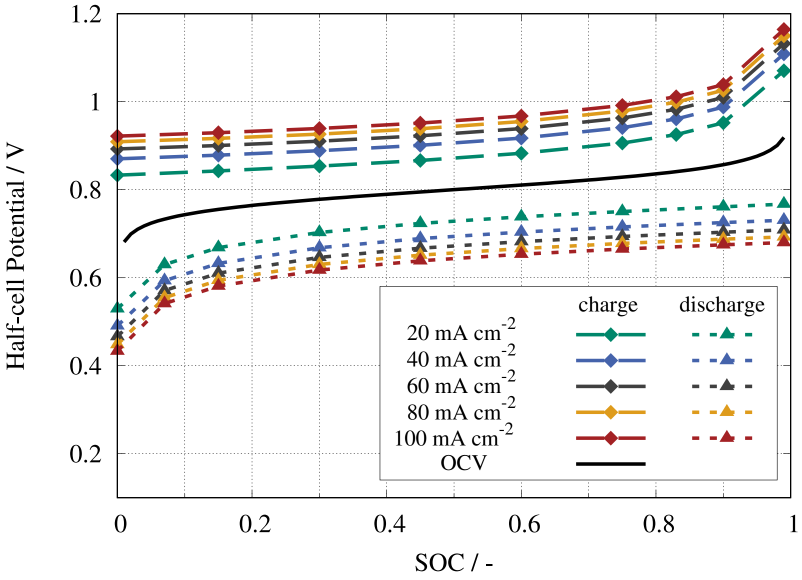

(a) 0.1 M TEMPOL in 1 M NaCl

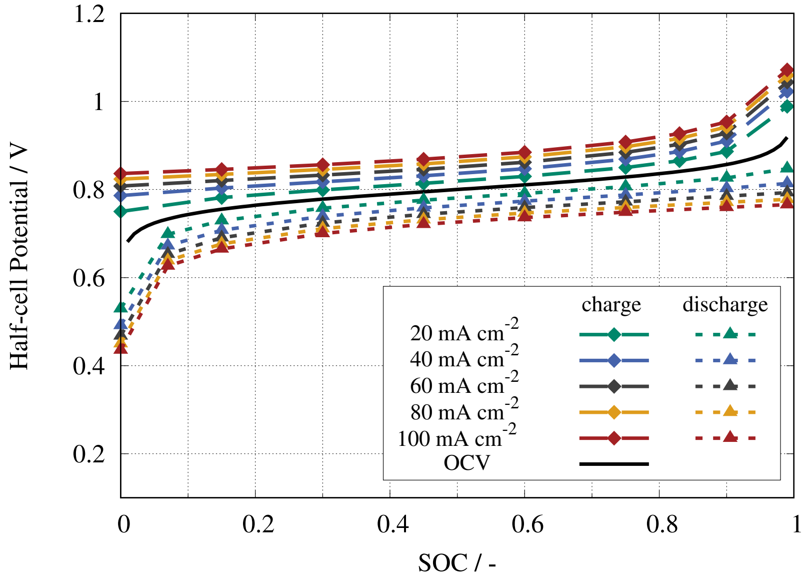

(b) 0.5 M TEMPOL in 1.5 M NaCl

Figure 5.2: Half-cell potential versus SOC for two different initial concentrations of TEMPOL in NaCl. Simulations are conducted for certain SOC with constant inlet concentration on domain Ω_1. Charging and discharging process are marked with dashed and dotted line respectively.

5.2.2 Effect of Active Surface Area

The active surface area of the electrode plays a crucial role in determining cell performance. A larger surface area facilitates greater interaction between the electrode and electrolyte.

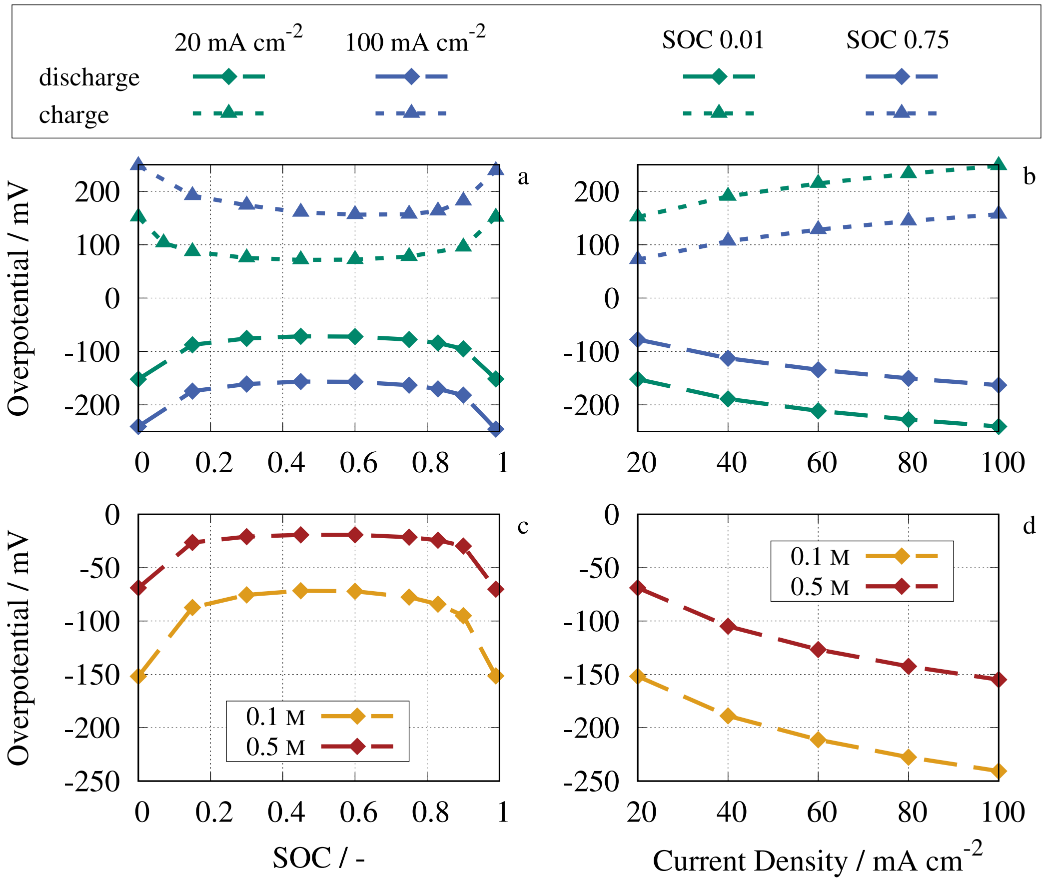

Figure 5.3: Overpotential versus SOC (a) and current density (b) for charge and discharge current densities of 20 and 100 mA cm^{-2}, and for SOC 0.01 and 0.75 with 0.1 M TEMPOL in 1.0 M NaCl. Overpotential at charging operation versus SOC (c) and current density (d) for 0.1 M TEMPOL in 1.0 M NaCl and 0.5 M TEMPOL in 1.5 M NaCl at current density of 20 mA cm^{-2} and SOC 0.01 respectively. Simulations are performed on domain Ω_1. Charging and discharging process are marked with dashed and dotted line respectively.

Consequently, this promotes higher achievable current densities and enhances the diffusion of active materials, thereby facilitating faster reaction rates.

Figure 5.4 shows the half-cell potentials versus SOC for the three simplified electrode domains Ω_1, Ω_2, and Ω_3 at the same galvanostatic current density of 40 mA cm^{-2} and the same initial concentration of 0.5 M TEMPOL in 1.5 M NaCl. The charging and discharging processes are marked with dashed and dotted lines, respectively. Again, simulations are performed for certain SOCs using a constant inlet concentration. The domain Ω_1 has the lowest active surface area and the domain Ω_3 the highest. The current density within an electrochemical cell is related to the cross-sectional area of the membrane.

The red curve related to domain Ω_3 is closest to the OCV in both operation cases. The potential deviation, the overpotential being more precise, is hence smallest here. This phenomenon

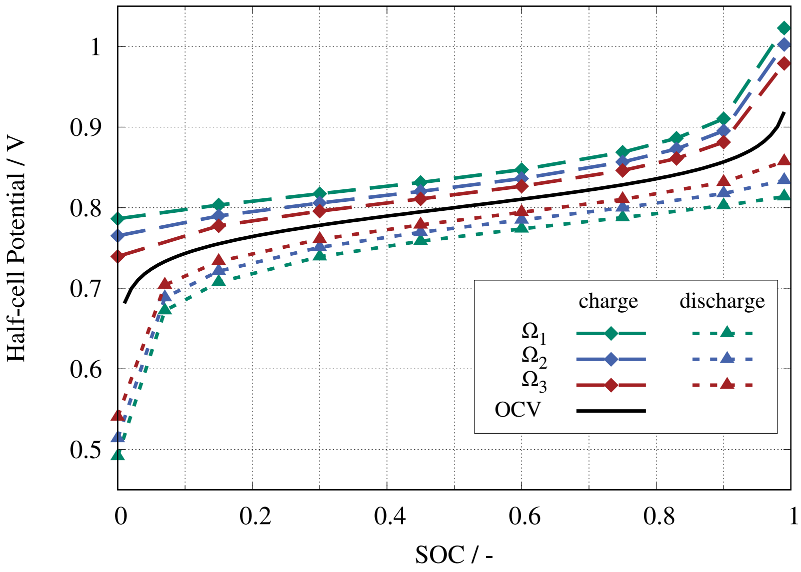

Figure 5.4: Half-cell potential versus SOC for the three different structured electrode domains Ω_1, Ω_2, and Ω_3. The concentration is 0.5 M TEMPOL in 1.5 M NaCl and the current density is 40 mA cm^{-2}. Charging and discharging process are marked with dashed and dotted line respectively.

arises from a reduction in activation and ohmic overpotential. The reduced activation overpotential is associated with the simulation geometry that features the largest surface area at the same current density. Although the current density remains constant across all three cases, the distribution of current over the surface is different. The presence of more electrode surface area in the domain Ω_3 leads to a reduced actual current at the interface. This is why the activation overpotential also decreases. Furthermore, the simulation space is largely taken up by the solid fiber space, which leads to a reduced ohmic overpotential due to the enhanced conductivity of the electrode.

5.2.3 Flow Resistance of the Electrode

The pressure drop in FB systems is a critical operating parameter. The electrolyte must be pumped through the cells and the energy consumed should be considered in the overall efficiency of the system. Figure 5.5 illustrates the pressure drop between the inlet and outlet versus the flow velocity characterized by the Reynolds (Re) number for the three simplified electrode domains Ω_1, Ω_2, and Ω_3 on a double logarithmic scale.

As anticipated, it is evident that with increasing flow rate, the pressure drop increases linearly for all structured electrodes, representing exponential growth. When comparing the different electrode domains at a particular flow rate, it becomes apparent that the pressure drop is highest for the domain Ω_3. This can be attributed to the higher flow resistance within the domain, a consequence of the increase in the number of fibers present.

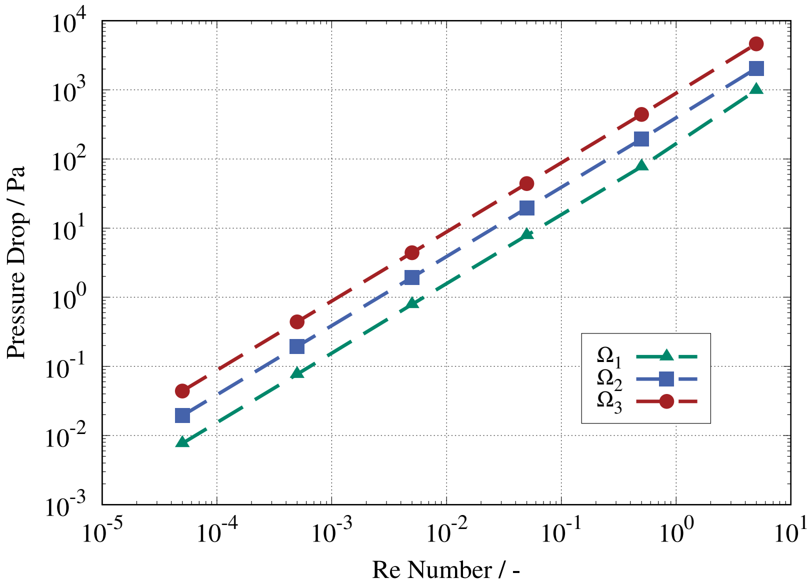

Figure 5.5: Pressure drop versus Re number for the three different simplified electrode domains Ω_1, Ω_2, and Ω_3.

The findings of Figure 5.4 and Figure 5.5 underscore the trade-off inherent in the design of the FB electrode. On the one hand, a greater specific surface area is intended, as it mitigates overpotential and enhances performance. In contrast, a larger surface area correlates with a greater use of solid material, consequently increasing flow resistance. Therefore, achieving a balance between these conflicting characteristics is important in electrode design. This aspect will be elaborated upon further in the subsequent sections of this chapter.

5.3 Numerical Investigations using the Reconstructed Electrode

The following section presents detailed investigations of flow battery phenomena using the reconstructed microstructure as a computational domain. In the beginning, the capabilities of the MSM are illustrated followed by investigations of the velocity and concentration distribution within the microstructure. In addition, the electrolyte conductivity, current density, and potential are analyzed. The section closes with performance investigations in dependence of the applied Re number, concentration level, and current density. In the respective sub-chapters, the Re number is examined in a logarithmic division and in the range from 5×10^{-5} to 5. This range is chosen because it includes the general operating range of FBs and slow flows are easier to study numerically using the MSM.

Figures 5.6 and 5.7 provide a detailed description of the microscale architecture, highlighting the comprehensive insights that the MSM can offer.

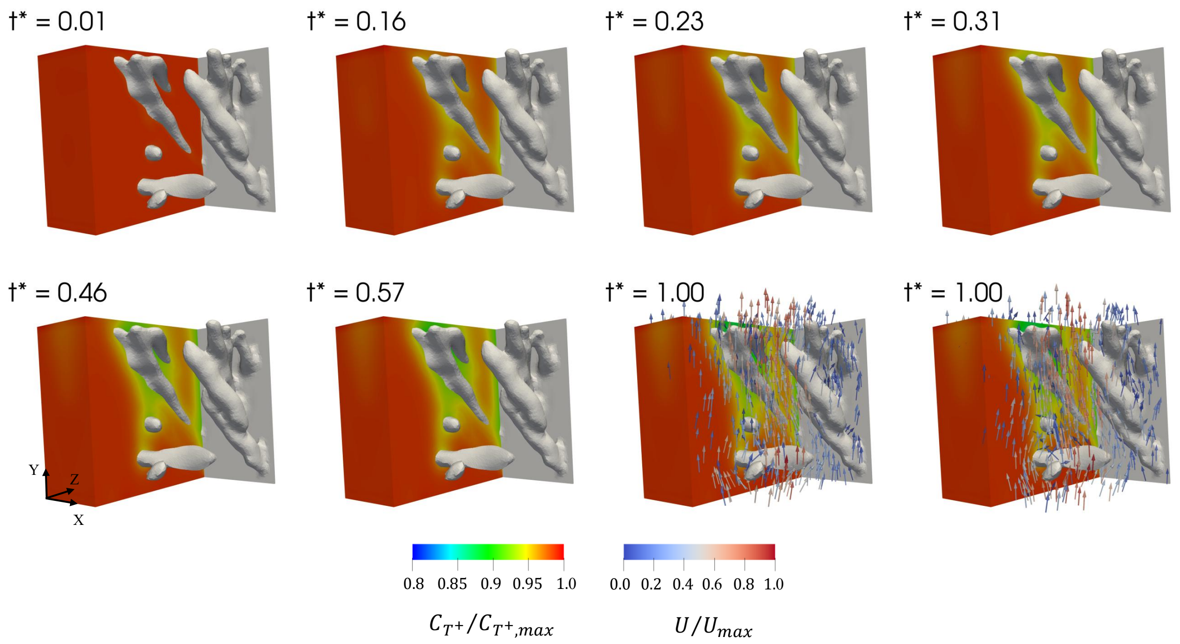

Figure 5.6: Reconstructed microstructure surrounded by electrolyte colored according to the non-dimensional concentration of TEMPOL$^+$. Additional velocity vectors are displayed and colored according to their magnitude. The different time steps correspond to the normalized discharge operation.

In Figure 5.6, the normalized concentration profile of TEMPOL$^+$ is presented, with concentration values scaled relative to the constant maximum concentration at the inlet. The visualization focuses on the electrode microstructure, with half of the electrolyte region cropped for clarity. Various time steps during discharge operation are depicted on a normalized time horizon. Additionally, the velocity vectors are overlaid at the end, indicating a relatively high flow velocity corresponding to a Re number of 0.5. Near the fiber surface, the depletion of active material can be observed. The concentration profile exhibits characteristics of convection-dominated behavior, closely following the velocity streamlines.

Figure 5.7 illustrates the normalized electrolyte potential. To enhance clarity, the opacity of the electrolyte is reduced to the left, allowing for better visualization. Furthermore, the current density at the electrolyte-electrode interface (i_{BV}) is displayed. On the right side of the figure, the electrolyte current density is presented.

5.3.1 Velocity Distribution

Understanding the impact of velocity variations on flow and concentration profiles is essential for the optimal FB operation. This subsection gives a comprehensive analysis of the velocity distribution within the microstructure at different Re numbers.

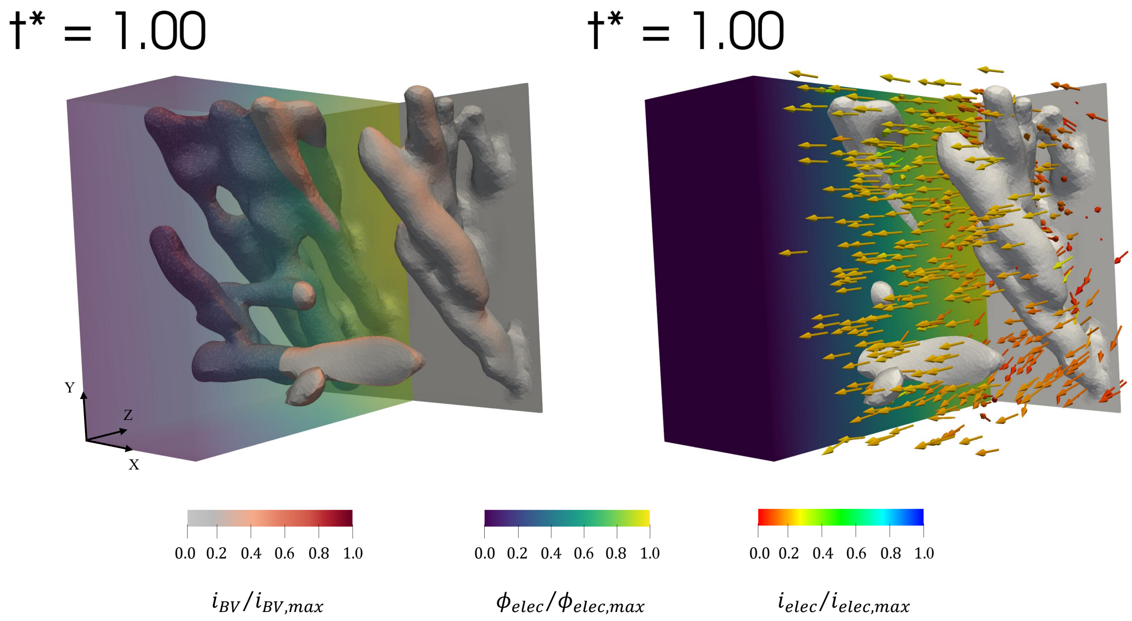

Figure 5.7: Reconstructed microstructure surrounded by electrolyte colored according to the non-dimensional potential. On the left, the current density at the interface is additionally shown. On the right, the electrolyte current density vectors are included.

Figure 5.8 shows the velocity profiles observed within the reconstructed microstructure simulations. Throughout this investigation, the flow direction consistently aligns with the positive Y direction. In the left column of the figure, the non-dimensional, volume-weighted mean velocity magnitude $\langle\overline{U}\rangle = \langle|\mathbf{u}|\rangle/|\mathbf{u}_{in}|$ is depicted along the three different unit lengths (compare Figure 2.2). To achieve this, the volume-weighted mean value of the velocity magnitude is computed for slices perpendicular to each axis, with the axes discretized into 50 slices. The velocity magnitude value and the volume of each computational cell, which has its cell center within the respective slice, contribute to the calculation of the corresponding mean value. Subsequently, the resulting average magnitude is normalized by the inlet velocity magnitude to facilitate comparison across different flow rates. The graph represents three distinct curves, representing flow scenarios characterized by Re numbers of 0.05, 0.5, and 5. Notably, the curves corresponding to lower Re numbers align closely with the curve for Re number of 0.05 and are therefore omitted from the illustration.

Taking into account all three domain directions, the velocity profiles of flows characterized by different Reynolds numbers exhibit minimal variation from each other. This observation leads to the conclusion that at the microscale, the influence of the structure on the velocity profile remains consistent across the investigated flow rates. As mentioned earlier, the selection of the investigated flow regimes originates from the application in flow batteries. Within these ranges, the flow is dominated by laminar behavior and turbulence is not likely

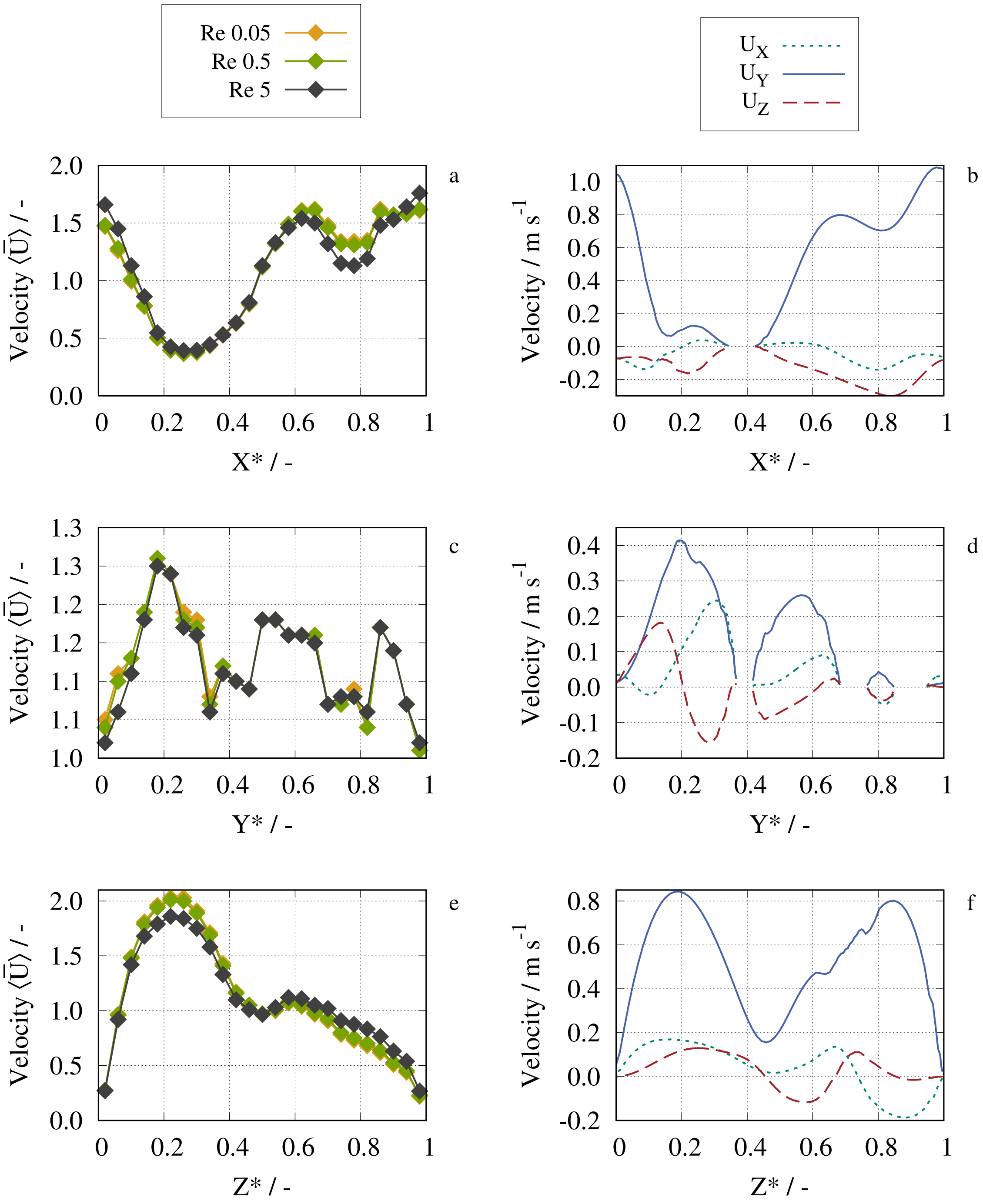

Figure 5.8: Non-dimensional, volume-weighted mean velocity magnitude versus the three unit lengths of the domain for three Re numbers (left column). Velocity components along central plot lines in each dimension for flow with Re number of 0.5 (right column).

to occur due to the small Re numbers [135]. However, the model is theoretically feasible to capture turbulence effects. The deviation of the velocity at the highest Re numbers may arise from flow instabilities, but a detailed investigation of this phenomenon is out of the scope of this work.

Along the X^* direction (a), the velocity reaches its maximum value at the boundaries, where identical values are maintained due to the cyclic conditions of the full electrolyte boundary, indicating that there is no flow resistance due to the absence of solid material. In the first third, the velocity diminishes due to the presence of fibers. Subsequently, the velocity escalates as the amount of fibers decreases along the course.

In terms of the Y^* direction (c), the inlet and outlet velocities are predominantly equal, primarily due to the mapping boundary conditions, although minor discrepancies emerge as a result of volume averaging. Continuing along the flow direction, the velocity surpasses the inlet value owing to the reduced cross-sectional area for flow arising from the electrode fibers. The velocity decreases towards the outlet as a result of the increased presence of fibers.

Regarding the Z^* direction (e), the velocity approaches zero at the membrane and at the current collector boundary due to the no-slip boundary condition. Notably, the velocity attains its maximum near the membrane side and gradually diminishes towards the current collector, attributed to the increasing presence of solid electrode material along this direction.

In the right column of Figure 5.8, the three different velocity components regarding the flow with Re number of 0.5 are presented across the three different unit lengths. They are plotted against a line located in the center of the surface normal to the direction of interest. It should be noted that the line intersects with the electrode fibers in certain instances, leading to interruptions in the graphs for sub-figures (b) and (d). The velocity component in the Y^* direction aligns closely with the velocity magnitude depicted above, given that this axis represents the primary flow direction. In contrast, the magnitudes of the other two components are comparatively smaller. At the points of interruption, the velocity attains a value of zero owing to the application of the no-slip condition.

5.3.2 Electrolyte Concentration Profiles

In the following, a comprehensive analysis of the relationship between velocity and concentration profiles within the reconstructed microstructure is presented. The investigation explores how differences in Re number affect the distribution of species within the system.

Figures 5.9 and 5.10 show several slices of the TEMPOL^+ concentration normalized to the constant inlet concentration during discharge operation. Both sets of figures represent identical operating conditions, the only difference being that the first shows the flow corresponding to a Re number of 5×10^{-5}, while the latter shows the flow at a Re number of 5×10^{-2}. The discharge current density is $40\,\mathrm{mA\,cm^{-2}}$ and at the inlet, the SOC is 0.5 at an initial concentration of 0.1 M TEMPOL in 1.0 M NaCl. The 2D slices are located in the center of the domain, normal to the X^* direction. Hence, the membrane is located on the left side, and the current collector is located on the right side of each slice. The electrolyte flow occurs from the bottom to the top. It is important to note the different color scales used in each visualization. In the first scenario, characterized by a relatively low Re number, significant concentration gradients are evident. The concentration profile predominantly reflects diffusion-dominated behavior, with a notable absence of TEMPOL$^+$ observed in the upper right region (highlighted in red). Over time, the profile of the depleted TEMPOL$^+$ moves from the top right to the bottom left. This phenomenon arises from an inadequate supply from the inlet and increased conversion attributed to the increased presence of fibers in the upper region. Additionally, it should be noted that the reaction extends to the current collector side as well.

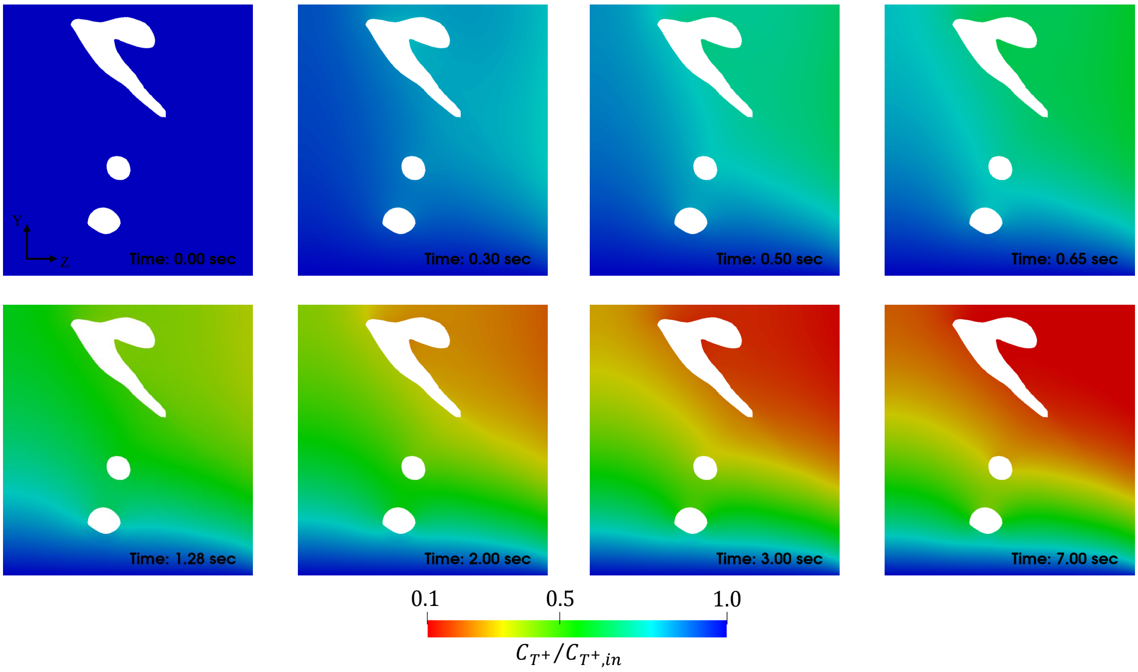

Figure 5.9: Normalized TEMPOL$^+$ concentration at a flow corresponding to Re number of 5×10^{-5}. The slices are located in the center of the domain, normal to the X^* direction with membrane on the left and current collector on the right side of each slice.

The second scenario characterized by a higher Re number shows a convection-dominated concentration profile. The concentration level is globally elevated, attributed to adequate mass transfer of TEMPOL$^+$ to the active surface of the fibers. Over time, the concentration profile develops to align with the flow direction. While noticeable depletion of TEMPOL$^+$ is evident in the vicinity of the fiber surface, the concentration within the bulk electrolyte remains consistent with the inlet value. Nonetheless, regions with reduced mass transfer are discernible in flow-averted areas, such as the central region near the outlet. In particular, the conversion of TEMPOL$^+$ is also pronounced on the current collector side. The attainment of the quasi-stationary status takes several seconds in the diffusion-dominated case, while it is achieved in less than a second in the convection-dominated case. In addition, investigations on the achievement of the quasi-stationary status are presented in Section 5.4.2.

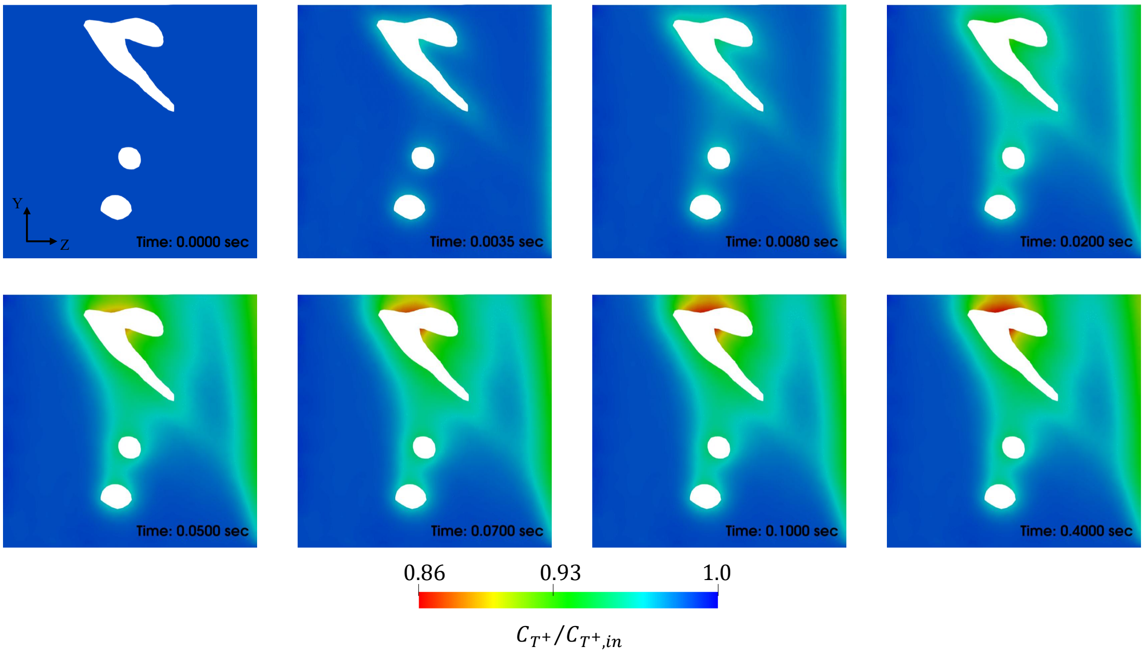

Figure 5.10: Normalized TEMPOL$^+$ concentration at a flow corresponding to Re number of 5×10^{-2}. The slices are located in the center of the domain, normal to the X^* direction with membrane on the left and current collector on the right side of each slice.

Figure 5.11 shows the non-dimensional, volume-weighted mean concentration of TEMPOL$^+$, denoted as $\langle \overline{C} \rangle = \langle C_{T+} \rangle / C_{T+,in}$, across three distinct unit lengths of the computational domain. The concentration is normalized to the constant inlet concentration. In the left column, concentration profiles corresponding to six different Re numbers are depicted, while in the right column, the standard deviations for selected Re numbers are displayed. Note that in this case, the standard deviation is not a measure of the error but rather represents the spread of the concentration within a slice. The simulations are conducted under galvanostatic discharge conditions of 40 mA cm^{-2} with a constant supply of electrolyte having a SOC of 0.5 at the inlet. The initial concentration is 0.1 M TEMPOL in 1.0 M NaCl. During the discharge process, TEMPOL$^+$ is depleted. The averaging process is the same as that used previously for the velocity magnitude.

In general, the lower the Re number, the more pronounced the depletion of TEMPOL$^+$. The concentration curves with respect to Re numbers 5×10^{-5} to 5×10^{-2} exhibit a similar shape at different levels, while the concentration profiles for Re numbers 0.5 and 5 mostly overlap.

Along the X^* direction (Figures 5.11 a and b), the mean concentration profiles remain relatively constant for all Re numbers. Regarding Re numbers greater than 5×10^{-2}, the concentration profiles overlap and remain close to unity, indicating near-equality with the inlet concentration. In such cases, the velocity is high enough that the depletion of TEMPOL$^+$ has a minimal impact on the overall concentration. The high velocity ensures a comprehensive supply of new reactant to the reaction surface. Furthermore, as shown in Figure 5.11 (b), the standard deviation for these conditions is exceedingly small, necessitating limited representation in the diagram. Collectively, these findings suggest complete convection-dominated mass transfer for Re numbers greater than 5×10^{-2}. Under these operating conditions, further increases in flow rate are unlikely to enhance the distribution of active material and, consequently, the performance of the system. Instead, they would demand additional pumping power.

The concentration profiles corresponding to the Re numbers 5×10^{-2} or lower exhibit minor fluctuations along the X^* direction, accompanied by a general decrease in the TEMPOL$^+$ concentration. These fluctuations arise due to the microstructure's characteristics, wherein the majority of fibers reside in the lower half of the X^* direction, resulting in a notable bulge at $X^* = 0.3$. Generally, concentrations decrease with decreasing Re number as a result of insufficient flow rates to compensate for the depleted reactant resulting from reactions at the interface. The concentration is the same at $X^* = 0$ and $X^* = 1$ due to the cyclic boundary conditions. Moreover, the standard deviation of the mean concentration within a slice increases as the Re number decreases. This trend is attributed to the amplified gradient between the constant inlet concentration and the concentration at the outlet.

Regarding flow in the Y^* direction, similar trends in the concentration profile are discernible with decreasing Re number. High Re numbers ensure an expansive supply of active material even at the outlet. However, as the Reynolds number decreases to 5×10^{-2} and below, the pronounced concentration gradients indicate a significant depletion of the incoming reactant as it traverses the domain. At the lowest Re numbers, the concentration gradient between the inlet and outlet intensifies, signifying diffusion as the dominant transport mechanism. Furthermore, the standard deviations of the mean concentrations are lower in comparison to those observed in the X^* direction, indicating a relatively homogeneous concentration perpendicular to the flow direction. Notably, these deviations are minimal at the inlet as a result of the imposition of fixed-value boundary conditions.

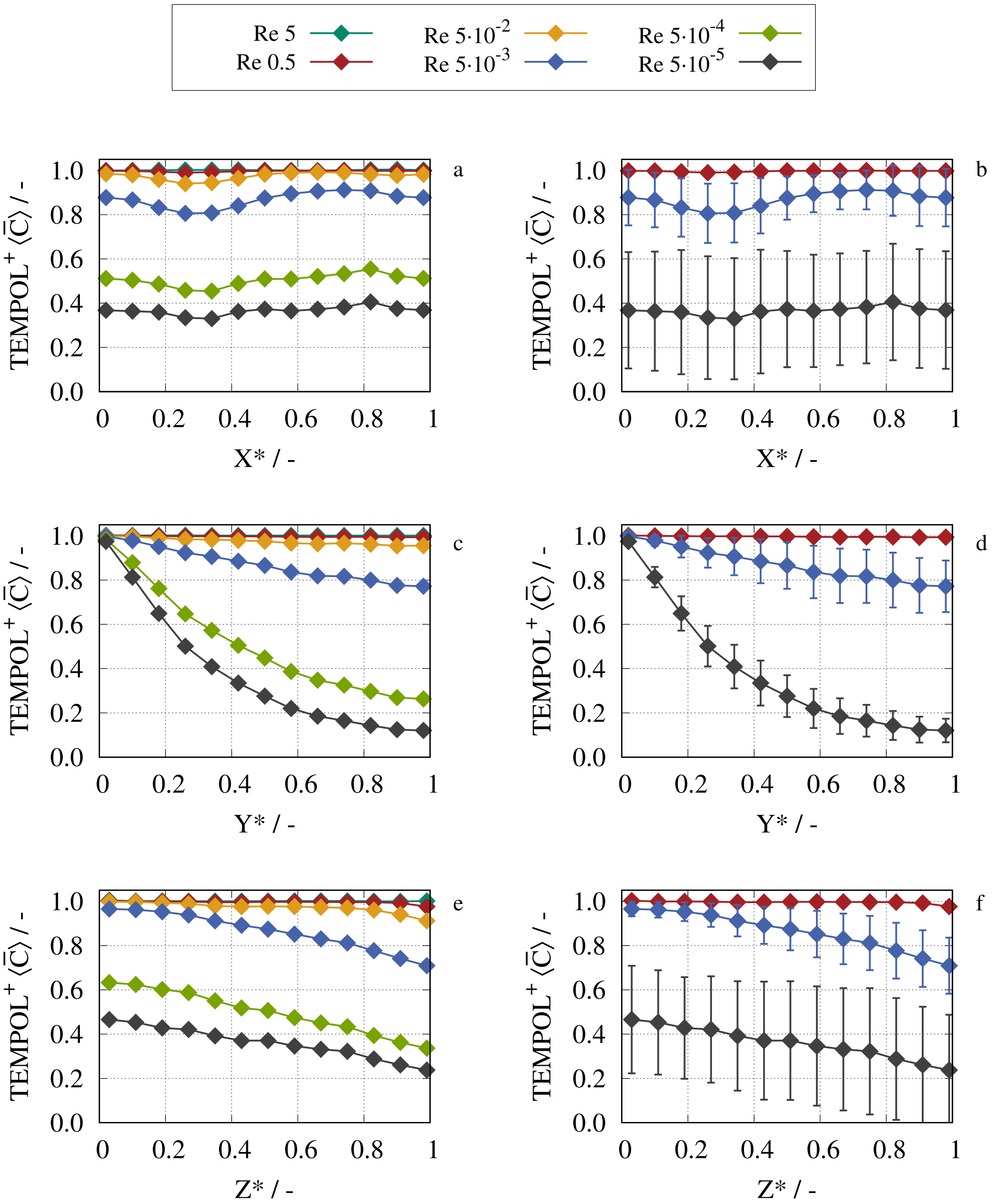

Figure 5.11: Non-dimensional and volume-weighted mean concentration of TEMPOL$^+$ during discharge operation versus the three unit lengths of the domain for different Re numbers (left column). Standard deviation for selected Re numbers (right column). The simulations are conducted at galvanostatic discharge of 40 mA cm^{-2} and a constant supply of electrolyte with SOC 0.5 at the inlet is specified.

Concerning the Z^* direction, the concentration profiles and the corresponding standard deviations exhibit characteristics similar to those observed in the X^* direction. However, in contrast, a more pronounced depletion of active material toward the current collector is evident. This phenomenon arises from the presence of the chemically active boundary on this side and the limited convective mass transfer, resulting from the imposition of the no-slip boundary condition.

In summary, flow corresponding to a Re number of 5×10^{-2} or higher effectively supplies enough active material to the reaction zones. In contrast, for smaller Re numbers, mass transport limitations become more pronounced, particularly with decreasing flow velocity. An optimal Re number, which ensures adequate delivery of active materials to the reaction zones while minimizing pumping power requirements, falls within the range of around 5×10^{-2}. Further discussion of the optimal Re number will be provided later in this chapter.

5.3.3 Electrolyte Conductivity

Figure 5.13 shows the non-dimensional and volume-weighted mean electrolyte conductivity ($\langle\overline{\kappa_e}\rangle = \langle\kappa_e\rangle/\kappa_{e,in}$) during discharge operation versus Z^* unit length for different Re numbers. It is normalized to the inlet conductivity of 7.248 S m^{-1} obtained with Equation 2.16 using the parameters values mentioned above and considering the initial concentration of 0.1 M TEMPOL in 1.0 M NaCl. It should be noted that conductivity is mostly affected by concentration of charged species, hence varying TEMPOL$^+$ concentration affect it the most.

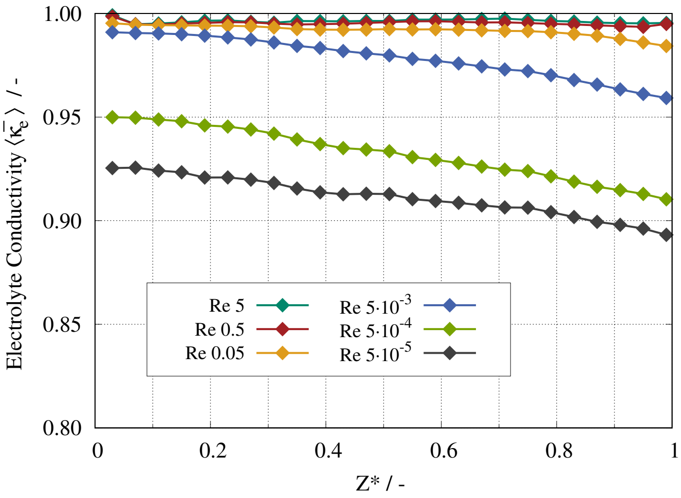

Figure 5.12: Non-dimensional and volume-weighted mean electrolyte conductivity normalized to the initial conductivity of 7.25 S m^{-1}. The simulations are conducted at galvanostatic discharge of 40 mA cm^{-2} and constant supply of electrolyte with SOC 0.5 at the inlet is specified.

The electrolyte conductivity exhibits a similar trend to the TEMPOL$^+$ concentration depending on the Re number. It remains constant at the inlet value for Re numbers of 5×10^{-2} and higher, owing to slight variations in concentration distribution. Conversely, at lower Re numbers, conductivity decreases due to a decline in the concentration of TEMPOL$^+$. In particular, the presence of evolving TEMPOL species does not have an impact on conductivity due to the absence of charge. The conductivity is observed to be lower on the current collector side, attributed to heightened conversion processes in that region. Furthermore, the conductivity at SOC of 0 and 1 deviates by 13% from the one at SOC of 0.5. At Re Number of 5×10^{-5}, the conductivity reaches its minimum in the vicinity of the current collector. In general, this analysis confirms previous findings that indicate an optimal Re number of 5×10^{-2} with maximal conductivity.

5.3.4 Current Density and Potential

Figure 5.13 shows the non-dimensional and volume-weighted mean magnitude current densities and potentials within the electrolyte and electrode during discharge operation versus the Z^* direction. Different Re numbers are depicted and the Z^* direction is chosen as the main direction of migration. Current densities are normalized to the discharge current density of $40\,\mathrm{mA\,cm^{-2}}$ and potentials are normalized to the redox potential of $0.8\,\mathrm{V}$.

The graphs of the electrolyte current density magnitudes i_e in Sub-figure 5.13a show all similar trends regarding different Re numbers. The curves range from 0.8 to 1 at $Z^* = 0$, remaining relatively stable during the first third of the Z^* direction. Subsequently, all curves exhibit a steady decline toward values between 0.2 and 0.4 as they approach the current collector. It is important to note that charge is conserved throughout its transport from the membrane to the current collector. The observed reduction in electrolyte current density can be attributed to an increasing presence of fibers, resulting in a greater portion of charge being transported within the solid component of the half-cell. Discrepancies in the values on the membrane side ($Z^* = 0$) can be attributed to variations in the electrolyte conductivity. Lower conductivity at low Re numbers leads to higher electrolyte resistance and consequently lower current density. In particular, at Reynolds numbers of 0.5 and 5, an unexpected increase in current density is observed at $Z^* = 0.2$. In these cases, numerical effects at the boundaries cannot be discounted as potential contributors, due to the complexity of the reconstruction and grid generation processes.

The electrolyte potential ϕ_e in Sub-figure 5.13b shows the typical decrease from membrane to current collector originating by Ohm's law. The potential at the membrane is zero by definition and decreases within the electrolyte to ensure the notation of the electric field and

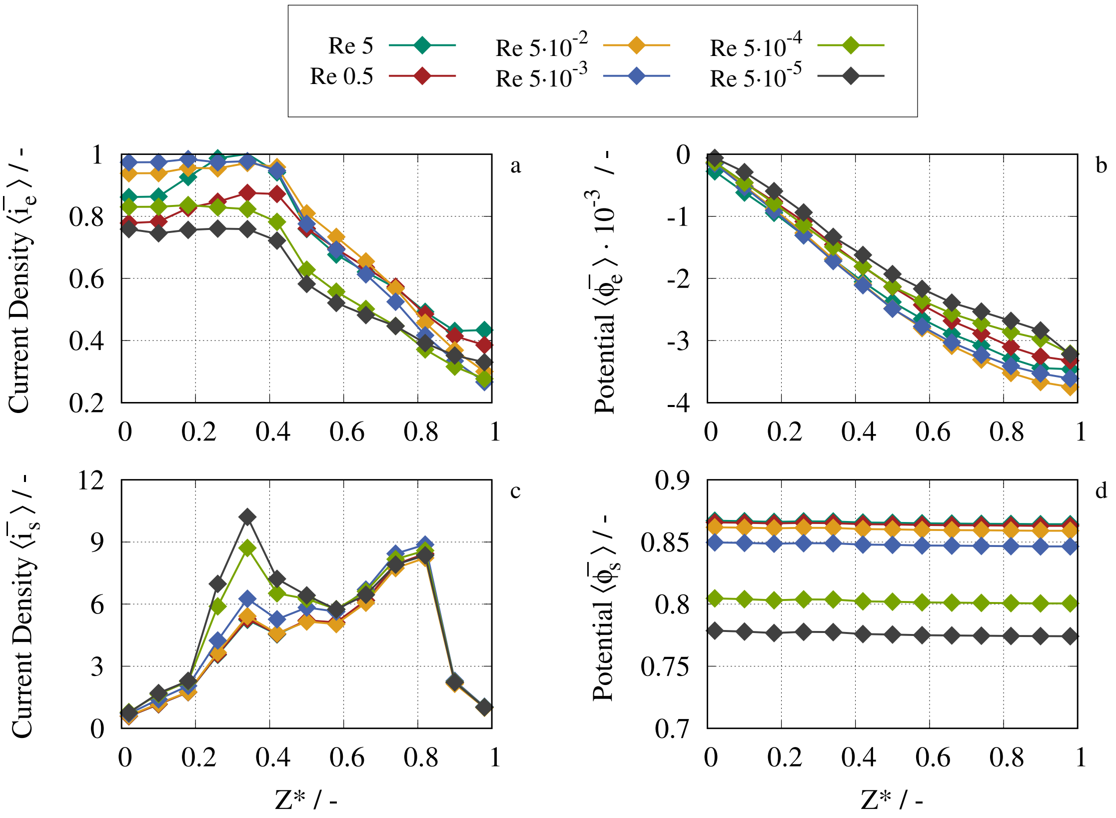

Figure 5.13: Non-dimensional and volume-weighted mean current densities and potentials during discharge operation versus the Z^* direction for different Re numbers. The current densities are normalized to the galvanostatic discharge current density of 40 mA cm^{-2}. The potentials are normalized to the redox potential of 0.8 V. Constant supply of electrolyte with SOC 0.5 at the inlet is specified for all simulations.

the transport of chloride anions to the membrane. Compared with the redox potential, the potential drop in the electrolyte is relatively small.

Sub-figure 5.13c presents the current density magnitude within the solid electrode i_s along the Z^* direction. The curves for different Re numbers all have a similar trend, with varying deflection at $Z^* = 0.35$. The curves start near zero because in this region few fibers exist that carry the charge. Due to a constriction where several fibers coincide, the current density significantly increases as the cross-section is considerably reduced. Numerical influences on the height of the deflection cannot be completely ruled out here. Towards the current collector the current density decreases as a result of the immense extension of the cross-sectional area.

The potential in the solid electrode ϕ_s along the Z^* direction is presented in 5.13d. Different Re numbers result in different potential levels because of different concentration distributions at the interface and hence different overpotential and conductivity. It is difficult to discern, but the different potentials decrease along the Z^* direction according to Ohm's law. The resulting electric field enables the transport of electrons from the external load to the interface during discharge.

5.3.5 Performance Investigations

This section highlights the influence of flow rate, concentration, and current density on half-cell potential, power density, and consequently the performance of the flow battery. To assess this impact, the half-cell potential is analyzed in various Re numbers for different SOC. In addition, combinations of distinct initial concentrations and current densities are examined across a range of Re numbers. It should be noted that additional 75 mV obtained from the experimental validation in Section 4.2.2 are included to calculate the resulting half-cell potentials and power densities.

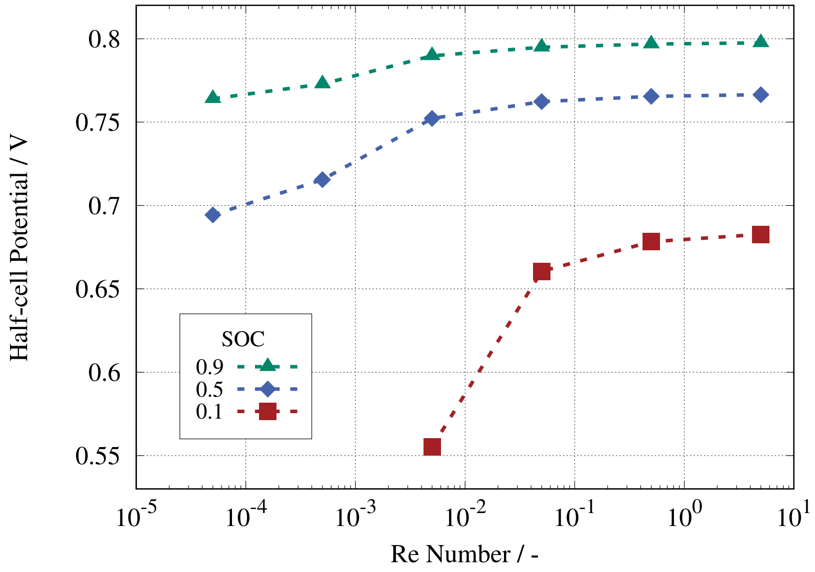

Figure 5.14: Half-cell potential versus Re number under galvanostatic discharge of 40 mA cm^{-2} conditions and with constant supply of electrolyte at the inlet. Simulations are conducted for certain flow rates and dashed lines are used for orientation.

The impact of flow rate on half-cell potential is illustrated in Figure 5.14, where the curves represent different SOC values of 0.9, 0.5, and 0.1. Simulations are carried out for specific Re numbers under galvanostatic discharge conditions of 40 mA cm^{-2} with a constant supply of electrolyte at the inlet. Generally, higher SOC values result in elevated half-cell potentials as a result of a greater amount of active material available for conversion. Across all three curves, a decrease in half-cell potential is observed with decreasing flow rate, with the decrease more pronounced at lower SOC levels. Reduced flow rates correspond to worse mass transport to the reaction area. In diffusion-dominated flow regimes, concentration limitations are evident, particularly characterized by a marked drop in the half-cell potential for SOC of 0.1. This phenomenon arises from regions with inadequate reactant supply. In particular, simulations for the SOC of 0.1 with Re numbers below 5×10^{-3} could not be performed due to these conditions. Furthermore, the curves illustrate that flow rates with Re numbers exceeding 5×10^{-2} do not lead to significant performance improvements under constant operating conditions. It can be inferred, as previously, that an optimal Re number exists in the range of 5×10^{-2} independent of the SOC.

The power density is a critical parameter in flow batteries, influenced by factors such as flow rate, concentration, and current density. In the subsequent analysis, it is explored under varying operational conditions. Simulation studies are performed that capture two different initial concentrations and discharge current densities according to Liu et al. [38]. The chosen values orient towards the solubility of the active material and towards the appropriate current density. The concentrations are 0.1 M TEMPOL in 1 M NaCl and 0.5 M TEMPOL in 1.5 M NaCl, while the latter represents the limit of solubility of TEMPOL in sodium chloride [38]. The simulations are performed using a constant inlet concentration with an SOC of 0.5. The galvanostatic discharge current density is set to $20\,\mathrm{mA\,cm^{-2}}$ and $80\,\mathrm{mA\,cm^{-2}}$. The Re number range, which was previously described as optimal, and its immediate surroundings are subjected to detailed examination. Consequently, the flow rate ranges investigated correspond to the Re numbers of 5×10^{-4}, 5×10^{-3}, and 5×10^{-2}. Figure 5.15 illustrates the power

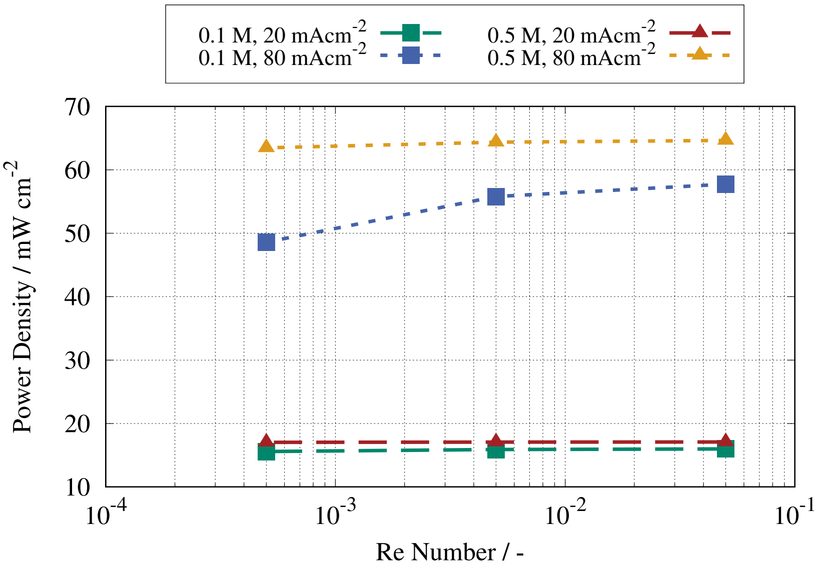

Figure 5.15: Power density versus Re number for two different initial concentration levels and discharge current densities. Simulations are conducted for certain Re number with constant inlet concentration with SOC of 0.5.

density obtained as a function of the Re number for four combinations of the operating conditions aforementioned. At a current density of $20\,\mathrm{mA\,cm^{-2}}$, the power density for both concentrations remains relatively constant at the same level throughout the range of Re numbers. The variation in electrolyte velocities does not significantly impact the power density because an adequate supply of active material is ensured regardless. Similarly, the same observation applies to the current density, which is provided without significant voltage loss. Thus, even the lowest flow rate is sufficient to ensure a satisfactory supply of active material at the reaction surface.

At a high current density of $80\,\mathrm{mA\,cm^{-2}}$, varying concentrations result in different levels of power density. The utilization of a more concentrated electrolyte yields higher power density as a result of enhanced electrolyte conductivity and improved migration at higher concentrations. Additionally, the influence of flow rate on power density becomes more pronounced. In both scenarios, the power density shows a decline with decreasing Re number. This decline is slight for a high concentration of $0.5\,\mathrm{M}$, while it becomes more pronounced for a lower concentration of $0.1\,\mathrm{M}$. In the latter case, mass transfer limitations become evident. Low concentration coupled with low flow rate leads to a discernible loss of power density at high current density.

5.4 Statistical Resilience of the Reconstructed Microstructure

The reconstructed microstructure provides an accurate representation of the electrode, but it reflects only an excerpt of the µCT scanned sample. It cannot be said with complete certainty that the selected section of the microstructure is representative of the entire electrode material. Naturally, it cannot be assumed that the manufactured electrode material is 100% homogeneous and production issues or the assembly of the electrode into the cell lead to irregularities in terms of porosity and active surface area. Due to the complex reconstruction process, a statistical study of different microstructure excerpts is not possible. Therefore, in this section, the reconstructed domain is examined in different flow directions. This leads to a better understanding of the flow characteristics within the electrode, its effects on performance, and strengthens the statistical resilience of the reconstruction process. Furthermore, the structured fiber domain (cf. Figure 2.2) is included in the comparison. In addition to flow along the positive Y^* direction ($\mathrm{Y_{pos}}$) used in the previous investigation, flow along the negative Y^* direction ($\mathrm{Y_{neg}}$) and along the positive and negative X^* directions ($\mathrm{X_{pos}}$ and $\mathrm{X_{neg}}$) is considered. Flow along the Z^* direction is not considered due to the presence of the current collector plate. Due to the symmetric geometry of the structured fiber domain (SFD), only one flow direction is considered. The focus in the underlying section includes the analysis of the mean velocity magnitude, pressure drop, TEMPOL$^+$ concentration, and half-cell potential related to individual flow directions during discharge operation.

5.4.1 Flow in Different Directions

As mentioned in Section 5.3.1, the velocity profiles within the microstructure do not differ significantly in the dependence of different Re numbers. Therefore, the velocity profiles in different flow directions are examined for the flow corresponding to the Re number of 5×10^{-2} in the following. Figure 5.16 shows 2D slices of the velocity magnitude in different flow directions and normalized to the prescribed flow velocity. The slices are perpendicular to the axis not shown and are taken in the center of the domain. From top to bottom, the $\mathrm{Y_{pos}}$, $\mathrm{Y_{neg}}$, $\mathrm{X_{pos}}$, $\mathrm{X_{neg}}$ direction and the SFD are displayed. The flow directions are marked with yellow arrows, whereas crosses in the circle mark flow into the drawing plane, and dots indicate flow out of the drawing plane.

The normalized velocity magnitude ranges from zero to three in all flow configurations. Maximum velocity is attained when a specific channel configuration is formed, facilitated by the arrangement of the electrode fibers and the direction of the flow. This phenomenon is notably observed in both Y^* directions, as depicted in sub-figures (b), (c), (e), and (f). Regarding the flow in negative Y^* direction shown in sub-figure (e), the top fiber structure acts as a barrier for the flow, resulting in reduced flow velocities. Furthermore, the darker red in sub-figure (c) evidences higher velocity.

In the X^* direction, a similar flow behavior is observed due to the presence of fibers, particularly noticeable in the top-left corner of sub-figures (i) and (l). Here, the flow in negative X^* direction is reduced due to presence of the barrier directly after the inlet.

The most distinctive and uniform channel flow configuration is observed in the SFD, as shown in sub-figures (n) and (o). The cross-section in sub-figure (m) indicates relatively low velocities in between and outside of the fibers located in the center of the domain.

Close to the fibers and at boundaries perpendicular to the Z^* direction, velocity is comparatively lower due to the no-slip boundary condition. Additionally, cyclic boundary conditions are apparent in the Y^* and X^* directions.

To facilitate comparison among flow directions, Figure 5.17 shows the non-dimensional volume-weighted mean velocity magnitude plotted against the respective inlet-to-outlet distance L^*, representing the primary flow direction. The velocity magnitude average is computed over 50 equal slices, with every second interval depicted in the figure. Regarding the reconstructed microstructure, the velocity profiles exhibit relatively similar behavior in different flow directions, ranging between 1.0 and 1.3. Fluctuations in the profile result from

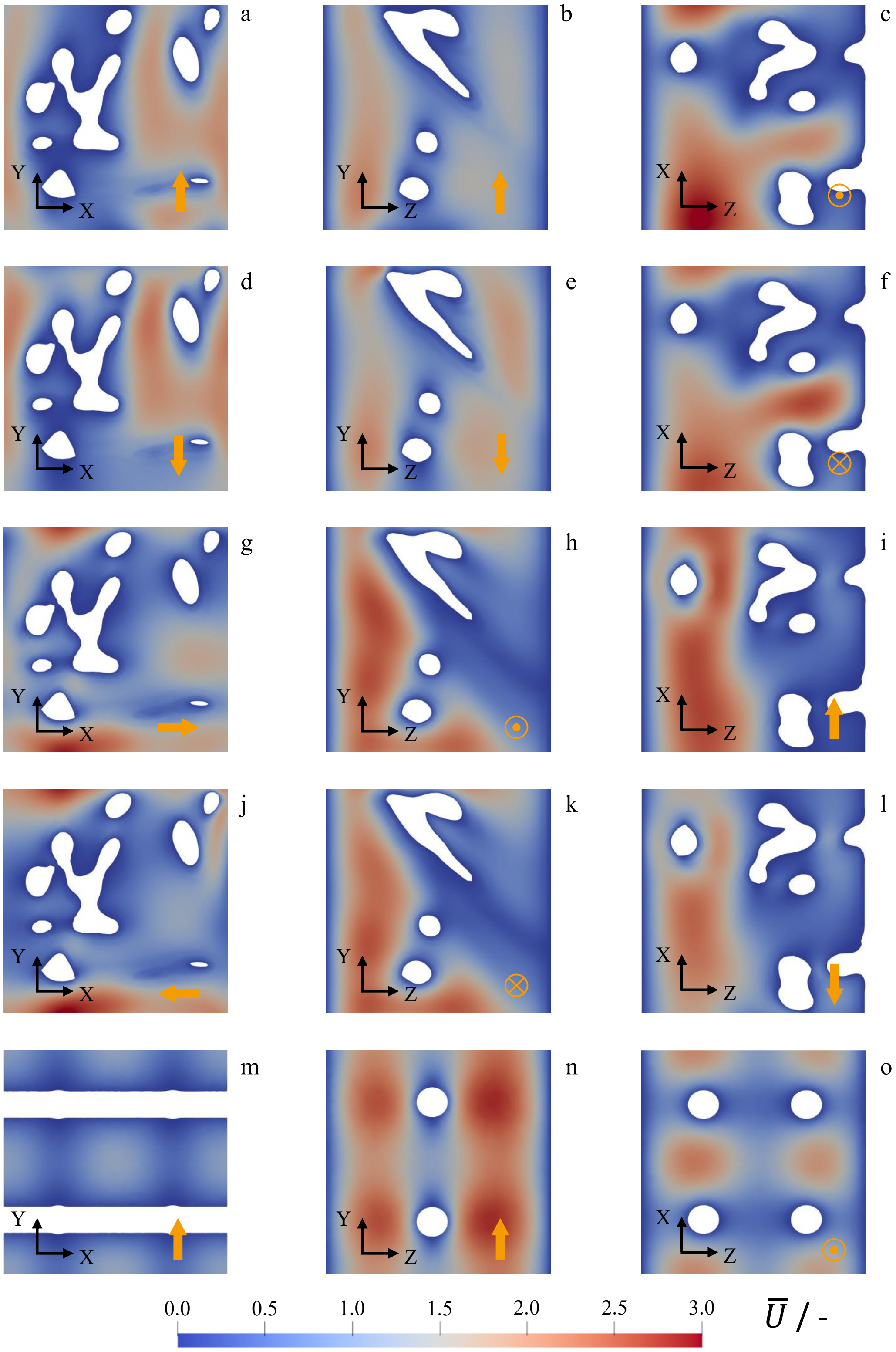

Figure 5.16: 2D slices of the velocity magnitude in different flow directions and normalized to the flow velocity of Re number of 5×10^{-2}. The yellow arrows denote the flow direction, whereas crosses mark flow into the drawing plane and dots indicate flow out of the drawing plane.

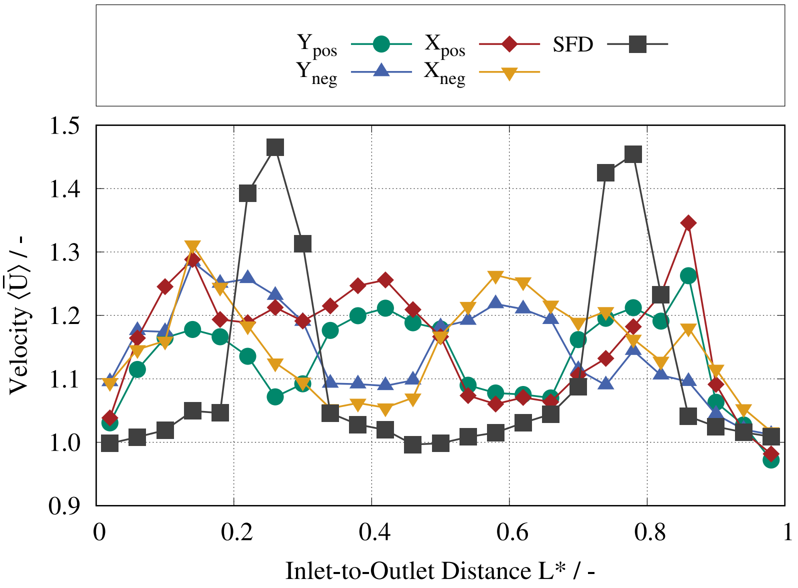

Figure 5.17: Non-dimensional volume-weighted mean velocity magnitude versus the respective inlet-to-outlet distance L^* for different flow directions and normalized to the flow velocity of Re number of 5×10^{-2}.

changes in flow cross sections induced by the presence of fibers; narrower cross sections result in increased electrolyte velocity.

In contrast, the velocity profile of the SFD shows a distinct characteristic. Two prominent maxima are evident, corresponding to the main flow channels within the structured fiber configuration (cf. Figure 5.16n). Velocity nearly reaches 1.5 at these maxima and remains close to 1.0 elsewhere in the domain.

In particular, the mean velocities of the slices after the inlet and before the outlet differ as the cyclic boundary condition applies only to the faces of the domain.

Figure 5.18 shows the pressure drop for each flow direction of the reconstructed microstructure and for the SFD, all corresponding to a Re number of 5×10^{-2}. The pressure drop is taken between the respective inlet and outlet boundaries, whereas an average is taken over the inlet boundary. The pressure at the outlet boundary is zero per definition.

Distinct variations in pressure drop are observed for the respective flow directions depending on the alignment and arrangement of the fibers. The pressure drop is highest for flow along the positive and negative X^* directions, where the fiber arrangement creates a disadvantageous scenario. In these directions, the flow behaves more like a direct perpendicular impact on the fibers rather than smoothly sliding along their surfaces. Differences in pressure drop between the positive and negative X^* directions arise from the fiber placement and their proximity to the inlet boundary, a trend also observed in both Y^* directions. The lowest pressure drop occurs for flow along the positive Y^* direction, where the fiber alignment is

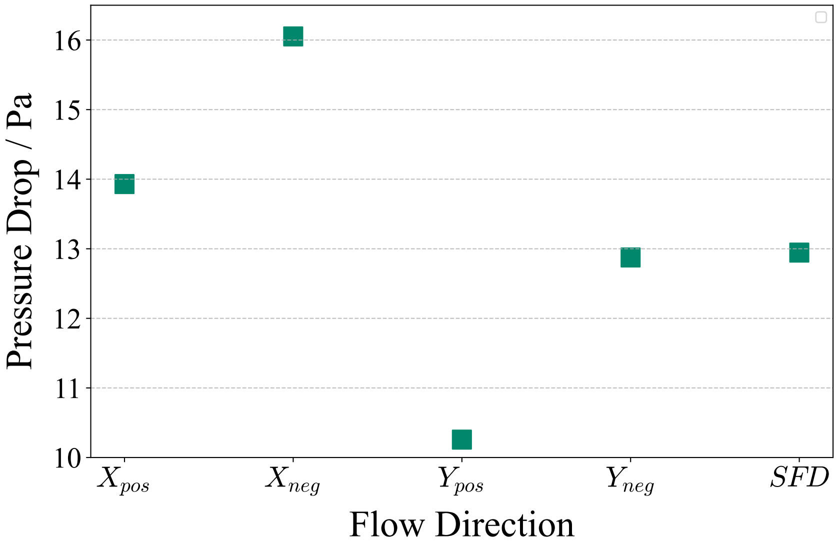

Figure 5.18: Pressure drop for each flow direction of the reconstructed microstructure and the SFD corresponding to a Re number of 5×10^{-2}. The average pressure is taken at the inflow boundary.

the most favorable, and the first obstacles are positioned farther from the inlet compared to other directions. The pressure drop for the SFD aligns with that of the negative Y^* direction. However, no significant benefit in terms of flow resistance for the SFD can be inferred based on the observed Re number. To holistically evaluate the electrode's performance, it is essential to consider its mass transfer properties, which are discussed in the following paragraph.

5.4.2 Concentration Comparison

In the following, quasi steady-state discharge simulations with constant inlet concentration are conducted for specific combinations of operating parameters. The initial concentrations are 0.1 M TEMPOL in 1 M NaCl and 0.5 M TEMPOL in 1.5 M NaCl with SOC of 0.5. The investigated discharge current densities are $20\,\mathrm{mA\,cm^{-2}}$ and $80\,\mathrm{mA\,cm^{-2}}$. As stated in Section 5.3.5, mass transfer limitations are likely to occur below the flow corresponding to a Re number of 5×10^{-2}. Therefore, the flow rates investigated correspond to the Re numbers of 5×10^{-4}, 5×10^{-3}, and 5×10^{-2}. The combination of all these parameters with each other results in 60 unique microscale simulations that provide a quantitative examination of the reliability of the reconstructed microstructure.

Figure 5.19 exemplarily shows the mean TEMPOL$^+$ concentration within the whole electrolyte region over time during discharge for flow corresponding to Re number of 5×10^{-2} (a) and 5×10^{-4} (b). The current density is $80\,\mathrm{mA\,cm^{-2}}$ and the initial concentration is 0.1 M TEMPOL in 1 M NaCl in both cases. The courses of the respective flow directions are highlighted in different colors. After a certain time, the system reaches steady-state concentration, where

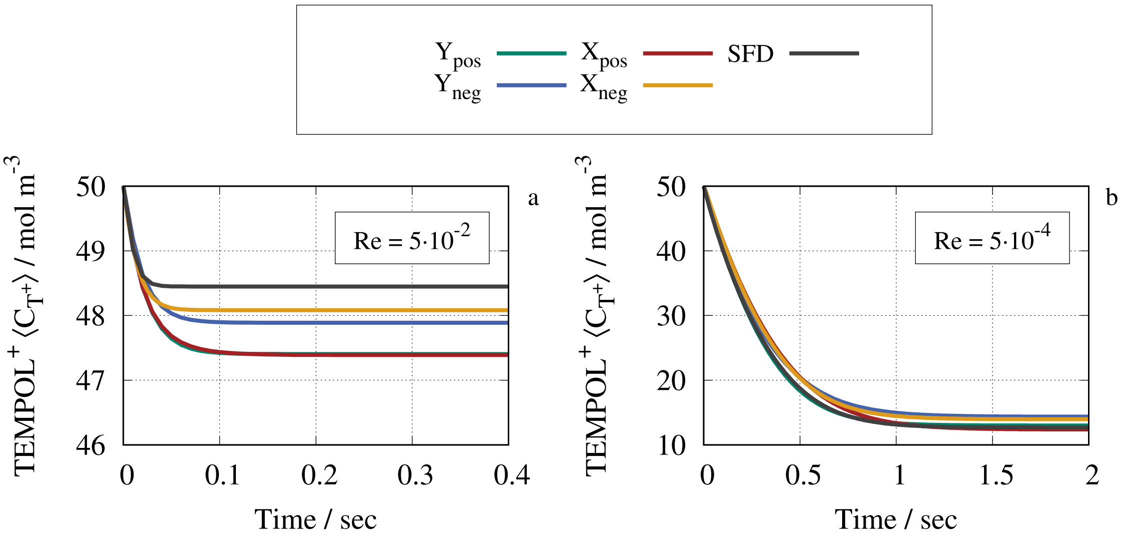

Figure 5.19: Mean TEMPOL$^+$ concentrations during discharge operation versus time. Different flow directions are depicted for flow corresponding to Re number of 5×10^{-2} (a) and 5×10^{-4} (b). The current density is $80\,\mathrm{mA\,cm^{-2}}$ and the initial concentration is 0.1 M TEMPOL in 1 M NaCl in both cases.

supply and consumption of the active material are balanced. This holds true for all flow directions. When analyzing all simulation cases, it becomes clear that the SFD attains equilibrium earlier compared to the reconstructed microstructure. This disparity arises from the uniform geometry of the solid fiber domain across the simulation domain, resulting in reduced flow resistance and improved mass transport.

The 60 unique microscale simulations used for the comparison consist of 12 distinct operating conditions and five flow directions, including SFD. For each operating condition, the mean value of the steady-state concentration is calculated using the five different flow directions. The deviations of the respective steady-state concentrations from the mean steady-state concentration can thus be determined to illustrate the influence of the microstructure on the concentration profile. For each flow direction, we obtain twelve deviation values, each of which is assigned to one of the different operating conditions.

Figure 5.20 shows box plots for each flow direction to illustrate the deviations from the mean value. The height of the boxes represents the interquartile range, indicating that the middle 50% of the deviations fall within this interval. For all flow directions, the box spans from zero to one-and-a-half percent, suggesting similar behavior among different directions in most operating conditions. The solid colored line within the box denotes the median, dividing the data set into two equal halves. In every case, the median deviates less than one percent from the mean value, indicating consistent behavior across flow directions. Moreover, it tends to reside predominantly in the lower portion of the box due to data skewness. The antennas outside the box (whiskers) mark the farthest data points within 1.5 times the interquartile range. Notably, the box plot includes outliers, plotted individually due to their significant deviation from the rest of the dataset. It turns out that the farthest outliers correspond to the operating condition of 0.1 M TEMPOL in 1 M NaCl, 80 mA cm^{-2}, and Re number of 5×10^{-4}. In this scenario, the steady-state concentrations exhibit the greatest disparity among themselves, resulting in relatively high deviations. This discrepancy is mainly attributed to the significant impact of the flow field within the electrolyte on the mass transfer dynamics.

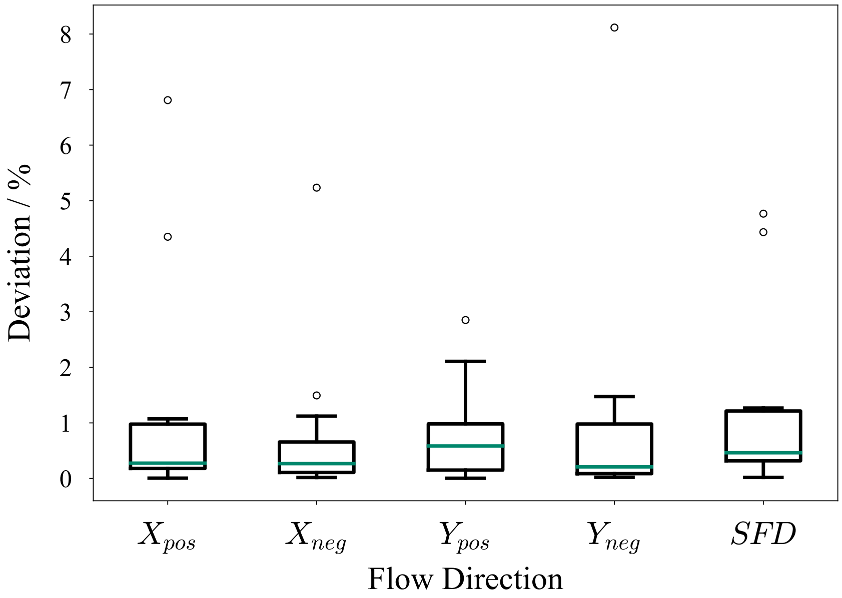

Figure 5.20: Box plot for each flow direction and the SFD to illustrate the deviations of steady-state TEMPOL$^+$ concentration from the mean value of twelve different operating conditions.

In summary, the impact of different flow directions on the steady-state concentration of TEMPOL$^+$ appears to be minimal. The fixed concentration boundary condition at the inlet and sufficiently high values of SOC and velocity ensure the presence of active material throughout the domain, mitigating significant differences among flow directions. However, under extreme operating conditions, discernible variations emerge, but no superior flow direction can be clearly determined. Furthermore, the choice of steady-state mean concentration for comparison is favored due to its simplicity and numerical stability. Future investigations of complete discharge cycles reveal more detailed differences, as shown in the next section.

5.4.3 Half-Cell Potential Comparison

Figure 5.21, presents the discharge characteristics of the flow directions of the microstructure and SFD. It shows half-cell potential versus SOC (a) and time (b) for Re numbers of 5×10^{-2} and 5×10^{-4} (c and d). The initial concentration is 0.1 M TEMPOL in 1 M NaCl and current density is $80\,\mathrm{mA\,cm^{-2}}$. These operating conditions are chosen on the basis of the previous investigation in which mass transfer limitations are most likely to occur.

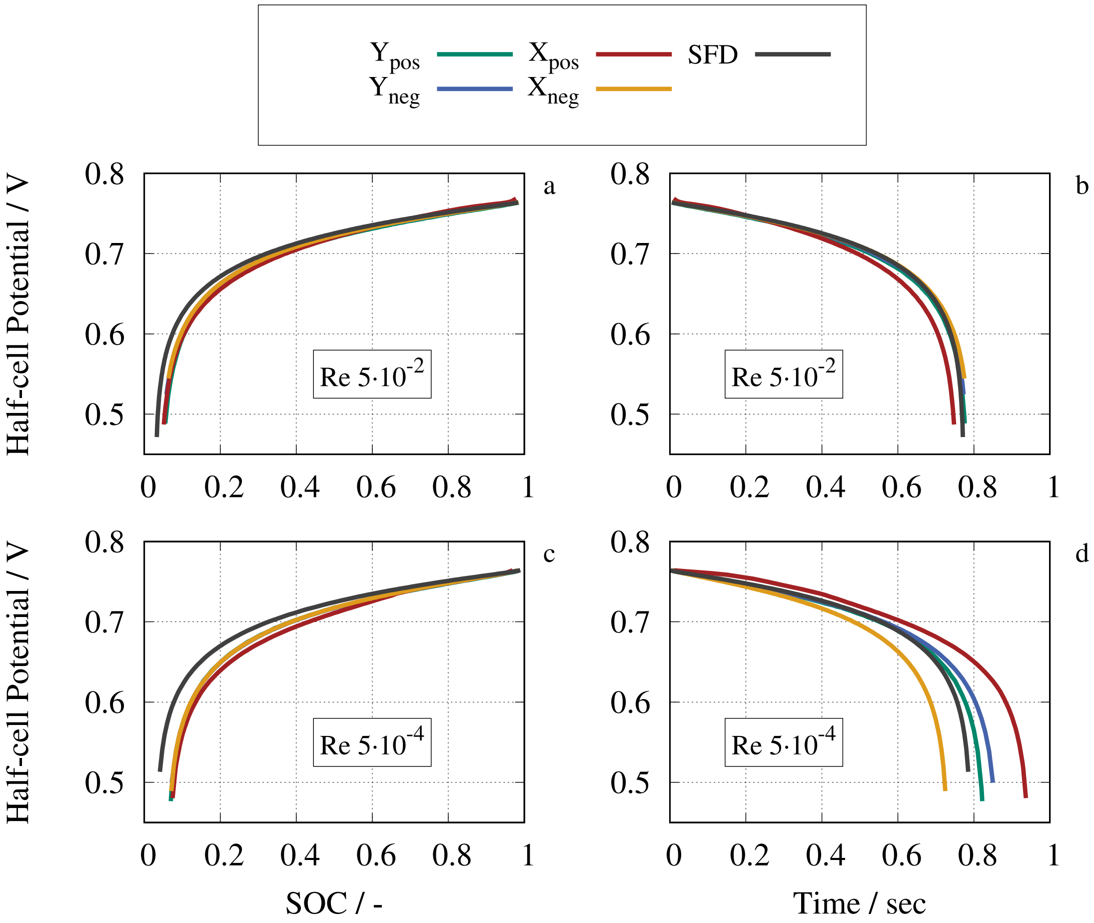

Figure 5.21: Half-cell potential during discharge for flow corresponding to Re number of 5×10^{-2} versus SOC (a) and time (b). Half-cell potential during discharge for flow corresponding to Re number of 5×10^{-4} versus SOC (c) and time (d). Different flow directions are depicted with different colors. The current density is $80\,\mathrm{mA\,cm^{-2}}$ and the initial concentration is 0.1 M TEMPOL in 1 M NaCl.

The respective curves of half-cell potential versus SOC proceed comparatively similarly regardless of the Re number, especially at high SOC. Differences in half-cell potential become more apparent towards the end of discharge and occur earlier for Re number of 5×10^{-4}. The influence of the microstructure is therefore greater at lower flow velocities. With regard to both Re numbers, the SFD exhibits a higher potential as the reconstructed microstructure at the same SOC. The relative positioning of the curves yields an interesting observation, as the SFD exhibits a slightly smaller active surface area compared to the reconstructed domain. Consequently, a lower potential for SFD might be expected due to increased overpotentials. At an equivalent discharge current density, the actual current at the interface is higher owing to the reduced surface area. This would typically result in elevated overpotentials, thereby diminishing the overall half-cell potential. However, this phenomenon does not occur in the present investigation. The simpler structure and more uniform expansion within the simulated volume contribute to a superior distribution of active material, effectively mitigating dead zones characterized by a shortage of reactant. For example, at SOC of 0.1, the half-cell potential of SFD is 4% higher for the Re number of 5×10^{-2} and 10% higher for the Re number of 5×10^{-4}. All discharge curves end before reaching SOC 0, as the surface concentration falls below zero somewhere earlier, and as a result the simulations crash.

The progression of the half-cell potential over time shows small differences for the Re number of 5×10^{-2}. The discharge processes of all flow directions end around 0.75 s and exhibit the same shape, with a slight exception for the positive X^* direction (X_{pos}). With respect to the lower Re number, the curves deviate significantly from each other over time. The discharge processes end between 0.7 s and 0.9 s. In these diffusion-dominated flow regimes, the microstructure has a significant influence on the half-cell potential over time. This originates primarily from the reduced mass transfer to the active surface.

5.5 Conclusion

In this chapter, the successful development of a microscale model for flow batteries has been demonstrated, allowing for accurate performance predictions. The model is versatile and can be applied to both structured fiber and complex reconstructed electrode domains. The primary focus has been on the TEMPOL half-cell system.

The model has effectively illustrated the impact of different concentrations of active materials and current densities on the half-cell potential, as well as the effect of SOC and current density on overpotential. It captures the well-known trade-off between active surface area and pressure drop, validating its accuracy.

Detailed investigations into the velocity profiles within the reconstructed microstructure revealed that these normalized profiles are independent of flow rate. However, the effect of flow rate on concentration profiles highlighted mass transfer limitations around Re numbers of 10^{-2}. Therefore, an optimal Re number in this range is recommended to balance the acceptable half-cell potential with the lowest possible pumping power, thus maximizing round-trip efficiency. Limiting cases in terms of power density were identified, with highly concentrated electrolytes handling a wider range of applied current densities, while mass transfer limitations became apparent with lower concentrations and higher current densities.

Differences in flow velocity directions within the microstructure were observed, with greater discrepancies observed in the SFD compared to the reconstructed one. Despite these differences, the impact on steady-state concentration distribution was minimal. However, variations in half-cell potential were noticeable at low Reynolds numbers.

Key takeaways include: The MSM is successfully developed and capable of predicting operating conditions and their influence on performance. Practical electrode design should consider structured repetitive geometries such as foams, graphene, or glassy carbon to avoid dead zones. For modeling purposes, a complicated reconstruction process is not necessary. SFDs are sufficient to investigate basic microscale phenomena and are much easier to generate.

For prospective work, the implementation of a larger computational domain, capturing the full width of FB electrodes is essential. This will necessitate improvements to the reconstruction framework, e.g. employing alternative imaging techniques with higher resolution (e.g. FIB-SEM). Additionally, a critical question arises regarding whether the focus should be on a detailed recreation of the microstructure or on the use of cyclic boundary conditions for the solid region. Combining both objectives is challenging because of the inherent inhomogeneity of real electrode materials. Achieving this requires consistent fluid-solid segmentation at opposing boundaries that do not exist in real samples.

With respect to the mathematical algorithm of the model, one main issue can be identified. The implementation of back-coupling between concentration and velocity of the electrolyte would significantly improve the model. In the underlying modeling approach, the velocity field is calculated beforehand using a constant viscosity. This is appropriate for the vanadium and the TEMPOL system. Regarding other electrolyte systems this holds not true because the velocity field changes depending on the variable viscosity, originating by the variable concentration. In order to realize that, a new velocity field must be calculated each time step where Equation 2.4 is solved.

6 Multiscale Modeling Approach

This chapter introduces a novel approach that bridges the gap between microscale and homogenized cell-scale models in the context of flow batteries by utilizing mass transfer coefficients. The primary focus is on how these coefficients, extracted from detailed microscale simulations, can be effectively transferred to homogenized scale simulations and compared with empirical formulations from the literature. Exchanging information between different scale models is inherently challenging, yet the proposed approach establishes a new way to connect these diverse scales, enhancing the fidelity and applicability of multiscale modeling in flow batteries.

The chapter begins with a comprehensive review of homogenized modeling, discussing general approaches connecting different scales, and detailing how mass transfer coefficients are typically derived. Following this, the proposed method is elaborated upon, starting with the extraction of mass transfer coefficients from microscale simulations. The method then addresses how these coefficients are implemented in the homogenized scale as functions of SOC and velocity. Finally, the chapter concludes with a comparison of the developed approach with empirical formulations from the literature, highlighting its advantages and potential applications in improving the design and performance of flow batteries.

The results presented correspond to the work entitled *A Multiscale Flow Battery Modeling Approach Using Mass Transfer Coefficients* published in the journal *Energy Technology* [128].

6.1 State of the Art

The following review explores the latest advances in homogenized cell-scale models, which distill complex details into more comprehensible and practical representations. In addition, different multiscale approaches for flow battery modeling and mass transfer coefficient derivation are presented.

Shah et al. introduced a dynamic 2D model that integrates principles of mass, momentum, and charge conservation, along with a kinetic representation of vanadium reactants [136]. This model was subsequently expanded to also cover thermal effects by including an energy balance equation [137]. Furthermore, gassing side reactions such as hydrogen evolution and oxygen evolution were taken into account [138]. Shah et al. also developed a dynamic unit cell model that established a relationship between process time, conditions, and state of charge [80]. Building upon Shah's transient 2D models, Ma et al. extended the stationary 2D cell model previously proposed by You et al. [72] to a steady-state 3D model for the negative half-cell of a VFB [139]. Subsequently, other researchers adapted this model to optimize FB featuring flow-through porous electrodes [88, 96, 140]. For a more detailed roundup of flow battery modeling approaches, the reader is referred to recent extensive reviews on these fields [45, 48, 49, 133, 134].

Generally, it is remarkable that few simulation approaches of connecting scales in FB modeling have been reported in the literature. Franco et al. [141] reviewed different concepts and approaches to multiscale modeling with a focus on lithium ion batteries. Recently, Bao et al. [142] coupled a flow battery 1D half-cell device model with a deep neural network model to optimize the time-varying inlet velocity of the electrolyte. The neural network was trained using pore-scale simulations. Tao et al. [143] reported a framework for modeling ion transport in porous material, combining molecular dynamics simulation at the nanopore level and continuum modeling for the pore network. Lately, Yu et al. [144] presented kinetic rate calculations for mesoscale modeling to close the gap between microscopic properties obtained from atomistic level approaches and their association with macroscopic observables. Several representative application examples were discussed in flow batteries or similar porous media modelings.

Typically, the mass transfer coefficient is derived from the principles of gas absorption [145] and serves to characterize the resistance to mass transfer. Empirical correlations based on velocity [84, 146, 147] or limiting current density [148, 149] can be utilized to obtain this coefficient. You et al. [150] quantified the influence of velocity on the mass transfer coefficient in a Fe^{2+}/Fe^{3+} lab-scale flow battery, integrating the resulting correlation into a 2D numerical model for comparison with experimental voltage losses. Milshtein et al. [151] developed a 1D flow battery model using iron chloride to explore electrode polarization and extract mass transfer coefficients for different flow fields by experimental fitting. Kok et al. [101] introduced a direct numerical simulation method to assess the impact of microstructural anisotropy on the mass transfer coefficient, employing the LBM on µCT-derived digital twins of three distinct fibrous electrode materials, and determining dimensionless correlations relative to the permeability of the materials.

Various homogenized modeling approaches utilize the mass transfer coefficient to account for the unknown surface concentration of active material on the electrode surface [72, 136]. However, since MSM simulations resolve the mass transfer between the bulk and the active surface, this relationship is not a prerequisite [104, 152]. Consequently, the coefficient is extracted from the MSM and integrated into the HCSM as a function of state of charge and velocity in this chapter. Additionally, it is compared to empirical formulations of the mass transfer coefficient based solely on flow velocity.

6.2 Extraction of the Mass Transfer Coefficient

According to Lewis and Whitman [145], the mass transfer coefficient is defined in the film theory of mass transfer:

$$N_c = k_m A\,(c^b - c^s) \tag{6.1}$$

where N_c is the molar flux of concentration c, A is the active surface area, c^b is the concentration in the bulk electrolyte, and c^s is the concentration at the active surface. By dividing by the active area, Equation 6.1 can be written as

$$k_m = \frac{r}{c^b - c^s}. \tag{6.2}$$

The reaction rate r is evaluated using Faraday's law (cf. Equation 2.10) and the applied current density at the interface. In addition, knowledge of bulk and surface concentrations is required. The bulk concentration is assumed to represent the average concentration of active material within the electrolyte domain, while the surface concentration can be extracted directly due to the inherent nature of the MSM, with an average also considered. The accessibility of the TEMPOL surface concentration is exemplarily shown in Figure 6.1, which illustrates the surface values of every thousand face of the solid-electrolyte interface surface mesh. The mean value and standard deviation are also depicted, of which the former is used for the calculation of k_m. Compared to the similar approach by Kok et al. [101], the determination of k_m is achieved here using detailed Butler-Volmer-type kinetics, migration, and specification of the TEMPOL system. In fact, mass transfer relies on flow velocity. However, the flow regime within the porous electrode exhibits relative uniformity, which justifyes the investigation at a constant Reynolds number, as undertaken in the following. Furthermore, the influence of SOC on the mass transfer coefficient is examined.

To obtain the mass transfer coefficients, three complete discharge processes are computed for both the reconstructed and SFD at different Re numbers 5×10^{-4}, 5×10^{-3} and 5×10^{-2}. Within the discharge operation, the SOC decreases from zero to one. For every SOC value shown, the average bulk and surface concentration value is evaluated. Using the applied current density, the mass transfer coefficient can be obtained. The current density is $80\,\mathrm{mA\,cm^{-2}}$ and the initial concentration is $0.1\,\mathrm{M}$ TEMPOL in $1\,\mathrm{M}$ NaCl. Mapped boundary conditions are used for the electrolyte species. Figure 6.2 shows the mass transfer coefficient extracted according to Equation 6.2 as a function of SOC. As mentioned in Section 2.2, the HCSM accounts for the generation of a single species up to a maximum concentration. This is why TEMPOL

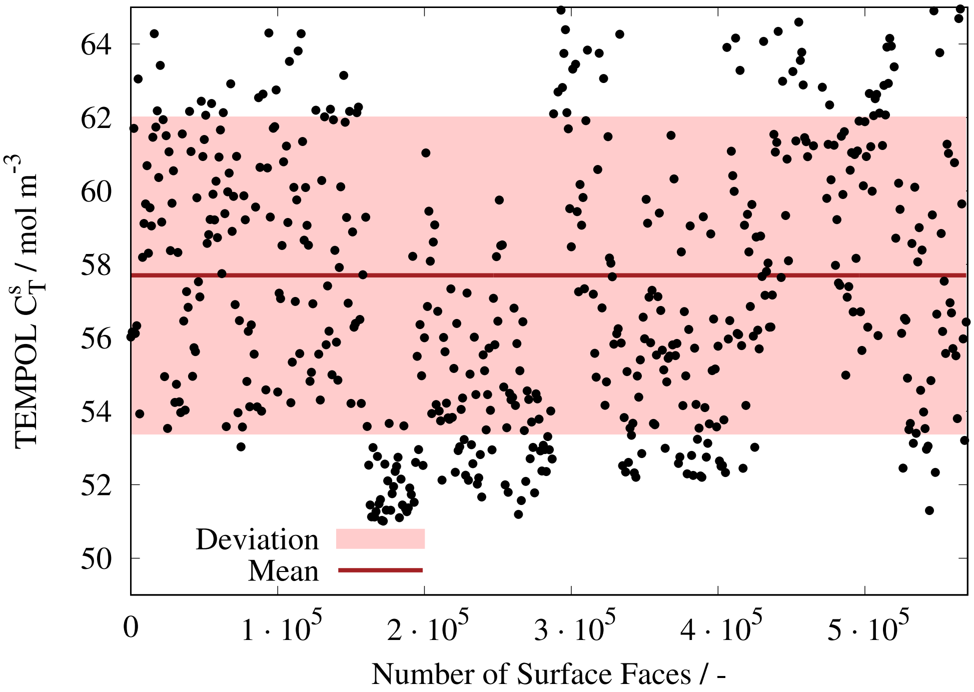

Figure 6.1: TEMPOL concentration values on the solid-electrolyte surface mesh versus number of faces of the surface mesh (black dots). Every thousand face is depicted. Mean value and standard deviation are included in red.

concentration is observed in the further course to characterize the mass transfer in particular and the discharge behavior of the flow battery in general.

When comparing the different domains, an enhanced mass transfer is evident in the SFD due to its isotropic nature. The mass transfer coefficient of the reconstructed microstructure is inferior because of the irregular and intricate fiber structure, which leads to higher concentration gradients between the surface and bulk. In both domains, a clear correlation is evident between the Re number and the mass transfer coefficient, with higher Re numbers corresponding to increased k_m values. In general, the influence of velocity on k_m is minimal, likely due to the relatively high discharge rate. This is also evident for the Reynolds numbers of 5×10^{-4} and 5×10^{-3}, where the graphs show nearly identical trends. In terms of the trajectory of the graph, the coefficient remains constant within the central range of SOC, which is attributed to the maximum concentration gradient between the bulk and the surface. At extreme SOC values, the coefficient value increases as a result of a decreasing concentration gradient. At high SOC, TEMPOL is nearly absent in the system, while at low SOC, the majority of TEMPOL$^+$ has already been converted into TEMPOL.

Concerning the mass transfer of TEMPOL$^+$, the course of the respective graphs can be envisioned as mirrored along the abscissa with negative values.

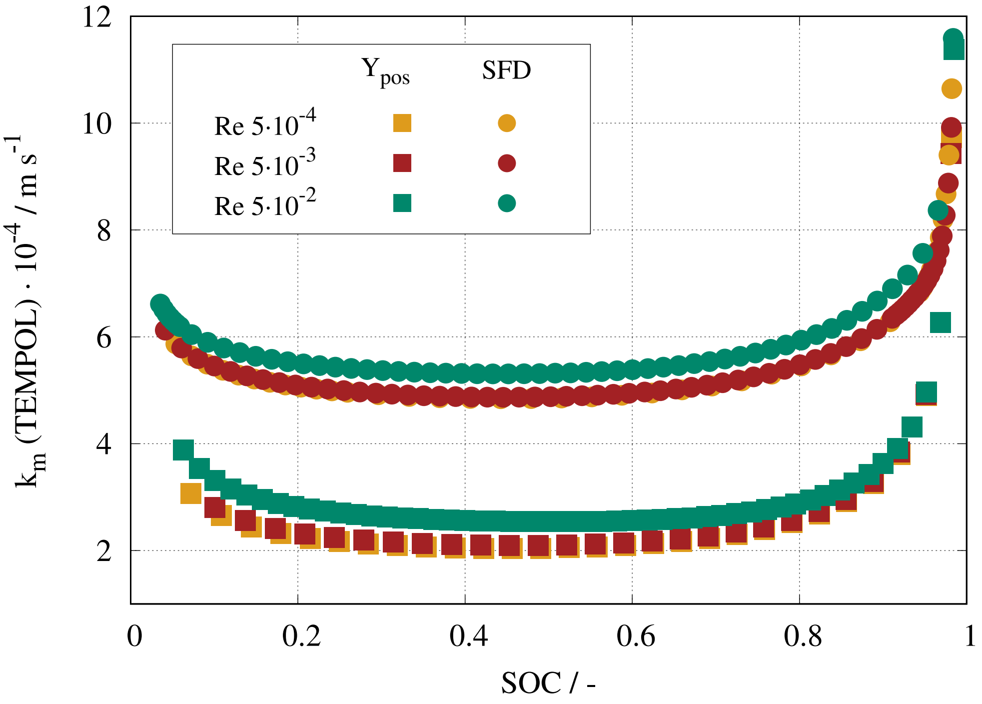

Figure 6.2: Comparison of the extracted TEMPOL mass transfer coefficient as a function of SOC for different Re numbers and computational domains. The current density is 80 mA cm^{-2} and the initial concentration is 0.1 M TEMPOL in 1 M NaCl.

In Figure 6.3, the simulation results of the mass transfer coefficient in relation to the reconstructed microstructure domain and the corresponding fitting function are shown in more detail. For better visualization, every third data point is depicted. The fitting function consists of five independent parameters and is related to the flow velocity and SOC. It is defined as

$$k_m = c + d \cdot U + \frac{b}{sin\left(\pi \cdot a \cdot \left(SOC + 0.5 \cdot \left(\frac{1}{a} - 1\right)\right)\right)} + e \cdot SOC \tag{6.3}$$

where U is the magnitude of the mean velocity within the electrode, and the SOC is defined to be in the range between zero and one. The fitting parameters are listed in Table 6.1. To create the function, 320 simulation data points are used. The root mean square error between the fit and the data is 2.45×10^{-5}. Further, it is worth mentioning that the parameter a within the sinus is constrained to $a < 0.97$. Otherwise, the fitting function predicts $k_m = \infty$ at $SOC = 0$ and $SOC = 1$. Finite values at the boundaries are mandatory to successfully implement the function into the HCSM model as shown hereafter.

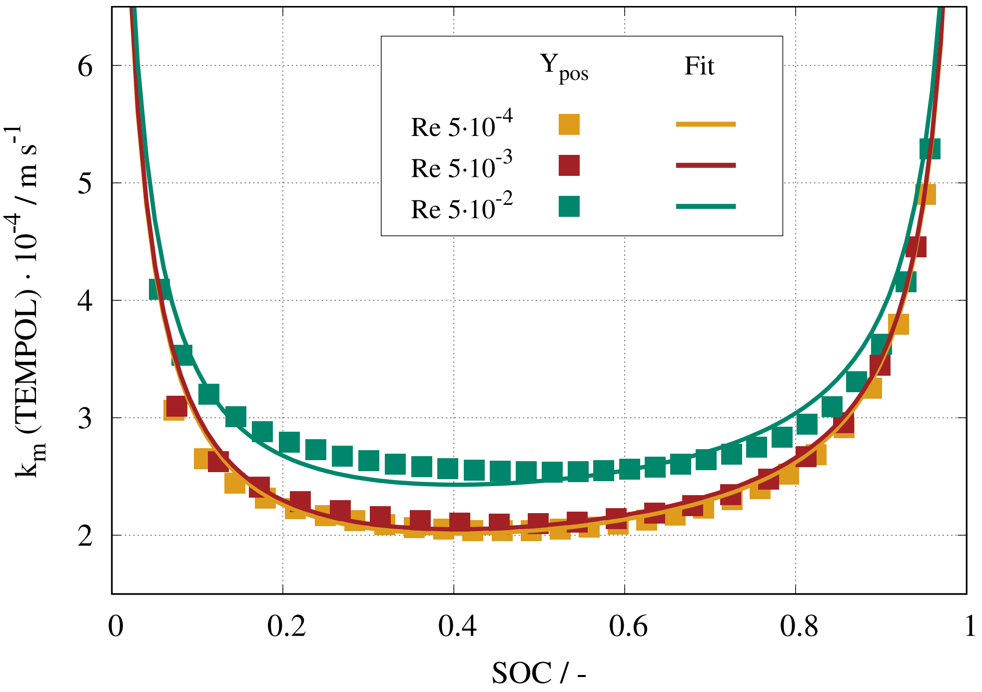

Figure 6.3: Result of the mass transfer coefficient extraction with corresponding fitting function regarding the reconstructed microstructure domain.

Table 6.1: Parameter of the fitting function according to Equation 6.3.

Parameter	Value	Unit
a	0.9695	-
b	6.241×10^{-5}	$\mathrm{m\,s^{-1}}$
c	1.114×10^{-4}	$\mathrm{m\,s^{-1}}$
d	8.425×10^{-3}	-
e	6.036×10^{-5}	$\mathrm{m\,s^{-1}}$

6.3 Implementation of the Mass Transfer Coefficient

In the subsequent HCSM investigation, the fitting function obtained is used to calculate the mass transfer coefficient based on the local velocity magnitude and the SOC in the electrode. To this end, a parameter study is conducted to illustrate the impact of various flow rates (Q) on the aforementioned parameters. Specifically, the flow rates at the inlet of the manifold correspond to 10, 50, 100 and 150 $\mathrm{mL\,min^{-1}}$. All other operating parameters are configured to match the discharge conditions employed for the extraction of the mass transfer coefficient in Section 6.2. The remaining quantities regarding the HCSM are listed in Table 6.2.

Table 6.2: Operating conditions of the HCSM parameter study.

Description	Symbol	Value
Initial active material concentration	c_{init}	$0\,\mathrm{mol\,m^{-3}}$
Inlet active material concentration	c_{inlet}	$0\,\mathrm{mol\,m^{-3}}$
Maximum active material concentration	c_{max}	$100\,\mathrm{mol\,m^{-3}}$
Inlet velocity	$Q/(w_m \cdot d_d)$	$\mathrm{m\,s^{-1}}$

To assess the impact of different flow rates, we define horizontal (LX) and vertical (LY) cutlines within the electrode domain. The horizontal cutline is positioned above the fifth inlet manifold channel, extending to the midpoint of the adjacent channels, respectively. The vertical cutline is located in the center of the fifth inlet manifold channel, starting at the transition from channel to electrode, and spanning ten percent of the electrode's height. The cutlines are depicted in Figure 6.6. This specific region is chosen because the majority of the reaction occurs here. Table 6.3 presents the starting and ending points of these lines, with the spatial origin of the model domain located at the center of the flow battery cell.

Table 6.3: Cutlines within the electrode.

Description	Start	End	Unit
LX (horizontal)	(-0.0075 | -0.03975)	(0.0045 | -0.03975)	m
LY (vertical)	(-0.0015 | -0.0400)	(-0.0015 | -0.0320)	m

Figure 6.4 illustrates the velocity magnitude, SOC, and mass transfer coefficient calculated using Eqn. 6.3 along the dimensionless length of the horizontal (LX) and vertical (LY) cutlines for the specified flow rates.

Sub-figures 6.4a and b depict the velocity magnitude. Along the horizontal direction, the velocity exhibits oscillations, peaking above the channels and reaching the minimum between the channels. Across all flow rates, the velocity remains close to zero above the lands. These minima arise from the lateral counter-flow between the channels and the no slip boundary condition at the wall. The local minima observed above the channels stem from the porous electrode that impeded the free flow within the manifold channels. Upon impact, part of the flow is redirected from the interior to the channel margins, resulting in increased velocities at the edges, influencing the first few millimeters of the electrode. In the vertical direction, the velocity decreases along the cutline, with a more pronounced decrease observed at higher flow rates. Generally, the velocity decreases within the initial five percent of the electrode height before stabilizing to a constant value thereafter. In particular, the highest velocity recorded within the electrode corresponds to a Re number of 0.25.

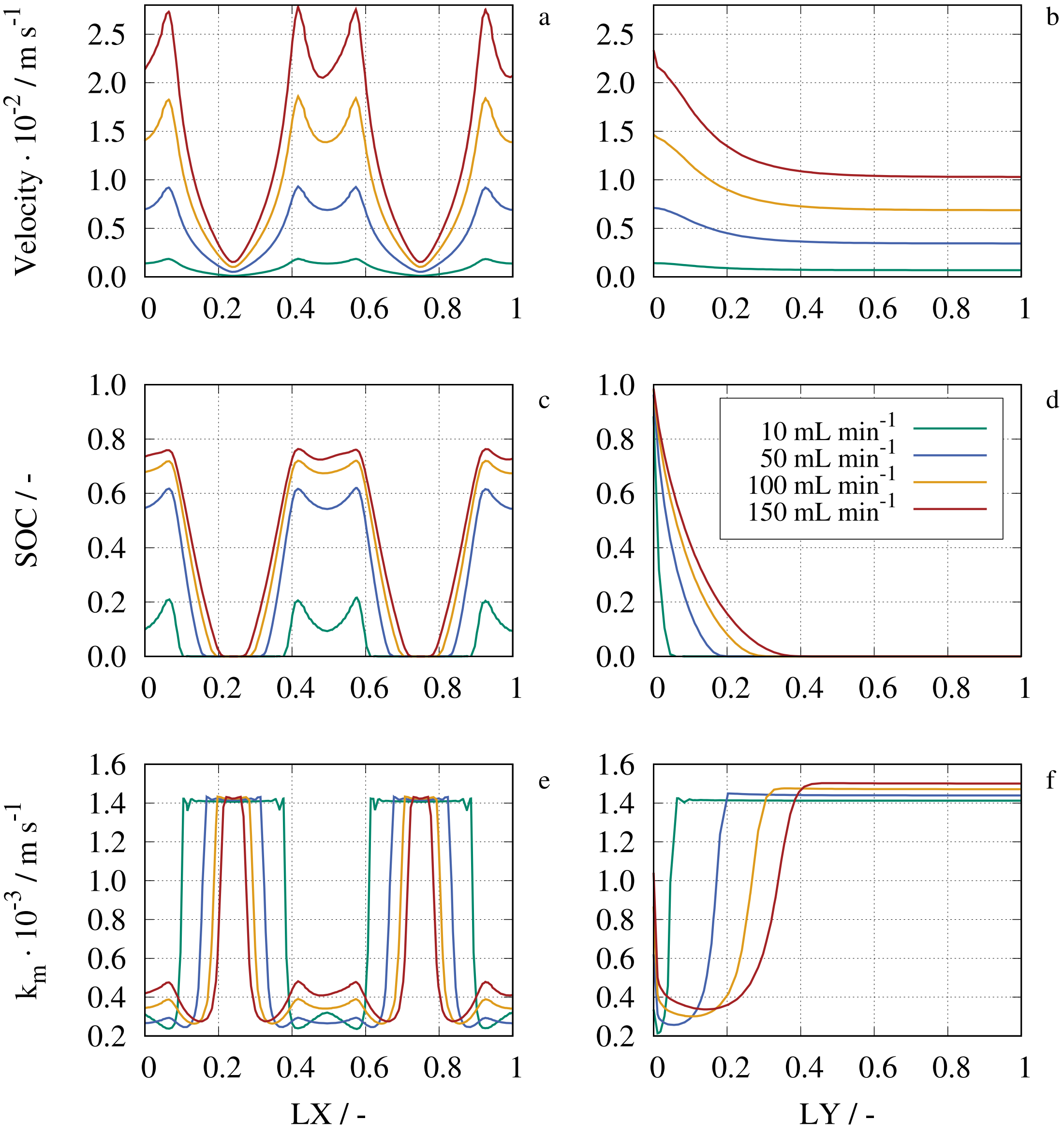

Figure 6.4: Velocity magnitude, SOC, and mass transfer coefficient along the horizontal cutline (LX) and vertical cutline (LY) for different flow rates. The key in Sub-figure d holds true for all sub-figures.

The trends observed for the SOC curves mirror those of velocity for both horizontal and vertical cutlines. Regarding the horizontal direction shown in Sub-figure 6.4c, SOC values are elevated above the channels where the fully charged electrolyte enters the electrode. The differences between the flow rates are non-linear, attributed to reduced mass transfer resulting from lower velocities. The local minima in SOC follow a similar trend to velocity as well. Interestingly, above the lands, the SOC reaches zero for each flow rate. This is due to the relatively high mass transfer coefficient, particularly at the SOC boundaries, as influenced by the fitting function (cf. Figure 6.3). This phenomenon will be discussed in more detail in Chapter 6.4. Furthermore, SOC decreases in the vertical direction due to the discharge process as shown in Sub-figure 6.4d, with a more pronounced reduction observed at lower flow rates, leading to complete discharge within the initial 5% of the electrode height.

The behavior of the mass transfer coefficient is depicted in Sub-figures 6.4e and f. In the horizontal direction (LX), it exhibits inverse trends compared to the velocity and the SOC. Above the channels, the fully charged electrolyte is consumed, resulting in SOC values ranging from 0.8 to 0.1 depending on the flow rate. As a result, the values of k_m show little variation from each other. The curves demonstrate a similar trend, with a local minimum observed above the center of the channel, except for the case of $10\,\mathrm{mL\,min^{-1}}$. Here, the SOC reaches values that are comparatively low, leading to enhanced mass transfer because of proximity to the extrapolation zone of the fitting function. Above the lands, the electrolyte approaches SOC of zero, resulting in k_m reaching one of its maximum values derived from the fit. It is worth noting that this maximum may vary with different fitting functions. Furthermore, a wider maximum plateau above the lands is observed at lower flow rates, indicating a reduced supply of active material in the reaction zone as a result of slower velocities.

Along the vertical direction shown in Sub-figure 6.4f, the U-shaped trend of the k_m curve is evident, reflecting SOC values ranging from one to zero. The curve becomes more pronounced with higher flow rates, allowing more non-converted electrolyte to penetrate deeper into the electrode. Finally, the SOC value drops to zero at different locations of the cutline and a constant value of k_m is achieved, highlighting the impact of varying velocities within the electrode.

In summary, the implementation of the extracted mass transfer coefficient into the HCSM is successful. However, the reaction zone above the channels is relatively limited, and most parts of the cell do not experience reaction. Consequently, the cell appears to be overdesigned for the intended system and its chosen operating conditions. Further investigations are required to accurately elucidate the validity of the fitting and extraction approach, in general.

6.4 Comparison of Mass Transfer Coefficient Calculations

In the last section of multiscale modeling, the HCSM is used to compare the extracted fit of k_m with empirical formulations that correlating the mass transfer coefficient and velocity only. The selected references are based on the work of Schmal et al. [84] and Zhang et al. [64]. The approach of Schmal et al. according to Equation 2.28 is widely used to characterize mass transfer. Despite the fact that the experiments are conducted with potassium hexacyanoferrate, the empirical coefficients obtained $\beta = 1.6 \times 10^{-4}$ and $\alpha = 0.4$ have widespread application in the modeling of vanadium flow batteries [72, 139, 153, 154]. In contrast, the method proposed by Zhang et al. involves the derivation of an empirical correlation by fitting simulated data with experimental results. Here, the TEMPOL system and different electrodes are employed. The correlation is formulated as

$$k_m = \left(\left(1 + exp\left(-4665 \frac{U}{1\,\mathrm{m\,s^{-1}}} + 42.302 \right) \right)^{-1} + 0.235 \right) \cdot 8.511 \times 10^{-5} \cdot 1\,\mathrm{m\,s^{-1}}. \tag{6.4}$$

In both reference approaches, the mass transfer coefficient is solely dependent on the average velocity within the electrode. The comparison is carried out using an inlet flow rate of $70\,\mathrm{mL\,min^{-1}}$. This ensures a flow regime in the electrode corresponding to the Re numbers of 5×10^{-2}, where k_m is extracted from the MSM.

Figure 6.5 shows the comparison of the empirical formulations mentioned with the multiscale approach proposed in this work. SOC and mass transfer coefficient are depicted versus the dimensionless length of the horizontal (LX) and vertical (LY) cutlines.

Along the horizontal cutline depicted in Sub-figure 6.5a, the SOC demonstrates fluctuations between the channels and the lands, with maxima observed above the channels. This phenomenon holds for all three approaches and stems from enhanced velocity above the channels and the presence of non-converted electrolyte in these regions. In comparison, the SOC is notably higher for the reference formulations, which is attributed to the smaller mass transfer coefficient. The two peaks observed at the sides of the maximum above the channels are evident in the approach by Zhang et al. and the underlying multiscale approach. They arise from a more detailed inclusion of the velocity profile above the channel.

Sub-figure 6.5b presents the vertical direction towards the outlet. The SOC curves of the reference cases decrease slightly, whereas the SOC of the underlying approach decreases more significantly along the cutline. However, in both cases, complete discharge is achieved within the first 25% of the electrode height.

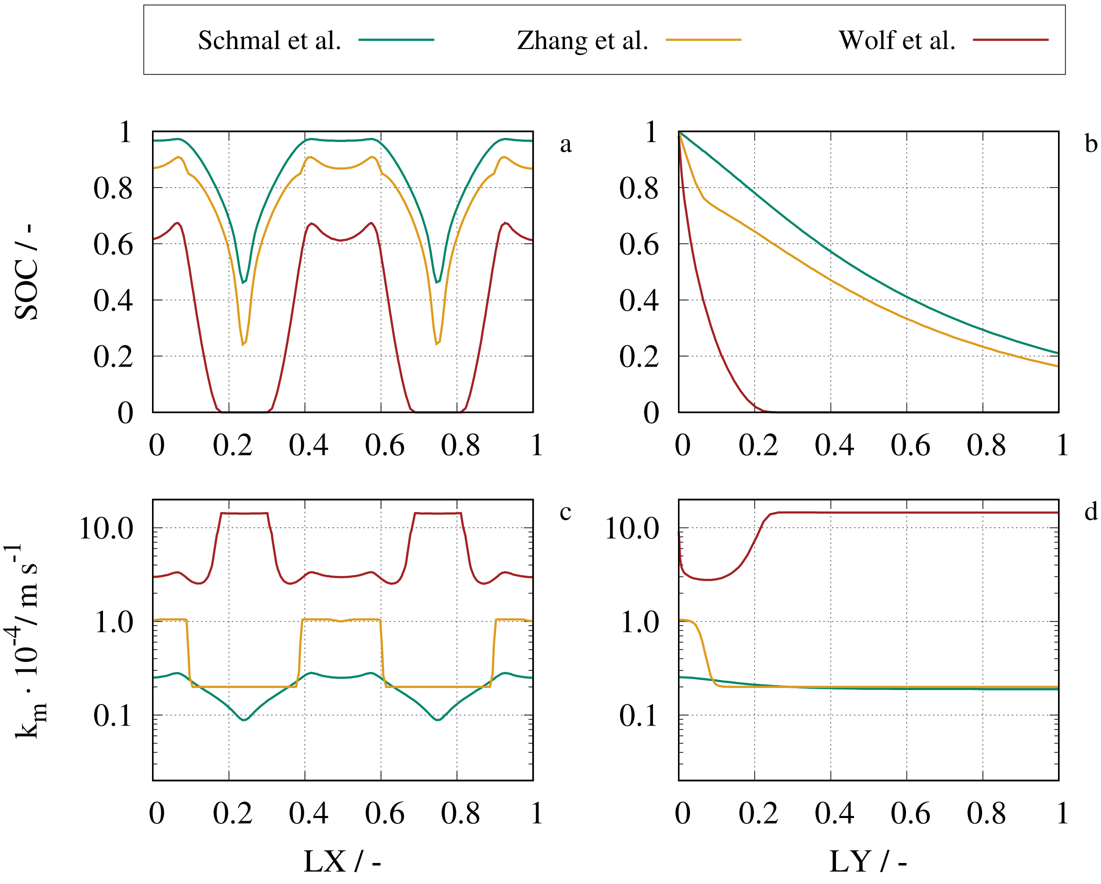

Figure 6.5: SOC and mass transfer coefficient along the dimensionless length of the horizontal (LX) and vertical cutlines (LY) for the empirical formulations of k_m. The key in Sub-figure b holds true for all sub-figures.

In general, the extracted mass transfer coefficient from the underlying approach is approximately one order of magnitude higher than those predicted by the comparative functions. Along the horizontal cutline shown in Sub-figure 6.5c, a reverse trend is observed, with maxima occurring above the lands. This can be attributed to the significant increase in k_m in regions with low SOC as determined by the fit. In contrast, for the other curves, k_m is elevated above the channels due to enhanced velocity in those areas.

In the vertical direction shown in Sub-figure 6.5d, the mass transfer coefficient varies within the initial 40% of the cutline and remains constant thereafter. It reaches its maximum at low SOC as a result of the fit, whereas the others reach the minimum as a result of decreasing velocity.

Figure 6.6 shows an excerpt of the inlet manifold and electrode for all three approaches. In addition, the horizontal (LX) and vertical (LY) cutlines mentioned above are delineated in the central sub-figure. The domains are colored according to the SOC, calculated with

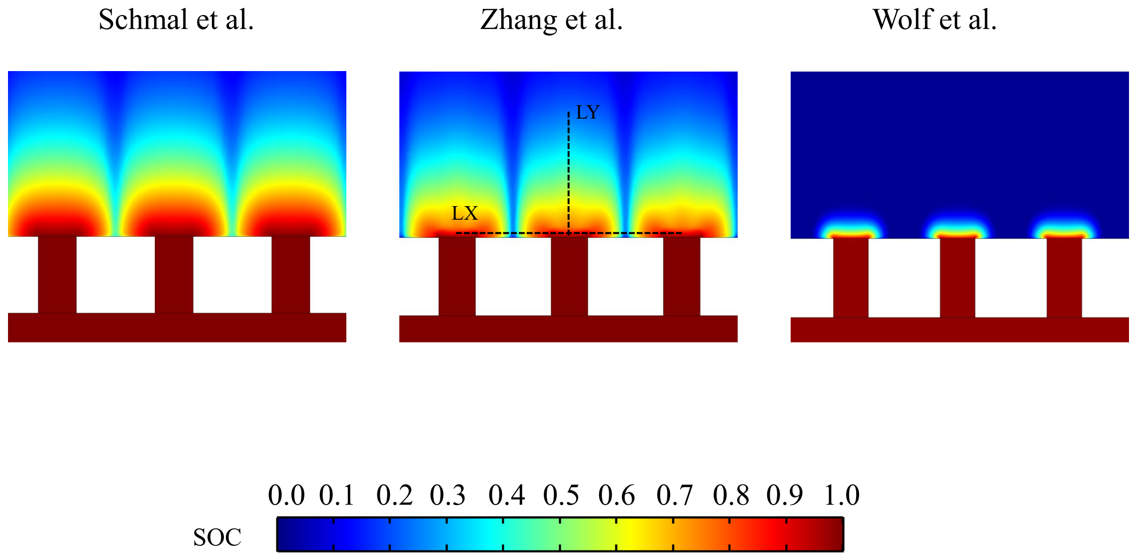

Figure 6.6: Excerpts of the inlet manifold and electrode colored according to the SOC for the respective mass transfer coefficient correlations. Additional representation of the horizontal (LX) and vertical (LY) cutlines in the central sub-figure.

the respective mass transfer coefficient correlations. The electrolyte enters the electrode fully charged and is consumed along the flow. Concerning the approaches by Schmal et al. and Zhang et al., the stepped progression of the reaction can be distinguished. As mentioned above, the reaction is completed relatively expeditiously in this approach. Generally speaking, differences originating from the respective approaches are negligible regarding the comprehensive behavior of the entire cell. The discharge process is completed within the lowest quarter of the cell in all cases.

6.5 Conclusion

In summary, the development and implementation of the multiscale modeling approach has proven to be successful. Through MSM simulations, the mass transfer coefficient was effectively extracted and subsequently integrated into the HCSM. Comparison with empirical reference formulations from the literature highlights the advantages of this approach, demonstrating enhanced species conversion in the electrode. These findings underscore the potential of the multiscale framework to provide more accurate and detailed insights into the performance of flow batteries.

However, the reaction zone above the channels is relatively small, and most parts of the cell did not experience reaction. For the applied operating conditions, the cell appears to be over-designed in vertical flow direction and can be engineered smaller. Clearly, inactive zones can be potential sources of undesirable side reactions. The exact amount of height reduction depends on several operating and system parameters. For instance, reducing the rather high current density would lead to more pronounced reaction zones. Furthermore, the composition of the electrolyte and the concentration of the active material play a significant role in the creation of the reaction area. For further research, a detailed parameter study is recommended in order to be able to estimate the optimal height of the electrode. However, in Section 7.3, the optimal height of the cell is investigated using shape optimization.

Furthermore, it is worth mentioning that the reference correlations from the literature are obtained by using different porosities of the electrode. This can be considered as reason for the different results as well. Schmal et al. used porosities of 0.83 and 0.96. Zhang et al. considered porosities of 0.8 to 0.85. In this multiscale approach, the porosity is 0.91, originating from the reconstructed microstructure. Furthermore, it must be mentioned that the mass transfer extraction takes place under certain operating conditions that take current density into account. This is not addressed in the equations of the reference correlations.

In addition to this, our study shows that the reaction kinetics play a crucial role in the design of the cell. The kinetic parameters extracted with our method predict a much faster species conversion in the vicinity of the channels compared to values commonly assumed in the literature. This underlines the urgent need for accurate parameterization of reaction kinetics in redox flow batteries. In addition, full electrochemistry on the homogenized modeling level and experimental investigations are inevitable to extend and proof the numerical results. Taken together, the presented approach is convincing because it accounts for the microstructural characteristics of the system and the discharge current density obtained with detailed electrochemistry. Compared to the reference cases, it represents the mass transfer coefficient not only as a function of velocity but also as a function of velocity and SOC.

However, the approach is restricted to a specific discharge state characterized by a fixed current density and initial concentrations. This operating point represents an extreme case where mass transfer limitations are particularly pronounced. Moreover, the investigated velocity range is relatively restricted, leading to the adaptation of the velocity exponent in the derived equation to unity. This deviates from most empirical correlations in the literature, which typically assume laminar flow behavior with the use of an exponent of approximately 0.4 [84]. A broader range of investigated conditions is required to improve the accuracy in capturing the mass transfer coefficient. In summary, while the developed approach is simplified, it offers a valuable opportunity to determine the mass transfer coefficient more precisely through computational modeling rather than relying solely on experimental methods.

7 Topology and Shape Optimization

Despite existing research, the optimal porosity distribution within the electrode and the optimal geometric dimensions of novel cell designs remain unclear. The question arises whether a homogeneous porosity distribution is ideal. This study addresses this gap with a twofold objective: Firstly, determining the optimal porosity distribution through topology optimization, and secondly, exploring the existence of an optimal geometry for novel FB cell designs through shape optimization. To achieve this, the HCSM is introduced with parameters of the vanadium flow battery system.

Previous work predominantly concentrated on the individual optimization of either total power loss or reaction rate, while this approach formulates a multiobjective functional to simultaneously enhance the reaction rate and reduce pressure drop within the cell. This dual optimization aims to identify the optimal compromise between these opposing factors. While several novel cell designs have been introduced, their optimal geometric dimensions have not undergone systematic optimization utilizing a multiobjective functional.

This chapter delves into the realm of flow battery optimization, beginning with a comprehensive review of existing optimization techniques and their applications in this context.

The section about topology optimization starts by defining porosity intervals and ensuring mesh independence to validate the reliability of the model and optimization framework. Following this, more generic investigations, such as simple sanity checks and the influence of initial guesses on the porosity distribution, are presented to establish the robustness of the optimization approach. The section culminates with in-depth studies involving different flow rates and designs, and concludes with a sensitivity study to evaluate the impact of various parameters on the optimization outcomes.

In the last section, the results of shape optimization are showcased. This involves optimizing geometric parameters such as height, width, and other critical dimensions of the flow battery design.

The chapter corresponds to the work entitled *Enhancing Flow Batteries: Topology Optimization of Electrode Porosity and Shape Optimization of Cell Design* published in the journal *Energy Technology* [155].

7.1 State of the Art

Topology optimization [52, 53] gained importance in recent years and is currently used in various disciplines. Originating from structural mechanics and additive manufacturing [156–158], this method is also used in fluid dynamics [159, 160], and in fuel cell [161–164] and FB technologies. In the latter case, the flow field or manifold of the cell as well as the electrode properties are optimized mainly.

Yaji et al. [82] introduced a 2D topology optimization method for the flow fields of the VRFB as a maximization problem of the generation rate of vanadium species. Instead of a electrochemical reaction formulation, a simplified term was used to account for species generation. They identified the interdigitated flow field as the optimized configuration and revealed that the dimensioning of the electrode thickness is affected by porosity and pressure loss settings. Based on this work, Chen et al. [165] applied a three-dimensional topology optimization model for the VRFB using electrochemical Butler-Volmer-type reaction kinetics. They revealed that the interdigitated-type flow field is best under the investigated operating conditions. Beck et al. [166] presented a computational optimization of a VRFB half-cell to design 3D porous electrodes composed of unit cells that incorporate spatially variable geometries. The porosity was redistributed to minimize the power loss within the electrode. They found a variable porosity distribution that led to higher power efficiencies in operating flow directions and currents. Gilmore et al. [167] applied two-dimensional topology optimization to adaptable manifold configurations that can be used for FB, among others. They found an optimal and experimentally validated baffle configuration that minimized pressure loss. He et al. [168] developed a three-dimensional VRFB model to understand the effects of the electrode's structural parameters on battery performance. Among other things, they investigated the gradient porosity within the electrode and found that a high porosity can minimize concentration overpotentials and reduce pressure loss.

Roy et al. [92] used density-based topology optimization for the design of porous electrodes in different electrochemical applications. The optimization problem was formulated to minimize the energy loss in a half-cell. They found nontrivial optimized designs that showed improved performance compared to monolithic single-porosity electrodes in terms of effective conductivity and energy loss. Lin et al. [169] extended the work of Beck et al. [166] to utilize topology optimization to generate flow field designs with well-defined solid and liquid regions. As pioneers in the field, they devised an optimization strategy using a multiobjective cost function that aims at concurrent minimization of electrical and flow pressure power losses. They found an optimized, interdigitated flow field design with three-dimensional ramp features that lead to a better distribution of reactant and reaction. Charoen-amornkitt et al. [170] developed a topology optimization model of porosity distribution in a reaction-diffusion system. They connected the numerical approach with an entropy generation analysis to obtain a physical understanding. The results showed a slight improvement in maximizing the response within the reactor for the 0D and 1D cases, while optimization for higher dimensionalities yielded significant improvements. Wang et al. [171] introduced the topology optimization of microchannel reactors using an improved multiobjective algorithm based on the weighted-sum method. They found that geometries and fluid properties have a significant impact on the optimal topology for both Newtonian and non-Newtonian fluids.

The porous electrode within an FB is a key component that influences charge and mass transport. Most systems use felt electrodes composed of carbonized polymer-based fibers on the micrometer scale. For optimal operation, they must provide a large active surface area for the electrochemical reaction, but also high porosity to minimize pressure loss [172]. Hence, optimizing electrode material and design can lead to a significant improvement in performance and cost reduction [173].

However, in most modeling approaches, the porosity of the electrode is assumed to be homogeneously distributed. In practice, the porosity of the electrode varies locally due to manufacturing tolerances or clamping pressures. According to Guan et al. [174], this results in low-flow regions or dead zones that lead to concentration overpotential or undesirable side reactions. Prumbohm et al. [175] showed that homogenized models cannot be used to predict the partly inhomogeneous flow distribution observed experimentally within the electrode. Recently, Wan et al. [176] presented a method based on nonsolvent-induced phase separation, allowing for the consistent production of electrodes without macrovoids and featuring clearly defined porosity gradients across the thickness. They observed that the performance remains consistent regardless of the direction of the porosity gradient and is comparable to that of state-of-the-art electrodes documented in the current literature.

As noted previously, the main focus has been on optimizing the flow field, the flow rate, and the electrode configuration [169, 177–179]. The conventional rectangular vertical-format cell design, which is commonly accepted, has seldom been subject to questioning. Gurieff et al. [96] explored novel design concepts for flow-through electrodes, including rectangular, trapezoidal, and radial geometries. These designs aim to improve velocity from the inlet to the outlet, thereby improving mass transport within the cell. Gurieff et al. [180] also investigated the combination of static mixers within wedge-shaped cells to improve performance. They found a design with a 12 % lower pressure drop. Kok et al. [181] investigated the morphology of electrode structures and the cell architecture of a hydrogen-bromine FB with a interdigitated flow-through configuration. They found that the width of the domain is crucial in terms of the reaction rate, meaning that the narrowest rib performed best. Meng et al. [182] introduced the first trapezoidal cell design for FB. They used a stepping optimization method to reduce the concentration polarization at constant porosity. They discovered that the novel structure was efficient in improving mass transport and reducing polarization without an increase in energy consumption.

The physical modeling and optimization calculations in this chapter are implemented in COMSOL Multiphysics software version 6.1 using the *Laminar Flow*, *Transport of Diluted Species*, *Topology Optimization*, and *Optimization* interfaces. The software uses the finite element method (FEM). Topology optimization is performed using the gradient-based SNOPT algorithm [95], while the convergence criterion is set to 1×10^{-6}. The topology optimization time is around five to ten minutes on a simulation computer using an AMD Ryzen 9 3900X 12-core processor with 3.79 GHz and 64 GB RAM. The calculation time for a parameter sweep in shape optimization is around twenty minutes using a convergence criterion of 1×10^{-6} as well. During the geometric adaptations, the domain is re-meshed.

7.2 Topology Optimization of Electrode Porosity

In this section, the findings related to topology optimization of the porosity distribution are discussed. Firstly, the investigated porosity intervals are introduced and a mesh independence study is presented. A sanity check of combined and separate optimization regarding the multiobjective functional is conducted, followed by investigations about the impact of different initial values, flow rates, and designs. In addition, a performance comparison between electrodes with a uniform porosity and the obtained two-part porosity distribution is conducted. Finally, a sensitivity study quantifying the influence of model parameters on the porosity distribution and on cell performance is presented.

7.2.1 Porosity Intervals

In general, porosity values range between zero and one, where zero represents a solid material with no void spaces, and one denotes a complete void space. This study explores the optimization characteristics employing three different porosity intervals for the electrode. In order to cover a broad spectrum of potential values, the first selected range extends from 0.05 to 0.95. Expanding the interval further is computationally unfeasible. In the context of flow batteries, electrode porosity values typically tend to fall within the upper third. Consequently, this study takes into consideration the intervals of 0.7 to 0.95 and 0.6 to 0.8. Figure 7.1 shows the optimization results of the three intervals for flow rates of $10\,\mathrm{mL\,min^{-1}}$ (top row) and $25\,\mathrm{mL\,min^{-1}}$ (bottom row). For the largest interval, porosity varies in an unstructured manner. Given the interval's magnitude, optimization has to cope with an extensive design space, posing challenges in identifying an optimal minimum. As the flow rate increases, the flow

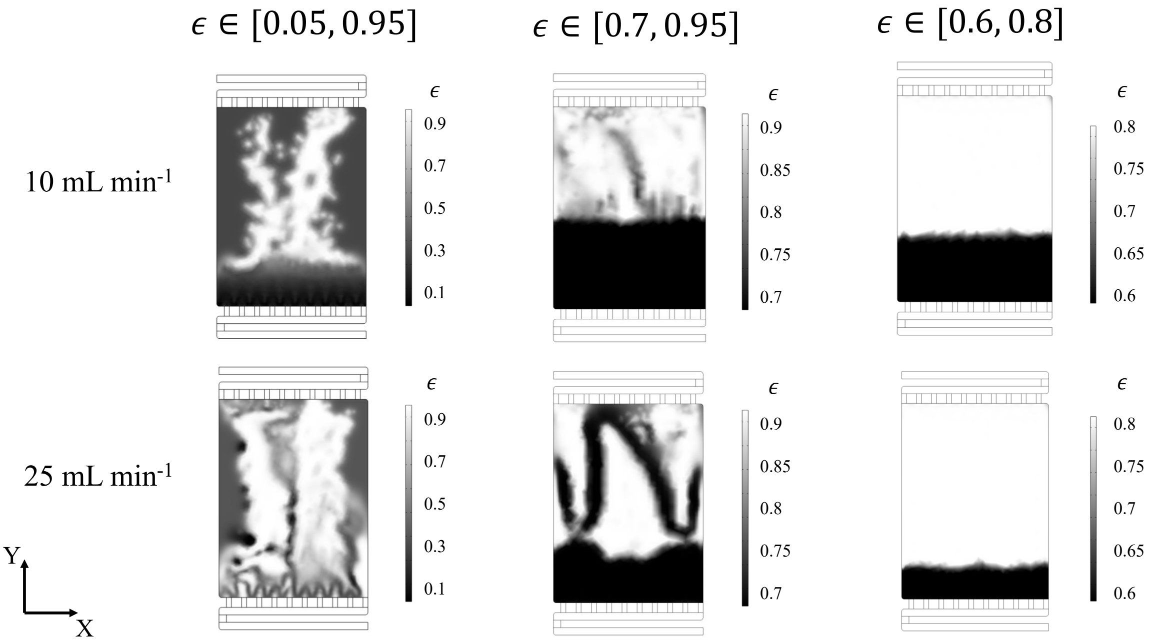

Figure 7.1: Results of topology optimization using different porosity intervals and flow rates. The top row corresponds to a flow rate of $10\,\mathrm{mL\,min^{-1}}$ and the bottom row to $25\,\mathrm{mL\,min^{-1}}$.

resistance becomes more important. Consequently, porosity values are higher at elevated flow rates to minimize energy dissipation, indicated by a lighter shade of gray. In contrast, the constrained intervals exhibit a clearer porosity distribution. Although the 0.7 to 0.95 interval still exhibits irregularities at its upper end, a lower porosity downstream of the inlet manifold is obtained consistently for all illustrated cases. This finding is in line with the experimental results of Yoon et al. [183], where a similar design resulted in improved energy efficiency. Furthermore, it can be observed that the area of reduced porosity downstream of the inlet decreases with higher flow rates to mitigate energy losses resulting from flow resistance.

7.2.2 Mesh Independence

The half-cell geometry is discretized into numerous mesh elements. In order to ensure that the simulation results are independent of the number of elements used, a mesh independence test is conducted. The study maintains consistent simulation conditions for all cases, with the only variation being the number of mesh elements employed. Figure 7.2 presents the pressure drop between inlet and outlet (Δp), the integrated reaction rate (R_c), and the mean porosity versus the number of electrode mesh elements. With respect to the results for the pressure drop and reaction rate, no topology optimization is conducted, and for the mean porosity, the three distinct porosity intervals are chosen. Since porosity is defined within the electrode only, both diagrams indicate the number of elements in the electrode. The mesh independence study encompasses seven different meshes, each with an increasing number of elements, to thoroughly evaluate the impact of mesh refinement on the results.

As observed, there is a significant variation in the results obtained from simulations using the first three meshes. To ensure independent results, a mesh containing at least 8,314 elements is required. The relative error between the mesh with 8,314 elements and that with 18,530 elements is consistently below 1% for all parameters, except for the porosity interval $\epsilon \in [0.05, 0.95]$, where the error reaches 4%. Given this observation and the considerably higher computational costs associated with finer meshes, the grid comprising 8,314 electrode elements is selected. This choice results in a total of 17,198 mesh elements for the whole geometry.

7.2.3 Sanity Check: Single and Multiobjective Cost Functional

To investigate the effect of optimization using a combined and separate cost functional, identical optimization calculations are carried out for reaction rate and pressure drop individually and in combination. This is done for different flow rates and the previously described porosity intervals.

Figure 7.3 illustrates the mean porosity resulting from individual and combined optimization at various flow rates for different intervals. The results indicate that during individual optimization, porosity tends to approach either the minimum or maximum value within the defined interval. This behavior stems from the pursuit of the lowest pressure drop, which is achieved by maximizing porosity to reduce flow resistance. In contrast, when optimization is performed solely for the reaction rate, the minimum porosity value is favored because of the increased active surface area, which enhances the reaction. The linear inverse relationship observed between the quantities is governed by Equations 2.37 and 2.38, and remains largely consistent between different flow rates, except for comparatively small rates. This may be due to a sufficient residence time at small flow rates.

In contrast, the combined optimization yields a rise in mean porosities as the flow rate increases, ultimately trending towards the upper limit of the interval at the highest flow rates. This trend is primarily driven by the increased importance of minimizing pressure loss as the flow rate increases. It is important to note that the two components of the cost functional are equally weighted in this context. When comparing the three different porosity intervals, it becomes apparent that the individual values exhibit a greater range within larger intervals. This phenomenon can be attributed to the increased design freedom resulting from the broader porosity range.

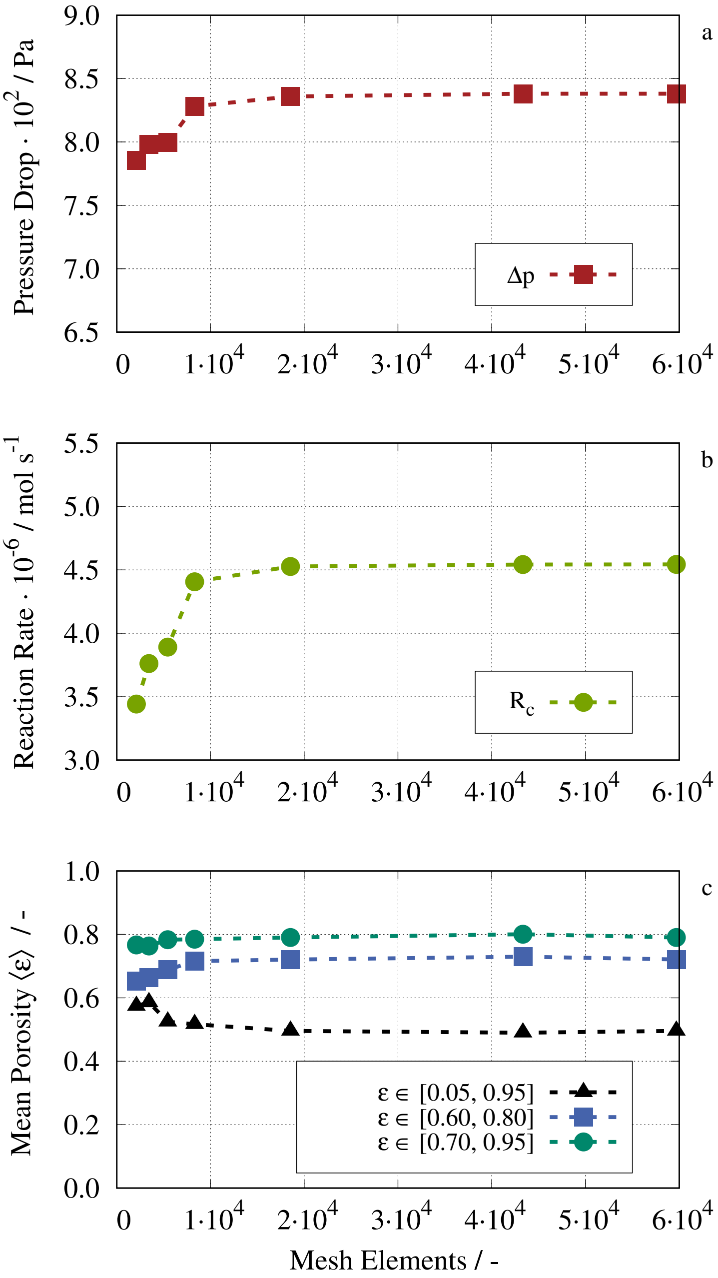

Figure 7.2: Mesh independence of pressure drop between inlet and outlet (a), integrated reaction rate R_c (b), and mean porosity of the electrode (c) versus the number of mesh elements.

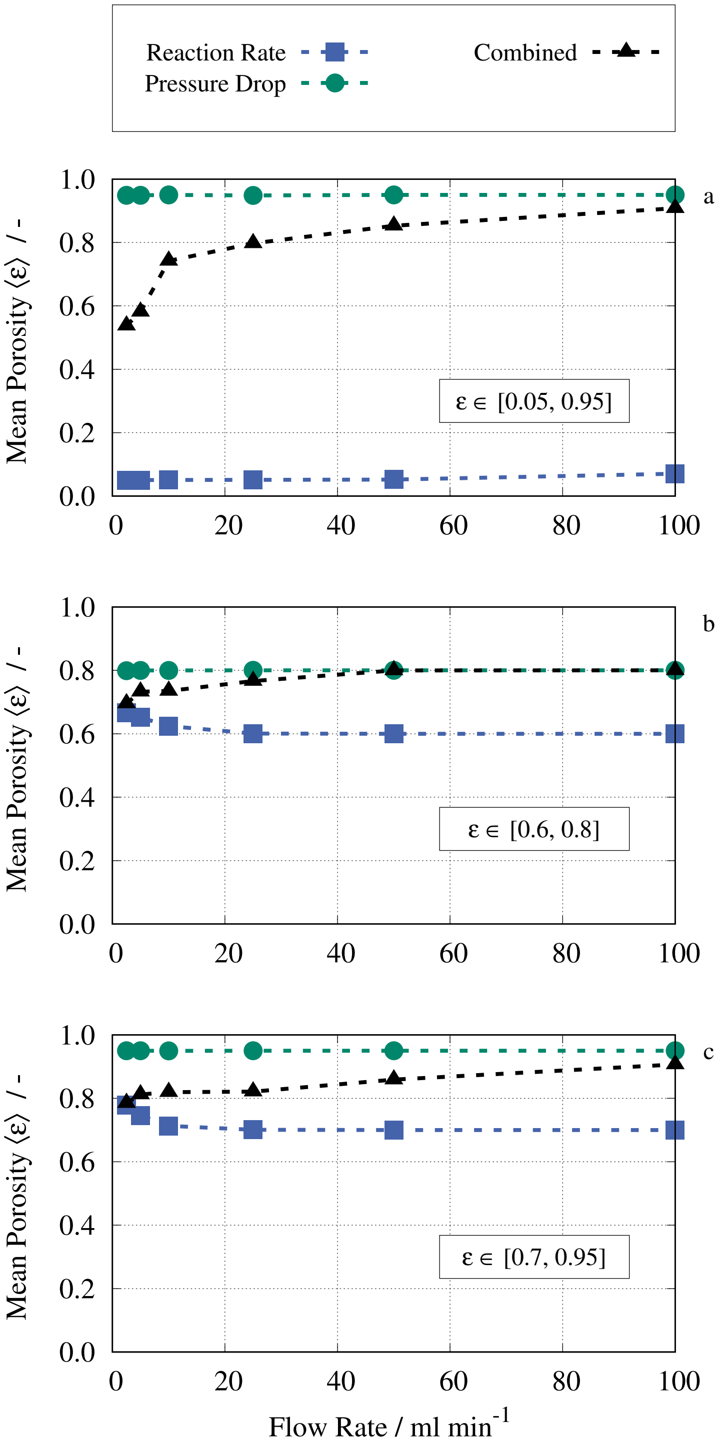

Figure 7.3: Mean porosity resulting from topology optimization versus flow rate. Comparison of topology optimizations for pressure drop and reaction rate and combined multiobjective optimization. The sub-figures show different porosity intervals: a) $\epsilon \in [0.05, 0.95]$, b) $\epsilon \in [0.6, 0.8]$, c) $\epsilon \in [0.7, 0.95]$.

7.2.4 Influence of the Initial Value

The selection of the initial value in topology optimization using gradient-based solvers is a critical consideration, as it can significantly influence the outcome of the optimization process. Gradient-based optimization algorithms aim to minimize the cost functional but can end up in different local minima depending on the chosen starting position. A well-chosen initial value improves the likelihood of finding a global minimum or a better local minimum. Furthermore, the selection of the initial porosity distribution at the outset of the optimization has an impact on the convergence behavior, which, in turn, affects the final result.

To investigate the influence of the initial value of the penalized material volume factor on porosity distribution, Figure 7.4 shows six graphs that illustrate the horizontal mean porosity ϵ_h as a function of the normalized electrode height. These graphs represent three porosity intervals: $\epsilon \in [0.05, 0.95]$ (top), $\epsilon \in [0.6, 0.8]$ (middle), $\epsilon \in [0.7, 0.95]$ (bottom), along with two flow rates $2.5\,\mathrm{mL\,min^{-1}}$ (left) and $25\,\mathrm{mL\,min^{-1}}$ (right). In this instance, porosity is displayed as an average for horizontal slices and subsequently graphed relative to electrode height. In each graph, every curve represents a porosity distribution calculated with a variable initial value (θ_0) ranging from zero to one. The initial value of the starting porosity can be determined using θ_0 and Equation 2.37.

The solutions exhibit varied characteristics depending on the initial values, with more diverse outcomes observed for larger porosity ranges. However, a clear correlation between porosity fluctuations and the choice of the initial value is not evident.

In the case of the largest interval $\epsilon \in [0.05, 0.95]$ (top), the solutions exhibit substantial variability, making it challenging to make unequivocal statements about trends. In principle, higher porosity values are generally preferred, and these tend to increase with higher flow rates, which is attributed to the increasing influence of the pressure drop.

In contrast, the smallest interval $\epsilon \in [0.6, 0.8]$ (middle) yields the smallest deviations in the porosity distribution. For $25\,\mathrm{mL\,min^{-1}}$, the curves of different initial values closely overlap, while at $2.5\,\mathrm{mL\,min^{-1}}$, discrepancies become more pronounced, especially in the upper third of the electrode. Here, the influence of the initial value is marginal.

Within the interval $\epsilon \in [0.7, 0.95]$ (bottom), characterizing the various solutions proves to be challenging. The previously described pattern of low porosity in the lower region and high porosity in the upper region of the electrode is partly true only. For initial values of 0 and 0.25, high porosity is observed in the lower region, while the trend in the porosity distribution remains discernible for the remaining initial values.

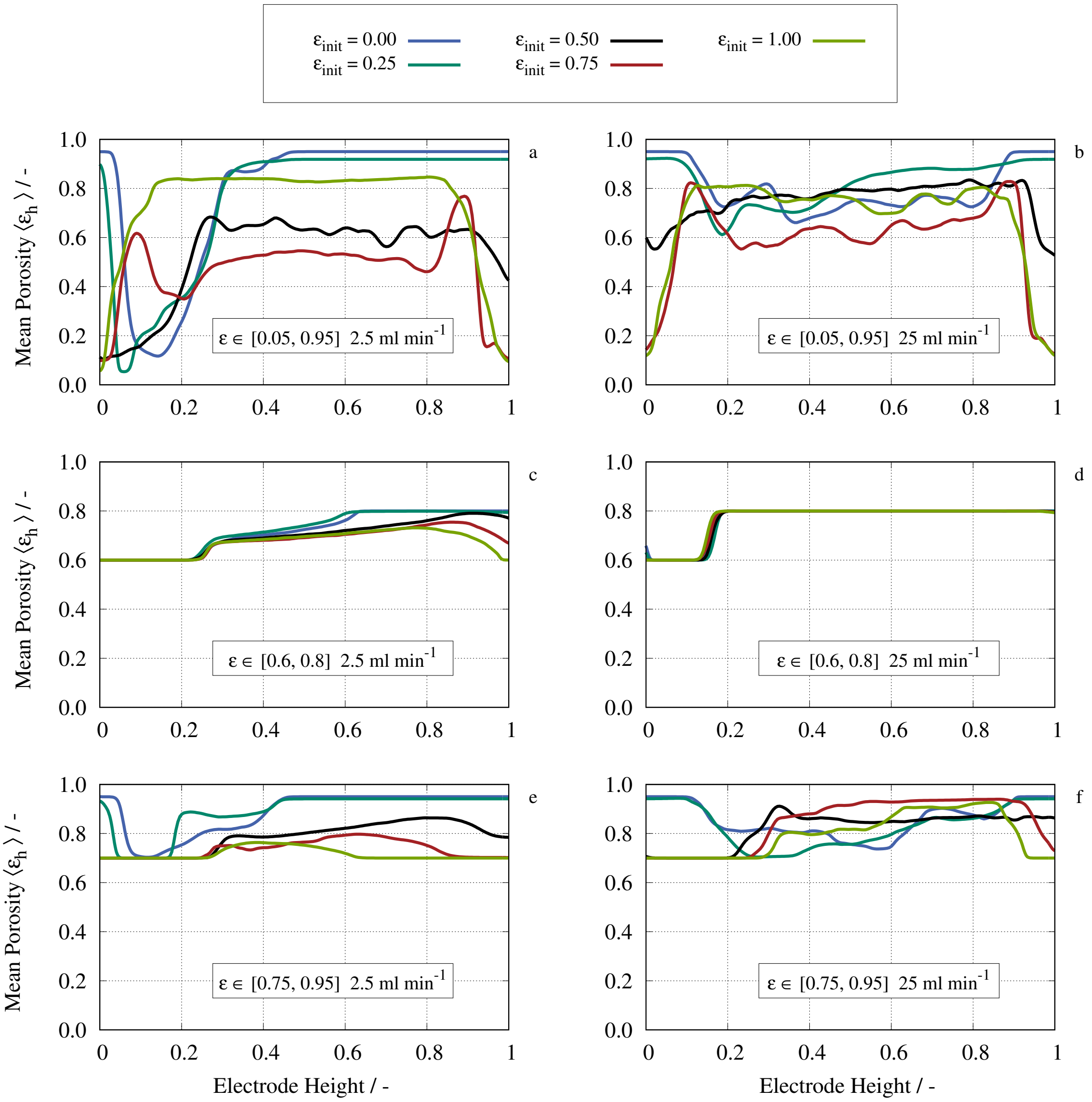

Figure 7.4: Influence of different initial values θ_0 of the optimization penalization factor on porosity distribution. Different porosity intervals $\epsilon \in [0.05, 0.95]$ (top), $\epsilon \in [0.6, 0.8]$ (middle), $\epsilon \in [0.7, 0.95]$ (bottom) and flow rates $2.5\,\mathrm{mL\,min^{-1}}$ (left) and $25\,\mathrm{mL\,min^{-1}}$ (right) are depicted. The graphs show horizontal mean porosity ϵ_h as a function of the normalized electrode height.

In conclusion, it is evident that the initial value and optimization constraints significantly impact the solution. A parameter space has been identified where the solution is largely independent of the initial value.

7.2.5 Flow Rate Comparison

Figure 7.5 illustrates the horizontal mean porosity ϵ_h along the electrode height for different flow rates and the three porosity intervals. Table 7.1 shows the flow rates investigated and their corresponding mean velocities within the electrode. In this comparison, the distribution of the actual porosity value along the flow direction is analyzed in more detail.

Table 7.1: Flow rates and corresponding flow velocities within the electrode.

Flow rate	Flow speed
$2.5\,\mathrm{mL\,min^{-1}}$	$1.76 \times 10^{-4}\,\mathrm{m\,s^{-1}}$
$5.0\,\mathrm{mL\,min^{-1}}$	$3.60 \times 10^{-4}\,\mathrm{m\,s^{-1}}$
$10\,\mathrm{mL\,min^{-1}}$	$6.89 \times 10^{-4}\,\mathrm{m\,s^{-1}}$
$25\,\mathrm{mL\,min^{-1}}$	$1.72 \times 10^{-3}\,\mathrm{m\,s^{-1}}$
$50\,\mathrm{mL\,min^{-1}}$	$3.50 \times 10^{-3}\,\mathrm{m\,s^{-1}}$
$100\,\mathrm{mL\,min^{-1}}$	$7.05 \times 10^{-3}\,\mathrm{m\,s^{-1}}$

In fact, as previously observed, lower flow rates tend to correspond to lower porosity levels in general. In the case of the highest flow rate investigated ($100\,\mathrm{mL\,min^{-1}}$), the porosity tends to approach or reach the maximum value within the specified interval.

The porosity distribution at lower flow rates generally exhibits a consistent pattern: Toward the lower section of the electrode, close to the inlet, a preference for low porosity and subsequent larger active surface area is observed. With an increase in electrode height, the porosity typically experiences a sudden and pronounced increase. In the further course, it then either tends to the maximum value of the interval or remains in the range of high values.

Under certain conditions, a porosity distribution with lower values downstream of the inlet and higher values in front of the outlet may be beneficial. Experimental studies have also shown that an increase in porosity within the electrode downstream can result in enhanced energy efficiency [183, 184]. This design offers a larger active area in the region of a high reactant concentration and enhances the mass transport of the product.

When comparing the different intervals, it becomes evident that porosity exhibits more pronounced fluctuations with larger interval sizes. The increased design freedom associated with longer intervals can explain these fluctuations. When optimization is subject to tighter

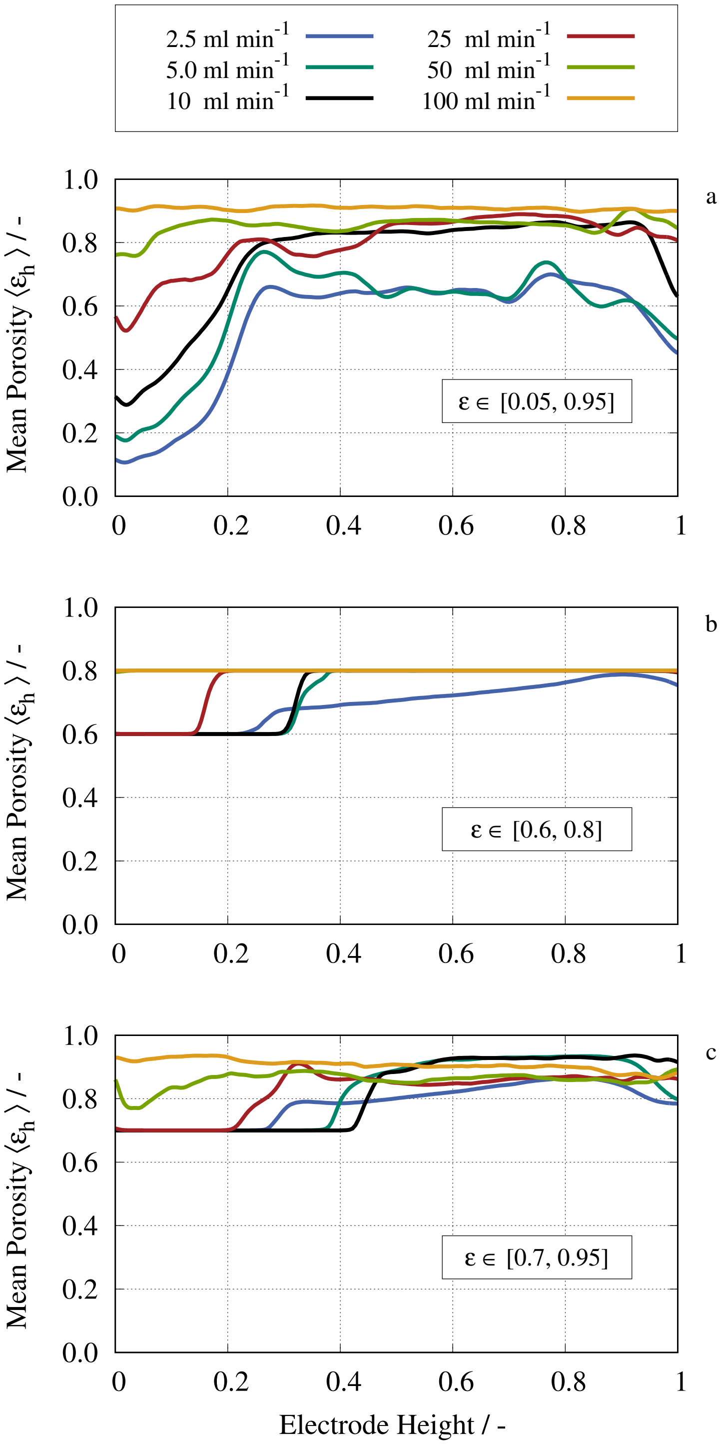

Figure 7.5: Horizontal mean porosity ϵ_h resulting from topology optimization versus the normalized electrode height. Comparison of different flow rates for the multiobjective functional optimization. The sub-figures show different porosity intervals: a) $\epsilon \in [0.05, 0.95]$, b) $\epsilon \in [0.6, 0.8]$, c) $\epsilon \in [0.7, 0.95]$.

constraints, as observed in the case of $\epsilon \in [0.6, 0.8]$, the transition between low and high porosity becomes more distinct and evident. This is promising because such a distribution is more likely to be feasible in real-world applications.

7.2.6 Performance Comparison of Homogeneous and Two-Part Electrodes

In this section, homogeneous electrodes, each possessing uniform maximum and minimum porosity values within their respective intervals, are compared with an optimized two-part design. From a practical perspective, implementation of the two-part electrode design is most feasible. It consists of denser material with lower porosity in the lower 20% of the electrode height (cf. Figure 7.1 bottom right). The porosities are homogeneous and the flow rate is $25\,\mathrm{mL\,min^{-1}}$. The performance comparison is based on the pressure drop (Δp), the integrated reaction rate (R_c) and rate of conversion (RoC). The RoC is a physical measure to describe the conversion efficiency of active material within the electrode and is defined as

$$RoC = \frac{c_{outlet}}{c_{max}} \tag{7.1}$$

where c_{outlet} is the average concentration at the outlet of the domain. Figure 7.6 shows the performance comparison using the values of intervals $\epsilon \in [0.6, 0.8]$ (top) and $\epsilon \in [0.7, 0.95]$ (bottom). The results of the electrode with the minimum porosity are shown in green and set to 100% for a better comparison of the different physical quantities. The electrodes of maximum porosity and made of two parts are shown in blue and red, respectively.

In terms of pressure drop and reaction rate, the expected outcomes of both diagrams agree with our findings. With regard to pressure drop, both the higher porosity and the two-part electrode configurations demonstrate a decrease by reduced flow resistance. It is noted that this enhancement is more pronounced with higher porosity values. However, the reaction rate shows a decrease with higher porosity for the two-part electrode configuration as a result of the reduced active surface area.

With regard to the RoC, our analysis reveals intriguing findings. For porosity values of 0.6 and 0.8, RoC remains nearly constant for all three electrodes. The actual RoC of $\epsilon = 0.6$ reaches 99%, indicating the nearly complete conversion of the active material. Consequently, favoring the highest porous electrode ($\epsilon = 0.8$) would be ideal due to the energy saved when the pressure drop is reduced.

In contrast, for porosity values of 0.7 and 0.95, the actual RoC at $\epsilon = 0.7$ also reaches 99%. However, both studied electrodes exhibit a lower RoC in comparison. As a result, it can be deduced that in this scenario, the two-part electrode configuration is preferable. Despite

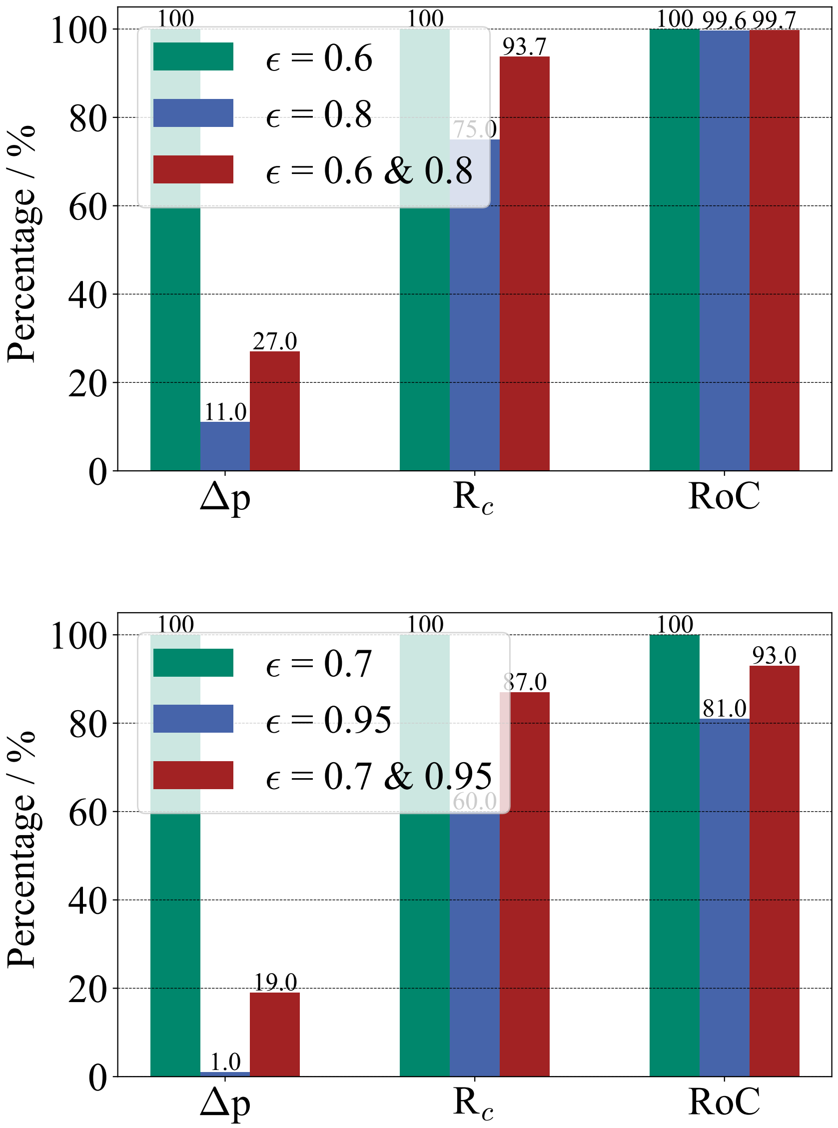

Figure 7.6: Performance comparison of electrodes with homogeneous single porosity and two-part porosity in terms of pressure drop (Δp), reaction rate (R_c), and rate of conversion (RoC). The two-part electrode configuration has the lower porosity value within the initial 20% of the electrode height downstream of the inlet manifold. The electrode porosities are 0.6 & 0.8 (top) and 0.7 & 0.95 (bottom).

the acceptable reduction in RoC of around seven percent, it reduces pressure loss by 81% compared to $\epsilon = 0.7$, making it a more advantageous choice.

This comparison underscores that an optimized design may not necessarily align with practical applicability. Moreover, the outcome of optimization is largely dependent on specific electrode parameters, such as porosity or active surface area, along with operational factors such as flow rate.

7.2.7 Topology Optimization Using Novel Cell Designs

In order to investigate the behavior of topology optimization in different cell geometries, three additional designs according to Gurieff et al. [96] are examined. Figure 7.7 shows the designs of *horizontal*, *trapezoidal* and *radial* shape. The porosity interval is $\epsilon \in [0.7, 0.95]$ and the flow rate is $2.5\,\mathrm{mL\,min^{-1}}$ in this example. The different designs show optimization results similar to those of the previously described *vertical* cell. In a horizontal design, the cell exhibits a wider width than height, while in a vertical design, the cell displays a greater height than width.

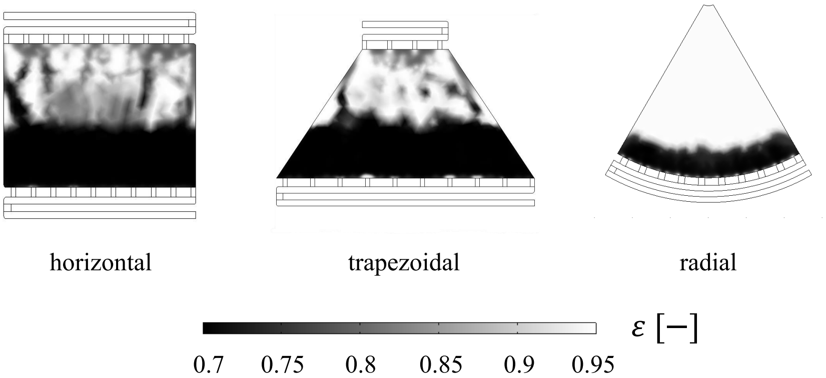

Figure 7.7: Different flow battery cell designs according to studies from Gurieff et al. [96]. Within the electrodes, the porosity distribution is shown for $\epsilon \in [0.7, 0.95]$ and $2.5\,\mathrm{mL\,min^{-1}}$.

Figure 7.8 highlights the horizontal mean porosity over the electrode height for the different designs and intervals. The default design *rec vert* of previous investigations is included for comparison. The flow rate is $10\,\mathrm{mL\,min^{-1}}$. We observe low porosity values downstream of the inlet, with values gradually ascending towards higher levels as we approach the outlet. Within the broadest porosity interval, $\epsilon \in [0.05, 0.95]$, porosity shows a moderate overall increase despite fluctuations and decreases near the outlet. These variations may be attributed to the greater design freedom resulting from the broader interval. In contrast, when narrower porosity intervals are considered, porosity initially remains at its minimum value and then experiences a rapid and pronounced increase to the maximum. This transition is more pronounced within the smallest interval and occurs at lower heights.

Comparison of various design configurations reveals that the transition occurs earliest in the radial design. This can be attributed to the increased flow velocity near the outlet, resulting from the narrowed cross-section. With respect to the different flow rates, the behavior is in agreement with that described in Section 7.2.5, where porosity tends to approach the maximum value as the flow rate increases.

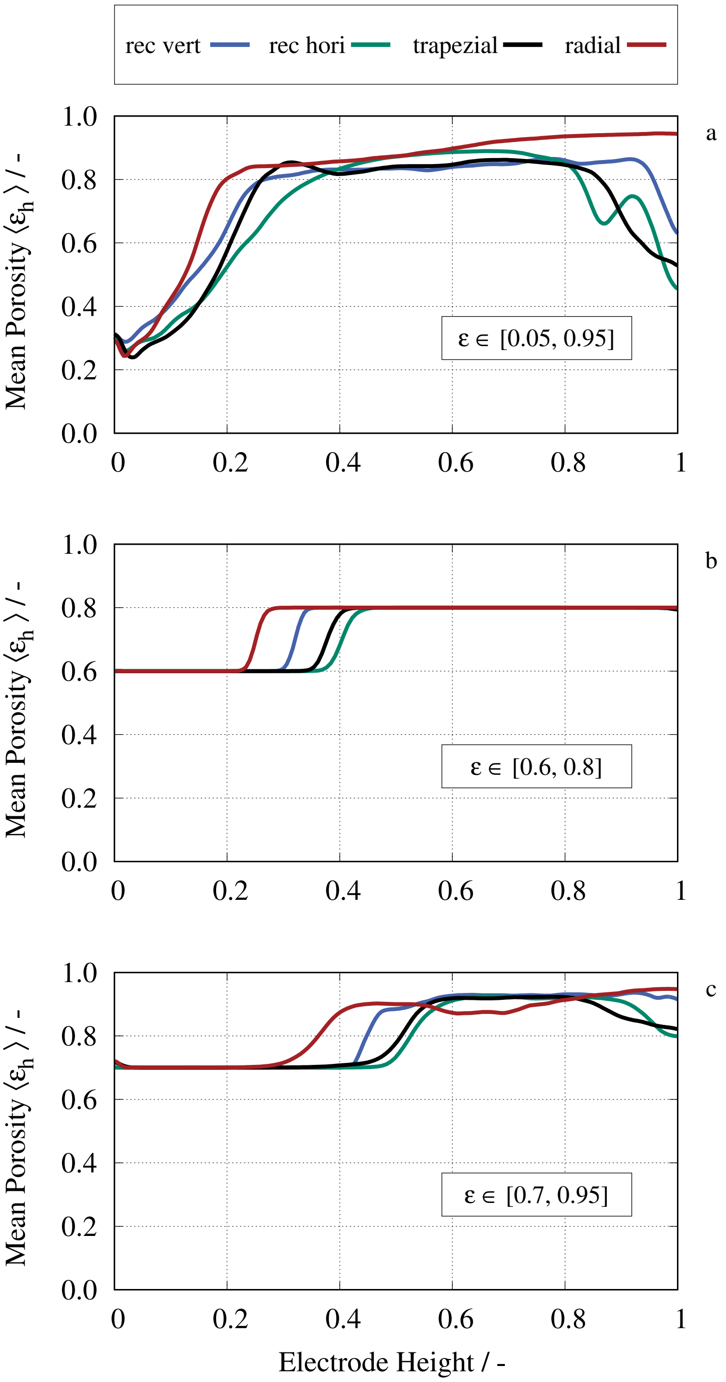

Figure 7.8: Comparison of different cell designs, with horizontal mean porosity ϵ_h plotted versus normalized electrode height. The sub-figures show the different porosity intervals: a) $\epsilon \in [0.05, 0.95]$, b) $\epsilon \in [0.6, 0.8]$, c) $\epsilon \in [0.7, 0.95]$. The flow rate is $10\,\mathrm{mL\,min^{-1}}$.

7.2.8 Sensitivity Analysis

To investigate the influence of the respective model parameters on performance and topology optimization, a sensitivity analysis is performed. For this purpose, the elementary effect method is employed [185]. This method is a local sensitivity measurement, often referred to as the one at a time (OAT) measurement. It evaluates partial derivatives to determine how variations of one factor of the input parameters $(X_1, X_2, ..., X_k)$ affect the model output $Y(X_1, X_2, ..., X_k)$ while keeping all other factors constant at a nominal value. The elementary effect $d_i^{(j)}(\mathbf{X})$ is defined as

$$d_i^{(j)}(\mathbf{X}) = \frac{\mathbf{Y}(X_1, ..., X_{i-1}, X_i + \Delta, X_{i+1}, ..., X_k) - \mathbf{Y}(X_n)}{\Delta} \tag{7.2}$$

where the first part in the numerator represents the model output moved OAT of a step Δ in the inputs' domain and $\mathbf{Y}(X_n)$ is the output at nominal values of all parameters. The number of steps is j. To characterize the sensitivity of the input parameters, the average μ_i and standard deviations σ_i of the respective elementary effects are determined according to

$$\mu_i = \frac{1}{r}\sum_{j=1}^{r} d_i^{(j)}(\mathbf{X}), \quad \sigma_i = \sqrt{\frac{1}{r}\sum_{j=1}^{r}\left(d_i^{(j)}(\mathbf{X}) - \mu_i\right)^2}. \tag{7.3}$$

In the so-called Morris plane, the standard deviation is plotted against the average value. High values of the average indicate high influential parameters, and high values of the standard deviation indicate nonlinear and/or interacting parameters. In order to characterize the input parameters influence on the optimization result, the coefficient of variation (CoV) is defined as the ratio of the standard deviation and the average of the optimized porosity distribution within the electrode:

$$CoV = \frac{\sigma(\epsilon_{opt})}{\mu(\epsilon_{opt})}. \tag{7.4}$$

It is a measure to characterize the variation in porosity relative to the mean. Physical input parameters are documented in Table 7.2 with their nominal values and reasonable ranges. The nominal value is placed at the midpoint of the interval. Each parameter range is subdivided into seven values, including the nominal and extreme values. These divisions are linear for all parameters except for diffusivity, for which an exponential division is employed. The simulations adhere to the OAT methodology, with one parameter altered at a time, while the others remain constant at their nominal values. This procedure yields a total of 189 simulations covering nine physical parameters, each tested with seven values at three porosity intervals. Consequently, 18 elementary effects can be derived for each parameter.

The results of the sensitivity analysis are shown in Figure 7.9 showing the standard deviation versus the average value of the elementary effects for both CoV (top) and RoC (bottom).

Table 7.2: Nominal input parameters and ranges of variation for sensitivity analysis.

Parameter	Symbol	Unit	Nominal	Range	Reference
Flow rate	$\dot{V}$	$\mathrm{mL\,min^{-1}}$	51.25	$[2.5, 100]$	[186]
Viscosity	μ	$\mathrm{Pa\,s}$	5.5×10^{-3}	$[0.001, 0.001]$	[169]
Density	ρ	$\mathrm{kg\,m^{-3}}$	1075	$[950, 1200]$	[85]
Diffusivity	D_c	$\mathrm{m^2\,s^{-1}}$	5×10^{-10}	$\left[10^{-11}, 10^{-8}\right]$	^{a}
Mass transfer parameter	α	–	1.05	$[0.1, 2.0]$	^{a}
Mass transfer parameter	β	–	5.5×10^{-4}	$\left[10^{-4}, 10^{-3}\right]$	^{a}
Temperature	T	K	325.5	$[298, 353]$	^{a}
Specific area	A_V	$\mathrm{m^{-1}}$	2.55×10^5	$\left[10^4, 5 \times 10^5\right]$	[168]
Maximum concentration	c_{max}	$\mathrm{mol\,m^{-3}}$	1550	$[100, 3000]$	[187]

^{a} Estimation

For the CoV, the order of influence is as follow: $T < \rho < D < A_V < \beta < c_{max} < \mu < \dot{V} \ll \alpha$. Temperature, density, and diffusivity are found at the lower end, indicating their limited impact on the optimization process. In general, the temperature and density range is quite narrow in flow batteries as a result of the essential presence of liquid water. The diffusivity in the porous media has hardly any influence on the pressure drop and reaction rate. Parameters associated with the reaction rate exert somewhat greater influence, followed by viscosity and flow rate. The latter factors are directly related to the pressure drop and play a crucial role in the optimization process. It is interesting to see that the reaction parameter α has the highest influence. Although optimization is dominated by the minimization of pressure loss, especially at high flow rates, the reaction term still has a decisive influence.

The order of the parameters that influence the RoC is as follows: $T \ll \rho < c_{max} < \mu, D \ll \dot{V} < A_V, \beta < \alpha$. In this modeling approach, temperature does not exert any influence on the reaction. For this reason, it is not represented on the Morris plane. Similarly to the CoV results, density and diffusivity have a low impact on RoC. Compared with the other reaction rate parameters, the maximum concentration only slightly influences the RoC. The flow rate has a higher influence because of its impact on the residence time of the active material. In summary, the study provides a qualitative statement with respect to the influence of the model parameters only. However, it allows for a good assessment of the importance of individual parameters. This should be taken into account when designing cells and electrodes.

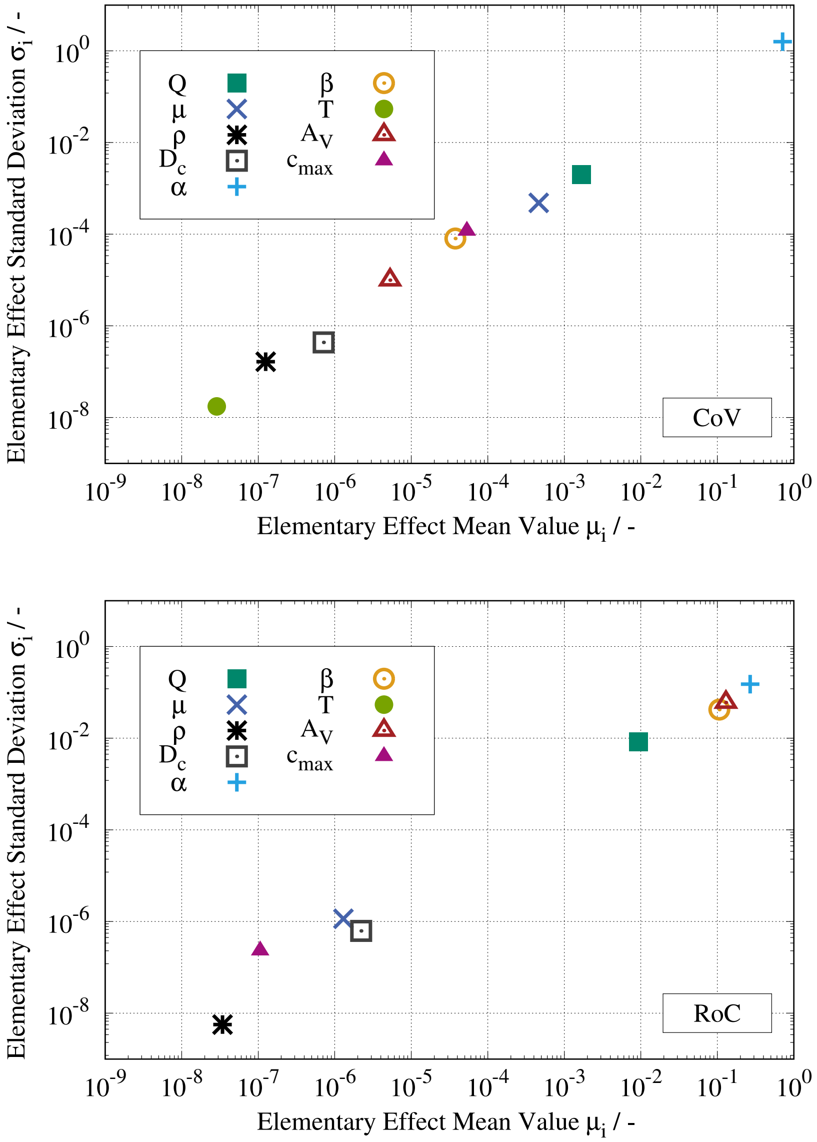

Figure 7.9: Representation of the sensitivity analysis in the Morris plane showing the standard deviation (σ_i) over the mean value (μ_i) of the respective elementary effects. High values on the x-axis indicate high influential parameters, while high values on the y-axis indicate non-linear and/or interacting parameters. (top) The Morris plane of the elementary effects on the CoV. (bottom) The Morris plane of the elementary effects on the RoC.

7.3 Shape Optimization of Cell Designs

This section centers on the optimization of geometric parameters for cell design introduced in Section 7.2.7. In particular, optimization covers the cell's height, the ratio of its height to width, and the ratio between the top and bottom widths of the cell. Moreover, the angle is adjusted in the radial design. Throughout this investigation, the porosity of the electrode remained the same. The cost functional is the same as in topology optimization. In the study, flow rates between $5\,\mathrm{mL\,min^{-1}}$ and $100\,\mathrm{mL\,min^{-1}}$ are investigated in a porosity range of 0.6 to 0.95 due to practical feasibility.

7.3.1 Rectangular Cell Design

For the optimization of the default rectangular cell design, Table 7.3 presents details regarding the initial value and the optimization limits. For height optimization, the initial height and width are set to 80 mm and 60 mm, respectively. Throughout the optimization process, the control variable ψ is adjusted within the specified limits until the cost functional reaches its minimum, while keeping the width of the cell constant. In case of optimizing the height-to-width ratio, the initial values of height and width are the same, while the width of the cell is varied simultaneously within the given limits using a second control variable λ. The height is optimized between 4 mm and 200 mm and the width between 30 mm and 120 mm.

Table 7.3: Optimization of the initial rectangular cell design.

Optimization	Height	Height-to-Width Ratio
Height	$\psi \cdot 80\,\mathrm{mm}$	$\psi \cdot 80\,\mathrm{mm}$
Width	$60\,\mathrm{mm}$	$\lambda \cdot 60\,\mathrm{mm}$
Bounds height	$0.05 < \psi < 2.5$	$0.05 < \psi < 2.5$
Bounds width	-	$0.5 < \lambda < 2.0$

Figure 7.10 shows the results of the shape optimization with respect to electrode height (top) and electrode height-width ratio (bottom) as a function of porosity for different flow rates. For height optimization, it can be stated that the lower the porosity, the more optimal it is to have a shorter cell. A reduced cell height leads to a lower pressure drop, and in the case of low porosity, it ensures a sufficiently long residence time for the effective conversion of active material. As porosity increases, the optimal height also increases, reflecting the reduced impact of the pressure drop and the need for more space to achieve complete conversion. This behavior is consistent for all flow rates. However, at higher flow rates, the increase in optimal height is more pronounced. This steep increase is attributed to the exponential

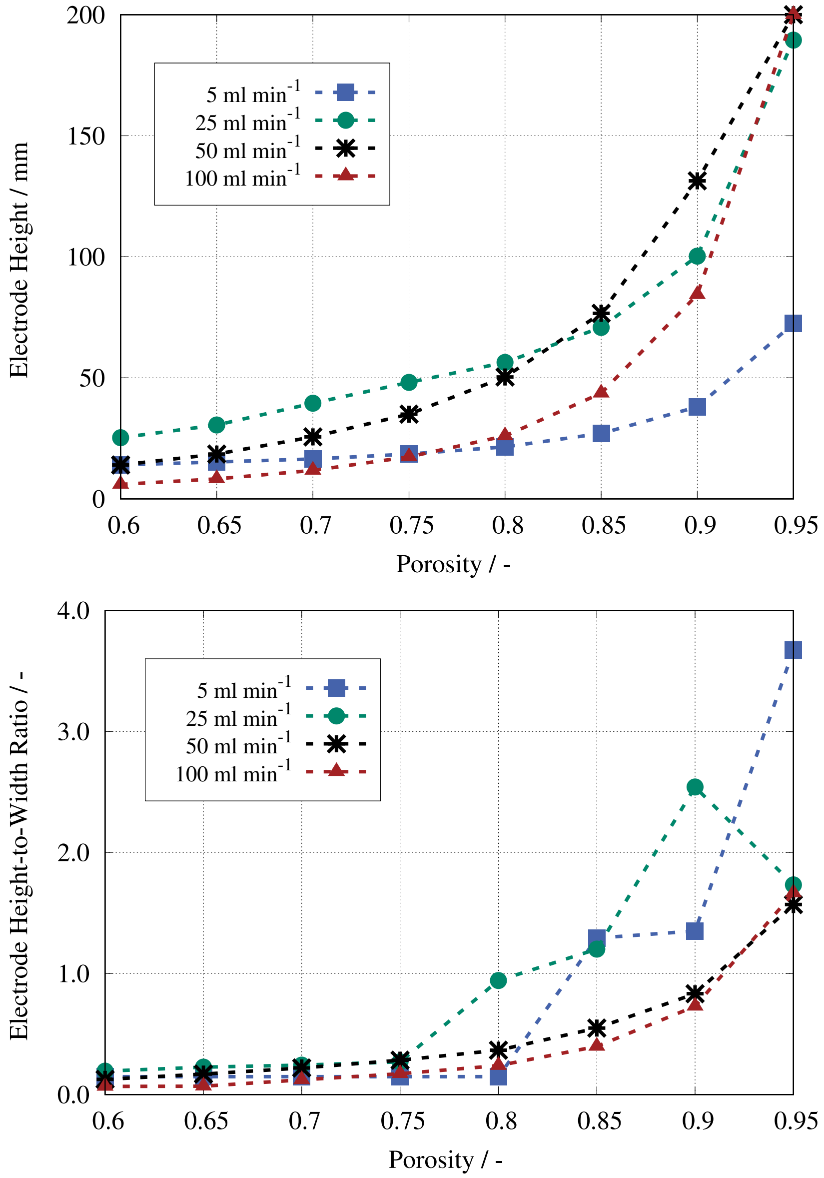

Figure 7.10: Results of shape optimization of the default rectangular cell design. The diagrams show optimized height (top) and optimized height-to-width ratio (bottom) versus porosity for different flow rates.

relationship between pressure drop and porosity. Additionally, it is crucial to note that the maximum is attained for the two highest flow rates.

When optimizing both height and width concurrently, a similar pattern is resulting. Within the porosity range of 0.6 to 0.8, the height-to-width ratio remains below one, suggesting a preference for a broader design. In this range, the emphasis is on minimizing pressure loss. As porosity continues to increase, the height-to-width ratio also increases. At the two highest flow rates, the increase is exponential because the maximum width is reached at every optimization. Therefore, the only option is to increase the height to enhance the reaction rate. Fluctuations observed at lower flow rates are caused by the fact that neither the height nor the width approaches the defined bounds. This indicates that the intuitive vertical format commonly used in many cells may not be the optimal shape and needs to be reconsidered.

7.3.2 Trapezoidal and Radial Cell Designs

In Table 7.4, the optimization parameters for both trapezoidal and radial designs are presented. For the trapezoidal design, the bottom width is fixed at 120 mm, while the top width is adjusted within the range of 40 mm to 120 mm. In the case of the radial design, the initial angle of 60° between the two sides is varied within the range of 30° to 90°. The graphs in Figure 7.11 show the shape optimization results of the top-to-bottom-width ratio of the trapezoidal design (top) and the angle of the radial design (bottom) versus porosity for different flow rates. Optimization calculations for the trapezoidal design were carried out successfully for the cases of 50 $\mathrm{mL\,min^{-1}}$ and 100 $\mathrm{mL\,min^{-1}}$ only, which is due to numerical limitations. The consistent top-to-bottom width ratio of one over all porosities suggests a preference for a rectangular design. This preference is driven by the objective to minimize pressure loss, as the tapering profile of the trapezoid leads to increased flow velocities.

Table 7.4: Optimization of the trapezoidal and radial cell design.

Optimization	Trapezoidal	Radial
Top width	$\psi \cdot 40\,\mathrm{mm}$	-
Bottom width	120 mm	-
Angle	-	$\psi \cdot 60°$
Bounds	$1.0 < \psi < 3.0$	$0.5 < \psi < 1.5$

The optimal angle of the radial design tends to the maximum of 90° for all flow rates regardless of porosity. This design offers a larger surface area for the conversion of active species, and pressure drop is reduced as the cross-section increases. An exception is found in the curve for 5 $\mathrm{mL\,min^{-1}}$. In this case, the optimal angle remains at the minimum of 30° and

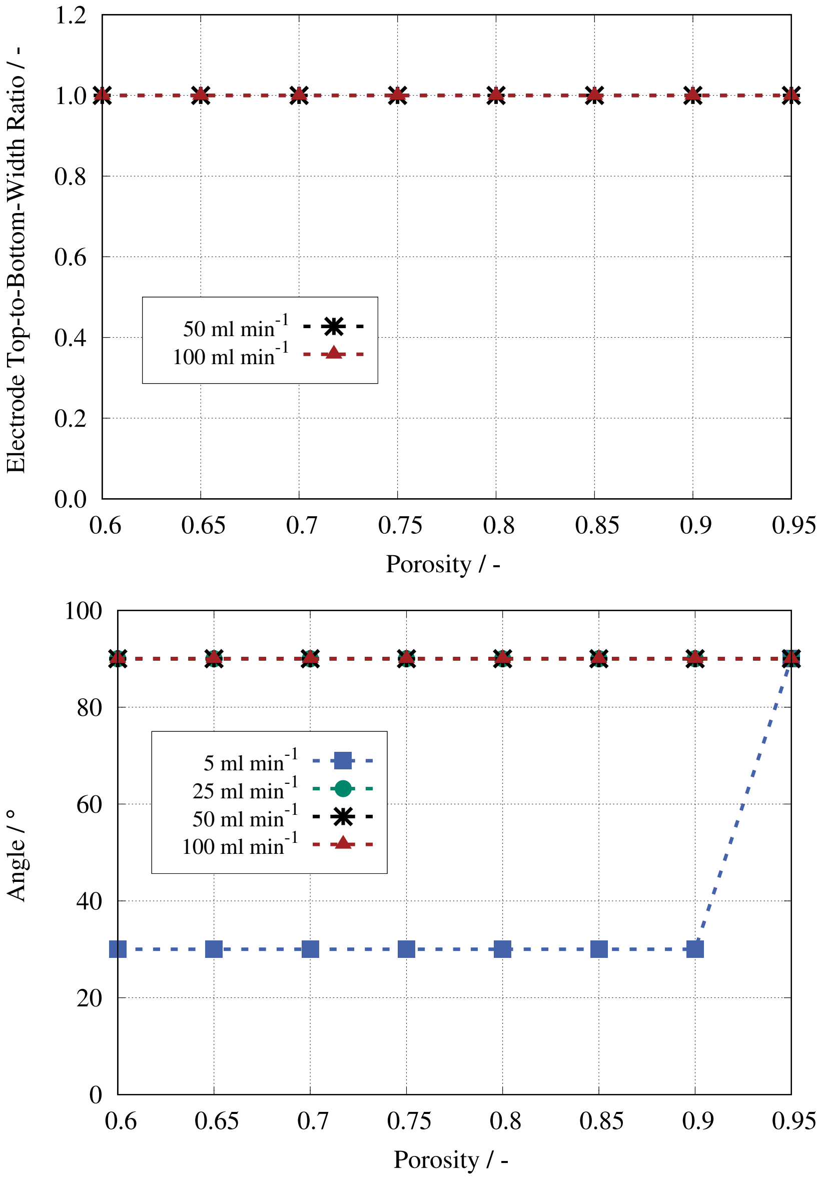

Figure 7.11: Results of shape optimization of the trapezoidal and radial cell designs. The graphs show the optimal top-to-bottom-width ratio (top) and and the optimized angle (bottom) versus porosity for different flow rates.

increases sharply to the maximum at the highest porosity investigated. In this flow regime, the reduction of pressure loss with increasing cross section is not significant. Moreover, the reaction rate is sufficient to convert all species, making an increase in the active area unnecessary.

7.4 Conclusion

This study introduced a comprehensive modeling and optimization framework for a VRFB, which combines topology and shape optimization approaches. The topology optimization method redistributes the porosity within the FB electrode, providing a novel perspective to reevaluating its design properties. Concurrently, shape optimization optimizes the cell geometry parameters for innovative cell designs, with the cost functional aimed at minimizing pressure drop while maximizing the reaction rate.

Gradient-based topology optimization over various porosity ranges and flow rates revealed the expected dependence on initial values and selected porosity intervals. The individual optimization sanity check of the target variables confirmed the expected results, with maximum porosity values for the optimization of the pressure drop and minimum values for the optimization of the reaction rate. Furthermore, optimization demonstrated a preference for a porosity distribution with lower values and a subsequent larger surface area downstream of the inlet when the pressure drop and reaction rate are optimized simultaneously. At this point, it is important to mention that in this work, a linear relationship between porosity and active surface was assumed. Indeed, there are many porous electrode materials with different, non-linear relationships between their porosity and active surface.

As flow rates increased, overall porosity tended to increase to compensate for energy loss as a result of the elevated pressure differential. The transition between high and low porosity was also influenced by the flow rate. Implementing the two-part design yielded acceptable conversion rates with significantly reduced pressure drop, although each individual case must be considered. A sensitivity study highlighted the significant role of viscosity, in addition to the reaction rate parameter α and the flow rate, in the influence of the porosity distribution. In terms of FB performance, flow rate, and all reaction rate parameters, particularly in achieving optimal conversion rates, proved crucial. This work underscores the importance of a comprehensive optimization framework for improving the efficiency and design adaptability of flow batteries.

In addition, further innovative cell designs were explored for their optimization potential. In addition to the original rectangular format, horizontal, trapezoidal, and radial designs were investigated. With respect to topology optimization, the behavior was similar to that previously observed. Once again, lower porosity was preferred downstream of the inlet. In comparison, the radial design exhibited a much earlier transition to lower porosities in flow direction because of the higher velocities resulting from the smaller cross section.

In the course of shape optimization, the height and height-to-width ratio of the original design were explored. It became evident that with increasing porosity and a fixed width, the electrode height increased. The investigations with flexible height and width revealed a preference for the horizontal format for cells with a porosity of less than 0.9. Examination of the trapezoidal design revealed a consistent preference for a rectangular design for the parameters used. For the radial design, optimization almost always produced the maximum angle. In both cases, the reduction of pressure loss by expanding the cross section was decisive.

In summary, shape optimization revealed that the intuitively assumed vertical format is not necessarily the optimal choice for cell design. More detailed investigation, including experimental studies, is imperative to identify the optimal design and remains the subject of ongoing research.

In a rigorous evaluation, it is imperative to define the limitations of both the HCSM and the optimization process. To enhance the model for more robust optimization results in the future, various improvements can be explored. Primarily, the inclusion of the Butler-Volmer kinetics deserves attention, as it offers a more precise depiction of the active material conversion. This inclusion also provides the opportunity to optimize electrochemical variables, such as voltage or current. In addition, determining the cost functional involves considering the weighting of individual terms. Conducting a parameter study in this context would yield insights into their optimal weighting. Furthermore, the assumption of a linear inverse relationship between porosity and active surface, as stated in Equation 2.38, requires further discussion. Experimental investigations have revealed the reduced concentration polarization of the trapezoidal design [182]. Employing shape optimization with electrochemical parameters could facilitate the trade-off between pressure loss and this polarization, potentially identifying an optimal ratio between the top and bottom widths.

In conclusion, this investigation has contributed to the advancement of optimization methods for flow battery cells. Despite the need for further refinement, the simplicity of the model presented provides a flexible optimization framework applicable to various systems. The incorporation of a multiobjective cost functional and the exploration of porosity distribution have pushed the state of research in this field. Importantly, the findings challenge the intuitive assumption that the vertical format of the cell is the optimal design. This work represents a significant step forward, offering valuable insights and paving the way for future improvements in the optimization of flow battery cells.

8 Conclusion and Outlook

Microscale Modeling The successful development of the 3D resolved microscale model marks a significant advance in the understanding of flow batteries [86]. This model captures the real geometry of the electrode, offering detailed insights into the microstructural processes occurring within the battery. By directly linking the governing equations of the physical and electrochemical processes to a microstructural representation of the electrode and the surrounding electrolyte, the model provides a powerful tool for understanding how microstructural features affect transport processes and overall cell performance.

Building on the work of Qiu et al. [57, 58] and Kespe et al. [61], a half-cell flow battery model has been developed that resolves the electrode microstructure and surrounding electrolyte in non-overlapping regions. The laminar and steady-state flow of the electrolyte is described using the Navier-Stokes equations, while the transport of species is modeled using the convection-diffusion equation, also considering migration. Charge transport within the electrode and electrolyte is connected with a Butler-Volmer-type kinetic boundary condition, ensuring charge and species conservation across all parts of the computational domain. This flexible model is applicable to various systems, including the all-vanadium and MV/TEMPOL systems, and can simulate both charge and discharge operations under different current densities and concentration levels. The results provide detailed current density, charge, and concentration profiles in both regions and at the interface, along with the half-cell potential at the current collector.

In addition, a successful reconstruction process of the electrode material has been developed. Using micro-CT images, a digital twin of the real electrode graphite felt was created, suitable for use in microscale simulations. The model was validated against established vanadium models and novel TEMPOL half-cell potential experiments, as well as full-cell MV/TEMPOL power densities, showing good agreement with modeled and experimental polarization curves, albeit requiring a small voltage correction typical for such models.

Focused investigations on the half-cell parameterized with TEMPOL demonstrated the model's capability to investigate the effects of different electrode surface areas and active material concentrations on the half-cell potential. Using simplified structured electrodes, the model illustrated the trade-off between active surface area and pressure drop. Higher active surface areas reduced overpotential at constant current density and increased cell potential but also increased pressure drop, reducing round-trip efficiency due to higher pumping power. The model successfully predicted active material concentration, current density and potential distribution dependent on flow rate in a range from the Re number of 5×10^{-5} to 5, revealing an optimal Reynolds number range around 10^{-2} to balance the sufficient concentration of active material and the appropriate half-cell potential with minimal pressure drop.

Investigations of velocity distribution revealed that normalized velocity profiles are independent of the flow rate, with slight differences observed in different flow directions within the reconstructed electrode. However, comparing the reconstructed electrode with a structured domain showed that the regular structure of the SFD created channel-like flows that resulted in higher velocity values. Differences in mean active material concentration were minimal between the domains, but at lower Re numbers differences in half-cell potential were revealed. Interestingly, the SFD domain performed better under the same operating conditions despite having a lower active surface area, suggesting better mass transfer properties due to its regular structure.

In summary, the development of the microscale model and the corresponding reconstruction process has been successful. The validation showed that the model accurately predicts real-life behavior, and the numerical study provided detailed information on microscale phenomena. An optimal Reynolds number was identified and the advantages of the SFD were demonstrated, highlighting their ease of construction and computation, as well as their enhanced mass transfer properties compared to reconstructed felt electrodes.

For future work, improving the reconstruction process to simulate larger domains approaching the real width of the flow battery electrodes is crucial. Alternatively, using other methods to create domains with equal parameters could offer advantages such as reduced effort, faster computational time, and the potential implementation of cyclic boundary conditions, which bring the simulation setup closer to reality. Additionally, implementing back-coupling to account for changes in electrolyte viscosity and density as a result of concentration changes would significantly enhance the model, despite the associated computational costs.

Multiscale Modeling In this work, a novel multiscale modeling approach is introduced that bridges the gap between the microscale and the homogenized cell-scale in the context of flow batteries. The inherent challenge of exchanging information between different scale models is successfully addressed using mass transfer coefficients extracted from the microscale model and applied to the homogenized cell-scale.

Initially, a 2D homogenized cell-scale model was set up. This model, while simple, is fast and also well suited for optimization calculations. It considers the in-plane direction of a flow battery experimental cell, incorporating inlet and outlet manifolds to distribute the electrolyte to a rectangular porous electrode. The model integrates Brinkmann-type Navier-Stokes equations with permeability determined by the Carman-Kozeny equation and accounts for the transport of an arbitrary single diluted species. The reaction kinetics focus on single-species conversion, employing a simplified reaction term based on the mass transfer coefficient. This versatile model can be applied to any chemical species and, in the multiscale modeling investigation, is parameterized with TEMPOL.

The homogenized cell-scale model was validated with an experimentally determined open-circuit voltage and combined half-cell potential during charge using a modified Nernst equation, specifically for the all-vanadium system. With adaptation of the mass transfer correlation parameters and voltage corrections, the model effectively predicted the experimental measurements.

The multiscale approach involves extracting mass transfer coefficients from the microscale model and using them in the homogenized scale model. Several homogenized modeling approaches use the mass transfer coefficient to compensate for the unknown surface concentration of the active material in the electrode. The microscale model resolves the mass transfer between the bulk and active surface, eliminating the need for this assumption as both concentrations are known. Discharge simulations were performed with fixed initial concentrations of 0.1 M TEMPOL in 1 M NaCl and current density of $80\,\mathrm{mA\,cm^{-2}}$ at different Re numbers: 5×10^{-4}, 5×10^{-3} and 5×10^{-2}, using the reconstructed graphite felt electrode domain and the structured fiber domain. It was found that the mass transfer coefficient of the SFD is higher than that of the reconstructed microstructure, confirming findings from MSM investigations. Using a derived equation, the mass transfer coefficient is obtained as a function of SOC and velocity, successfully implemented into the homogenized cell-scale model for parameter studies.

However, the reaction zone above the inlet channels was relatively limited, with most parts of the electrode experiencing no reaction, indicating that the cell may be overdesigned for the intended system and its chosen operating conditions. The proposed approach was compared with empirical formulations from the literature, which depend only on velocity and not on SOC and velocity. The electrochemical information obtained from the proposed approach, which accounted for the microstructural characteristics of the system and the detailed electrochemistry, was more convincing and predicted a species conversion that was much faster than the values from the literature.

In summary, a method for connecting different scale models has been successfully developed. For future work, it is recommended to improve the extraction process considering a larger range of parameters, such as different concentration levels and current densities. Additionally, implementing detailed electrochemistry, such as the Butler-Volmer equation, in the homogenized cell-scale model is necessary to better represent the reaction kinetics. This underlying approach highlights the crucial role of reaction kinetics in the design of flow battery cells.

Optimization In this work, a cell-scale modeling and optimization framework has been successfully developed using topology and shape optimization for flow batteries. The framework leveraged a 2D homogenized cell-scale model, parameterized with the all-vanadium system due to the availability of experimental data for validation. Initially, the default vertical format rectangular cell geometry was used, but the framework also explored novel cell designs such as trapezoidal and radial configurations.

The optimization problem was formulated with a novel multi-objective functional aimed at simultaneously minimizing the pressure drop and maximizing the reaction rate within the cell. This approach addressed the challenge of identifying a favorable compromise between these two opposing quantities. Typically, pressure drop is minimized at high porosity levels as a result of reduced flow resistance, whereas the reaction rate tends to increase with decreasing porosity driven by an increase in surface area. The two quantities were equally weighted within the objective functional.

In topology optimization, the optimal porosity distribution within the electrode was determined. The key question was whether a completely homogeneous porosity in the electrode is optimal or if a distribution is preferable. The model replaced the porosity of the electrode with an optimized porosity for every computational cell within a distinct porosity interval. A gradient-based optimizer varied the porosity in every cell to find the minimum of the multi-objective functional.

For shape optimization, different geometric measures of the electrode, such as height and height-to-width ratio, were optimized to minimize the objective functional. Here, the gradient-free Nelder-Mead method was used, with fixed and homogeneous porosity.

Regarding topology optimization, three porosity intervals ($\epsilon \in [0.05, 0.95]$,) $\epsilon \in [0.6, 0.8]$, $\epsilon \in [0.7, 0.95]$) were defined for investigation. A sanity check for these intervals showed expected trends and validated the optimization approach. Optimization conducted with both multi-objective and single-objective functionals revealed that maximum porosity values were obtained for the single pressure drop optimization, while minimum porosity values were found for single reaction rate optimization. The multi-objective optimization results were always intermediate, trending toward higher porosity values with increased flow rates.

Optimization favored a porosity distribution with lower values and larger surface areas downstream of the inlet when both the pressure drop and the reaction rate were optimized simultaneously. This led to the introduction of a two-part electrode with two porosity values, resulting in an acceptable conversion rate of the active material while significantly reducing the pressure drop using certain porosity values. Investigations of the influence of the initial value on the optimization results showed typical dependencies typical for gradient-based optimization.

A parameter study highlighted that the reaction rate parameter α and the flow rate were the most influential. Applying topology optimization to different cell designs yielded similar results as for the rectangular cell. However, the radial design showed an earlier transition to a lower porosity in the flow direction because of the higher velocities resulting from a smaller cross section.

In shape optimization, the optimization of the height and height-to-width ratio of the original rectangular design revealed that with increasing porosity and a fixed width, the electrode height increased. The investigations with flexible height and width indicated a preference for a horizontal format for cells with a porosity of less than 0.9. The trapezoidal design consistently favored a rectangular design for the parameters used. However, radial design optimization often produced the maximum angle, suggesting that reducing pressure loss by expanding the cross section is crucial, thus questioning the necessity of the portrait format as the optimal design.

In summary, the optimization framework was successfully developed and demonstrated significant potential for optimizing the flow battery design. The resulting two-part electrode configuration and the suggestion that a horizontal format cell design may not be optimal represent significant advancements. This work offers valuable insights and paves the way for future improvements in the optimization of flow battery cells.

Future recommendations for optimizing flow batteries are focused on several key areas that could significantly enhance the accuracy and effectiveness of the optimization framework. First, implementing detailed electrochemistry into the model is crucial. Currently, the model uses simplified reaction kinetics, which limits its ability to accurately predict reaction rates and overpotentials. By incorporating detailed electrochemical models, such as the Butler-Volmer equation, the framework can provide a more precise representation of the electrochemical reactions occurring at the electrode-electrolyte interface. This enhancement would allow for the optimization of cell potential, balancing it alongside pressure drop and reaction rate for a more comprehensive optimization approach.

Second, exploring different weightings for the components of the cost functional is recommended. In the current model, pressure drop and reaction rate were equally weighted in the multi-objective functional. However, in practical applications, the relative importance of minimizing pressure drop versus maximizing reaction rate can vary depending on specific operational goals. Adjusting the weights assigned to each objective would allow the optimization process to reflect these varying priorities, resulting in customized designs optimized for different scenarios.

Lastly, it is necessary to investigate alternative formulations for the dependency of porosity and active surface area. The current model assumed a linear inverse relationship between porosity and active surface area, which may not hold for all types of porous media. A more accurate representation of this relationship could be achieved through empirical studies or theoretical modeling, leading to more precise optimization results.

In summary, implementing detailed electrochemistry, adjusting the weighting of cost functional components, and refining the relationship between porosity and active surface area are critical steps toward advancing the optimization of flow battery cells. These improvements will enhance the accuracy and effectiveness of the model, leading to more efficient and optimized flow battery designs.

List of Figures

List of Tables

List of Publications

Peer-reviewed Publications

Wolf, A., Baudrin, E., and Nirschl, H.: A Multiscale Flow Battery Modeling Approach Using Mass Transfer Coefficients. *Energy Technology* **2023**, 11.7, 2300175. DOI: `https://doi.org/10.1002/ente.202300175`.

Wolf, A., Kespe, S., and Nirschl, H.: Pore-scale Modeling of Flow Batteries. In: *Flow Batteries - From Fundamentals to Applications*. John Wiley & Sons, Ltd, 2023. Chap. 18, 413–442. DOI: `https://doi.org/10.1002/9783527832767.ch18`.

Wolf, A., Noack, J., Krause, M. J., and Nirschl, H.: Enhancing Flow Batteries: Topology Optimization of Electrode Porosity and Shape Optimization of Cell Design. *Energy Technology* **2024**, 12.7, 2400244. DOI: `https://doi.org/10.1002/ente.202400244`.

Conference Contributions

Wolf, A., Gerbig, F., Cernak, S., and Nirschl, H.: Total Organic Aqueous Redox Flow Batteries Pore-scale Numerical Investigations. *Advanced Battery Power Conference* (Online, Apr. 27–29, 2021). 2021.

Wolf, A. and Nirschl, H.: Pore-scale Resolved 3D Simulation of Aqueous Organic Flow Batteries. *Nordic Flow Battery Network* (Turku, Finland, Nov. 24–27, 2021). 2021.

Noack, J., Baudrin, E., Fornari, R., Franco, A. A., Gerlach, D., Guan, X., Hamaekers, J., Maaß, A., Menictas, C., Mourouga, G., Nirschl, H., Roznyatovskaya, N., Schaerer, R., Schumacher, J., Silva, P. de, Skyllas-Kazacos, M., Wlodarczyk, J., Wolf, A., and Yu, J.: Modelling and Simulation for the Search for New Active Materials for Redox Flow Batteries - Results of the International Project Sonar. *241st ECS Meeting* (Vancouver, Canada, May 29–June 2, 2022). 2022.

Wolf, A. and Nirschl, H.: Cell Performance Simulation and Cell Design Optimization. *Pre-Conference SONAR and COMBAT Workshop* (Brussels, Belgium, June 27, 2022). 2022.

Wolf, A. and Nirschl, H.: Pore-scale Resolved 3D Simulation of Aqueous Organic Flow Batteries. *18th Symposium on Modeling and Experimental Validation of Electrochemical Energy Technologies* (Hohenkammer, Germany, Mar. 14–16, 2022). 2022.

Wolf, A. and Nirschl, H.: Pore-scale Resolved 3D Simulations of Aqueous Organic Flow Batteries. *The International Flow Battery Forum* (Brussels, Belgium, June 28–29, 2022). 2022.

Wolf, A., Baudrin, E., and Nirschl, H.: A Multi-scale Flow Battery Modeling Approach Using Mass Transfer Coefficients. *19th Symposium on Fuel Cell and Battery Modeling and Experimental Validation* (Duisburg, Germany, Mar. 21–23, 2023). 2023.

Wolf, A., Baudrin, E., and Nirschl, H.: A Multi-scale Flow Battery Modeling Approach Using Mass Transfer Coefficients. *The International Flow Battery Forum* (Prague, Czech Republic, June 27–Mar. 29, 2023). 2023.

Wolf, A. and Nirschl, H.: An Introduction into Microscale Simulation of Flow Batteries. *SONAR Workshop – Computational Access to Flow Batteries* (Sankt Augustin, Germany, Sept. 21, 2023). 2023.

Wolf, A., Noack, J., Baudrin, E., Fornari, R., Franco, A. A., Gerlach, D., Guan, X., Hamaekers, J., Maaß, A., Menictas, C., Mourouga, G., Roznyatovskaya, N., Schaerer, R., Schumacher, J., Silva, P. de, Skyllas-Kazacos, M., Wlodarczyk, J., Yu, J., and Nirschl, H.: Results of the European Project SONAR with Deeper Insight into Microstructure Simulations of Flow Batteries. *HIGREEW Workshop: Flow batteries, bringing the technology to the market* (Vitoria-Gasteiz, Spain, May 15–16, 2023). 2023.

Bibliography

[1] Chu, S., Cui, Y., and Liu, N.: The path towards sustainable energy. *Nature Materials* **2017**, 16, 16–22. DOI: `10.1038/nmat4834`.

[2] Arbabzadeh, M., Sioshansi, R., Johnson, J. X., and Keoleian, G. A.: The role of energy storage in deep decarbonization of electricity production. *Nature Communications* **2019**, 10, 2041–1723. DOI: `10.1038/s41467-019-11161-5`.

[3] Heptonstall, P. J. and Gross, R. J. K.: A systematic review of the costs and impacts of integrating variable renewables into power grids. *Nature Energy* **2021**, 6.1, 72–83. DOI: `10.1038/s41560-020-00695-`.

[4] Noack, J., Roznyatovskaya, N., Herr, T., and Fischer, P.: The Chemistry of Redox-Flow Batteries. *Angewandte Chemie International Edition* **2015**, 54.34, 9776–9809. DOI: `https://doi.org/10.1002/anie.201410823`.

[5] Park, M., Ryu, J., Wang, W., and Cho, J.: Material design and engineering of next-generation flow-battery technologies. *Nature Reviews Materials* **2016**, 2, 16080. DOI: `10.1038/natrevmats.2016.80`.

[6] Poullikkas, A.: A comparative overview of large-scale battery systems for electricity storage. *Renewable and Sustainable Energy Reviews* **2013**, 27, 778–788. DOI: `https://doi.org/10.1016/j.rser.2013.07.017`.

[7] Wang, W., Luo, Q., Li, B., Wei, X., Li, L., and Yang, Z.: Recent Progress in Redox Flow Battery Research and Development. *Advanced Functional Materials* **2013**, 23.8, 970–986. DOI: `https://doi.org/10.1002/adfm.201200694`.

[8] Sum, E. and Skyllas-Kazacos, M.: A study of the V(II)/V(III) redox couple for redox flow cell applications. *Journal of Power Sources* **1985**, 15.2, 179–190. DOI: `https://doi.org/10.1016/0378-7753(85)80071-9`.

[9] Sum, E., Rychcik, M., and Skyllas-kazacos, M.: Investigation of the V(V)/V(IV) system for use in the positive half-cell of a redox battery. *Journal of Power Sources* **1985**, 16.2, 85–95. DOI: `https://doi.org/10.1016/0378-7753(85)80082-3`.

[10] Huang, Z., Mu, A., Wu, L., Yang, B., Qian, Y., and Wang, J.: Comprehensive Analysis of Critical Issues in All-Vanadium Redox Flow Battery. *ACS Sustainable Chemistry & Engineering* **2022**, 10.24, 7786–7810. DOI: `10.1021/acssuschemeng.2c01372`.

[11] Khaki, B. and Das, P.: Voltage loss and capacity fade reduction in vanadium redox battery by electrolyte flow control. *Electrochimica Acta* **2022**, 405, 139842. DOI: `https://doi.org/10.1016/j.electacta.2022.139842`.

[12] Winsberg, J., Hagemann, T., Janoschka, T., Hager, M. D., and Schubert, U. S.: Redox-Flow Batteries: From Metals to Organic Redox-Active Materials. *Angewandte Chemie International Edition* **2017**, 56.3, 686–711. DOI: `https://doi.org/10.1002/anie.201604925`.

[13] Kapoor, M. and Verma, A.: Technical benchmarking and challenges of kilowatt scale vanadium redox flow battery. *WIREs Energy and Environment* **2022**, 11.5, e439. DOI: `https://doi.org/10.1002/wene.439`.

[14] Simandl, G. J. and Paradis, S.: Vanadium as a critical material: economic geology with emphasis on market and the main deposit types. *Applied Earth Science* **2022**, 131.4, 218–236. DOI: `10.1080/25726838.2022.2102883`.

[15] Asenjo-Pascual, J., Salmeron-Sanchez, I., Avilés-Moreno, J. R., Mauleón, P., Mazur, P., and Ocón, P.: Understanding Aqueous Organic Redox Flow Batteries: A Guided Experimental Tour from Components Characterization to Final Assembly. *Batteries* **2022**, 8.10. DOI: `10.3390/batteries8100193`.

[16] Chai, J., Lashgari, A., and Jiang, J. ": Electroactive Materials for Next-Generation Redox Flow Batteries: From Inorganic to Organic. In: *Clean Energy Materials*. Chap. 1, 1–47. DOI: `10.1021/bk-2020-1364.ch001`. URL: `https://pubs.acs.org/doi/abs/10.1021/bk-2020-1364.ch001`.

[17] Galvani, L.: De viribus electricitatis in motu musculari. *Ex Typographia Instituti Scientiarium, Bononiae* **1791**. DOI: `https://doi.org/10.5479/sil.324681.39088000932442`.

[18] Volta, A.: On the electricity excited by the mere contact of conducting substances of different kinds. In a letter from Mr. Alexander Volta, F. R. S. Professor of Natural Philosophy in the University of Pavia, to the Rt. Hon. Sir Joseph Banks, Bart. K. B. P. R. S. *Abstracts of the Papers Printed in the Philosophical Transactions of the Royal Society of London* **1832**, 1, 27–29. DOI: `10.1098/rspl.1800.0016`.

[19] Ayrton, W. E.: *Practical Electricity*. Cassell, 1891.

[20] Kangro, W.: *Method for storing electrical energy*. Tech. rep. German Patent DE914264C, 1949.

[21] Hagedorn, N. H.: NASA Redox Storage System Development Project. Final report. **1984**. DOI: `10.2172/6472995`.

[22] Skyllas-Kazacos, M., Rychcik, M., Robins, R. G., Fane, A. G., and Green, M. A.: New All-Vanadium Redox Flow Cell. *Journal of The Electrochemical Society* **1986**, 133.5, 1057. DOI: `10.1149/1.2108706`.

[23] Leung, P., Li, X., Ponce de León, C., Berlouis, L., Low, C. T. J., and Walsh, F. C.: Progress in redox flow batteries, remaining challenges and their applications in energy storage. *RSC Adv.* **2012**, 2, 10125–10156. DOI: `10.1039/C2RA21342G`.

[24] Iwakiri, I., Antunes, T., Almeida, H., Sousa, J. P., Figueira, R. B., and Mendes, A.: Redox Flow Batteries: Materials, Design and Prospects. *Energies* **2021**, 14.18. DOI: `10.3390/en14185643`.

[25] Arenas, L. F., Ponce de León, C., and Walsh, F. C.: Redox flow batteries for energy storage: their promise, achievements and challenges. *Current Opinion in Electrochemistry* **2019**, 16. Electrochemical Materials and Engineering • Sensors and Biosensors, 117–126. DOI: `https://doi.org/10.1016/j.coelec.2019.05.007`.

[26] Gencten, M. and Sahin, Y.: A critical review on progress of the electrode materials of vanadium redox flow battery. *International Journal of Energy Research* **2020**, 44.10, 7903–7923. DOI: `https://doi.org/10.1002/er.5487`.

[27] Codina G.and Aldaz, A.: Scale-up studies of an Fe/Cr redox flow battery based on shunt current analysis. *Journal of Applied Electrochemistry* **1992**. DOI: `10.1007/BF01092617`.

[28] Codina, G., Perez, J., Lopez-Atalaya, M., Vasquez, J., and Aldaz, A.: Development of a 0.1 kW power accumulation pilot plant based on an Fe/Cr redox flow battery Part I. Considerations on flow-distribution design. *Journal of Power Sources* **1994**, 48.3, 293–302. DOI: `https://doi.org/10.1016/0378-7753(94)80026-X`.

[29] Parasuraman, A., Lim, T. M., Menictas, C., and Skyllas-Kazacos, M.: Review of material research and development for vanadium redox flow battery applications. *Electrochimica Acta* **2013**, 101, 27–40. DOI: `https://doi.org/10.1016/j.electacta.2012.09.067`.

[30] Hennessy, T.: Overcoming Transmission Constraints: Energy Storage and Wyoming Wind Power. *Science Applications International Corporation* **2007**.

[31] Groenendaal, B.: Bushveld Energy announces solar/redox flow battery hybrid mini grid project for vametco. *Green Building Africa* **2022**.

[32] Gilbert, N.: Coming Spring 2022 – the UK's largest public EV charging hub. *EnergyREV* **2022**.

[33] Murray, C.: BayWa r.e., Ampt and Fraunhofer complete 'European-first' wind-solar-flow battery hybrid project in Germany. *Energy Storage News* **2019**.

[34] Electric, S.: Grid Storage Batteries for Power Supply Stabilization– Minami. *Sumitomo Electric* **2022**.

[35] Lavars, N.: World's largest flow battery connected to the grid in China. *New Atlas* **2022**.

[36] Xu, Y., Wen, Y., Cheng, J., Yanga, Y., Xie, Z., and Cao, G.: Novel organic redox flow batteries using soluble quinonoid compounds as positive materials. In: *2009 World Non-Grid-Connected Wind Power and Energy Conference*. 2009, 1–4. DOI: `10.1109/WNWEC.2009.5335870`.

[37] Huskinson, B., Marshak, M. P., Suh, C., Er, S., Gerhardt, M. R., Galvin, C. J., Chen, X., Aspuru-Guzik, A., Gordon, R. G., and Aziz, M. J.: A metal-free organic–inorganic aqueous flow battery. *Nature* **2014**. DOI: `10.1038/nature12909`.

[38] Liu, T., Wei, X., Nie, Z., Sprenkle, V., and Wang, W.: A Total Organic Aqueous Redox Flow Battery Employing a Low Cost and Sustainable Methyl Viologen Anolyte and 4-HO-TEMPO Catholyte. *Advanced Energy Materials* **2016**, 6.3, 1501449. DOI: `https://doi.org/10.1002/aenm.201501449`.

[39] Xu, Z., Fan, Q., Li, Y., Wang, J., and Lund, P. D.: Review of zinc dendrite formation in zinc bromine redox flow battery. *Renewable and Sustainable Energy Reviews* **2020**, 127, 109838. DOI: `https://doi.org/10.1016/j.rser.2020.109838`.

[40] Sun, C. and Zhang, H.: Review of the Development of First-Generation Redox Flow Batteries: Iron-Chromium System. *ChemSusChem* **2022**, 15.1, e202101798. DOI: `https://doi.org/10.1002/cssc.202101798`.

[41] Alotto, P., Guarnieri, M., and Moro, F.: Redox flow batteries for the storage of renewable energy: A review. *Renewable and Sustainable Energy Reviews* **2014**, 29, 325–335. DOI: `https://doi.org/10.1016/j.rser.2013.08.001`.

[42] Cao, J., Tian, J., Xu, J., and Wang, Y.: Organic Flow Batteries: Recent Progress and Perspectives. *Energy & Fuels* **2020**, 34.11, 13384–13411. DOI: `10.1021/acs.energyfuels.0c02855`.

[43] Puleston, T., Clemente, A., Costa-Castelló, R., and Serra, M.: Modelling and Estimation of Vanadium Redox Flow Batteries: A Review. *Batteries* **2022**, 8.9. DOI: `10.3390/batteries8090121`.

[44] Ciriminna, R. and Pagliaro, M.: Industrial Oxidations with Organocatalyst TEMPO and Its Derivatives. *Organic Process Research & Development* **2010**, 14.1, 245–251. DOI: `10.1021/op900059x`.

[45] Chakrabarti, B. K., Kalamaras, E., Singh, A. K., Bertei, A., Rubio-Garcia, J., Yufit, V., Tenny, K. M., Wu, B., Tariq, F., Hajimolana, Y. S., Brandon, N. P., John Low, C. T., Roberts, E. P. L., Chiang, Y.-M., and Brushett, F. R.: Modelling of redox flow battery electrode processes at a range of length scales: a review. *Sustainable Energy Fuels* **2020**, 4, 5433–5468. DOI: `10.1039/D0SE00667J`.

[46] Wang, H., Pourmousavi, S. A., Soong, W. L., Zhang, X., and Ertugrul, N.: Battery and energy management system for vanadium redox flow battery: A critical review and recommendations. *Journal of Energy Storage* **2023**, 58, 106384.

[47] Barton, J. L. and Brushett, F. R.: A one-dimensional stack model for redox flow battery analysis and operation. *Batteries* **2019**, 5.1, 25.

[48] Ryan, E. M. and Mukherjee, P. P.: Mesoscale modeling in electrochemical devices—A critical perspective. *Progress in Energy and Combustion Science* **2019**, 71, 118–142. DOI: `https://doi.org/10.1016/j.pecs.2018.11.002`.

[49] Esan, O. C., Shi, X., Pan, Z., Huo, X., An, L., and Zhao, T.: Modeling and Simulation of Flow Batteries. *Advanced Energy Materials* **2020**, 10.31, 2000758. DOI: `https://doi.org/10.1002/aenm.202000758`.

[50] Fedkiw, P. S. and Watts, R. W.: A Mathematical Model for the Iron/Chromium Redox Battery. *Journal of The Electrochemical Society* **1984**, 131.4, 701. DOI: `10.1149/1.2115676`.

[51] Homma, T., Zhao, G., and Ohsawa, Y.: Theoretical Studies on Charge and Discharge Characteristics of Redox Flow Battery. *Electrical Engineering in Japan* **1990**, 110.4, 24–34. DOI: `10.1002/eej.4391100403`.

[52] Sigmund, O. and Maute, K.: Topology optimization approaches: A comparative review. English. *Structural and Multidisciplinary Optimization* **2013**, 48.6, 1031–1055. DOI: `10.1007/s00158-013-0978-6`.

[53] Deaton, J. D. and Grandhi, R. V.: A survey of structural and multidisciplinary continuum topology optimization: post 2000. *Structural and Multidisciplinary Optimization* **2014**, 49.1, 1–38. DOI: `10.1007/S00158-013-0956-Z`.

[54] Sokolowski, J., Zolésio, J.-P., Sokolowski, J., and Zolesio, J.-P.: *Introduction to shape optimization*. Springer, 1992.

[55] Sotola, M., Marsalek, P., Rybansky, D., Fusek, M., and Gabriel, D.: Sensitivity Analysis of Key Formulations of Topology Optimization on an Example of Cantilever Bending Beam. *Symmetry* **2021**, 13.4. DOI: `10.3390/sym13040712`.

[56] Painchaud-Ouellet, S., Tribes, C., Trépanier, J.-Y., and Pelletier, D.: Airfoil shape optimization using a nonuniform rational b-splines parametrization under thickness constraint. *AIAA journal* **2006**, 44.10, 2170–2178.

[57] Qiu, G., Joshi, A. S., Dennison, C., Knehr, K., Kumbur, E., and Sun, Y.: 3-D pore-scale resolved model for coupled species/charge/fluid transport in a vanadium redox flow battery. *Electrochimica Acta* **2012**, 64, 46–64. DOI: `https://doi.org/10.1016/j.electacta.2011.12.065`.

[58] Qiu, G., Dennison, C., Knehr, K., Kumbur, E., and Sun, Y.: Pore-scale analysis of effects of electrode morphology and electrolyte flow conditions on performance of vanadium redox flow batteries. *Journal of Power Sources* **2012**, 219, 223–234. DOI: `https://doi.org/10.1016/j.jpowsour.2012.07.042`.

[59] Kespe, M. and Nirschl, H.: Numerical simulation of lithium-ion battery performance considering electrode microstructure. *International Journal of Energy Research* **2015**, 39.15, 2062–2074. DOI: `https://doi.org/10.1002/er.3459`.

[60] Kespe, M., Gleiß, M., Hammerich, S., and Nirschl, H.: Numerical optimization of the spatial conductivity distribution within cathode microstructures of lithium-ion batteries considering the cell performance. *International Journal of Energy Research* **2017**, 41.14, 2282–2296. DOI: `https://doi.org/10.1002/er.3794`.

[61] Kespe, M. A.: *Simulation von Transportvorgängen in Lithium-Ionen Batterien auf der partikulären Ebene*. German. PhD thesis. Karlsruher Institut für Technologie (KIT), 2019. 188 pp. DOI: `10.5445/IR/1000097980`.

[62] *SIGRACELL® battery felts Datasheet*. SGL CARBON GmbH, 2019. URL: `https://www.sglcarbon.com/pdf/SGL-Datasheet-SIGRACELL-Battery-Felts-EN.pdf` (visited on 02/14/2024).

[63] Newman, J.: *Electrochemical systems*. Balsara, N. P. (Hrsg.). Fourth edition. The Electrochemical Society series. Hoboken, NJ: Wiley, 2021. URL: `http://swbplus.bsz-bw.de/bsz1664466789cov.htm`.

[64] Zhang, D., Forner-Cuenca, A., Taiwo, O. O., Yufit, V., Brushett, F. R., Brandon, N. P., Gu, S., and Cai, Q.: Understanding the role of the porous electrode microstructure in redox flow battery performance using an experimentally validated 3D pore-scale lattice Boltzmann model. *Journal of Power Sources* **2020**, 447, 227249. DOI: `https://doi.org/10.1016/j.jpowsour.2019.227249`.

[65] Bazant, M. Z.: Theory of Chemical Kinetics and Charge Transfer based on Nonequilibrium Thermodynamics. *Accounts of Chemical Research* **2013**, 46.5. PMID: 23520980, 1144–1160. DOI: `10.1021/ar300145c`.

[66] Bard, A. and Faulkner, L.: *Electrochemical Methods: Fundamentals and Applications*. Wiley, 2000. URL: `https://books.google.de/books?id=qPc-ngEACAAJ`.

[67] Zienkiewicz, O. C., Taylor, R. L., and Nithiarasu, P.: *The Finite Element Method for Fluid Dynamics*. 7th ed. Butterworth-Heinemann, 2013.

[68] Maubourguet, M.-M. and Tanguy, J.-M.: Finite Differences. In: *Numerical Methods*. John Wiley & Sons, Ltd, 2010. Chap. 6, 95–107. DOI: `https://doi.org/10.1002/9781118557877.ch6`.

[69] Council, N. R.: *International Critical Tables of Numerical Data, Physics, Chemistry and Technology*. Washington, DC: The National Academies Press, 1930. DOI: `10.17226/20230`. URL: `https://www.nap.edu/catalog/20230/international-critical-tables-of-numerical-data-physics-chemistry-and-technology`.

[70] Kestin, J., Khalifa, H. E., and Correia, R. J.: Tables of the dynamic and kinematic viscosity of aqueous NaCl solutions in the temperature range 20-150 °C and the pressure range 0.1-35 MPa. *Journal of Physical and Chemical Reference Data* **1981**, 10.1, 71–88. DOI: `10.1063/1.555641`.

[71] Potter, R. W. and Brown, D. L.: The volumetric properties of aqueous sodium chloride solutions from 0 degrees to 500 degrees C at pressures up to 2000 bars based on a regression of the available literature data. *U.S. Geological Survey* **1975**, 75-636. DOI: `10.3133/ofr75636`.

[72] You, D., Zhang, H., and Chen, J.: A simple model for the vanadium redox battery. *Electrochimica Acta* **2009**, 54.27, 6827–6836. DOI: `https://doi.org/10.1016/j.electacta.2009.06.086`.

[73] Roznyatovskaya, N., Herr, T., Küttinger, M., Fühl, M., Noack, J., Pinkwart, K., and Tübke, J.: Detection of capacity imbalance in vanadium electrolyte and its electrochemical regeneration for all-vanadium redox-flow batteries. *Journal of Power Sources* **2016**, 302, 79–83. DOI: `https://doi.org/10.1016/j.jpowsour.2015.10.021`.

[74] Yamamura, T., Watanabe, N., Yano, T., and Shiokawa, Y.: Electron-Transfer Kinetics of Np3+/Np4+, V2+/V3+, and VO2+/VO2+ at Carbon Electrodes. *Journal of The Electrochemical Society* **2005**, 152.4, A830. DOI: `10.1149/1.1870794`.

[75] Versteeg, H. K. and Malalasekera, W.: *An introduction to computational fluid dynamics - the finite volume method*. Addison-Wesley-Longman, 1995, I–X, 1–257.

[76] Ferziger, J. H. and Peric, M.: *Computational Methods for Fluid Dynamics*. 3rd ed. Springer-Verlag Berlin Heidelberg, 2002. DOI: `10.1007/978-3-642-56026-2`.

[77] Noack, J. N., Vorhauser, L., Pinkwart, K., and Tuebke, J.: Aging Studies of Vanadium Redox Flow Batteries. *ECS Transactions* **2011**, 33.39, 3. DOI: `10.1149/1.3589916`.

[78] Bear, J.: *Dynamics of Fluids in Porous Media*. Dynamics of Fluids in Porous Media Parts 1-2. American Elsevier Publishing Company, 1972. URL: `https://books.google.de/books?id=9JVRAAAAMAAJ`.

[79] Yazdchi, K., Srivastava, S., Luding, S., Oñate, E., and Owen, D.: On the validity of the Carman-Kozeny equation in random fibrous media. *Particle-Based Methods II - Fundamentals and Applications* **2011**.

[80] Shah, A. A., Tangirala, R., Singh, R., Wills, R. G. A., and Walsh, F. C.: A Dynamic Unit Cell Model for the All-Vanadium Flow Battery. *Journal of The Electrochemical Society* **2011**, 158.6, A671. DOI: `10.1149/1.3561426`.

[81] Verbrugge, M. W. and Hill, R. F.: Ion and Solvent Transport in Ion-Exchange Membranes: I . A Macrohomogeneous Mathematical Model. *Journal of The Electrochemical Society* **1990**, 137.3, 886. DOI: `10.1149/1.2086573`.

[82] Yaji, K., Yamasaki, S., Tsushima, S., Suzuki, T., and Fujita, K.: Topology Optimization for the Design of Flow Fields in a Redox Flow Battery. *Struct. Multidiscip. Optim.* **2018**, 57.2, 535–546. DOI: `10.1007/s00158-017-1763-8`.

[83] Xu, Q. and Zhao, T.: Determination of the mass-transport properties of vanadium ions through the porous electrodes of vanadium redox flow batteries. *Phys. Chem. Chem. Phys.* **2013**, 15, 10841–10848. DOI: `10.1039/C3CP51944A`.

[84] Schmal, D., Van Erkel, J., and Van Duin, P. J.: Mass transfer at carbon fibre electrodes. *Journal of Applied Electrochemistry* **1986**, 16.3, 422–430. DOI: `10.1007/BF01008853`.

[85] Tang, A., Ting, S., Bao, J., and Skyllas-Kazacos, M.: Thermal modelling and simulation of the all-vanadium redox flow battery. *Journal of Power Sources* **2012**, 203, 165–176. DOI: `https://doi.org/10.1016/j.jpowsour.2011.11.079`.

[86] Wolf, A., Kespe, S., and Nirschl, H.: Pore-scale Modeling of Flow Batteries. In: *Flow Batteries*. John Wiley & Sons, Ltd, 2023. Chap. 18, 413–442. DOI: `https://doi.org/10.1002/9783527832767.ch18`. URL: `https://onlinelibrary.wiley.com/doi/abs/10.1002/9783527832767.ch18`.

[87] Oleson, L. H., Okkels, F., and Bruus, H.: A high-level programming-language implementation of topology optimization applied to steady-state Navier–Stokes flow. *International Journal for Numerical Methods in Engineering* **2006**, 65, 975–1001. DOI: `0.1002/nme.1468`.

[88] Yaji, K., Yamada, T., Kubo, S., Izui, K., and Nishiwaki, S.: A topology optimization method for a coupled thermal–fluid problem using level set boundary expressions. *International Journal of Heat and Mass Transfer* **2015**, 81, 878–888. DOI: `https://doi.org/10.1016/j.ijheatmasstransfer.2014.11.005`.

[89] Bendsøe, M. P. and Sigmund, O.: Topology optimization by distribution of isotropic material. In: *Topology Optimization: Theory, Methods, and Applications*. Berlin, Heidelberg: Springer Berlin Heidelberg, 2004, 1–69. DOI: `10.1007/978-3-662-05086-6_1`. URL: `https://doi.org/10.1007/978-3-662-05086-6_1`.

[90] Lazarov, B. S. and Sigmund, O.: Filters in topology optimization based on Helmholtz-type differential equations. *International Journal for Numerical Methods in Engineering* **2011**, 86.6, 765–781. DOI: `https://doi.org/10.1002/nme.3072`.

[91] Borrvall, T. and Petersson, J.: Topology optimization of fluids in Stokes flow. *International Journal for Numerical Methods in Fluids* **2003**, 41.1, 77–107. DOI: `https://doi.org/10.1002/fld.426`.

[92] Roy, T., Salazar de Troya, M. A., Worsley, M. A., and Beck, V. A.: Topology optimization for the design of porous electrodes. *Structural and Multidisciplinary Optimization* **2022**, 65, 171. DOI: `10.1007/s00158-022-03249-2`.

[93] Jameson, A.: Gradient based optimization methods. *MAE Technical Report No* **1995**, 2057.

[94] Daoud, M. S., Shehab, M., Al-Mimi, H. M., Abualigah, L., Zitar, R. A., and Shambour, M. K. Y.: Gradient-based optimizer (GBO): a review, theory, variants, and applications. *Archives of Computational Methods in Engineering* **2023**, 30.4, 2431–2449.

[95] Gill, P. E., Murray, W., and Saunders, M. A.: SNOPT: An SQP Algorithm for Large-Scale Constrained Optimization. *SIAM Review* **2005**, 47.1, 99–131. DOI: `10.1137/S0036144504446096`.

[96] Gurieff, N., Cheung, C., Timchenko, V., and Menictas, C.: Performance enhancing stack geometry concepts for redox flow battery systems with flow through electrodes. *Journal of Energy Storage* **2019**, 22, 219–227. DOI: `https://doi.org/10.1016/j.est.2019.02.014`.

[97] Nelder, J. A. and Mead, R.: A Simplex Method for Function Minimization. *The Computer Journal* **1965**, 7.4, 308–313. DOI: `10.1093/comjnl/7.4.308`.

[98] Cheng, J. Y. and Mailund, T.: Ancestral population genomics using coalescence hidden Markov models and heuristic optimisation algorithms. *Computational Biology and Chemistry* **2015**, 57. 13th Asia Pacifi c Bioinformatics Conference, HsinChu, Taiwan, 21-23 January 2015, 80–92. DOI: `https://doi.org/10.1016/j.compbiolchem.2015.02.001`.

[99] Singer, S. and Nelder, J.: Nelder-mead algorithm. *Scholarpedia* **2009**, 4.7, 2928.

[100] Wang, P. C. and Shoup, T. E.: Parameter sensitivity study of the Nelder–Mead Simplex Method. *Advances in Engineering Software* **2011**, 42.7, 529–533. DOI: `https://doi.org/10.1016/j.advengsoft.2011.04.004`.

[101] Kok, M. D., Jervis, R., Tranter, T. G., Sadeghi, M. A., Brett, D. J., Shearing, P. R., and Gostick, J. T.: Mass transfer in fibrous media with varying anisotropy for flow battery electrodes: Direct numerical simulations with 3D X-ray computed tomography. *Chemical Engineering Science* **2019**, 196, 104–115. DOI: `https://doi.org/10.1016/j.ces.2018.10.049`.

[102] Sadeghi, M. A., Aganou, M., Kok, M., Aghighi, M., Merle, G., Barralet, J., and Gostick, J.: Exploring the Impact of Electrode Microstructure on Redox Flow Battery Performance Using a Multiphysics Pore Network Model. *Journal of The Electrochemical Society* **2019**, 166.10, A2121–A2130. DOI: `10.1149/2.0721910jes`.

[103] Banerjee, R., Bevilacqua, N., Eifert, L., and Zeis, R.: Characterization of carbon felt electrodes for vanadium redox flow batteries – A pore network modeling approach. *Journal of Energy Storage* **2019**, 21, 163–171. DOI: `https://doi.org/10.1016/j.est.2018.11.014`.

[104] Chen, L., He, Y., Tao, W.-Q., Zelenay, P., Mukundan, R., and Kang, Q.: Pore-scale study of multiphase reactive transport in fibrous electrodes of vanadium redox flow batteries. *Electrochimica Acta* **2017**, 248, 425–439. DOI: `https://doi.org/10.1016/j.electacta.2017.07.086`.

[105] Hereijgers, J., Schalck, J., and Breugelmans, T.: Mass transfer and hydrodynamic characterization of structured 3D electrodes for electrochemistry. *Chemical Engineering Journal* **2020**, 384, 123283. DOI: `https://doi.org/10.1016/j.cej.2019.123283`.

[106] Zhang, M., Mei, H., Chang, P., and Cheng, L.: 3D printing of structured electrodes for rechargeable batteries. *J. Mater. Chem. A* **2020**, 8, 10670–10694. DOI: `10.1039/D0TA02099K`.

[107] Mottaghi, M. and Pearce, J. M.: A Review of 3D Printing Batteries. *Batteries* **2024**, 10.3. DOI: `10.3390/batteries10030110`.

[108] Chakrabarti, M., Brandon, N., Hajimolana, S., Tariq, F., Yufit, V., Hashim, M., Hussain, M., Low, C., and Aravind, P.: Application of carbon materials in redox flow batteries. *Journal of Power Sources* **2014**, 253, 150–166. DOI: `https://doi.org/10.1016/j.jpowsour.2013.12.038`.

[109] Zhong, S., Padeste, C., Kazacos, M., and Skyllas-Kazacos, M.: Comparison of the physical, chemical and electrochemical properties of rayon- and polyacrylonitrile-based graphite felt electrodes. *Journal of Power Sources* **1993**, 45.1, 29–41. DOI: `https://doi.org/10.1016/0378-7753(93)80006-B`.

[110] Lv, Y., Li, Y., Han, C., Chen, J., He, Z., Zhu, J., Dai, L., Meng, W., and Wang, L.: Application of porous biomass carbon materials in vanadium redox flow battery. *Journal of Colloid and Interface Science* **2020**, 566, 434–443. DOI: `https://doi.org/10.1016/j.jcis.2020.01.118`.

[111] Jiang, Q., Ren, Y., Yang, Y., Wang, L., Dai, L., and He, Z.: Recent advances in carbon-based electrocatalysts for vanadium redox flow battery: Mechanisms, properties, and perspectives. *Composites Part B: Engineering* **2022**, 242, 110094. DOI: `https://doi.org/10.1016/j.compositesb.2022.110094`.

[112] Park, S.-K., Shim, J., Yang, J. H., Jin, C.-S., Lee, B. S., Lee, Y.-S., Shin, K.-H., and Jeon, J.-D.: The influence of compressed carbon felt electrodes on the performance of a vanadium redox flow battery. *Electrochimica Acta* **2014**, 116, 447–452. DOI: `https://doi.org/10.1016/j.electacta.2013.11.073`.

[113] Brown, L. D., Neville, T. P., Jervis, R., Mason, T. J., Shearing, P. R., and Brett, D. J.: The effect of felt compression on the performance and pressure drop of all-vanadium redox flow batteries. *Journal of Energy Storage* **2016**, 8, 91–98. DOI: `https://doi.org/10.1016/j.est.2016.10.003`.

[114] Chang, T.-C., Zhang, J.-P., and Fuh, Y.-K.: Electrical, mechanical and morphological properties of compressed carbon felt electrodes in vanadium redox flow battery. *Journal of Power Sources* **2014**, 245, 66–75. DOI: `https://doi.org/10.1016/j.jpowsour.2013.06.018`.

[115] Davies, T. J. and Tummino, J. J.: High-Performance Vanadium Redox Flow Batteries with Graphite Felt Electrodes. *C* **2018**, 4.1. DOI: `10.3390/c4010008`.

[116] Dobler, T., Radel, B., Gleiss, M., and Nirschl, H.: Quasi-Continuous Production and Separation of Lysozyme Crystals on an Integrated Laboratory Plant. *Crystals* **2021**, 11.6. DOI: `10.3390/cryst11060713`.

[117] Huang, T., Yang, G., and Tang, G.: A fast two-dimensional median filtering algorithm. *IEEE Transactions on Acoustics, Speech, and Signal Processing* **1979**, 27.1, 13–18. DOI: `10.1109/TASSP.1979.1163188`.

[118] Buades, A., Coll, B., and Morel, J.-M.: A non-local algorithm for image denoising. In: *2005 IEEE Computer Society Conference on Computer Vision and Pattern Recognition (CVPR'05)*. Vol. 2. 2005, 60–65 vol. 2. DOI: `10.1109/CVPR.2005.38`.

[119] *redoxme FEC H-Cell 2x1.5ML - Flow Electrochemical H-Cell*. redoxme AB, Sweden, 2022. URL: `https://redox.me/collections/all/products/fec-h-cell-2x1-5-ml-flow-electrochemical-h-cell` (visited on 02/14/2024).

[120] Noack, J. and Tübke, J.: A Comparison of Materials and Treatment of Materials for Vanadium Redox Flow Battery. *ECS Transactions* **2010**, 25.35, 235. DOI: `10.1149/1.3414022`.

[121] Knehr, K. and Kumbur, E.: Open circuit voltage of vanadium redox flow batteries: Discrepancy between models and experiments. *Electrochemistry Communications* **2011**, 13.4, 342–345. DOI: `https://doi.org/10.1016/j.elecom.2011.01.020`.

[122] Roznyatovskaya, N., Noack, J., Pinkwart, K., and Tübke, J.: Aspects of electron transfer processes in vanadium redox-flow batteries. *Current Opinion in Electrochemistry* **2020**, 19. Fundamental and Theoretical Electrochemistry and Bioelectrochemistry, 42–48. DOI: `https://doi.org/10.1016/j.coelec.2019.10.003`.

[123] Zhou, W., Liu, W., Qin, M., Chen, Z., Xu, J., Cao, J., and Li, J.: Fundamental properties of TEMPO-based catholytes for aqueous redox flow batteries: effects of substituent groups and electrolytes on electrochemical properties, solubilities and battery performance. *RSC Adv.* **2020**, 10, 21839–21844. DOI: `10.1039/D0RA03424J`.

[124] Hayer, N. and Kohns, M.: Thermodynamically Rigorous Description of the Open Circuit Voltage of Redox Flow Batteries. *Journal of The Electrochemical Society* **2020**, 167.11, 110516. DOI: `10.1149/1945-7111/ab9e85`.

[125] Mourouga, G., Chery, D., Baudrin, E., Randriamahazaka, H., Schmidt, T. J., and Schumacher, J. O.: Estimation of activity coefficients for aqueous organic redox flow batteries: Theoretical basis and equations. *iScience* **2022**, 25.9, 104901. DOI: `https://doi.org/10.1016/j.isci.2022.104901`.

[126] Gerlach, D., Noack, J., Bischof, K., Boulch, C. L., and Trupp, S.: Techno-Economic Optimization of Flow Batteries Using the Optimization Potential to Prioritize Different Optimization Possibilities. *Journal of The Electrochemical Society* **2023**, 170.6, 060540. DOI: `10.1149/1945-7111/acdda0`.

[127] Geiser, J., Natter, H., Hempelmann, R., Morgenstern, B., and Hegetschweiler, K.: Photometrical Determination of the State-of-Charge in Vanadium Redox Flow Batteries Part II: In Combination with Open-Circuit-Voltage. *Zeitschrift für Physikalische Chemie* **2019**, 233.12, 1695–1711. DOI: `doi:10.1515/zpch-2019-1380`.

[128] Wolf, A., Baudrin, E., and Nirschl, H.: A Multiscale Flow Battery Modeling Approach Using Mass Transfer Coefficients. *Energy Technology* **2023**, 11.7, 2300175. DOI: `https://doi.org/10.1002/ente.202300175`.

[129] Zhang, D., Cai, Q., Taiwo, O. O., Yufit, V., Brandon, N. P., and Gu, S.: The effect of wetting area in carbon paper electrode on the performance of vanadium redox flow batteries: A three-dimensional lattice Boltzmann study. *Electrochimica Acta* **2018**, 283, 1806–1819. DOI: `https://doi.org/10.1016/j.electacta.2018.07.027`.

[130] Fu, Y., Bao, J., Zeng, C., Chen, Y., Xu, Z., Kim, S., and Wang, W.: A three-dimensional pore-scale model for redox flow battery electrode design analysis. *Journal of Power Sources* **2023**, 556, 232329. DOI: `https://doi.org/10.1016/j.jpowsour.2022.232329`.

[131] Xiong, Q., Baychev, T. G., and Jivkov, A. P.: Review of pore network modelling of porous media: Experimental characterisations, network constructions and applications to reactive transport. *Journal of Contaminant Hydrology* **2016**, 192, 101–117. DOI: `https://doi.org/10.1016/j.jconhyd.2016.07.002`.

[132] Gayon Lombardo, A., Simon, B. A., Taiwo, O., Neethling, S. J., and Brandon, N. P.: A pore network model of porous electrodes in electrochemical devices. *Journal of Energy Storage* **2019**, 24, 100736. DOI: `https://doi.org/10.1016/j.est.2019.04.010`.

[133] Zheng, Q., Li, X., Cheng, Y., Ning, G., Xing, F., and Zhang, H.: Development and perspective in vanadium flow battery modeling. *Applied Energy* **2014**, 132, 254–266. DOI: `https://doi.org/10.1016/j.apenergy.2014.06.077`.

[134] Zhang, D., Bertei, A., Tariq, F., Brandon, N., and Cai, Q.: Progress in 3D electrode microstructure modelling for fuel cells and batteries: transport and electrochemical performance. *Progress in Energy* **2019**, 1.1, 012003. DOI: `10.1088/2516-1083/ab38c7`.

[135] Wood, B. D., He, X., and Apte, S. V.: Modeling Turbulent Flows in Porous Media. *Annual Review of Fluid Mechanics* **2020**, 52.Volume 52, 2020, 171–203. DOI: `https://doi.org/10.1146/annurev-fluid-010719-060317`.

[136] Shah, A., Watt-Smith, M., and Walsh, F.: A dynamic performance model for redox-flow batteries involving soluble species. *Electrochimica Acta* **2008**, 53.27, 8087–8100.

[137] Al-Fetlawi, H., Shah, A., and Walsh, F.: Non-isothermal modelling of the all-vanadium redox flow battery. *Electrochimica Acta* **2009**, 55.1, 78–89. DOI: `https://doi.org/10.1016/j.electacta.2009.08.009`.

[138] Al-Fetlawi, H., Shah, A., and Walsh, F.: Modelling the effects of oxygen evolution in the all-vanadium redox flow battery. *Electrochimica Acta* **2010**, 55.9, 3192–3205. DOI: `https://doi.org/10.1016/j.electacta.2009.12.085`.

[139] Ma, X., Zhang, H., and Xing, F.: A three-dimensional model for negative half cell of the vanadium redox flow battery. *Electrochimica Acta* **2011**, 58, 238–246. DOI: `https://doi.org/10.1016/j.electacta.2011.09.042`.

[140] Wandschneider, F., Finke, D., Grosjean, S., Fischer, P., Pinkwart, K., Tübke, J., and Nirschl, H.: Model of a vanadium redox flow battery with an anion exchange membrane and a Larminie-correction. *Journal of Power Sources* **2014**, 272, 436–447. DOI: `https://doi.org/10.1016/j.jpowsour.2014.08.082`.

[141] Franco, A. A., Rucci, A., Brandell, D., Frayret, C., Gaberscek, M., Jankowski, P., and Johansson, P.: Boosting Rechargeable Batteries R&D by Multiscale Modeling: Myth or Reality? *Chemical Reviews* **2019**, 119.7. PMID: 30859816, 4569–4627. DOI: `10.1021/acs.chemrev.8b00239`.

[142] Bao, J., Murugesan, V., Kamp, C. J., Shao, Y., Yan, L., and Wang, W.: Machine Learning Coupled Multi-Scale Modeling for Redox Flow Batteries. *Advanced Theory and Simulations* **2020**, 3.2, 1900167. DOI: `https://doi.org/10.1002/adts.201900167`.

[143] Tao, H., Chen, G., Lian, C., Liu, H., and Coppens, M.-O.: Multiscale modeling of ion transport in porous electrodes. *AIChE Journal* **2022**, 68.4, e17571. DOI: `https://doi.org/10.1002/aic.17571`.

[144] Yu, J. and Franco, A. A.: Mesoscale Modeling and Simulation for Flow Batteries. In: *Flow Batteries*. John Wiley & Sons, Ltd, 2023. Chap. 16, 355–378. DOI: `https://doi.org/10.1002/9783527832767.ch16`. URL: `https://onlinelibrary.wiley.com/doi/abs/10.1002/9783527832767.ch16`.

[145] Lewis, W. K. and Whitman, W. G.: Principles of Gas Absorption. *Industrial & Engineering Chemistry* **1924**, 16.12, 1215–1220. DOI: `10.1021/ie50180a002`.

[146] Storck, A., Robertson, P., and Ibl, N.: Mass transfer study of three-dimensional electrodes composed of stacks of nets. *Electrochimica Acta* **1979**, 24.4, 373–380. DOI: `https://doi.org/10.1016/0013-4686(79)87022-X`.

[147] Fedkiw, P. S. and Newman, J.: Mass-transfer coefficients in packed beds at very low reynolds numbers. *International Journal of Heat and Mass Transfer* **1982**, 25.7, 935–943. DOI: `https://doi.org/10.1016/0017-9310(82)90069-2`.

[148] Appel, P. W. and Newman, J.: Application of the limiting current method to mass transfer in packed beds at very low reynolds numbers. *AIChE Journal* **1976**, 22.6, 979–984. DOI: `https://doi.org/10.1002/aic.690220605`.

[149] Kinoshita, K. and Leach, S. C.: Mass-Transfer Study of Carbon Felt, Flow-Through Electrode. *Journal of The Electrochemical Society* **1982**, 129.9, 1993. DOI: `10.1149/1.2124338`.

[150] You, X., Ye, Q., and Cheng, P.: The Dependence of Mass Transfer Coefficient on the Electrolyte Velocity in Carbon Felt Electrodes: Determination and Validation. *Journal of The Electrochemical Society* **2017**, 164, E3386–E3394. DOI: `10.1149/2.0401711jes`.

[151] Milshtein, J. D., Tenny, K. M., Barton, J. L., Drake, J., Darling, R. M., and Brushett, F. R.: Quantifying Mass Transfer Rates in Redox Flow Batteries. *Journal of The Electrochemical Society* **2017**, 164.11, E3265. DOI: `10.1149/2.0201711jes`.

[152] Murthy, S. K., Sharma, A. K., Choo, C., and Birgersson, E.: Analysis of Concentration Overpotential in an All-Vanadium Redox Flow Battery. *Journal of The Electrochemical Society* **2018**, 165.9, A1746–A1752. DOI: `10.1149/2.0681809jes`.

[153] Bayanov, I. M. and Vanhaelst, R.: The numerical simulation of vanadium RedOx flow batteries. *Journal of Mathematical Chemistry* **2011**, 49, 1572–8897. DOI: `10.1007/s10910-011-9872-x`.

[154] Zheng, Q., Zhang, H., Xing, F., Ma, X., Li, X., and Ning, G.: A three-dimensional model for thermal analysis in a vanadium flow battery. *Applied Energy* **2014**, 113, 1675–1685. DOI: `https://doi.org/10.1016/j.apenergy.2013.09.021`.

[155] Wolf, A., Noack, J., Krause, M. J., and Nirschl, H.: Enhancing Flow Batteries: Topology Optimization of Electrode Porosity and Shape Optimization of Cell Design. *Energy Technology* **2024**, 12.7, 2400244. DOI: `https://doi.org/10.1002/ente.202400244`.

[156] Luo, Y., Sigmund, O., Li, Q., and Liu, S.: Topology optimization of structures with infill-supported enclosed voids for additive manufacturing. *Additive Manufacturing* **2022**, 55, 102795. DOI: `https://doi.org/10.1016/j.addma.2022.102795`.

[157] Behrou, R., Kirsch, K., Ranjan, R., and Guest, J. K.: Topology optimization of additively manufactured fluidic components free of internal support structures. *Computer Methods in Applied Mechanics and Engineering* **2022**, 389, 114270. DOI: `https://doi.org/10.1016/j.cma.2021.114270`.

[158] Gaynor, A. T. and Johnson, T. E.: Eliminating occluded voids in additive manufacturing design via a projection-based topology optimization scheme. *Additive Manufacturing* **2020**, 33, 101149. DOI: `https://doi.org/10.1016/j.addma.2020.101149`.

[159] Alexandersen, J. and Andreasen, C. S.: A Review of Topology Optimisation for Fluid-Based Problems. *Fluids* **2020**, 5.1. DOI: `10.3390/fluids5010029`.

[160] Aramendia, I., Fernandez-Gamiz, U., Martinez-San-Vicente, A., Zulueta, E., and Lopez-Guede, J. M.: Vanadium Redox Flow Batteries: A Review Oriented to Fluid-Dynamic Optimization. *Energies* **2021**, 14.1. DOI: `10.3390/en14010176`.

[161] C., K. and H., S.: Topology Optimization of Gas Flow Channels Routes in an Automotive Fuel Cell. *Int J Automot Technol* **2012**, 13.5, 783–789. DOI: `10.1007/s12239-012-0078-4`.

[162] Behrou, R., Pizzolato, A., and Forner-Cuenca, A.: Topology optimization as a powerful tool to design advanced PEMFCs flow fields. *International Journal of Heat and Mass Transfer* **2019**, 135, 72–92. DOI: `https://doi.org/10.1016/j.ijheatmasstransfer.2019.01.050`.

[163] Li, Q., Duan, Y., Chai, D., Zhang, X., Min, X., and Li, G.: Topology optimization of microstructure of solid-oxide fuel cell anode to minimize thermal mismatch. *International Journal of Energy Research* **2021**, 45.2, 3214–3230. DOI: `https://doi.org/10.1002/er.6018`.

[164] Zhang, Z., Zhang, J., and Zhang, T.: Endplate Design and Topology Optimization of Fuel Cell Stack Clamped with Bolts. *Sustainability* **2022**, 14.8. DOI: `10.3390/su14084730`.

[165] Chen, C.-H., Yaji, K., Yamasaki, S., Tsushima, S., and Fujita, K.: Computational design of flow fields for vanadium redox flow batteries via topology optimization. *Journal of Energy Storage* **2019**, 26, 100990. DOI: `https://doi.org/10.1016/j.est.2019.100990`.

[166] Beck, V. A., Wong, J. J., Jekel, C. F., Tortorelli, D. A., Baker, S. E., Duoss, E. B., and Worsley, M. A.: Computational design of microarchitected porous electrodes for redox flow batteries. *Journal of Power Sources* **2021**, 512, 230453. DOI: `https://doi.org/10.1016/j.jpowsour.2021.230453`.

[167] Gilmore, N., Hassanzadeh-Barforoushi, A., Timchenko, V., and Menictas, C.: Manifold configurations for uniform flow via topology optimisation and flow visualisation. *Applied Thermal Engineering* **2021**, 183, 116227. DOI: `https://doi.org/10.1016/j.applthermaleng.2020.116227`.

[168] He, Q., Yu, J., Guo, Z., Sun, J., Zhao, S., Zhao, T., and Ni, M.: Modeling of vanadium redox flow battery and electrode optimization with different flow fields. *e-Prime - Advances in Electrical Engineering, Electronics and Energy* **2021**, 1, 100001. DOI: `https://doi.org/10.1016/j.prime.2021.100001`.

[169] Lin, T. Y., Baker, S. E., Duoss, E. B., and Beck, V. A.: Topology Optimization of 3D Flow Fields for Flow Batteries. *Journal of The Electrochemical Society* **2022**, 169.5, 050540. DOI: `10.1149/1945-7111/ac716d`.

[170] Charoen-amornkitt, P., Alizadeh, M., Suzuki, T., and Tsushima, S.: Entropy generation analysis during adjoint variable-based topology optimization of porous reaction-diffusion systems under various design dimensionalities. *International Journal of Heat and Mass Transfer* **2023**, 202, 123725. DOI: `https://doi.org/10.1016/j.ijheatmasstransfer.2022.123725`.

[171] Wang, J., Liu, X., and Wang, Y.: Topology optimization of micro-channel reactors using an improved multi-objective algorithm. *Chemical Engineering Journal* **2023**, 458, 141420. DOI: `https://doi.org/10.1016/j.cej.2023.141420`.

[172] Tang, A., Bao, J., and Skyllas-Kazacos, M.: Studies on pressure losses and flow rate optimization in vanadium redox flow battery. *Journal of Power Sources* **2014**, 248, 154–162. DOI: `https://doi.org/10.1016/j.jpowsour.2013.09.071`.

[173] Forner-Cuenca, A. and Brushett, F. R.: Engineering porous electrodes for next-generation redox flow batteries: recent progress and opportunities. *Current Opinion in Electrochemistry* **2019**, 18. Energy Storage · Energy Transformation, 113–122. DOI: `https://doi.org/10.1016/j.coelec.2019.11.002`.

[174] Guan, X., Skyllas-Kazacos, M., and Menictas, C.: A Three-Dimensional Hydraulic Stack Model for Redox Flow Batteries Considering Porosity Variations in Porous Felt Electrodes and Bypass Flow in Side Gaps. *Batteries* **2023**, 9.7. DOI: `10.3390/batteries9070359`.

[175] Prumbohm, E. and Wehinger, G. D.: Exploring Flow Characteristics in Vanadium Redox-Flow Batteries: Optical Measurements and CFD Simulations. *Chemie Ingenieur Technik* **2019**, 91.6, 900–906. DOI: `https://doi.org/10.1002/cite.201800164`.

[176] Wan, C. T.-C., Jacquemond, R. R., Chiang, Y.-M., Forner-Cuenca, A., and Brushett, F. R.: Engineering Redox Flow Battery Electrodes with Spatially Varying Porosity Using Non-Solvent-Induced Phase Separation. *Energy Technology* **2023**, 11.8, 2300137. DOI: `https://doi.org/10.1002/ente.202300137`.

[177] Huang, Z., Mu, A., Wu, L., and Wang, H.: Vanadium redox flow batteries: Flow field design and flow rate optimization. *Journal of Energy Storage* **2022**, 45, 103526. DOI: `https://doi.org/10.1016/j.est.2021.103526`.

[178] Xiao, G., Yang, G., Zhao, S., Xia, L., Chu, F., and Tan, Z.: Battery performance optimization and multi-component transport enhancement of organic flow battery based on channel section reconstruction. *Energy* **2022**, 258, 124757. DOI: `https://doi.org/10.1016/j.energy.2022.124757`.

[179] Wu, M., Zhao, T., Zhang, R., Jiang, H., and Wei, L.: A Zinc–Bromine Flow Battery with Improved Design of Cell Structure and Electrodes. *Energy Technology* **2018**, 6.2, 333–339. DOI: `https://doi.org/10.1002/ente.201700481`.

[180] Gurieff, N., Keogh, D. F., Baldry, M., Timchenko, V., Green, D., Koskinen, I., and Menictas, C.: Mass Transport Optimization for Redox Flow Battery Design. *Applied Sciences* **2020**, 10.8. DOI: `10.3390/app10082801`.

[181] Kok, M. D. R., Khalifa, A., and Gostick, J. T.: Multiphysics Simulation of the Flow Battery Cathode: Cell Architecture and Electrode Optimization. *Journal of The Electrochemical Society* **2016**, 163.7, A1408. DOI: `10.1149/2.1281607jes`.

[182] Yue, M., Zheng, Q., Xing, F., Zhang, H., Li, X., and Ma, X.: Flow field design and optimization of high power density vanadium flow batteries: A novel trapezoid flow battery. *AIChE Journal* **2018**, 64.2, 782–795. DOI: `https://doi.org/10.1002/aic.15959`.

[183] Yoon, S. J., Kim, S., and Kim, D. K.: Optimization of local porosity in the electrode as an advanced channel for all-vanadium redox flow battery. *Energy* **2019**, 172, 26–35. DOI: `https://doi.org/10.1016/j.energy.2019.01.101`.

[184] Chen, W. and Kang, J.: Optimization of electrolyte flow and vanadium ions conversion by utilizing variable porosity electrodes in vanadium redox flow batteries. *Chemical Physics* **2020**, 529, 110577. DOI: `https://doi.org/10.1016/j.chemphys.2019.110577`.

[185] Morris, M. D.: Factorial Sampling Plans for Preliminary Computational Experiments. *Technometrics* **1991**, 33.2, 161–174. (Visited on 10/16/2023).

[186] Roznyatovskaya, N., Noack, J., Mild, H., Fühl, M., Fischer, P., Pinkwart, K., Tübke, J., and Skyllas-Kazacos, M.: Vanadium Electrolyte for All-Vanadium Redox-Flow Batteries: The Effect of the Counter Ion. *Batteries* **2019**, 5.1. DOI: `10.3390/batteries5010013`.

[187] Roe, S., Menictas, C., and Skyllas-Kazacos, M.: A High Energy Density Vanadium Redox Flow Battery with 3 M Vanadium Electrolyte. *Journal of The Electrochemical Society* **2015**, 163.1, A5023. DOI: `10.1149/2.0041601jes`.